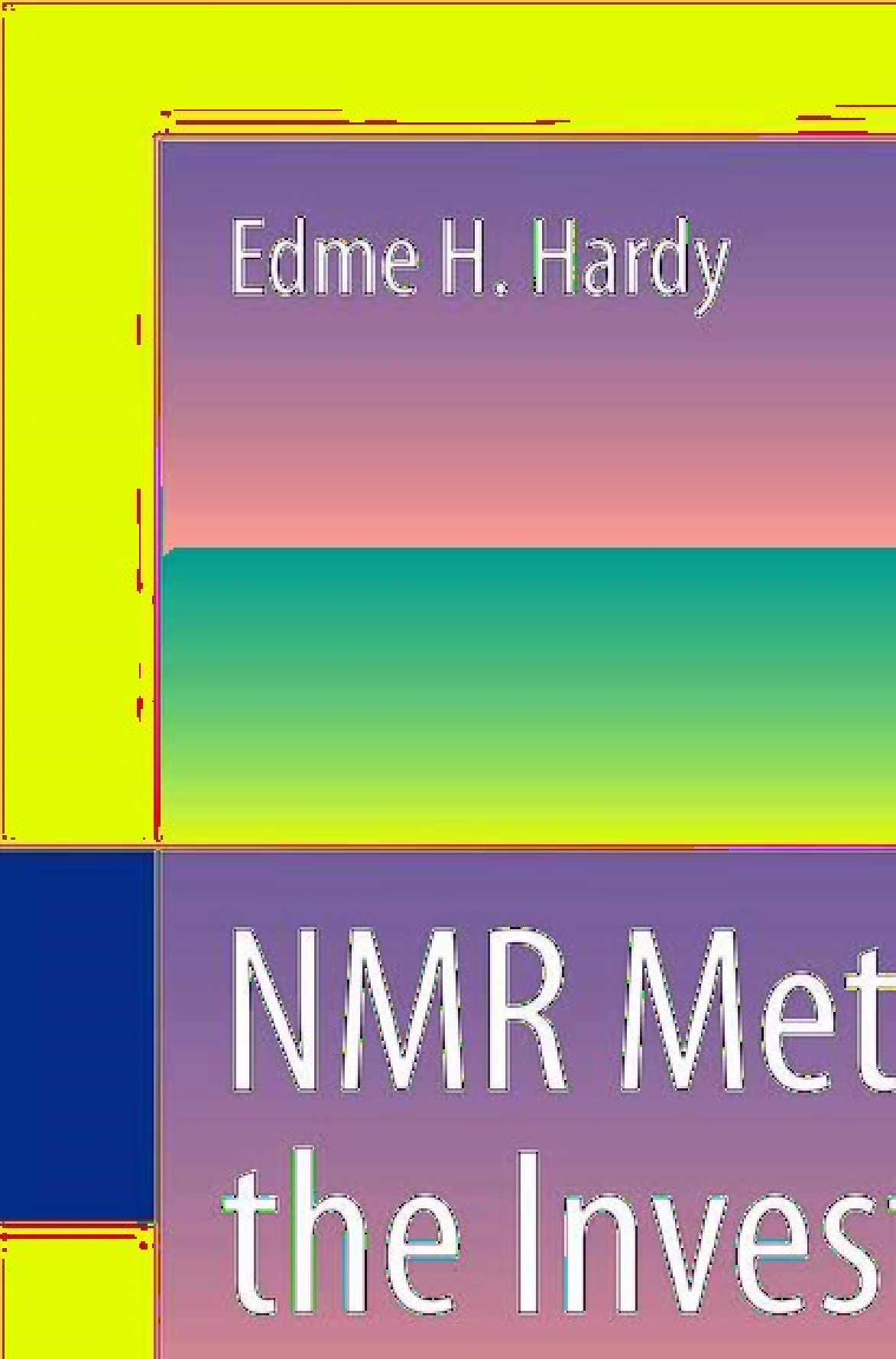
Edme H. Hardy
NMR Met
the Inves

NMR Methods for the Investigation of Structure and Transport

Edme H. Hardy

NMR Methods for the Investigation of Structure and Transport

Springer

Dr. Edme H. Hardy
Karlsruher Institut für
Technologie (KIT)
Institut für Mechanische
Verfahrenstechnik und Mechanik
Adenauerring 20b
76131 Karlsruhe
Germany
Edme.Hardy@kit.edu

ISBN 978-3-642-21627-5 e-ISBN 978-3-642-21628-2
DOI 10.1007/978-3-642-21628-2
Springer Heidelberg Dordrecht London New York

Library of Congress Control Number: 2011938145

Printed on acid-free paper

Springer is part of Springer Science+Business Media (www.springer.com)

Foreword

Nuclear magnetic resonance (NMR) is a physical phenomenon with many applications in medicine, science, and engineering. As the electronics and computer technology advances, the NMR instrumentation benefits, and along with it, the NMR methods for acquiring information expand as well as the areas of application. Originally physicists aimed at determining the gyro-magnetic ratio. As the magnetic fields could be made more homogeneous, line splittings were observed and found to be useful for determining molecular structures. The advent of computers led to a dramatic sensitivity gain by measuring in the time domain and computing the spectra by Fourier transformation of the measured data. This subsequently evolved into multidimensional NMR and NMR imaging, where the demands on computing power and advanced electronics are even more stringent. Superconducting magnets are being engineered at ever-increasing field strength to improve the detection sensitivity and information content in NMR spectra. Molecular biology and medicine were revolutionized by the advent of multidimensional NMR spectroscopy and NMR imaging.

Apart from chemical analysis and medical diagnostics, NMR turns out to be a great tool for studying soft matter, porous media, and similar objects. With the appropriate methods, spectra can be measured at high resolution, images be obtained with an abundance of contrast features, and relaxation signals be exploited to study fluid-filled porous media and devices. With NMR being so well established in chemistry and medicine, one may ask which is the next most important use of NMR. Probably this is in the oil industry for logging oil wells with portable devices that are lowered into the borehole to inspect the borehole walls. This is a genuine engineering application based on relaxation and diffusion measurements with instruments that use the low magnetic fields of permanent magnets instead of the high fields of superconducting magnets used elsewhere. Are there other uses of NMR in engineering? Clearly, there are a few groups worldwide that do research in this area. But it is difficult to convey the use and advantages of NMR to the engineering community. First of all, NMR is a complicated business. There are standard experiments only for some routine chemical analysis and medical imaging applications. Engineering applications require an in-depth understanding of the

NMR machine and, moreover, even modifications to address the particular needs of an emerging new community of users. Second, the types of applications where NMR is needed to advance the understanding of technical phenomena are by no means simple to identify.

This book addresses both issues. NMR methods and hardware explain the depth necessary to tackle engineering applications. These applications are in a way more demanding than chemical analysis and medical imaging as they are rather diverse. All three major methodical branches of NMR are needed. They are relaxometry, imaging, and spectroscopy. And imaging is not just about getting pictures but also about quantifying motion and transport phenomena. Also the hardware demands differ; measurements should be conducted at the site of the object outside the laboratory, where desktop instruments with permanent come in handy. But what are the applications? This book provides a convincing answer with descriptions of ten selected applications of technical relevance.

I find this book most useful to graduate students and scientists working in the chemical and engineering sciences. It is written with great insight into both the NMR methodology and the demands from the engineering community. I hope that it finds many readers and good use in advancing science and technology.

Aachen *Bernhard Blümich*

Preface

This book originates from activities in connection with a research unit at the Department of Chemical and Process Engineering of the Universität Karlsruhe (TH), now Karlsruhe Institute of Technology (KIT), applying nuclear magnetic resonance (NMR) in engineering sciences.[1] The actual research was accompanied by frequent seminars and scientific events. A lecture intended mainly for the Ph.D. students involved in the projects was implemented.[2] The presented NMR fundamentals are an extension of this lecture. Frequent tasks of quantitative image analysis are summarized later. In the experimental part, also specific hardware developments are described. The presented applications equally originate from this research unit.

The text is mainly intended for readers with engineering background applying NMR methods or considering to do so. Quantum mechanics are avoided in favor of a classical description. However, the relevant equations are worked out. Simple problems with solutions allow to check whether the fundamentals are understood.

Many persons from Karlsruhe contributed to this book. Prof. Buggisch initiated the research unit and led it with exceptional competence. He also thoroughly scrutinized the German version of this text. Prof. Nirschl suggested the idea of this book. Prof. Reimert organized the continuation of the research unit after the DFG funding as well as Prof. Kasper, Prof. Kind, Prof. Nirschl, and Prof. Elsner. Prof. Nirschl, Prof. Kind, Prof. Wilhelm, and Prof. Elsner contributed in the establishment of the shared research group confided to Dr. Guthausen, extending in particular research involving low-field NMR. I especially owe thanks to Mr. Mertens for his engaged and successful work on the rheometry project with Dr. Hochstein. Fortunately, it could be further developed into combined rheo-TD-NMR, thanks to Dr. Nestle and Dr. Wassmer from BASF SE, Ludwigshafen, and Ms. Herold. Technical assistance from Mr. Oliver and the workshops is gratefully acknowledged.

[1] Forschergruppe 338 der Deutschen Forschungsgemeinschaft (DFG) "Anwendungen der Magnetischen Resonanz zur Aufklärung von Stofftransportprozessen in dispersen Systemen," 1999–2005.

[2] Magnetic Resonance Imaging: Fundamentals and Applications in Engineering Sciences.

Productive collaborations took place with Mr. Dietrich, Dr. Erk, Dr. Geißler, Dr. Gordalla, Ms. Große, Ms. Hecht, Dr. Heinen, Mr. Hieke, Dr. Hoferer, Dr. Holz, Dr. Knoerzer, Ms. Kutzer, Dr. Lankes, Dr. Lehmann, Mr. Metzger, Mr. Neutzler, Mr. Nguyen, Dr. Regier, Dr. Schweitzer from IFP, Lyon, Mr. Spelter, Mr. Stahl, Dr. Terekhov, Dr. van Buren, Ms. von Garnier, and Mr. Wolf. Finally, I owe many thanks to my parents, wife, and children for their support and comprehension.

Assistance by Dr. Hertel from Springer is gratefully acknowledged.

Karlsruhe *Edme H. Hardy*

Contents

Acronyms

AlNiCo	Magnet material consisting of iron, aluminum, nickel, copper, cobalt
CPMG	Carr-Purcell-Meiboom-Gill
CSI	Chemical shift imaging
DW	Sampling intervall (“dwell time”)
FFT	Fast Fourier transform
FID	Free induction decay
FOV	Field of view
GEFI	Gradient echo fast imaging
GRP	Glass-fiber reinforce plastic
MRI	Magnetic resonance imaging
MRT	Magnetic resonance tomography
NdFeB	Magnet material consisting of neodymium, iron, boron (Nd2Fe14B)
NMR	Nuclear magnetic resonance
PDR	Pressure difference recording
PFG	Pulsed-field-gradient
PGSE	Pulsed-gradient spin echo
PGSTE	Pulsed-gradient stimulated echo
PMMA	Polymethylmethacrylate
PSF	Point spread function
PTFE	Polytetrafluoroethylene
PVC	Polyvinylchloride
PVP	Polyvinylpyrrolidone
ppm	Parts per million
RARE	Rapid acquisition with relaxation enhancement
rf	Radio frequency
SE	Spin echo
SmCo	Magnet material consisting of samarium and cobalt
SNR	Signal-to-noise ratio
SPI	Single-point imaging
STE	Stimulated echo
TR	Temperature recording
VPDF	Velocity probability-density function

Symbols and Constants

List of Latin symbols. Vectors are set in boldface

Symbol	Unit	Meaning
a_c	m	Coil radius
$(a)_{nm}$	p. u.	Distance matrix in pixel units
$\bar{a}_k$	p. u.	Vector with average distances
$\boldsymbol{B}$	T	Total magnetic flux density
$\boldsymbol{B_0}$	T	Magnetic flux density of the polarizing field
$\boldsymbol{B_1}$	T	Magnetic flux density of the transverse rf field
$\boldsymbol{B}_1^{\mathrm{dc}}$	T	Field of reception coil supplied with dc current
B_c	S	Coil susceptance
b_c	m	Coil length
C_m	F	Series trimmer capacitor
C_p	F	Parallel capacitor
C_s	F	Series capacitor
C_t	F	Parallel trimmer capacitor
c	p. u.	Minimum pore-center distance
D	$\mathrm{m^2\,s^{-1}}$	Translational self-diffusion coefficient
d_f	m	Average window diameter (sponge)
d_{ls}	–	Parameter in the assignment liquid $\rightarrow$ solid
d_{sl}	–	Parameter in the assignment solid $\rightarrow$ liquid
e	–	Distribution of rf field within sample
$(\hat{e})_{nmo}$	–	Distortion by B_1 inhomogeneity
E_m	J	Energy in state with eigenvalue m
$\boldsymbol{e_\alpha}$	–	Unit vector in α direction
$\boldsymbol{e}_{y,\theta,\varphi}$	–	Line with direction (θ, φ) passing through $\boldsymbol{y}$
F	–	Noise figure of preamplifier
$\boldsymbol{G}$	T/m	Gradient of z component of the magnetic flux density
$\boldsymbol{G}_\mathrm{m}$	T/m	Gradient mismatch
$\boldsymbol{G}_\mathrm{r}$	T/m	Read gradient
$\boldsymbol{G}_\mathrm{p}$	T/m	Phase gradient (imaging) or permanent gradient (imperfections)
$\boldsymbol{G}_\mathrm{s}$	T/m	Slice gradient
G_c	S	Coil conductance

(continued)

List of Symbols (continued)

Symbol	Unit	Meaning
$\boldsymbol{H}$	A/m	Magnetic field, in vacuum $\boldsymbol{B} = \mu_0 \boldsymbol{H}$
$\hat{H}_0$	J	Hamilton operator for Zeeman splitting
h_i	p. u.	Distance level
I	–	Nuclear spin quantum number
$\boldsymbol{I}$	Js	Angular momentum
$\hat{\boldsymbol{I}}$	Js	Nuclear spin vector operator
I^{dc}	A	Direct current
J	–	Number of local maximums with minimum distance
K	–	Number of local maximums without minimum distance
$\boldsymbol{k}$	rad/m	Wave vector in reciprocal distance space
$k_{\alpha\,\mathrm{inc}}$	rad/m	Increment of wave vector in α direction
L_c	H	Coil inductivity
$(L)_{kl}$	–	Low-pass matrix
L_α	m	Length of FOV in α direction
l	p. u.	Edge length in pixel units
l_c	m	Conductor length
$\boldsymbol{M}$	Am^{-1}	Macroscopic magnetization of observed nucleus
M	–	Row length, number of columns
m	–	Magnetic quantum number
M^+	–	Nondimensionalized transverse complex magnetization
M_z^{eq}	Am^{-1}	Magnetization in thermal equilibrium
N	–	Column length, number of rows
n	a. u.	Noise
n_c	–	Number of coil turns
N_α	–	Number of discretization points in α direction
N_{A}	–	Number of averages
N_{S}	–	Number of nuclear spins
O	–	Set of indexes (first index) or number of slices
P	–	Set of indexes (second index)
P_m	–	Population probability for state m
$P_{\mathrm{N}}(\mathrm{arg})$	1/[arg]	Normal distribution
$P_{\mathrm{Ra}}(\mathrm{arg})$	1/[arg]	Rayleigh distribution
$P_{\mathrm{Ri}}(\mathrm{arg})$	1/[arg]	Rice distribution
$\boldsymbol{q}$	rad/m	Wave vector in reciprocal displacement space
Q	$\mathrm{m}^3\mathrm{s}^{-1}$	Flow rate
$\boldsymbol{R}$	m	Displacement vector
R	m	Sphere radius
R_c	Ω	Coil resistance
$\boldsymbol{r}$	m	Position vector
r_c	m	Conductor radius
$r_{\alpha\,\mathrm{inc}}$	m	Increment of position vector in α direction
s	[arg]	Parameter of distribution density P(arg)
$\tilde{s}^2$	–	Variance of ideal discrete spin density
$\hat{s}^2$	–	Variance of discrete image with artifacts
s_e^2	–	Variance contribution by B_1 inhomogeneity

(continued)

List of Symbols (continued)

Symbol	Unit	Meaning
s_n^2	–	Variance contribution by noise
S_C	m^2	Surface by Crofton formula
S_D	m^2	Surface by triangulation
S_V	1/m	Specific surface
T	K	Temperature
T_c	K	Coil temperature
T_1	s	Longitudinal, spin-lattice relaxation time
T_2	s	Transverse relaxation time
T_2^*	s	Effective transverse relaxation time
T_2^+	s	Relaxation time for inhomogeneous broadening
t	s	Time
t_E	s	Time of spin echo
t_{expt}	s	Experimental time
t_{GE}	s	Time of gradient echo
t_R	s	Duration with relaxation
t_S	m	Strut diameter
U	V	Induced voltage
U_n	V	Noise voltage
U^+	–	Nondimensionalized signal
$\boldsymbol{v}$	m/s	Velocity vector
u, v, w	m/s	Components of velocity vector
V	m^3	Volume
X	–	Solid phase
Y_c	S	Coil admittance (complex conductance)
$\boldsymbol{y}$	–	Point in plane perpendicular to $\boldsymbol{e}_{y,\theta,\varphi}$
Z	Ω	Impedance
Z_0	Ω	System impedance
Z_c	Ω	Coil impedance
$(z)_{nm}$	–	Matrix with assignment to segmented regions

List of Greek symbols. Vectors are set in boldface

Symbol	Unit	Meaning
α	–	Packing density
χ	–	One-dimensional Euler number
Δ	s	Gradient pulses separation
δ(arg)	1/[arg]	Dirac function (distribution)
δ	s	Gradient duration
δ_s	m	Skin depth
ε	–	Porosity
Λ	–	Binary matrix with neighborhood positions
μ	[arg]	Parameter of distribution density P(arg)

(continued)

List of Greek symbols (continued)

Symbol	Unit	Meaning
$\boldsymbol{\mu}$	Am^2	Magnetic dipole moment (classical)
$\hat{\boldsymbol{\mu}}$	Am^2	Nuclear magnetic dipole moment (vector operator)
μ_r	–	Relative permeability
$\langle \mu_z \rangle$	Am^2	Average z component of nuclear magnetic dipole moment
Ω	rad/s	Spectroscopic frequency shift
$\boldsymbol{\omega}$	rad/s	Angular velocity
$\boldsymbol{\omega_0}$	rad/s	Angular velocity of Larmor precession
$\boldsymbol{\omega_1}$	rad/s	Angular velocity of Rabi nutation
$\boldsymbol{\omega}_{\mathrm{rf}}$	rad/s	Angular velocity of rf field
φ	rad	Azimuth angle
ϕ	rad	Phase of complex transverse magnetization
ϕ_1	rad	Phase of rf field
ρ	m^{-3}	Spin density
$(\tilde{\rho})_{nm}$	–	Discrete spin density
$(\hat{\rho})_{nm}$	–	Discrete spin density with artifacts
ρ_c	–	Constant spin density
ρ_s	–	Threshold for spin density
$(\tilde{\rho}')_{nm}$	–	Binary filtered Matrix $(\tilde{\rho})_{nm}$
$(\tilde{\rho}'')_{nm}$	–	Filtered Matrix $(\tilde{\rho}')_{nm}$
$(\tilde{\rho}_f)_{nm}$	–	Discrete spin density-Matrix with low-pass filter
σ	–	Isotropic magnetic shielding
σ_c	$\Omega^{-1}\mathrm{m}^{-1}$	Conductance
τ	s	Duration of rf pulse or pulse separation
Θ	–	Binary matrix with assigned positions
θ	rad	Polar angle
ξ	–	Bitshift vector for binary matrix
$\boldsymbol{\xi}$	[args]	NMR-relevant parameter vector for spin density

Constants

Constant	Value	Meaning
$\hbar$	$1.055 \times 10^{-34}\,\mathrm{J\,s}$	Planck constant
k	$1.381 \times 10^{-23}\,\mathrm{J/K}$	Boltzmann constant
$\mathcal{N}_\mathrm{A}$	$6.022 \times 10^{23}\,\mathrm{mol}^{-1}$	Avogadro constant
γ	$2.675 \times 10^{8}\,\mathrm{rad\,s}^{-1}\,\mathrm{T}^{-1}$	Gyromagnetic ratio of the proton (^{1}H)
$\gamma(^{13}\mathrm{C})$	$0.673 \times 10^{8}\,\mathrm{rad\,s}^{-1}\,\mathrm{T}^{-1}$	Gyromagnetic ratio of ^{13}C
$\gamma(^{19}\mathrm{F})$	$2.516 \times 10^{8}\,\mathrm{rad\,s}^{-1}\,\mathrm{T}^{-1}$	Gyromagnetic ratio of ^{19}F
$\gamma(^{31}\mathrm{P})$	$1.084 \times 10^{8}\,\mathrm{rad\,s}^{-1}\,\mathrm{T}^{-1}$	Gyromagnetic ratio of ^{31}P
μ_0	$4\pi \times 10^{-7}\,\mathrm{H/m}$	Magnetic constant

Chapter 1
Introduction

This book deals with the application of nuclear magnetic resonance (NMR [1]) in engineering sciences. Special emphasis is put on methods including spatial resolution (magnetic resonance imaging, MRI). The use of permanent-magnet systems is also treated.

The engineering competence was brought in by numerous colleagues that are acknowledged in the preface. In the common publications [1–23, 25] referred to in the following, details on the engineering background and investigations with other methods are reported.

First, fundamentals of the NMR methods and pertinent data analysis are summarized in Chap. 2. Concepts from quantum mechanics are not essential for the understanding of the methods used and are only briefly mentioned at the beginning. However, where helpful for the understanding, the relevant equations are worked out.

Obtaining quantitative results is a key issue. Qualitative evidence, that can already be valuable in medical applications, often represent no progress in engineering sciences. Thus the quantitative relation between the data obtained by discrete inverse Fourier transform of raw data and the continuous function of interest is formulated. The influence of gradient imperfections on velocity measurements is assessed. This is of particular importance for experiments using simpler permanent-magnet systems. Application of a post processing taking corresponding shifts in Fourier space into account is presented. For relaxation measurements on flowing samples, a data analysis including effects of inhomogeneous fields for polarization, excitation, and detection is elaborated.

In the domain of volume-image analysis an efficient implementation of a segmentation algorithm is presented. In the cases studied, the procedure gives better results than the standard watershed transformation. For the quantitative analysis of the uniformity of mixtures, the influence of artifacts on the signal variance is calculated. Finally, a method for automatic nonlinear phase correction of volume images is presented. For measurements with low signal-to-noise ratio (SNR), phase correction markedly improves the quantitative analysis.

E.H. Hardy, *NMR Methods for the Investigation of Structure and Transport*,
DOI 10.1007/978-3-642-21628-2_1, © Springer-Verlag Berlin Heidelberg 2012

Experimental aspects of NMR measurements are collected in Chap. 3. Emphasis is put on specifically designed hardware. Magnets, probes, and gradient coils are treated. Concerning probes, impedance matching is explained in detail. The design of an actively shielded gradient system for transverse field geometry using the target-field method is described.

The presentation of applications in Chap. 4 is based on the preceding chapters. Rather specific theoretical or experimental aspects are treated in the context of the respective application. They stem from the domains of mechanical process engineering (gas filtration, solid–liquid separation, powder mixing, rheometry), chemical process engineering (hydration reaction in a trickle-bed reactor, structure of ceramic sponges), bio process engineering (flow and growth in a biofilm reactor), and food process engineering (temperature mapping during microwave drying, droplet-size distribution in emulsions).

Exemplary implementations in MATLAB® are listed in Chap. 6. Further chapters present a new line-shape model for the "indirect hard modeling" of NMR spectra, diverse calculations on gradient echoes as well as an analytical expression for imaging in an inhomogeneous gradient field with realistic shape.

This book is not a complete description of NMR applications in chemical and process engineering, for this the reader is referred to the actual book edited by Stapf and Han [24]. However, it aims to provide tools required for the successful implementation of new applications. In the complex field of engineering, standard NMR methods and hardware are often not available and solid fundamentals are required to make best use of the technique.

References

1. Bloch F (1946) Nuclear induction. Phys Rev 70:460–474
2. Buggisch H, Hardy EH, Heinen C, Tillich (2004) Investigation of structure and mass transport processes in disperse systems by nuclear magnetic resonance. In: Zhuang F, Li JC (eds) Recent advances in fluid mechanics. 4th International conference on fluid mechanics, Dalian, Peoples Republic of China, 20–30 July 2004
3. Erk A, Hardy EH, Althaus T, Stahl W (2006) Filtration of colloidal suspensions – MRI investigation and numerical simulation. Chem Eng Technol 29(7):828–831. DOI 10.1002/ceat.200600054
4. von Garnier A, Hardy EH, Schweitzer JM, Reimert R (2007) Differentiation of catalyst and catalyst support in a fixed bed by magnetic resonance imaging. Chem Eng Sci 62(18–20, Sp. Iss. SI):5330–5334. DOI 10.1016/j.ces.2007.03.034
5. Grosse J, Dietrich B, Martin H, Kind M, Vicente J, Hardy EH (2008) Volume image analysis of ceramic sponges. Chem Eng Technol 31(2):307–314. DOI 10.1002/ceat.200700403
6. Hardy EH (2006) Magnetic resonance imaging in chemical engineering: basics and practical aspects. Chem Eng Technol 29(7):785–795. DOI 10.1002/ceat.200600046
7. Hardy EH, Hoferer J, Kasper G (2007) The mixing state of fine powders measured by magnetic resonance imaging. Powder Technol 177(1):12–22. DOI 10.1016/j.powtee.2007.02.042
8. Hardy EH, Hoferer J, Mertens D, Kasper G (2009) Automated phase correction via maximization of the real signal. Magn Reson Imaging 27(3):393–400. DOI 10.1016/j.mri.2008.07.009

9. Hardy EH, Mertens D, Hochstein B, Nirschl H (2009) Compact NMR-based capillary rheometer. In: Fischer P, Pollard M, Windhab E J (eds) Proceedings of the 5th ISFRS, http://www.isfrs.ethz.ch/proc/2009_proc. 5th International symposium on food rheology and structure, ETH Zürich, Zürich, 15–18 June 2009, pp 94–97
10. Hardy EH, Mertens D, Hochstein, B, Nirschl, H (2009) Kompaktes, NMR-gesttztes Kapillar-rheometer. Chem Ing Tech 81(8):1100–1101
11. Hardy EH, Mertens D, Hochstein B, Nirschl H (2010) Compact, NMR-based capillary rheometer. Nachr Chem 58(2):155–156
12. Hoferer J, Lehmann MJ, Hardy EH, Meyer J, Kasper G (2006) Highly resolved determination of structure and particle deposition in fibrous filters by MRI. Chem Eng Technol 29(7): 816–819. DOI 10.1002/ceat.200600047
13. Knoerzer K, Regier M, Hardy EH, Schuchmann HP, Schubert H (2009) Simultaneous microwave heating and three-dimensional MRI temperature mapping. Innov Food Sci Emerg 10:537–544
14. Lehmann MJ, Hardy EH, Meyer J, Kasper G (2003) Determination of fibre structure and packing density distribution in depth filtration media by means of MRI. Chem Ing Tech 75(9):1283–1286. DOI 10.1002/cite.200303229
15. Lehmann MJ, Hardy EH, Meyer J, Kasper G (2005) MRI as a key tool for understanding and modeling the filtration kinetics of fibrous media. Magn Reson Imaging 23(2):341–342. DOI 10.1016/j.mri.2004.11.048
16. Mertens D, Hardy, EH, Hochstein, B, Guthausen, G (2009) A low-field-NMR capillary rheometer. In: Guojonsdottir M, Belton P, Webb G (eds) Magnetic resonance in food science: challenges in a changing world, 9th International conference on applications of magnetic resonance in food science, Reykjavik, Iceland, 15–17 September 2008
17. Mertens D, Heinen C, Hardy EH, Buggisch HW (2006) Newtonian and non-Newtonian low Re number flow through bead packings. Chem Eng Technol 29(7):854–861. DOI 10.1002/ceat.200600048
18. Metzger U, Lankes U, Hardy EH, Gordalla BC, Frimmel FH (2006) Monitoring the formation of an Aureobasidium pullulans biofilm in a bead-packed reactor via flow-weighted magnetic resonance imaging. Biotechnol Lett 28(16):1305–1311. DOI 10.1007/s10529-006-9091-x
19. Nguyen NL, van Buren V, von Garnier A, Hardy EH, Reimert R (2005) Application of Magnetic Resonance Imaging (MRI) for investigation of fluid dynamics in trickle bed reactors and of droplet separation kinetics in packed beds. Chem Eng Sci 60(22):6289–6297. DOI 10.1016/j.ces.2005.04.083
20. Nguyen NL, Reimert R, Hardy EH (2006) Application of magnetic resonance imaging (MRI) to determine the influence of fluid dynamics on desulfurization in bench scale reactors. Chem Eng Technol 29(7):820–827. DOI 10.1002/ceat200600058
21. Regier M, Hardy EH, Knoerzer K, Leeb CV, Schuchmann HP (2007) Determination of structural and transport properties of cereal products by optical scanning, magnetic resonance imaging and Monte Carlo simulations. J Food Eng 81(2):485–491. DOI 10.1016/j.jfoodeng.2006.11.025
22. Regier M, Idda P, Knoerzer K, Hardy EH, Schuchmann HR (2006) Temperature- and water distribution in convective drying by means of inline magnetic resonance tomography. Chem Ing Tech 78(8):1112–1115. DOI 10.1002/cite.200600041
23. Reimert R, Hardy EH, von Garnier A (2005) Application of magnetic resonance imaging to the study of the filtration process. In: Stapf S, Han SI (eds) NMR imaging in chemical engineering, Wiley-VCH, Weinheim, pp 250–263
24. Stapf S, Han S (2005) NMR imaging in chemical engineering. Wiley-VCH, Weinheim
25. Wolf F, Hecht L, Schuchmann HP, Hardy EH, Guthausen G (2009) Preparation of W-1/O/W-2 emulsions and droplet size distribution measurements by pulsed-field gradient nuclear magnetic resonance (PFG-NMR) technique. Eur J Lipid Sci Tech 111(7):730–742. DOI 10.1002/ejlt.200800272

Chapter 2
Fundamentals

2.1 NMR Methods

Nuclear magnetic resonance (NMR) designates the resonant interaction of nuclear magnetic dipole moments[1] $\boldsymbol{\mu}$ in an external magnetic field[2] $\boldsymbol{B_0}$ with an electromagnetic field $\boldsymbol{B_1}$.

Resonant means that only an electromagnetic field of a certain frequency is able to interact with the nuclear dipole. Underlying new concepts from quantum mechanics are briefly mentioned in Sect. 2.1.1. The basic relations for the presented NMR methods are summarized in Sect. 2.1.2. In Sect. 2.1.3 the technique used to achieve spatial resolution is outlined. For NMR methods with spatial resolution, the term MRI is employed. Different quantities that can be measured by various NMR methods are presented in Sect. 2.1.4 and the following. More details can be found e.g. in the textbooks [1, 9, 10, 13, 14, 16, 22, 28, 34, 41, 49, 58, 67].

2.1.1 Notes on Quantum Mechanics

2.1.1.1 Energy Levels of a Nuclear Magnetic Dipole in an External Field

In classical magnetostatics the energy E of a magnetic dipole $\boldsymbol{\mu}$ in an external magnetic field $\boldsymbol{B_0}$ is given by the scalar product

$$E = -\boldsymbol{\mu}\,\boldsymbol{B_0}. \tag{2.1}$$

[1] Vectors are set in bold italic face.

[2] As common in NMR literature, the $\boldsymbol{B}$-field is designated as magnetic field. Alternative names are magnetic flux density or magnetic induction. In vacuum the magnetic $\boldsymbol{H}$-field is proportional to the magnetic induction with the induction constant μ_0: $\boldsymbol{B} = \mu_0 \boldsymbol{H}$.

E.H. Hardy, *NMR Methods for the Investigation of Structure and Transport*,
DOI 10.1007/978-3-642-21628-2_2, © Springer-Verlag Berlin Heidelberg 2012

In quantum-mechanical description, see e.g. [56], the dipole vector is replaced by the corresponding vector operator $\hat{\boldsymbol{\mu}}$ and the energy by the Hamilton operator:

$$\hat{H}_0 = -\hat{\boldsymbol{\mu}}\,\boldsymbol{B_0}. \tag{2.2}$$

The magnetic-dipole vector operator is proportional to the nuclear spin operator $\hat{\boldsymbol{I}}$:

$$\hat{\boldsymbol{\mu}} = \gamma\hat{\boldsymbol{I}}, \tag{2.3}$$

where γ is designated as gyromagnetic ratio.[3] Thus the energy quantization follows from the quantization of the nuclear spin. The corresponding spin quantum number I is integer or half-integer. Both I and γ are ground-state properties of the nucleus, as rest mass and charge. For an isolated nuclear spin in an external magnetic field, the quantization axis is given by the direction of the latter. It is usually chosen as z direction, i.e., $\boldsymbol{B_0} = B_0\boldsymbol{e_z}$. The scalar product in (2.2) can thus be written as

$$\hat{H}_0 = -\gamma\hat{I}_z B_0. \tag{2.4}$$

The eigenvalues of the z component of a quantum mechanical angular momentum are $m\hbar$ with the Planck constant $\hbar$ and the magnetic quantum number $m = -I, -I+1, \ldots, I$. It follows for the eigenvalues E_m of the Hamilton operator:

$$E_m = -\gamma m\hbar B_0. \tag{2.5}$$

Here only the selection rule $\Delta m = \pm 1$ is considered. Accordingly, the magnitude of the energy difference for a transition amounts to

$$|\Delta E| = \gamma\hbar B_0. \tag{2.6}$$

2.1.1.2 Notes on Photons and First Derivation of the NMR Master Equation

The Planck–Einstein equation

$$\Delta E = \hbar\omega \tag{2.7}$$

states that electromagnetic waves with angular frequency ω can behave as particles called photons with energy $\hbar\omega$ that can be absorbed or emitted in transitions with corresponding energy, see Fig. 2.1. For the moment the common assumption is made that this concept is also applicable for the excitation and detection of the NMR signal. Combination of the resonance condition (2.7) and the energy difference (2.6) yields the NMR master equation from quantum mechanical energy considerations:

[3] Sometimes more appropriate as magnetogyric ratio.

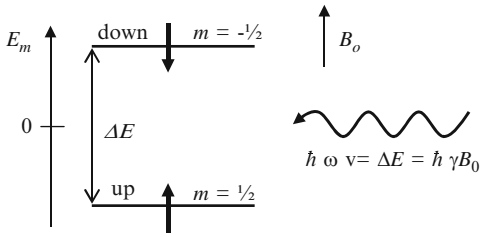

Fig. 2.1 Common representation of signal excitation and detection in NMR as resonant interaction of a photon with energy $\hbar\omega$ and a nuclear magnetic dipole in the field $\boldsymbol{B_0}$, here for spin quantum number $I = 1/2$. In the "up" state with magnetic quantum number $m = 1/2$ the z component of the dipole is parallel to the field. This is energetically more favorable than the "down" state ($m = -1/2$) with anti parallel orientation. The scalar form of the NMR master equation (2.8) follows from the energy difference (2.6) and the Planck–Einstein equation (2.7). Although this interpretation is widely held it leads to paradoxes concerning the detected signal [35, 36]. A detailed theoretical framework relying on the concept of virtual-photon exchange was presented recently [21]

$$\omega = -\gamma B_0. \tag{2.8}$$

Here the resonance frequency ω is obtained as a scalar. In the following Sect. 2.1.2 the master equation will be derived from the classical equation of motion. The angular resonance frequency appears as angular velocity and the choice of the sign gets explained.

Whereas this description is well suited in the far-field limit it does not hold for the excitation and detection of NMR signals where near-field contributions dominate [35,36]. Recently a detailed theoretical framework relying on the concepts of quantum electrodynamics (QED [23]) was presented [21]. It is concluded that during excitation both asymptotically free photons as well as virtual photons appear whereas detection can be characterized by virtual-photon exchange only. In this context it was verified experimentally that the classical description of NMR signal as near-field Faraday induction produces correct results[35]. This classical framework used in the following also comprises the reciprocity theorem, see Sects. 2.1.9 and 2.3.4.

2.1.2 Nuclear Magnetic Resonance

2.1.2.1 Macroscopic Magnetization

The population probability P_m of energy state E_m is given in thermal equilibrium by the Boltzmann distribution:

$$P_m = \frac{\exp\{-E_m/kT\}}{\sum_{m=-I}^{I} \exp\{-E_m/kT\}}. \tag{2.9}$$

For the small energy differences in NMR the high-temperature approximation is used, meaning that the linear approximation of the exponential function is employed. Inserting expression (2.5) for the energy yields for the population probability:

$$P_m \approx \frac{1 + \gamma m\hbar B_0/kT}{\sum_{m=-I}^{I} 1 + \gamma m\hbar B_0/kT}. \tag{2.10}$$

The equilibrium magnetization for N_S spins of a given kind in volume V is obtained from the sum of z components of nuclear magnetization in states m weighted with P_m. Given the eigenvalue $\gamma m\hbar$ for the nuclear z magnetization the equilibrium magnetization M_z^{eq} amounts to:

$$\begin{aligned} M_z^{eq} &= \frac{N_S}{V} \sum_{m=-I}^{I} \frac{1 + \gamma m\hbar B_0/kT}{\sum_{m'=-I}^{I} 1 + \gamma m'\hbar B_0/kT} \gamma m\hbar \\ &= \frac{N_S}{V} \frac{\gamma^2 I(I+1)\hbar^2}{3kT} B_0. \end{aligned} \tag{2.11}$$

This relation is known as Curie's law, see also problem 2.2 on p. 46.

2.1.2.2 Classical Equation of Motion and Bloch Equations

According to classical magnetostatics the magnetic dipole moment $\boldsymbol{\mu}$ in the external field $\boldsymbol{B}$ experiences a torque $\boldsymbol{\mu} \times \boldsymbol{B}$. This results in a change of angular momentum $\mathrm{d}\boldsymbol{I}/\mathrm{d}t$. Applying the proportionality (2.3) between the magnetic dipole moment and the nuclear spin to the macroscopic magnetization $\boldsymbol{M}$ the classical equation of motion is obtained:

$$\frac{\mathrm{d}\boldsymbol{M}}{\mathrm{d}\,t} = \gamma \boldsymbol{M} \times \boldsymbol{B}. \tag{2.12}$$

Application to the magnetization (dipole density) means summation over all dipoles and division by the volume V. It is assumed that $\boldsymbol{B}$ is homogeneous in V.

For a field $\boldsymbol{B}$ constant in space and time the solution of (2.12) is a precession of the magnetization around $\boldsymbol{B}$ with the angular frequency

$$\boldsymbol{\omega_0} = -\gamma \boldsymbol{B_0}. \tag{2.13}$$

This is a second derivation of the NMR master equation. Here, the angular velocity of the so-called Larmor precession is a vector.

In the phenomenological Bloch equations [6]

$$\frac{\mathrm{d}M_x}{\mathrm{d}\,t} = \gamma(\boldsymbol{M} \times \boldsymbol{B})_x - \frac{M_x}{T_2} \tag{2.14}$$

$$\frac{\mathrm{d}M_y}{\mathrm{d}\,t} = \gamma(\boldsymbol{M} \times \boldsymbol{B})_y - \frac{M_y}{T_2} \tag{2.15}$$

$$\frac{\mathrm{d}M_z}{\mathrm{d}t} = \gamma(\boldsymbol{M} \times \boldsymbol{B})_z - \frac{M_z - M_z^{\mathrm{eq}}}{T_1} \tag{2.16}$$

the classical equation of motion is extended by an exponential relaxation toward thermal equilibrium. In favorable cases the transverse relaxation time T_2 equals the longitudinal relaxation time T_1. Frequently, the decay of transverse magnetization is significantly faster than the return of longitudinal magnetization toward thermal equilibrium.[4]

2.1.2.3 Rotating Frame of Reference

The classical equation of motion is sufficient to describe the presented results. It is usually transformed into a frame of reference rotating around z in order to simplify the solution. Further down a circular polarized transverse radio-frequency field (rf field) $\boldsymbol{B_1}$ with angular frequency $\omega_{\mathrm{rf}} \approx \omega_0$ will be introduced.[5] It is made time-independent in the rotating frame by transformation with the angular frequency ω_{rf}.[6] The transformation can be carried out using different formalisms. In [22] the explicit representations of the vectors and their time derivatives in both coordinate systems are calculated with the rotation matrix. Here, the more abstract and concise transformation from [1] is chosen. The macroscopic magnetization $\boldsymbol{M}$ is considered as object that is identical in both coordinate systems.[7] However, the motion of the object is observed differently in the rotating frame compared to the laboratory frame of reference. In the rotating frame, index "R," additional terms are obtained upon time derivation due to the time-dependence of the unit vectors. Using the product rule for the derivation and the fact that the time derivative of the unit vector is the cross product of $\boldsymbol{\omega}_{\mathrm{rf}}$ with this vector it follows

$$\left.\frac{\mathrm{d}\boldsymbol{M}}{\mathrm{d}t}\right|_{\mathrm{L}} = \left.\frac{\mathrm{d}\boldsymbol{M}}{\mathrm{d}t}\right|_{\mathrm{R}} + \boldsymbol{\omega}_{\mathrm{rf}} \times \boldsymbol{M}. \tag{2.17}$$

[4]The relation $T_2 \leq T_1$ is obtained in theoretical calculations for several relaxation mechanisms [8]. The condition that the magnitude of the magnetization cannot exceed the magnitude of the equilibrium magnetization through relaxation leads to the weaker condition $T_2 \leq 2T_1$.

[5]Usually a linear polarized field is irradiated. It can be decomposed into two counter rotating circular polarized fields. For $B_1 \ll B_0$ the component rotating with the magnetization acts as described in (2.23). The counter rotating component leads to the Bloch–Siegert Shift, see [7] and Fig. 2.2. Advanced NMR systems allow to generate only the required circular polarized component [18, 27].

[6]Experimentally, this corresponds to the signal being mixed with the rf frequency and subsequent low-pass filtering.

[7]In contrast to the representation in the form of coordinates in a column vector, denoted as "matrix representation," that differs between coordinate systems.

The left-hand side of (2.17) signifies the time derivation in the laboratory frame, index "L." Here, no additional terms arise. Insertion of the right-hand side of (2.17) in (2.12) yields

$$\left.\frac{\mathrm{d}\boldsymbol{M}}{\mathrm{d}\,t}\right|_{\mathrm{R}} = \gamma \boldsymbol{M} \times \left(\boldsymbol{B} + \frac{1}{\gamma}\,\boldsymbol{\omega}_{\mathrm{rf}}\right). \tag{2.18}$$

Distributivity and anti commutativity of the cross product has been used. The Bloch equations in the rotating frame are obtained by addition of the relaxation terms, in coordinates

$$\frac{\mathrm{d}M_x}{\mathrm{d}\,t} = \gamma\left[M_y(B_z + \omega_{\mathrm{rf}}/\gamma) - M_z B_y\right] - \frac{M_x}{T_2} \tag{2.19}$$

$$\frac{\mathrm{d}M_y}{\mathrm{d}\,t} = \gamma\left[M_z B_x - M_x(B_z + \omega_{\mathrm{rf}}/\gamma)\right] - \frac{M_y}{T_2} \tag{2.20}$$

$$\frac{\mathrm{d}M_z}{\mathrm{d}\,t} = \gamma\left[M_x B_y - M_y B_x\right] - \frac{M_z - M_z^{\mathrm{eq}}}{T_1}. \tag{2.21}$$

The objects in the right-hand side of (2.18) do not depend on the coordinate system. However, (2.19)–(2.21) contain components of the matrix representation that have to be expressed in the rotating frame.

2.1.2.4 Generation of Transverse Magnetization

If $\boldsymbol{\omega}_{\mathrm{rf}}$ and $\boldsymbol{\omega_0}$ are identical, the influence of $\boldsymbol{B_0}$ on the motion of $\boldsymbol{M}$ disappears in the rotating frame, see (2.13). At first, one additional field is considered, $\boldsymbol{B} = \boldsymbol{B_0} + \boldsymbol{B_1}$ with

$$\begin{aligned}\boldsymbol{B_1} &= B_1[\cos(\omega_{\mathrm{rf}}t + \phi_1)\boldsymbol{e_x} + \sin(\omega_{\mathrm{rf}}t + \phi_1)\boldsymbol{e_y}] \\ &= B_1[\cos(\phi_1)\boldsymbol{e_x}' + \sin(\phi_1)\boldsymbol{e_y}'].\end{aligned} \tag{2.22}$$

Primed unit vectors refer to the rotating frame of reference. Neglecting relaxation the equation of motion in the rotating frame of reference reads:

$$\frac{\mathrm{d}\boldsymbol{M}}{\mathrm{d}\,t} = \gamma \boldsymbol{M} \times \boldsymbol{B_1}. \tag{2.23}$$

The solution is denoted as Rabi nutation around $\boldsymbol{B_1}$. The angular velocity amounts to

$$\boldsymbol{\omega_1} = -\gamma \boldsymbol{B_1}. \tag{2.24}$$

Accordingly the equilibrium magnetization can be rotated e.g. on the x' axis of the rotating frame by application of a resonant $\boldsymbol{B_1}$-field with constant amplitude along the negative y' axis, i.e., $\phi_1 = -\pi/2$. The duration τ of such a "90 degree" rf pulse is related to its amplitude by $\omega_1\tau = \pi/2$, see also Fig. 2.2. The following

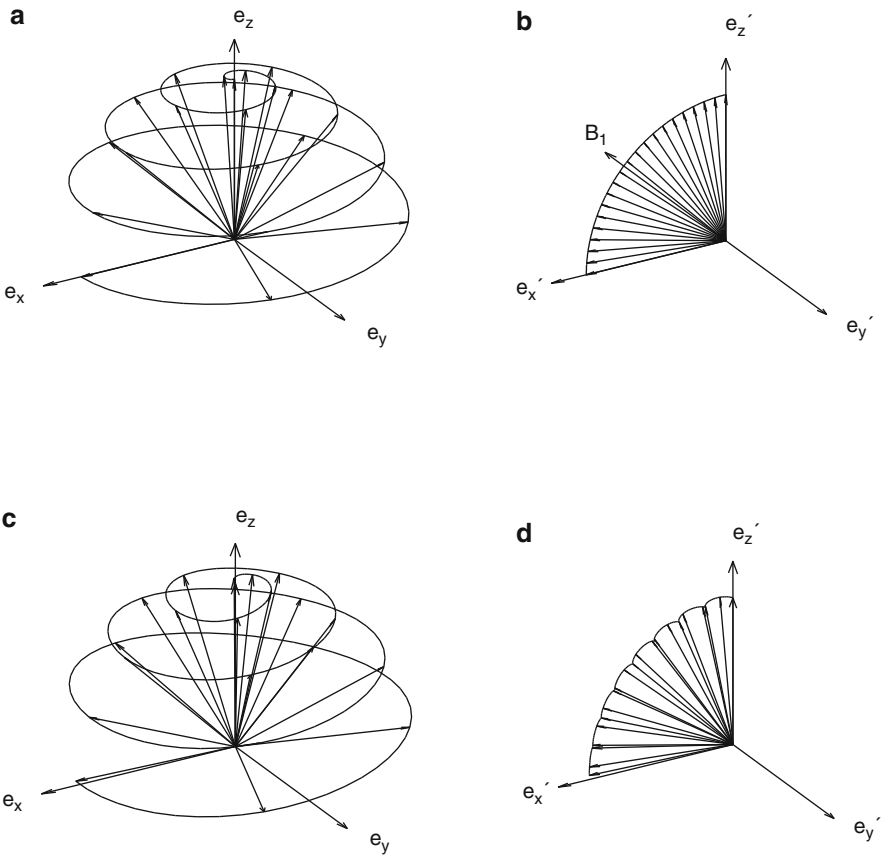

Fig. 2.2 (**a**), (**c**) numerical solution of the equation of motion (2.12) in the laboratory frame of reference. (**b**), (**d**) solution of the equation in the rotating frame (2.18). Initial magnetization is parallel to the static field $B_0 \boldsymbol{e}_z$. The resonant circular polarized $\boldsymbol{B_1}$-field, see (2.22) allows to generate transverse magnetization. For the sake of clearness, $B_0 = 16 B_1$ was chosen in (**a**). Typically, the ratio is about three powers of ten. In the experiment frequently a linear polarized field of twice the amplitude is used. The perturbance of the contained counter rotating circular polarized component is visible in the laboratory frame (**c**) and clearer in the rotating frame (**d**). For $B_1 \ll B_0$ the perturbance is marginal

precession of magnetization with ω_0 induces a weak voltage in the receiver coil,[8] see also Sect. 2.3.4. This situation is the starting point for the classical description of Fourier imaging in Sect. 2.1.3.

[8] Usually the coil transmitting $\boldsymbol{B_1}$ and the receiver coil are identical. Between transmit and receive mode a dead time of some microseconds has to be waited. For the distinction of x and y component of transverse magnetization pairs of data points can be digitized with a delay corresponding to a precession by $\pi/2$. This procedure is denoted as "sequential quadrature detection."

Finally the case of $\boldsymbol{\omega}_{\mathrm{rf}} \neq \boldsymbol{\omega_0}$ with a remaining field $B_z = B_0 + \omega_{\mathrm{rf}}/\gamma$ is mentioned. Here the nutation in the rotating frame occurs around the effective field

$$\boldsymbol{B}_{\mathbf{1}\mathrm{eff}} = B_1[\cos(\phi_1)\boldsymbol{e}_{\boldsymbol{x}}{}' + \sin(\phi_1)\boldsymbol{e}_{\boldsymbol{y}}{}'] + (B_0 + \omega_{\mathrm{rf}}/\gamma)\boldsymbol{e}_z. \tag{2.25}$$

2.1.3 Fourier Imaging

2.1.3.1 Basic Principle

Fourier imaging relies on a position-to-frequency transformation. In addition to the homogeneous fields $\boldsymbol{B_0}$ and $\boldsymbol{B_1(t)}$ required for NMR a field with homogeneous gradient is necessary. The basic principle is readily formulated using the classical equation of motion in the rotating frame [31].

As stated at the end of Sect. 2.1.2 the magnetization in the observable volume V having the x direction of the rotating frame is the starting point. Furthermore $\boldsymbol{\omega}_{\mathrm{rf}}$ and $\boldsymbol{\omega_0}$ are supposed to be identical, relaxation is neglected. Without additional fields the right-hand side of (2.18) is zero, the magnetization appears to be static.

Additional coils allow to superimpose the polarizing $\boldsymbol{B_0}$-field by fields with linear variation of the z component along the directions of the laboratory frame of reference:

$$B_z = B_0 + \frac{\partial B_z}{\partial x}x \equiv B_0 + G_x x \quad \text{or} \tag{2.26}$$

$$B_z = B_0 + \frac{\partial B_z}{\partial y}y \equiv B_0 + G_y y \quad \text{or} \tag{2.27}$$

$$B_z = B_0 + \frac{\partial B_z}{\partial z}z \equiv B_0 + G_z z, \quad \text{in general} \quad B_z = B_0 + \boldsymbol{G}\boldsymbol{r}. \tag{2.28}$$

Due to the inhomogeneous field Eqs. (2.12)ff have to be applied locally for "macroscopic magnetization" $\boldsymbol{M}(\boldsymbol{r})$ in the volume element $\mathrm{d}V$. The volume element has to be small enough to consider $\boldsymbol{B}(\boldsymbol{r})$ as homogeneous within it. "Macroscopic" signifies that the number $\mathrm{d}N_{\mathrm{S}}$ of observed spins is large enough for a meaningful averaging according to the Boltzmann distribution in (2.11). As example a cubical water sample with a volume V of one milliliter and a mass of one gram is considered. Given the molar mass of 18 g/mol this corresponds to 0.056 mol water molecules and 0.111 mol hydrogen nuclei, respectively. Even if the cube is divided into 10^9 volume elements $\mathrm{d}V$ with 10 micrometer length of side, each volume element still contains $\mathrm{d}N_{\mathrm{S}} = 6.7 \times 10^{13}$ ^{1}H nuclei, with $\mathcal{N}_{\mathrm{A}} = 6.022 \times 10^{23}\,\mathrm{mol}^{-1}$ for the Avogadro number. Introducing the local spin density

$$\rho(\boldsymbol{r}) = \mathrm{d}N_{\mathrm{S}}(\boldsymbol{r})/\mathrm{d}V \tag{2.29}$$

and the z component of the Boltzmann-averaged nuclear magnetic dipole

$$\langle \mu_z \rangle = \frac{\gamma^2 I(I+1)\hbar^2}{3kT} B_0. \tag{2.30}$$

Curie's law can be formulated locally as[9]

$$M_z^{\mathrm{eq}}(\boldsymbol{r}) = \rho(\boldsymbol{r}) \langle \mu_z \rangle. \tag{2.31}$$

The solution of (2.18) with the initial condition

$$\boldsymbol{M}(\boldsymbol{r}) = \rho(\boldsymbol{r}) \langle \mu_z \rangle \boldsymbol{e_x}' \tag{2.32}$$

at $t = 0$ and the additional field $(\boldsymbol{Gr})\,\boldsymbol{e}_z$ is a precession with the space- and possibly time-dependent angular velocity

$$\boldsymbol{\omega}(\boldsymbol{r}, t) = -\gamma(\boldsymbol{Gr})\,\boldsymbol{e}_z \tag{2.33}$$

around the z axis. The time-dependence applies for gradients $\boldsymbol{G}(t)$ that are a function of time. Motion of the nuclear spins that contribute to the spin density $\rho(\boldsymbol{r})$ will be treated in Sects. 2.1.7 and 2.1.8. The angle of precession is denoted as phase. It is obtained by integrating (2.33) to

$$\phi(\boldsymbol{r}, t) = -\gamma \int_0^t \boldsymbol{G}(t')\boldsymbol{r}\, \mathrm{d}t' \tag{2.34}$$

$$\equiv -\boldsymbol{k}\boldsymbol{r}. \tag{2.35}$$

In (2.35) the definition of the wave vector

$$\boldsymbol{k} = \gamma \int_0^t \boldsymbol{G}(t')\, \mathrm{d}t' \tag{2.36}$$

has been introduced.[10] The measuring system samples the integrated transverse magnetization in the observable volume V, see Sect. 2.3.4. Division by V yields for the average magnetization

$$\bar{\boldsymbol{M}}(t) = \frac{\langle \mu_z \rangle}{V} \iiint_V \rho(\boldsymbol{r}) \left[\cos(\phi(\boldsymbol{r}, t)) \boldsymbol{e_x}' + \sin(\phi(\boldsymbol{r}, t)) \boldsymbol{e_y}' \right] \mathrm{d}x\mathrm{d}y\mathrm{d}z. \tag{2.37}$$

[9] A spatial variation of $\langle \mu_z \rangle$ due to the superposition of $\boldsymbol{B_0}$ with $\boldsymbol{Gr}$ can be neglected. On the one hand the additional gradient fields are typically at least three orders of magnitude weaker than $\boldsymbol{B_0}$. On the other hand the gradient fields are usually switched on as pulses with a duration that is short compared to the longitudinal relaxation time T_1.

[10] A more general definition with the effective gradient will be given in Sects. 2.1.7 and 2.1.8. The concept of effective gradients includes the effect of rf pulses with $\omega_1 \tau = \pi$.

Nondimensionalization with $\langle \mu_z \rangle / V$ and identification of the transverse plane of the rotating frame of reference with the complex plane leads to the concise expression

$$\boxed{M^+(\boldsymbol{k}) = \iiint_V \rho(\boldsymbol{r}) \exp(-i\,\boldsymbol{k}\,\boldsymbol{r}) \mathrm{d}x \mathrm{d}y \mathrm{d}z} \tag{2.38}$$

with $\mathrm{Re}(M^+) = \bar{M}_x V / \langle \mu_z \rangle$ and $\mathrm{Im}(M^+) = \bar{M}_y V / \langle \mu_z \rangle$. According to this the average transverse magnetization $M^+(\boldsymbol{k})$ is the Fourier transform of the spin density at point $\boldsymbol{k}$ in reciprocal position space.[11] Thus the sought-after spin density can be determined approximately by inverse Fourier transform if $M^+(\boldsymbol{k})$ can be suitably sampled in reciprocal position space.

With the exception of research described in Sects. 4.5 and 4.10, all applications presented in Chap. 4 use the principle of Fourier imaging. The effect of small deviations from linear field variations are treated analytically for a special case in Chap. 9.

2.1.3.2 Pair of Continuous and Discrete Fourier Transform

If it were possible to sample reciprocal position space continuously and completely, the spin density could be calculated by inverse Fourier transform:

$$\rho(\boldsymbol{r}) = \frac{1}{(2\pi)^3} \iiint M^+(\boldsymbol{k}) \exp(i\,\boldsymbol{k}\,\boldsymbol{r}) \mathrm{d}k_x \mathrm{d}k_y \mathrm{d}k_z. \tag{2.39}$$

This can be seen quite simply by inserting (2.38) in (2.39), which leads to the Fourier representation of the Dirac or delta function. Experimentally, neither a continuous nor an infinitely expanded sampling is possible. Usually reciprocal space is sampled on a regular Cartesian grid. In one dimension, the expression for the discrete inverse Fourier transform then reads

$$\tilde{\rho}_n = \frac{1}{N} \sum_{k=1}^{N} M^+_k \exp[i\,2\pi(k-1)(n-1)/N], \quad 1 \le n \le N. \tag{2.40}$$

For multidimensional data the procedure (2.40) has to be applied sequentially for all dimensions. In the expressions $\tilde{\rho}_n$ and M^+_k the naturals n and k signify the index of the result and measured data vectors, respectively. The latter results from the discretization of e.g. k_x in (2.38). For the sake of completeness, the discrete Fourier transform is also indicated. Assuming a discrete spin density $\tilde{\rho}_n$, the expression of the measured signal would be

[11] See also problems 2.5 and 2.6.

$$\tilde{M}^{+}_{k} = \sum_{n=1}^{N} \tilde{\rho}_n \exp[-i\,2\pi(k-1)(n-1)/N], \quad 1 \le k \le N. \tag{2.41}$$

For the hypothetical discrete pair it is also rather simple to see that insertion of $\tilde{M}^{+}_{k}$ from (2.41) instead of M^{+}_{k} into (2.40) leads to the identity. The Kronecker delta occurs in place of the delta function.

Here it is necessary to examine the less simple question what the discrete inverse Fourier transform (2.40) of the measured continuous Fourier transform (2.38) signifies. To this end the discrete $\boldsymbol{k}$ values have to be expressed as a function of the index k and inserted into (2.38). Only one dimension is considered, the extension to higher dimensions gives corresponding results. In order to achieve the highest resolution with a given number of discretization points, the length L of the field of view (FOV) is chosen to just contain the sample. According to the sampling or Nyquist theorem the increment in reciprocal space is then calculated from[12]

$$k_{\text{inc}} = 2\pi/L. \tag{2.42}$$

For the fast Fourier transform (FFT) the number N of points sampled is a power of two. They are chosen as

$$\frac{2\pi}{L}(k-1-N/2), \quad 1 \le k \le N. \tag{2.43}$$

Now (2.38) can be expressed as a function of index k and inserted into (2.40):

$$\begin{aligned}\tilde{\rho}_n = \frac{1}{N}\sum_{k=1}^{N}\int_{-L/2}^{L/2} \rho(r)\exp[-i\,(2\pi/L)(k-1-N/2)r]\mathrm{d}r \\ \times \exp[i\,2\pi(k-1)(n-1)/N], \quad 1 \le n \le N.\end{aligned} \tag{2.44}$$

The integration limits are reduced assuming that no spin density is observed outside the FOV. Interchanging summation and integration as well as collection of the exponential functions lead to

$$\begin{aligned}\tilde{\rho}_n = \frac{1}{N}\int_{-L/2}^{L/2} \mathrm{d}r\,\rho(r)\sum_{k=1}^{N}\exp\left\{i\,2\pi\left[-\frac{r}{L}\left(k-1-\frac{N}{2}\right)\right.\right. \\ \left.\left.+\frac{(k-1)(n-1)}{N}\right]\right\}, \quad 1 \le n \le N.\end{aligned} \tag{2.45}$$

[12]This corresponds to the claim of unambiguous phase increments $k_{\text{inc}}r$ for all positions within the FOV. For magnetization outside the FOV the phase increment between two discretization points calculated from (2.35) and (2.42) is outside the interval $[-\pi\ \ \pi]$. This violation of the sampling theorem leads to a folding of spin density in the calculated image.

Rearranging finally yields:

$$\tilde{\rho}_n = \frac{\exp\{i\,(n-1)\pi\}}{N} \int_{-L/2}^{L/2} \mathrm{d}r\, \rho(r) \sum_{k=1}^{N} \exp\left\{-i\,2\pi \left(k - 1 - \frac{N}{2}\right)\left(\frac{r}{L} - \frac{n-1}{N}\right)\right\}, \quad 1 \le n \le N. \tag{2.46}$$

The first exponential is one for odd index n and minus one for even index. This corresponds to a first-order phase error, analogous to the shift theorem of the Fourier transformation. In two dimensions a checkerboard pattern is obtained. This effect can be removed by a simple phase correction. The correction of non trivial phase errors will be treated in Sect. 2.3.5. The sum in (2.46) is a superposition of sine and cosine functions. The common origin depends on the index n of the result vector, the scaling of the argument on index k of the measured data in reciprocal space. As the sum is finite, it only represents an approximation of the delta function. The position of the origin and the degree of approximation shall be illustrated for four cases in Fig. 2.3.

For $n = 1$ the origin is at zero, i.e., $\tilde{\rho}_1$ is an approximation of $\rho(0)$. In Fig. 2.3a the sum is represented for a coarse discretization of $N = 16$. Obviously not only $\rho(0)$ contributes to the real part of $\tilde{\rho}_1$, but predominantly the weighted integral of $\rho(r)$ in an interval of width $2L/N$ around $r = 0$. Additionally on each side alternately $N/4$ integrals with decreasing negative weight and $N/4 - 1$ integrals with decreasing positive weight in intervals of width L/N contribute. Although $\rho(r)$ is real, the oscillating imaginary part of the sum in general leads to a small imaginary part of $\tilde{\rho}_n$. The maximum of the real part of the sum is N times higher than the amplitude of the oscillating imaginary part.

For $n = 2$ the origin is at L/N, i.e., $\tilde{\rho}_2 \approx \rho(L/N)$. Apart from that there is a cyclic shift of the function. All N points are equidistant with the "digital resolution"

$$r_{\mathrm{inc}} = L/N = 2\pi/(N k_{\mathrm{inc}}). \tag{2.47}$$

For $n = N/2$ the origin is such that $\tilde{\rho}_{N/2}$ is dominated by $\rho(r)$ in the vicinity of the right boundary of the FOV. Still for a rather coarse discretization of $N = 32$ the corresponding sum is shown in Fig. 2.3b.

The first point of the result vector with $n = N/2 + 1$ samples the left and right ends of the FOV in equal measure. This is demonstrated in Fig. 2.3c for $N = 64$, which depending on the application is already a suitable discretization.

Due to the cyclic shift the following points of the result vector with $N/2 + 2 \le n \le N$ sample the spin density predominantly at negative positions. This is shown in Fig. 2.3d for $N = 128$ and $n = 96$. To obtain the correct image, the halves of $\tilde{\rho}$ calculated by (2.46) are shifted.

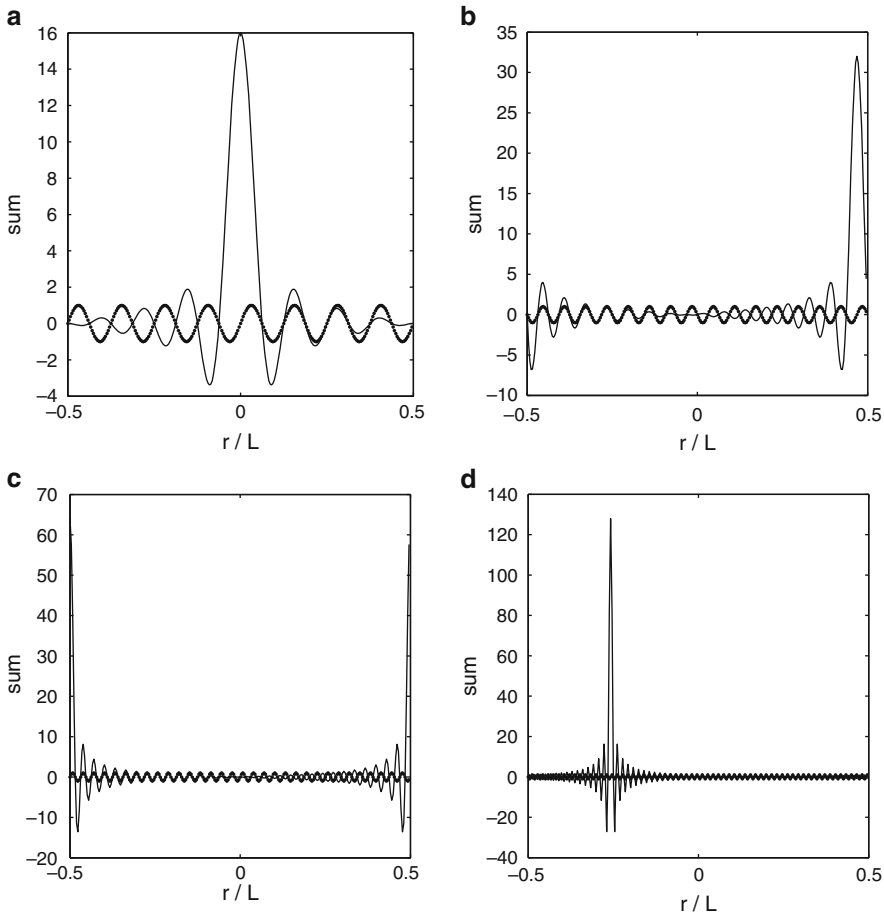

Fig. 2.3 Representation of the sum in (2.46). Real part: *solid line*, imaginary part: *dotted line*. Results for varying discretization N of the discrete Fourier transform and varying index n of the result vector are shown. (**a**) $N = 16$, $n = 1$; (**b**) $N = 32$, $n = N/2 = 16$; (**c**) $N = 64$, $n = N/2 + 1 = 33$; (**d**) $N = 128$, $n = 96 > N/2 + 1$

In summary the first point of the shifted result vector is related to both boundaries of the FOV. It is followed by $N/2 - 1$ points corresponding to negative r. The point of origin is at index $n = N/2 + 1$. Positive r are represented by the last $N/2 - 1$ points. If the sampled spin density $\rho(r)$ shows only minor variation on the length scale of the oscillations of the sum, contribution from side lobes with alternating polarity cancel and $\tilde{\rho}$ is a faithful approximation. For steep jumps in the spin density it is comprehensible from the preceding that artifacts such as the Gibbs effect can result from discrete sampling and Fourier transformation. An example for the investigation of artifacts by discrete sampling is given in Sect. 4.9.

2.1.3.3 Simple Pulse Sequence, Resolution

There are two common methods to conduct the transverse magnetization $M^+(\boldsymbol{k})$ to the required sampling points in $\boldsymbol{k}$ space.

In the method called frequency encoding the gradient in (2.36) is kept constant and is denoted as read gradient $\boldsymbol{G}_\mathrm{r}$. Data acquisition is performed with a dwell time (DW) calculated such that the chosen $k_{\alpha\,\mathrm{inc}}$ is obtained, where α designates the gradient direction. Usually α is x, y, or z but other directions can be realized by simultaneous switching of gradients. In order to conduct the first point to $-(N_\alpha/2)k_{\alpha\,\mathrm{inc}}$ a gradient with opposite polarity and corresponding time integral is applied before data acquisition, see Fig. 2.4. This gradient is denoted as read dephase gradient. Its magnitude can be higher than that of the read gradient in order to reduce its duration, the read dephase time. For $\boldsymbol{k} = 0$ the magnetization phase is independent of position and the signal is at its maximum. The maximum is denoted as gradient echo and the corresponding time as t_{GE}.

In order to sample the remaining dimensions frequency encoding can be supplemented by a method denoted as phase encoding. The phase gradient $\boldsymbol{G}_\mathrm{p}$ perpendicular to the read gradient is switched on after generation of transverse

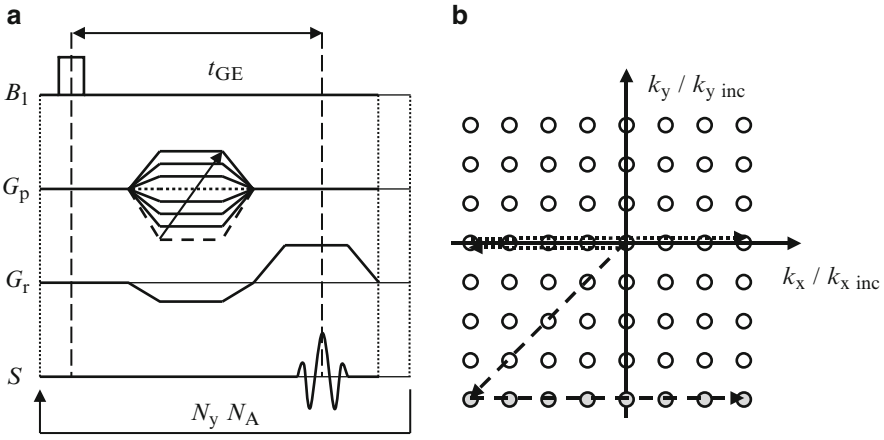

Fig. 2.4 Simple experimental scheme for the sampling of reciprocal position space. (**a**) Synchronization of excitation with B_1, phase encoding with G_p, frequency encoding with G_r, and data acquisition. (**b**) Corresponding path in $\boldsymbol{k}$ space. Just after excitation the magnetization state corresponds to the origin of $\boldsymbol{k}$ space. The simultaneous action of the phase gradient and read dephase gradient produces the straight lines to sampling points at the left border of $\boldsymbol{k}$ space. During acquisition of the signal S the read gradient leads the magnetization along horizontal lines. In the example the read gradient has x direction and the phase gradient y direction. The depicted signal is a sketch of the real part of the total observable magnetization for $G_\mathrm{p} = 0$. It exhibits a maximum at time t_GE of the gradient echo. The imaginary part, corresponding to the y component of the magnetization, is not shown. After a relaxation delay a loop is executed until the signal is acquired for all values of the phase gradient. If necessary, each acquisition can be repeated N_A times to improve SNR and reduce artifacts. [31]

magnetization and off before data acquisition, see Fig. 2.4. As rotations due to both gradients occur around the z axis the phase gradient can be applied simultaneously to the read dephase gradient. The procedure is repeated with varying amplitude of $\boldsymbol{G}_\mathrm{p}$ so that for the dimension of the phase gradient the values calculated by (2.36) and (2.43) are obtained. The remaining third dimension can be sampled by an additional phase encoding gradient.

The achievable spatial resolution and the experimental time required depend on several factors. According to (2.47) the distance between discretization points in real space equals π divided by the maximum value of the wave vector. As can be seen from (2.36) a technical limit for the resolution is thus imposed by the maximum gradient time integral that can be realized by the gradient system, see Sect. 3.1. As discussed in [13] the spatial resolution can be limited by the SNR that decreases with increasing digital resolution. Further limitations to the spatial resolution by transverse T_2 relaxation, translational self diffusion, and susceptibility artifacts are also treated in [13]. Let N_α be the number of frequency-encoding steps and N_β, N_γ the number of encoding steps in the two phase-encoded dimensions of the simple experiment described above. The duration of each frequency encoding is of the order of milliseconds and is neglected. If after each frequency encoding step the relaxation of magnetization toward thermal equilibrium is awaited, about four times the longest longitudinal relaxation time T_1 is required. In this case the experimental time amounts to

$$t_\mathrm{expt} = N_\beta N_\gamma \, 4T_1 N_\mathrm{A}, \tag{2.48}$$

where N_A designates the number of averages used to improve SNR and reduce artifacts. In favorable cases the experimental time can be drastically reduced, see e.g. [9] or [31] and Fig. 2.7.

2.1.3.4 Slice Selection

Abandoning sampling of the third dimension by phase encoding reduces the experimental time in (2.48) by the factor N_γ. Let z be the direction that is not sampled. For $G_z \equiv 0$ and thus $k_z \equiv 0$ the spin density integrated along z is obtained according to (2.38). Alternatively a slice of thickness Δz perpendicular to the z direction can be selected and a two-dimensional (2D) image of the slice produced. Slice selection by selective excitation is described in the following first in a linear approximation and then on the basis of the classical equation of motion.

According to (2.8) nuclear spins are excited by a resonant electromagnetic field if $\omega_\mathrm{rf} = \gamma B_0$ is fulfilled. If during excitation a slice gradient $\boldsymbol{G}_\mathrm{s}$ is applied along z the energy difference in (2.6) depends on z:

$$\Delta E = \gamma\hbar(B_0 + G_\mathrm{s} z). \tag{2.49}$$

In this case and for a continuous electromagnetic wave of angular frequency $\omega_{rf} = \gamma B_0$ the resonance condition would only be fulfilled at $z = 0$, producing hardly any signal. Excitation by a pulsed electromagnetic field generates not only a single frequency but also a frequency distribution around the carrier frequency. The form of the spectrum around the carrier frequency is given by the Fourier transform of the pulse shape. For a block pulse with rectangular shape a sinc spectrum is obtained, with $\mathrm{sinc}(x) = \sin(x)/x$. The pulse bandwidth $\Delta\omega$ can be defined e.g. as frequency difference between the first zeros of the spectrum on both sides of the maximum. It is inversely proportional to the duration of the pulse. Using (2.8) the approximate thickness Δz of the slice in which the resonance condition is fulfilled is calculated as:

$$\Delta\omega = \gamma G_s \Delta z. \tag{2.50}$$

A slice with sharper profile is obtained for a rf pulse with sinc amplitude shape as its frequency spectrum is rectangular. A sinc pulse truncated at the third zero of the shape on both sides of the maximum is shown in Fig. 2.5a. The corresponding

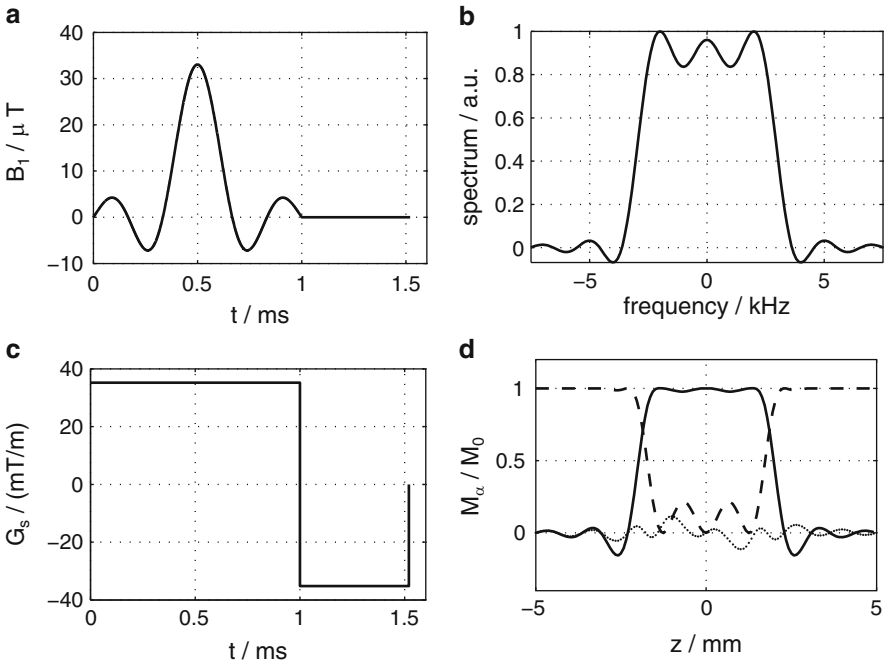

Fig. 2.5 Simulation of slice selection. (**a**) Amplitude shape of a narrow-banded sinc rf pulse. (**b**) Fourier transform of the pulse shape. (**c**) Slice gradient G_s followed by a slice-refocusing gradient. (**d**) Numerical calculation of resulting magnetization-vector components in the rotating frame of reference as a function of position perpendicular to the slice, here z. *Solid line*: x component. *Dotted line*: y component. *Dashed line*: z component. [31]

frequency spectrum is depicted in 2.5b. Deviations from a rectangular spectrum are due to the necessary truncation and represent a compromise. A description in the framework of linear systems is given in [9].

The process of slice selection can be studied accurately by numerical solution of the equation of motion (2.18). For $\boldsymbol{\omega}_{\mathrm{rf}} = \boldsymbol{\omega_0}$ and including the rf as well as gradient field it reads:

$$\frac{\mathrm{d}\boldsymbol{M}}{\mathrm{d}\,t} = \gamma \boldsymbol{M} \times \left[B_1(t)(\boldsymbol{e_x}' \cos\phi_1 + \boldsymbol{e_y}' \sin\phi_1) + (\boldsymbol{G}_{\mathrm{s}}\boldsymbol{r})\,\boldsymbol{e}_z \right]. \tag{2.51}$$

The result of a simple piecewise constant integration with 20,000 equal time steps, see Sect. 6.4,is shown in Fig. 2.5d. A typical duration of $\tau = 1$ ms was chosen for the sinc pulse. The amplitude of the rf field is calculated considering the center of the slice where the slice gradient produces no additional field. The integral of the Rabi nutation is set to the required pulse angle, here 90 degrees:

$$-\gamma \int_0^{\tau} B_1(t)\,\mathrm{d}t = \pi/2. \tag{2.52}$$

As starting point 128 points along the slice direction between −5 mm and 5 mm with constant equilibrium magnetization were chosen. The desired slice thickness was set to $\Delta z = 4$ mm. For an infinite sinc pulse with (1/6) ms between the maximum and first zero amplitude the bandwidth amounts to $\Delta\omega/(2\pi) = 6$ kHz. With the slice thickness and bandwidth the slice gradient G_{s} is calculated by (2.50). Ideal slice selection means z component zero and e.g. maximum x component within the slice. Outside the slice the situation is inverse. The remaining y component is zero at all positions. Integration up to the pulse length τ yields for the z component approximately the desired result as shown in Fig. 2.5d. Deviations from ideal slice selection exhibit features already visible in the linear approximation, see Fig. 2.5b. The transverse components however oscillate along the slice direction. Application of the slice refocusing gradient after the rf pulse, see Fig. 2.5c, produces the profiles of x and y magnetization depicted in Fig. 2.5d. The area of the optimal simulated slice refocusing gradient is −0.52 times the integral of the slice gradient. For higher flip angles such as π in Fig. 2.9 the simulation reveals larger deviations of the obtained slice thickness compared to the result of linear approximation in (2.50). Such simulations are used in the optimization of parametrized pulse shapes with respect to given properties such as sharp slice boarders without oscillation of transverse components [25].

If all rf pulses in an experiment are slice selective a pseudo 3D image can be obtained in the experimental time of a 2D image. Waiting about $4T_1$ between two phase encoding steps for each slice usually leaves enough time for the measurement of further slices. However, the achievable spatial resolution in slice direction in multi slice imaging is about one order of magnitude inferior to that of full 3D sampling of reciprocal space, e.g., 1 mm versus 100 μ m. Again, the directions of $\boldsymbol{G}_{\mathrm{r}}$, $\boldsymbol{G}_{\mathrm{p}}$, $\boldsymbol{G}_{\mathrm{s}}$ can be chosen arbitrarily through rotation, i.e., linear combinations of $\boldsymbol{G}_x$, $\boldsymbol{G}_y$, $\boldsymbol{G}_z$.

2.1.4 Contrast

2.1.4.1 Additional Dimensions

According to (2.38) the complex signal in Fourier imaging is determined by the spin density $\rho(\boldsymbol{r})$. In fact, constituting the strength of NMR, a multitude of additional parameters influence the measured NMR response. In the following Sects. frequently employed parameters are briefly reviewed. Instead of the simple 3D spin density, generally a distribution density with high dimensionality is considered:

$$M_{\boldsymbol{B}}^{+}(t) = \int_{\xi} \rho(\xi) \exp\{i\,\phi_B(t,\xi)\}\,\mathrm{d}\boldsymbol{\xi} \tag{2.53}$$

with

$$\boldsymbol{\xi} = (\boldsymbol{r}, \Omega, T_1, T_2, D, \boldsymbol{v}, \ldots). \tag{2.54}$$

In (2.54) Ω designates a frequency shift in the sense of NMR spectroscopy. It is due to the magnetic shielding σ.[13] T_1 and T_2 are the relaxation times introduced in (2.14)–(2.16). D is the translational self-diffusion coefficient.[14] The velocity in case of coherent displacement is denoted by $\boldsymbol{v}$. The phase $\phi_{\boldsymbol{B}}(t, \boldsymbol{\xi})$ in (2.53) is a function of time and parameters $\boldsymbol{\xi}$ as well as a functional of the experimentally chosen $\boldsymbol{B}(\boldsymbol{r}, t)$. For a real-valued phase as in (2.38) the integral transform is a Fourier transform. Relaxation corresponds to an imaginary phase and a Laplace transform.

Even a coarse resolution of the above distribution in ten dimensions is prohibited by the required experimental time and the amount of data. Hence the experiments integrate the distribution totally or partially over variables ($\boldsymbol{r}$ and Ω) or the influence of parameters in the form of a weighting is avoided, used, or accepted (T_1, T_2, D, and $\boldsymbol{v}$). Further notes on distribution densities are given in Sect. 2.1.8 on p. 32ff.

As example, consider the pair of variables position and spectroscopic frequency. Common experiments are:

- Spectroscopic resolution and total integration of position space
- Spectroscopic resolution for a small selected volume
- Spectroscopic resolution and 2D spatial resolution within a slice
- Spectroscopic and full 3D spatial resolution
- 2D or 3D spatial resolution and total integration of the spectroscopic dimension
- 2D or 3D spatial resolution and integration of the spectroscopic dimension in a range of chemical shifts

In all combinations the influence of longitudinal relaxation can be avoided by waiting about five times the longest T_1 of the sample between two scans. Weighting

[13] More precisely the isotropic magnetic shielding, i.e., one-third of the trace of the shielding tensor, see also Sect. 2.1.5.

[14] To be replaced by the corresponding tensor in case of anisotropic diffusion, see also Sect. 2.1.7.

by transverse T_2 relaxation is reduced by minimizing the time between excitation and detection of magnetization. Signal attenuation due to translational self diffusion is avoided if no or only moderate gradients of the magnetic field are present. If convection can be suppressed the signal is not influenced by $\boldsymbol{v}$.

Another example is the variable pair transverse relaxation and translational self diffusion. If inhomogeneities of the polarizing field or the sample do not allow for spectroscopic resolution, 2D T_2-D spectra are increasingly used as valuable source of information. Without space encoding the signal is integrated over the spatial dimensions. However, the experimental setup can be designed to possess a detection volume of suitable size and shape. Spatial resolution is then possible by moving the sensor relative to the sample. For the remaining parameters the considerations given above are still valid.

In the following all distribution densities are denoted by the same symbol "ρ," even if the considered distribution results from an integration over some parameters. To be mathematically correct, a new symbol would have to be introduced in each case.

2.1.5 Spectroscopy

The surrounding electron density causes a shielding of the polarizing field at the positions of the nuclei. For different chemical groups this chemical shielding has slightly different values.[15] In the simplest case NMR spectroscopy consists of a pulse excitation followed by a free induction decay (FID). The broad-banded rf pulse rotates the nuclear magnetization of the observed kind (e.g. ^{1}H or ^{13}C) in the transverse plane, see (2.24). The pulse response is sampled and a frequency analysis performed by Fourier transformation. During the FID the magnetic field in (2.18) amounts to $(1-\sigma)B_0$ for a given magnetic shielding σ. Consequently a residual precession with angular velocity $\Omega = -\sigma\omega_0$ remains in the rotating frame, similar to the situation in (2.33). Integrating over the observed sample, i.e., the occurring residual frequencies, the nondimensionalized magnetization reads

$$M^+(t) = \int_{-\infty}^{\infty} \rho(\Omega)\exp(i\,\Omega t)\mathrm{d}\Omega \tag{2.55}$$

similar to the expression in (2.38). Here, the total transverse magnetization $M^+(t)$ and the spectrum $\rho(\Omega)$ form a Fourier pair.[16] According to (2.55) the magnetization at time $t = 0$ reflects the integral of the observed spectrum. This still holds if the signal decays by transverse relaxation to be discussed in Sect. 2.1.6. Signal decay

[15] In the range of 10 ppm (parts per million) for hydrogen nuclei, 200 ppm for the NMR-observable carbon isotope ^{13}C.

[16] The angular frequency has been used as variable. In spectroscopy it is common to use the chemical shift δ relative to a reference: $\delta = 10^6(\sigma_{\mathrm{ref}} - \sigma)/(1-\sigma_{\mathrm{ref}}) \approx 10^6(\sigma_{\mathrm{ref}} - \sigma)$.

by relaxation results in a peak height-reduction and broadening in the measured spectrum. Nevertheless, following from the Fourier relation, the integral of the measured spectrum is directly related to the magnetization at $t = 0$ and hence the number of spins. By linearity of the Fourier transform the direct relation between the peak integral and the number of spins of the corresponding chemical group holds for the spectrum of superposed lines with chemical shift.[17] In favorable cases this experiment is sufficient to analyze which chemical groups are present and in which number. The fine structure by through-bond coupling is not to be discussed here. It should simply be mentioned that this additional information is used to determine the primary structure. The secondary structure e.g. in solution can be assessed by measurement of dipolar through-space coupling. By this, NMR is one of the most important analysis tools in chemistry and biochemistry.

Broadening, overlap and artifacts hamper the inference from the measured spectrum on the true spectrum. One strategy in the analysis of spectra is a fit of the weighted superposition of parametrized lines to the measured spectrum. Ideally the parametrized line shape should be physically motivated. In spectroscopy the symmetric Voigt profile is popular. It is the convolution of a Lorentzian line resulting from monoexponential relaxation and a Gaussian line accounting for a statistical broadening. Analysis with a pseudo Voigt function[18] have been conducted on severely distorted spectra with a largely automated program [43]. In order to account for the frequently asymmetric line shape, a new physically motivated line-shape function was derived, see Chap. 7.

An application exploiting the temperature dependence of chemical shielding in water is presented in Sect. 4.9. In the diffusion measurements described in Sect. 4.10, spectroscopic resolution is used to differentiate between the phases of an emulsion.

2.1.6 Relaxometry

In the following the three variables spectroscopic frequency ω, transverse relaxation time T_2, and longitudinal relaxation time T_1 are jointly considered. Including these parameters the rotating frame equations (2.19)–(2.21) read:

$$\frac{\mathrm{d}M_x}{\mathrm{d}t} = -\Omega M_y - \frac{M_x}{T_2^*} \tag{2.56}$$

$$\frac{\mathrm{d}M_y}{\mathrm{d}t} = \Omega M_x - \frac{M_y}{T_2^*} \tag{2.57}$$

$$\frac{\mathrm{d}M_z}{\mathrm{d}t} = -\frac{M_z - M_z^{\mathrm{eq}}}{T_1}. \tag{2.58}$$

[17] In contrast e.g. to infrared spectroscopy, where band integrals are influenced by further parameters.

[18] There is no closed analytical expression for the convolution.

After the excitation pulse again a FID is obtained, i.e., no rf or gradient fields are applied. It is assumed that $\omega_{\mathrm{rf}} = \omega_0 = -\gamma B_0$ holds. As in (2.55) Ω designates the product $\gamma B_0 \sigma$. The effective transverse relaxation time is denoted by T_2^*. It is shorter than the natural relaxation time T_2 if inhomogeneities of the polarizing field lead to a dephasing of magnetization. Using the symbol T_2^+ for this relaxation time due to inhomogeneous broadening, the relation

$$\frac{1}{T_2^*} = \frac{1}{T_2} + \frac{1}{T_2^+} \tag{2.59}$$

holds for additive relaxation rates [22].

Without rf fields (2.58) is decoupled from (2.56) and (2.57). However, the time evolution of M_z influences the initial condition of transverse magnetization if the time t_{R} between two excitations is insufficient for return to thermal equilibrium. Here it is assumed that each excitation totally converts longitudinal to transverse x magnetization that decays to zero before the next excitation. Longitudinal magnetization builds up during the time interval t_{R}. Starting the time axis after the excitation the solution of (2.56) and (2.57) reads

$$M^+(t, t_{\mathrm{R}}) = M_z^{\mathrm{eq}}(1 - \exp(-t_{\mathrm{R}}/T_1)) \exp(i\,\Omega t) \exp(-t/T_2^*). \tag{2.60}$$

With the spatially integrated density $\rho(\Omega, T_1, T_2^*)$ (2.55) is extended to

$$\begin{aligned} M^+(t, t_{\mathrm{R}}) = &\int_{-\infty}^{\infty} \mathrm{d}\Omega \int_0^{\infty} \mathrm{d}T_1 \int_0^{\infty} \mathrm{d}T_2^* \rho(\Omega, T_1, T_2^*) \\ &\times (1 - \exp(-t_{\mathrm{R}}/T_1)) \exp(i\,\Omega t) \exp(-t/T_2^*). \end{aligned} \tag{2.61}$$

First the common case of spectroscopy with relaxation is further discussed. Let individual chemical groups with frequency shift Ω_k and relaxation times $T_{1,k}, T_{2,k}^*$ contribute with fraction ρ_k. The spin density is then expressed as

$$\rho(\Omega, T_1, T_2^*) = \sum_k \rho_k \delta(\Omega - \Omega_k) \delta(T_1 - T_{1,k}) \delta(T_2^* - T_{2,k}^*). \tag{2.62}$$

Insertion of (2.62) in (2.61) yields for the complex signal a superposition of damped oscillations as in (2.60) for a single group. Fourier transformation with respect to t can be calculated quite simply leading to the experimental spectrum

$$\begin{aligned} &\frac{1}{2\pi} \int_{-\infty}^{\infty} M^+(t, t_{\mathrm{R}}) \mathrm{e}^{-i\,\Omega t} \mathrm{d}t \\ &= \frac{1}{2\pi} \sum_k \rho_k (1 - \exp(-t_{\mathrm{R}}/T_{1,k})) \\ &\quad \left(\frac{1/T_{2,k}^*}{(1/T_{2,k}^*)^2 + (\Omega_k - \Omega)^2} + i \frac{\Omega_k - \Omega}{(1/T_{2,k}^*)^2 + (\Omega_k - \Omega)^2} \right). \end{aligned} \tag{2.63}$$

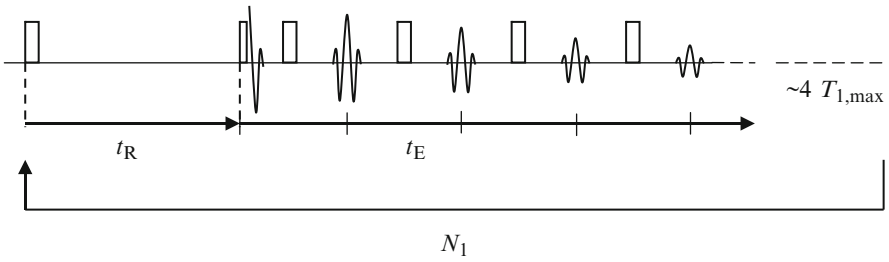

Fig. 2.6 Inversion recovery pulse sequence with CPMG detection for the determination of T_1–T_2 distributions. The first rf pulse with flip angle π prepares the magnetization. It is inverted to the $-z$ axis. During the evolution period t_R longitudinal relaxation occurs. The following $\pi/2$ rf pulse transforms the longitudinal magnetization into precessing, i.e., detectable transverse magnetization. It decays by T_2^* relaxation which can be fast due to dephasing magnetization. Dephasing is refocused repeatedly by the train of π pulses generating a series of echoes as in the CPMG sequence (Carr-Purcell-Meiboom-Gill). The first dimension of the experiment is the recovery time t_R. This dimension is sampled by incrementing t_R for different passes of the sequence. The second dimension is the time t_E at which the echoes occur. Several thousand echoes can be observed. The third dimension is the time axis for each individual echo. Frequently, this dimension is not sampled and only the center of each spin echo is detected

In the integration it has to be regarded that the above expression for the signal only holds for $t > 0$ and zero has to be inserted for $t < 0$. This asymmetry leads to the imaginary dispersion line in the spectrum. As already mentioned on p. 24 the real part for each group is a Lorentzian line centered around Ω_k. The full line width at half maximum (FWHM) amounts to $2/T_{2,k}^*$.[19] Thus experimentally a superposition of Lorentzian distributions instead of delta distributions assumed in (2.62) is obtained. The direct relation between the line integral and the fraction of associated spins mentioned on p. 24 is expressed in the prefactor ρ_k in (2.63). The additional T_1 weighting can be avoided allowing for a sufficiently long t_R.

A second case of increasing interest is the determination of a continuous distribution of longitudinal T_1 and transverse natural T_2 relaxation times [59]. For this purpose the pulse sequence shown in Fig. 2.6 can be used. Each time it starts with fully relaxed magnetization, e.g., between two repetitions about four times the longest longitudinal relaxation time is waited. The first inversion pulse produces a flip angle of π. For this initial condition the solution of (2.58) which contains $1 - 2\exp(-t_R/T_1)$ has an additional factor 2 compared to (2.61). The second pulse with nutation angle $\pi/2$ rotates the magnetization to the transverse plane. It dephases by natural T_2 relaxation, differences in chemical shielding and inhomogeneities of the polarizing field. The following train of π pulses inverts repeatedly the sign of magnetization phase if the rotation axis is x. This generates

[19]The prefactor of a normalized Lorentzian distribution is $1/\pi$ and not $1/(2\pi)$ as in (2.63). The factor 1/2 is a consequence of the missing signal for negative times. If the distribution is expressed with the linear frequency instead of angular frequency the full width at half maximum amounts to $1/(\pi T_{2,k}^*)$.

at echo times t_E between the pulses refocused magnetization denoted as spin echo. The envelope of the spin echo series only[20] decays by the occurring natural T_2 times as contributions by chemical shielding and field inhomogeneities are refocused. The echo maximums are therefore given by

$$M^+(t_E, t_R) = \int_0^\infty dT_1 \int_0^\infty dT_2\, \rho(T_1, T_2) \times (1 - 2\exp(-t_R/T_1))\exp(-t_E/T_2). \quad (2.64)$$

In this case the relation between the measured signal and the distribution $\rho(T_1, T_2)$ is a 2D Laplace transformation and not a Fourier transformation.[21] The difficulty in the analysis of T_1-, T_2 consists in the performance of a robust 2D inverse Laplace transformation. Recently progress has been achieved by the methods described in [59].

Finally a pulse sequence for the investigation of transverse relaxation in a slice with spatial resolution is presented, see Fig. 2.7. It combines read and phase encoding, see Fig. 2.4 with slice selection, see Fig. 2.5 and CPMG (Carr-Purcell-Meiboom-Gill) detection, see Fig. 2.6. After every spin echo with frequency encoding the effect of the phase gradient is revoked by a gradient of opposite polarity. The position in $\boldsymbol{k}$ space thus corresponds to the position before the slice selective π pulse. Starting with a further π pulse the trajectory in $\boldsymbol{k}$ space can be cycled through repeatedly. If r echoes are acquired for each of the N_y phase encoding steps r slice images with incremented echo time are obtained. Transverse relaxation can be analyzed for each point in the slice. Alternatively, the phase gradient can be incremented for each echo. Only N_y/r repetitions of the sequence are required, reducing drastically the experimental time. The fast spin echo imaging is denoted as turbo spin echo or RARE (rapid acquisition with relaxation enhancement). In favorable cases $r = N_y$ can be chosen for a "single shot" image acquisition.

One application is shown in Sect. 4.2, p. 110f. A tracer is used to generate relaxation contrast. Relaxation measurements on flowing samples are discussed in Sect. 2.1.9 with results presented in Sect. 4.5. For a relaxation measurement with 3D spatial resolution, see Sect. 4.6, p. 133f.

2.1.7 Diffusometry

In the following three Sects. the consequence of displacements of the spin carrying nuclei on the detected transverse magnetization is considered. A basic experiment

[20] Neglecting translational self diffusion and experimental artifacts.

[21] Fourier transformation can be treated as special case of Laplace transformation. The latter is a special case of Fredholm integral equation of the first kind, i.e., a linear integral equation with constant integral limits and the unknown function occurring only in the integral. This general case is treated in [59].

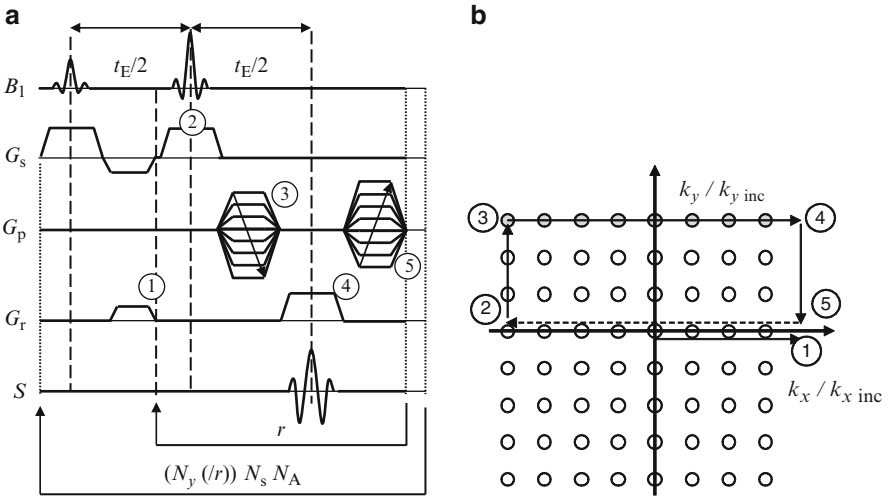

Fig. 2.7 Slice image with CPMG detection: (**a**) Pulse sequence. (**b**) Corresponding path and sampling points in $\boldsymbol{k}$ space. After excitation with B_1 and G_s the magnetization state in the selected slice corresponds to the origin of reciprocal position space. The read-dephase gradient G_r (1) leads to the point $(N_x k_{x\,\mathrm{inc}}/2,\ 0)$. In order to reduce the echo time, the slice refocusing gradient can be applied simultaneously. The following multi echo part is executed r times. The refocusing π pulses act selectively on the excited slice and produce a reflection with respect to the origin (2). The π pulses are self refocusing, no slice refocusing gradient is required. Prior to data acquisition the phase gradient G_p takes the magnetization to the beginning of a line in $\boldsymbol{k}$ space (3). After frequency encoding (4) the action of the phase gradient is revoked by a second gradient of opposite polarity (5). After N_y passes with N_A averages r slice images with incremented echo time are obtained. Alternatively, the phase gradient can be incremented for each of the r echoes. Only N_y/r instead of N_y repetitions are necessary, considerably speeding up data acquisition ("turbo spin echo" or "rapid acquisition with relaxation enhancement, RARE"). As all rf pulses are slice selective, the sequence can be applied to N_s further sliced during relaxation of one slice ("multi slice"). For 3D spatial resolution a second phase encoding is applied instead of slice selection. [31] © Wiley-VCH Verlag GmbH & Co. KGaA. Reproduced with permission

for the characterization of displacements is shown in Fig. 2.8. Transverse magnetization with phase zero is created by the first rf pulse with nutation angle $\pi/2$. Neglecting chemical shielding, relaxation, and displacement during the gradient-pulse width δ, integration of (2.33) results in the magnetization phase $-\gamma \boldsymbol{G_q r}\,\delta$ at position $\boldsymbol{r}$ after the first gradient pulse, where $\boldsymbol{G_q}$ designates the amplitude and direction of the gradient pulse. As already described on p. 26 the following rf pulse with nutation angle π inverts the sign of the magnetization phase. Further integration of (2.33) until the end of the second gradient pulse yields

$$\begin{aligned}\phi(\boldsymbol{R}(\Delta), t_E) &= \gamma \boldsymbol{G_q r}\,\delta - \gamma \boldsymbol{G_q}(\boldsymbol{r} + \boldsymbol{R}(\Delta))\,\delta \\ &\equiv -\boldsymbol{q}\,\boldsymbol{R}(\Delta),\end{aligned} \tag{2.65}$$

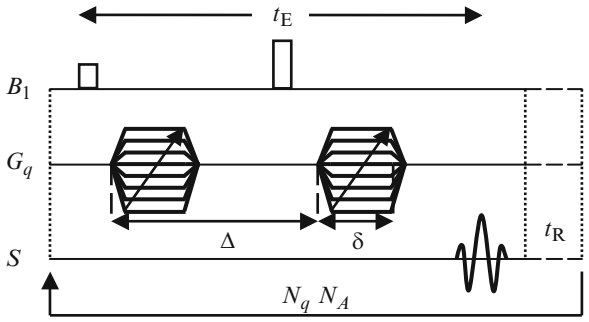

Fig. 2.8 Pulsed-Gradient Spin-Echo Sequence (PGSE). Transverse magnetization with phase zero is generated by the initial $\pi/2$ rf pulse (B_1). The first gradient pulse with amplitude G_q and duration δ creates a linear dependence of the phase to the position in direction of the gradient. A π rf pulse inverts the sign of the magnetization phase. After the observation time Δ the first gradient pulse if followed by a second pulse with identical amplitude and duration. Without displacements the magnetization helix created by the first pulse is unwound by the second pulse and a spin echo occurs at t_E. In the presence of displacements the amplitude of the spin echo is damped. A phase shift of the echo indicates coherent displacements. The displacement probability density function is usually sampled incrementing the gradient amplitude in N_q steps. N_A: number of averages. [31]

where $\boldsymbol{R}(\Delta)$ denotes the displacement during the observation time Δ. In (2.65) the definition of the reciprocal displacement vector

$$\boldsymbol{q} = \gamma \boldsymbol{G_q} \delta \tag{2.66}$$

has been introduced. Equations (2.65) and (2.66) correspond to (2.35) and (2.36), respectively, the position being replaced by the displacement. As in (2.38), the result for a distribution of displacements is expressed as

$$M^+(\boldsymbol{q}, \Delta) = \iiint \rho(\boldsymbol{R}(\Delta)) \exp(-i\boldsymbol{q}\boldsymbol{R}) \mathrm{d}R_x \mathrm{d}R_y \mathrm{d}R_z. \tag{2.67}$$

The nondimensionalized transverse magnetization is the Fourier transform of the displacement probability density function at position $\boldsymbol{q}$ in reciprocal displacement space. As in this simple experiment the starting point for the displacement is not resolved, $\rho(\boldsymbol{R}(\Delta))$ is also designated as average propagator $P(\boldsymbol{R}, \Delta)$. It can be determined approximately by inverse Fourier transform if reciprocal displacement space is suitably sampled. Concerning sampling the considerations on p. 14ff also apply for the measurement of displacements.

For unrestricted translational self diffusion the average propagator is determined by the self-diffusion coefficient D:

$$\rho(\boldsymbol{R}(\Delta)) = (4\pi D\Delta)^{-3/2} \exp(-\boldsymbol{R}^2/(4D\Delta)). \tag{2.68}$$

Inserting this propagator in (2.67) for only one gradient direction yields for the signal

$$M^{+}(q, \Delta) = M_z^{\mathrm{eq}} \exp(-q^2 D \Delta), \tag{2.69}$$

see e.g. [13].

The assumption in (2.65) and (2.67) that displacements during the gradient pulses can be neglected ("narrow-pulse approximation") can be inaccurate. For self diffusion the Bloch equations (2.14)–(2.16) have been extended by Torrey [65]. In [40] the solution without relaxation is given:

$$\ln(M^{+}(t)/M_z^{\mathrm{eq}}) = -D\gamma^2 \int_0^t \left(\int_0^{t'} \tilde{G}_q(t'')\mathrm{d}t'' \right)^2 \mathrm{d}t'. \tag{2.70}$$

The effective gradient $\tilde{G}_q$ in (2.70) accounts for the influence of π rf pulses by inversion of the sign of the preceding gradient pulses. For the basic pulse sequence shown in Fig. 2.8 integration yields the equation of Stejskal and Tanner [60, 61]:

$$M^{+}(G_q, \delta, \Delta) = M_z^{\mathrm{eq}} \exp(-\gamma^2 G_q^2 \delta^2 D(\Delta - \delta/3)). \tag{2.71}$$

Further solutions for pulse sequences applied in case of short T_2 or background gradients are given by Cotts et al. [19].

For unrestricted diffusion the self-diffusion coefficient D is usually determined by a fit of (2.71) to experimental data with varying G_q and constant δ, Δ. No tracer is required. Uncertainties are in the range of percent. An application with restricted diffusion is presented in Sect. 4.10. Dependence of the measured diffusion on the observation time in a tortuous porous medium as well as in a spherical confinement is treated.

Including magnetic shielding and the three introduced relaxation times the basic experiment shown in Fig. 2.8 already leads to rather complex results. As simple case the distribution in (2.62) is extended by a contribution from natural relaxation times ($\delta(T_2 - T_{2,k})$) and diffusion ($\delta(D - D_k)$) per chemical group. Monoexponential relaxation and unrestricted diffusion are assumed. In order to study diffusion for different components of a multi-component system spectroscopic resolution can be used. To sample the diffusion dimension, the experiment is repeated with varying gradient amplitude. Each time the second half of the echo is digitized. The time axis t starts at t_{E}. Background gradients contributing to T_2^* are assumed to be insignificant for diffusion encoding. Natural T_2 relaxation is neglected compared to T_2^* relaxation during data acquisition.[22] After Fourier transform with respect to t the real part of the result then reads:

$$\mathrm{Re}\left(\int_{-\infty}^{\infty} M^{+}(t, t_{\mathrm{E}}, t_{\mathrm{R}}, G_q, \delta, \Delta) \mathrm{e}^{-i\Omega t} \mathrm{d}t \right)$$

[22] Condition for symmetric echoes.

$$= \sum_k \rho_k (1 - \exp(-t_R/T_{1,k})) \exp(-t_E/T_{2,k})$$
$$\frac{1/T^*_{2,k}}{(1/T^*_{2,k})^2 + (\Omega_k - \Omega)^2} \exp(-\gamma^2 G_q^2 \delta^2 D_k (\Delta - \delta/3)). \tag{2.72}$$

Before diffusion coefficients can be determined by a fit of the gradient dependence a deconvolution of the spectra can be necessary.

The case of continuous distribution of diffusion coefficients and longitudinal relaxation in analogy to (2.64) is treated e.g. in [38].

2.1.8 Velocimetry

In Sect. 2.1.7 first the measurement of displacements with the pulsed-gradient spin-echo experiment (PGSE) sequence in the "narrow-pulse approximation" was presented, see (2.67). For unrestricted self diffusion without coherent displacement the expression for the signal without this approximation was then formulated in (2.71). Here the case of coherent displacement is treated. Integration of (2.33) without the narrow-pulse approximation yields for the magnetization phase

$$\phi(t) = -\gamma \int_0^t \tilde{\boldsymbol{G}}(t')\boldsymbol{r}(t')\mathrm{d}t', \tag{2.73}$$

where $\tilde{\boldsymbol{G}}$ denotes the effective gradient introduced in (2.70). Expansion of $\boldsymbol{r}(t')$ to the linear term leads to the expression of the magnetization phase for displacements with velocity $\boldsymbol{v} = (u, v, w)$

$$\begin{aligned}\phi(t) &= -\gamma \left\{ \boldsymbol{r}(0) \int_0^t \tilde{\boldsymbol{G}}(t')\mathrm{d}t' + \boldsymbol{v} \int_0^t \tilde{\boldsymbol{G}}(t')t'\mathrm{d}t \right\} \\ &= -\gamma \tilde{\boldsymbol{m}}_0(t)\boldsymbol{r}(0) - \gamma \tilde{\boldsymbol{m}}_1(t)\boldsymbol{v},\end{aligned} \tag{2.74}$$

where $\tilde{\boldsymbol{m}}_0$ and $\tilde{\boldsymbol{m}}_1$ denote the zeroth and the first moment of the effective gradient, respectively. With the relation

$$\boldsymbol{k} = \gamma \tilde{\boldsymbol{m}}_0(t) \tag{2.75}$$

the signal without relaxation, diffusion, and chemical shielding reads

$$M^+(t) = \iiint \iiint \rho(\boldsymbol{r}, \boldsymbol{v}) \exp(-i\boldsymbol{k}\boldsymbol{r}(0)) \exp(-i\gamma \tilde{\boldsymbol{m}}_1(t)\boldsymbol{v}) \, \mathrm{d}x\mathrm{d}y\mathrm{d}z \, \mathrm{d}u\mathrm{d}v\mathrm{d}w. \tag{2.76}$$

Thus the spin density $\rho(\boldsymbol{r}, \boldsymbol{v})$ with respect to the parameters position and velocity can in principle be determined by inverse Fourier transformation of the measured signal if the 6D reciprocal space is suitably sampled. In the following measurements of

velocity without and with spatial resolution are presented. Finally the influence of gradient imperfections is discussed.

2.1.8.1 Velocity Probability Density Function

As simplest case the experiment shown in Fig. 2.8 is treated for the case of perfect gradients and time-independent velocity field. During data acquisition the reciprocal position vector $\boldsymbol{k}$ calculated with the effective gradient is zero. With the definition of the velocity probability density function (VPDF)

$$f(\boldsymbol{v}) = \iiint \rho(\boldsymbol{r}, \boldsymbol{v}) \mathrm{d}x \mathrm{d}y \mathrm{d}z \tag{2.77}$$

equation (2.76) reduces to

$$M^{+}(t_{\mathrm{E}}, \boldsymbol{q}_v) = \iiint f(\boldsymbol{v}) \exp(-i\,\boldsymbol{q}_v \boldsymbol{v})\, \mathrm{d}u \mathrm{d}v \mathrm{d}w, \tag{2.78}$$

where the reciprocal velocity vector $\boldsymbol{q}_v = \gamma \tilde{\boldsymbol{m}}_1(t_{\mathrm{E}})$ has been introduced. The time point t_{E} for data acquisition in (2.78) refers to the situation where an echo is observed due to field inhomogeneities or chemical shielding. For the PGSE experiment the calculation of the first moment of the effective gradient yields for the reciprocal velocity vector $\boldsymbol{q}_v = \gamma \boldsymbol{G}_{\boldsymbol{q}} \delta \Delta$. It is related to the reciprocal displacement vector in the narrow-pulse approximation (2.66) by $\boldsymbol{q}_v = \boldsymbol{q} \Delta$. The VPDF is obtained by discrete inverse Fourier transform of the data sampled by a variation of $\boldsymbol{G}_{\boldsymbol{q}}$.

In terms of probabilities $\rho(\boldsymbol{r}, \boldsymbol{v})$ can be denoted as joint probability with $\rho(\boldsymbol{r} \cap \boldsymbol{v})$ as alternative symbol. Probability density is insofar incorrect as the integral e.g. in (2.76) is not unity but the total number of observed spins N_{S}. The function $f(\boldsymbol{v})$ in (2.77) is a 3D marginal probability obtained by integration over x, y, and z. In the following also the cases "conditional probability" and "independent probabilities" occur. Distribution here denotes the distribution density per infinitesimal interval. The integral or sum in the discrete case up to a given value of the variable is denoted as cumulative distribution.

An application of VPDF measurement in symmetric capillary flow to rheometry is presented in Sect. 4.4 on p. 115ff.

2.1.8.2 Position and Velocity Distribution

A simple pulse sequence for sampling of position and velocity space is shown in Fig. 2.9, see also [52]. The first rf pulse generates transverse magnetization with phase zero in the entire coil. As in Fig. 2.8 the first gradient pulse of the pair for velocity encoding follows. The subsequent π rf pulse is slice selective, see p. 19. It refocuses evolution due to field inhomogeneities and chemical shielding.

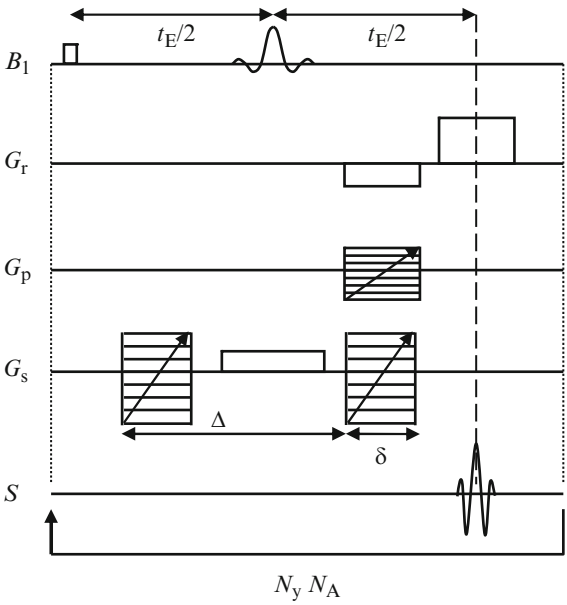

Fig. 2.9 Simple pulse sequence for the measurement of the velocity component perpendicular to an imaged slice, see also [52]

Note that the slice selective π rf pulse requires no slice-refocusing gradient as the excitation pulse in Fig. 2.5. Gradients for velocity encoding and slice selection have the same direction so the velocity component perpendicular to the observed slice is sampled. The result is integrated over the remaining velocity components. The second velocity-encoding gradient acts as described for the PGSE experiment within the observed slice. Outside the slice both gradients of the PGSE pair cause rotations in the same sense and the magnetization is spoiled. Simultaneously to the second velocity-encoding gradient a phase gradient G_p and read-dephase gradient G_r are applied as in Fig. 2.4a. Finally the total transverse magnetization is sampled under the action of a read gradient. The experiment is designed to allow for a short echo time t_E. This is advantageous if the velocity of a spin is not constant in time. In addition it allows the measurement on systems with relatively short transverse relaxation time T_2. An example is given in [52] where the velocity of SF_6 gas was measured. The ^{19}F nuclei were observed. This is possible with reasonable SNR, especially if SF_6 is used under pressure. Drawbacks of the pulse sequence are that only the velocity component perpendicular to the slice can be measured and that no "flow compensation" of space encoding is present. This means that the first moment of the slice, phase, and read gradient are not zero during data acquisition. Thus, depending on velocity, deviations from the sampling of reciprocal position space represented in Fig. 2.4b occur. On the other hand, deviations are minimized by the application of these gradients immediately before data acquisition.

One of the first pulse sequences for velocity imaging is described in [50]. It consists of only one rf pulse and is able to detect all three velocity components. In [9] an experiment with flow compensated slice and phase gradient is explained.

The read gradient is also flow compensated at time t_E, of course not for the entire acquisition time. Further methods for the phase encoding of velocity are presented in [13]. Selection of the best pulse sequence for the system under investigation requires a deeper understanding of the NMR methods.

The experimental time can be reduced drastically if the spatial resolution is assumed to be sufficiently high so that at each point in position space only one velocity is present. Following [41] the marginal spin density in position space is denoted as $\rho(\boldsymbol{r})$ and $p(\boldsymbol{v}|\boldsymbol{r})$ denotes the conditional probability that spins at position $\boldsymbol{r}$ have velocity $\boldsymbol{v}$. The above assumption signifies

$$\begin{aligned}\rho(\boldsymbol{r},\boldsymbol{v}) &= \rho(\boldsymbol{r})\,p(\boldsymbol{v}|\boldsymbol{r}) \\ &= \rho(\boldsymbol{r})\delta(\boldsymbol{v}-\boldsymbol{v}(\boldsymbol{r})).\end{aligned} \tag{2.79}$$

Insertion into (2.76) results in

$$M^{+}(t) = \iiint \rho(\boldsymbol{r}) \exp(-i\boldsymbol{k}\boldsymbol{r}(0)) \exp(-i\boldsymbol{q}_v\boldsymbol{v}(\boldsymbol{r}))\,\mathrm{d}x\mathrm{d}y\mathrm{d}z. \tag{2.80}$$

Fourier transformation with respect to position space yields $\rho(\boldsymbol{r})\exp(-i\boldsymbol{q}_v\boldsymbol{v}(\boldsymbol{r}))$. The magnitude of this complex image is the marginal spin density in position space. If the product $\boldsymbol{q}_v\boldsymbol{v}(\boldsymbol{r})$ is within the range $[-\pi\ \pi[$ velocity is unequivocally related to image phase. Instead of sampling reciprocal velocity space, first a reference image without velocity encoding is acquired. For each velocity component, a single image with encoding in the respective direction is sufficient for the calculation of the velocity field from the phase difference. Due to imperfections, a phase difference can occur experimentally even for velocity zero. In this case the image with velocity encoding without flow can be used as phase-reference image [52]. An application of this method is shown in Fig. 4.27, p. 139.

2.1.8.3 Influence of Gradient Imperfections

Up to here ideal gradient pulses and a homogeneous static field have been assumed. This is a good approximation for the presented measurements conducted in the high field tomograph. The static field is homogenized by superconducting and adjustable resistive coils to the ppm range and better. Gradient coils are also sophisticated and actively shielded. Transient effects by eddy currents are minimized. Persisting effects after gradient pulses are not observed.

However, for measurements in permanent-magnet systems as described in Sect. 4.4, p. 115ff, important effects occur. Calculations for static samples are presented in Chap. 8. Here the influence on the VPDF measurement is treated. As explained in Chap. 8.1 it is assumed that the dominant effects can be represented by background gradients.[23]

[23] That is unintended gradients by eddy currents or remanent changes of the permanent-magnet system that act in the "background."

A fully developed laminar, isothermal, and macroscopically homogeneous flow through a cylindrical tube is considered. Choosing the tube axis as z axis only the radially varying w component of velocity is non-zero. To measure the VPDF of w only gradients in z direction are required. Thus the moments in (2.74) are scalar functions. For the sake of simplicity the direction z is not written as index. Equation (2.76) simplifies to

$$M^+(t) = \iiint\iiint \rho(\boldsymbol{r},\boldsymbol{v}) \exp(-i\gamma\tilde{m}_0(t)z(0)) \exp(-i\gamma\tilde{m}_1(t)w)\,\mathrm{d}x\mathrm{d}y\mathrm{d}z\,\mathrm{d}u\mathrm{d}v\mathrm{d}w. \tag{2.81}$$

Integration over x, y, u, and v leads to the 2D marginal probability $\rho(z,w)$. A dependence of the observed spin density on z results from the axial distribution of the rf field. Again only one symbol ρ is used and variables over which the distribution is not integrated are listed as arguments. The argument of $z(0)$ is not written. As velocity in the tube flow depends on x and y but not on z it holds

$$\begin{aligned}\rho(z,w) &= \rho(z)\,p(w|z)\\ &= \rho(z)\,p(w)\\ &\equiv \rho(z)\,f(w).\end{aligned} \tag{2.82}$$

In (2.77) $f(\boldsymbol{v})$ is normalized to the total number of observed spins. If in the above equation $\rho(z)$ is normalized to the total number of observed spins, $f(w) \equiv p(w)$ is normalized to one. Given the independence of the distributions $\rho(z)$ and $f(w)$ the integral in (2.81) can be simplified to the product

$$M^+(t) = \int \mathrm{d}z\rho(z)\exp(-i\gamma\tilde{m}_0(t)z)\int \mathrm{d}w\,f(w)\exp(-i\gamma\tilde{m}_1(t)w). \tag{2.83}$$

In contrast to (2.78) it is not assumed that the zeroth moment vanishes as for the ideal sequence in Fig. 2.8. If permanent and transient effects as described in Sect. 8.4.1 are not compensated as explained in Sect. 8.4.2, the effects can be studied using a simple model for the gradient imperfections, the spatial spin density, and VPDF.

Regarding the permanent effects a constant gradient G_p acting in the background from excitation to detection is assumed. A permanent gradient is a remanent gradient that persists after a switched gradient pulse until it possibly gets altered by a subsequent switched gradient pulse. The existence of a permanent gradient is obvious if imaging by frequency encoding is possible without switched gradient. Concerning the dependence of the permanent-gradient amplitude on the amplitude of the previously switched gradients a marked hysteresis was observed. In general for different steps of displacement encoding different permanent gradients act. A reproducible situation can be achieved by steady-state methods, see Figs. 4.11 and 8.2. Transient effects are described as an additional amplitude contribution G_m for the

second gradient pulse, see Sect. 8.4.3. The direction of the permanent and transient gradients is the same as that of the switched gradients, here z.

The spin density detected by an ideal coil is a constant ρ within the length of the coil from $z = -a/2$ to $z = a/2$ and zero outside the coil. This corresponds to a rectangular rf profile. For the VPDF a parabolic velocity profile is assumed. This also corresponds to a constant value $1/w_\mathrm{m}$ from velocity zero to the maximum velocity w_m. Inserting these assumptions concerning the distributions and gradient imperfections into (2.83) the expression

$$M^+(t) = a\rho\,\mathrm{sinc}\left(\gamma\tilde{m}_0\frac{a}{2}\right)\left[\mathrm{sinc}(\gamma\tilde{m}_1 w_\mathrm{m}) + \frac{i\,(\cos(\gamma\tilde{m}_1 w_\mathrm{m}) - 1)}{\gamma\tilde{m}_1 w_\mathrm{m}}\right] \tag{2.84}$$

with

$$\tilde{m}_0(t) = G_\mathrm{p}(t - t_\mathrm{E}) + G_\mathrm{m}\delta \tag{2.85}$$

and

$$\tilde{m}_1(t) = \frac{1}{2}\left(G_\mathrm{p}(t^2 - t_\mathrm{E}^2/2) + G_\mathrm{m}\delta(\delta + t_\mathrm{E}) + \hat{G}\delta t_\mathrm{E}\right) \tag{2.86}$$

is obtained for the signal. In (2.84) "sinc" denotes the sine function divided by its argument. The amplitude of the ideal gradient pulse is denoted in (2.86) as $\hat{G}$. In (2.86) it has been assumed that the gradient pulses immediately follow the rf pulses what usually is the case in the experiment.

The influence of gradient imperfections on the magnetization dynamics described in (2.84)–(2.86) is shown in Fig. 2.10 for typical experimental parameters. In Fig. 2.11 the resulting distortion of the VPDF is depicted. The length of the rectangular rf profile was set to $a = 40\,\mathrm{mm}$ and $\rho = 1/a$. A maximum velocity of $w_\mathrm{m} = 10\,\mathrm{mm/s}$ was chosen. An echo time of $t_\mathrm{E} = 28\,\mathrm{ms}$ and gradient-pulse duration of $\delta = 3\,\mathrm{ms}$ was used. Four times the maximum velocity was taken as field of flow. For 128 flow-encoding steps the resulting maximum amplitude of the pulsed gradient is $0.9\,\mathrm{T/m}$.

Figure 2.10 shows the real part of the signal for four situations. The ideal situation without permanent and transient effects is depicted in Fig. 2.10a. It is approximately realized in a high-field tomograph or in the permanent-magnet system using the compensated pulse sequence of Fig. 8.2. The calculated signal for the permanent-magnet system without any compensation is shown in Fig. 2.10b. Transient effects resulting in a gradient mismatch prevent the formation of a complete echo. In Fig. 2.10c only this effect is included. As transient effects increase with increasing amplitude of the pulsed gradient this corresponds to a low-pass filter in the sampling of the VPDF, see also Fig. 2.11c. The permanent gradient additionally included in Fig. 2.10b can cause the formation of an echo which however is shifted with respect to the spin-echo (SE) time. The width of the echo decreases with increasing magnitude of the permanent gradient. Values for the permanent gradient were obtained from a measured hysteresis curve. The transient effect was calculated from a function fitted to experimental results:

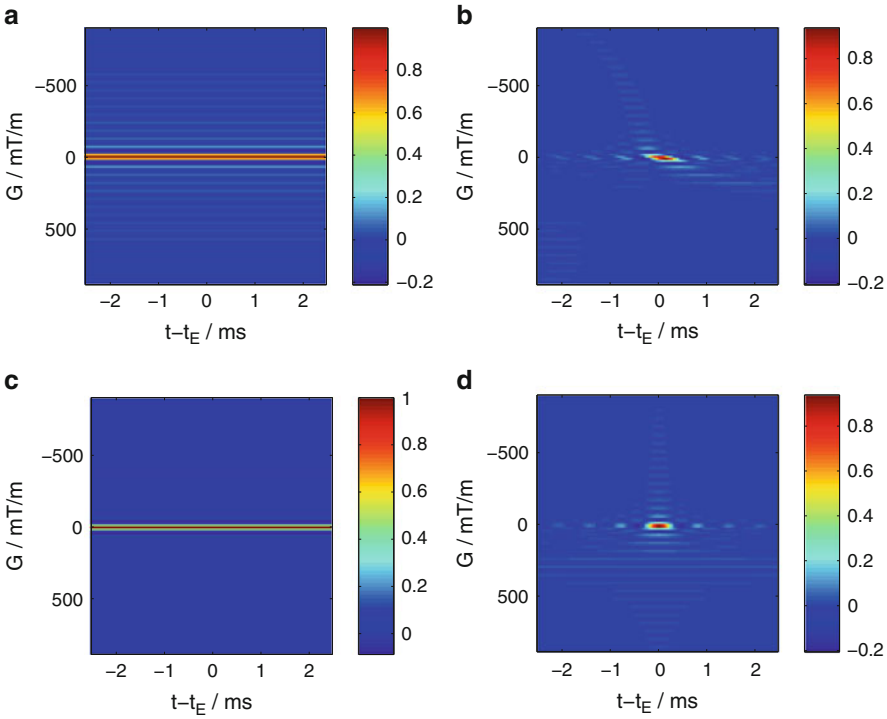

Fig. 2.10 Real part of PGSE signal for a rectangular rf profile and a Newton fluid calculated using (2.84)–(2.86) and typical experimental parameters. The four cases with and without permanent gradient G_p and gradient mismatch G_m are shown, respectively. (**a**) $G_p = G_m = 0$. (**b**) $G_p \neq 0$ and $G_m \neq 0$. (**c**) $G_p = 0$ and $G_m \neq 0$. (**d**) $G_p \neq 0$ and $G_m = 0$

$$G_{\mathrm{m}} = \mathrm{sign}(\hat{G}) \left[1 - \exp\left(-\frac{|\hat{G}|}{0.0136\,\mathrm{T/m}} \right) \right] 1.14 \times 10^{-4}\,\mathrm{T/m} + 4.91 \times 10^{-4} \hat{G}. \tag{2.87}$$

In (2.87) the sign function is plus or minus one in accordance with the sign of its argument. Figure 2.10d shows the calculated signal in the presence of the permanent gradient from the hysteresis curve without transient effects. This corresponds to the situation achieved with the steady-state sequences, See Fig. 4.11. Without gradient mismatch G_{m} the signal maximum occurs at the spin-echo time t_{E}. The width of the echo varying with the permanent gradient does not influence the velocity encoding at the echo time. However, according to (2.86) the first moments of the sampling points at t_{E} are shifted with respect to the ideal values by $G_{\mathrm{p}}(t_{\mathrm{E}}/2)^2$.

Figure 2.11 shows the VPDF calculated from the signal at time t_{E} for the data represented in Fig. 2.10. A low-pass Hamming filter was applied prior to the discrete inverse Fourier transform. It effectively reduces Gibbs artifacts without important broadening. This is evident for the ideal case shown in Fig. 2.11a. The calculated

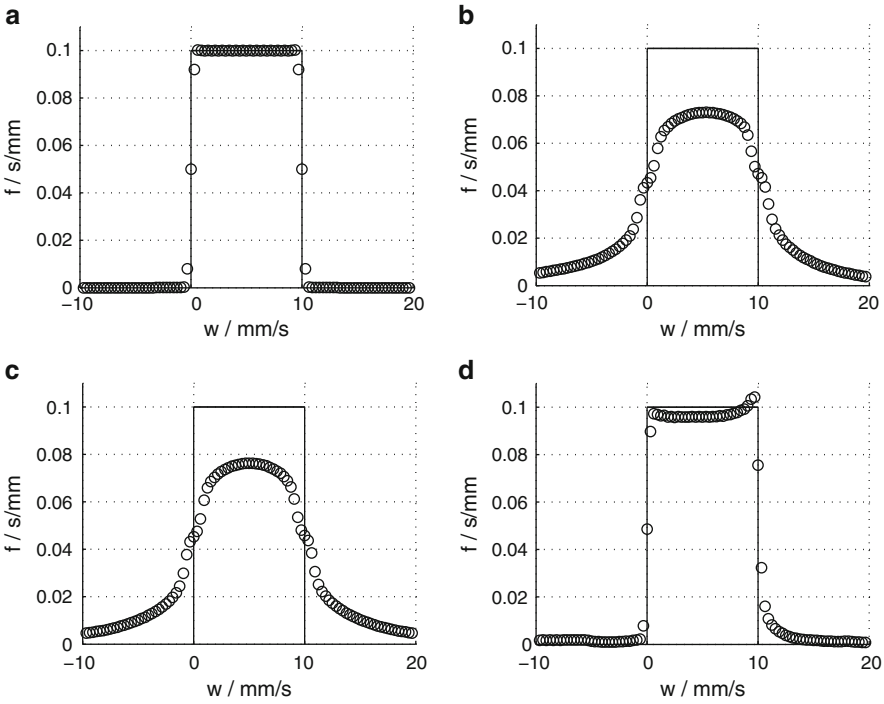

Fig. 2.11 VPDF calculated using the signals shown in Fig.2.10 at t_E. The *solid line* corresponds to the rectangular VPDF of a Newton fluid with the given maximum velocity. A Hamming filter was applied prior to the discrete inverse Fourier transform to reduce Gibbs artifacts. (**a**) $G_p = G_m = 0$. (**b**) $G_p \neq 0$ and $G_m \neq 0$. (**c**) $G_p = 0$ and $G_m \neq 0$. (**d**) $G_p \neq 0$ and $G_m = 0$

points represented by circles are in good agreement with the input VPDF plotted as solid line. In Figs. 2.11b and 2.11c the low-pass filtering by transient effects is obvious. The VPDF is significantly broadened. A difference between Fig. 2.11b with permanent gradients and Fig. 2.11c without is hardly noticeable. However, in the absence of transient effects the influence of sampling-point shifts by permanent gradients is evident in Fig. 2.11d. Besides the bending of the VPDF with a peak at the highest velocity a broadening of the high-velocity edge of the VPDF is obtained. This calculated result closely resembles the experimental result shown in Fig. 2.12 for a Newton fluid and the pulse sequence of Fig. 4.11. If the values of sampling-point shifts by permanent gradients are known, their effect can be treated by a post processing described further on.

One method for measurements in presence of gradient imperfections is presented in [12]. However, it is only suited for the study of diffusion, not of velocities. Experimentally, the generation of permanent gradients can be avoided by actively shielded gradient systems as described in Sect. 3.3.1.

2.1.8.4 Post Processing

In the inverse discrete Fourier transform it is assumed that data points are sampled on a grid of equidistant sampling points, see p. 14ff. The N ideal sampling points in reciprocal velocity space are denoted as $q_{vn} = n q_{v\,\mathrm{inc}}$ with $n = -N/2, \ldots, N/2-1$. The irregular grid resulting from a permanent-gradient hysteresis is designated by q_{vG}. Regriding aims to infer the signal $M^+(q_{vn})$ on the ideal grid from the measured $M^+(q_{vG})$. The inverse transform is then applied to the regrided data. This problem is also known in MRI, where in some methods reciprocal position space is deliberately sampled on an irregular grid [51, 54]. For a 1D VPDF the number of data points is manageable. Thus the direct method of "uniform resampling" was implemented. Its explanation in [51] starts with the inverse problem. First the data points $M^+(q_{vn})$ on the ideal grid are assumed to be known and the result $M^+(q_{vG})$ for the irregular grid to be wanted. According to the Whittaker–Shannon interpolation formula the solution is

$$M^+(q_{vG}) = \sum_n K(q_{vG} - q_{vn}) M^+(q_{vn}) \tag{2.88}$$

with the ideal sinc interpolation kernel

$$K(q) = \frac{\sin(\pi q/q_{v\,\mathrm{inc}})}{\pi q/q_{v\,\mathrm{inc}}}. \tag{2.89}$$

The interpolation formula assumes that the function M^+ is bandlimited. The inverse Fourier transform or spectrum of M^+ is the VPDF. As the spectrum is limited by zero and the maximum velocity $w_{\max}$ this condition is fulfilled. It is further assumed that the sampling interval is smaller than the inverse Nyquist rate, i.e., $q_{v\,\mathrm{inc}} < \pi/w_{\max}$ has to be ensured in the experiment.[24] The sum in (2.88) extends from $-\infty$ to ∞. Therefore it has to be finally assumed that the contribution of points outside the N points sampled in the center of q_v space can be neglected. Collecting M calculated results on an irregular grid in a vector $\boldsymbol{b}$ and the N sampled points on a regular grid in a vector $\boldsymbol{x}$, the M equations (2.88) can be represented in matrix notation:

$$\boldsymbol{b} = \boldsymbol{A}\boldsymbol{x} \quad \text{with} \quad A_{Gn} = K(q_{vG} - q_{vn}). \tag{2.90}$$

The situation in the experimental problem is inverse, i.e., $\boldsymbol{b}$ is known and $\boldsymbol{x}$ is wanted. For $M > N$ $\boldsymbol{x}$ is overdetermined. It can be optimally determined in the least-squares sense by multiplication of (2.90) with the $N \times M$ Moore-Penrose pseudo inverse of $\boldsymbol{A}$. From the singular-value decomposition (SVD) USV' of $\boldsymbol{A}$ it is calculated to $VS^{-1}U'$.

[24] The magnetization phase angle is given by $\phi = q_v w$. Thus $w_{\max}$ corresponds to an angular frequency.

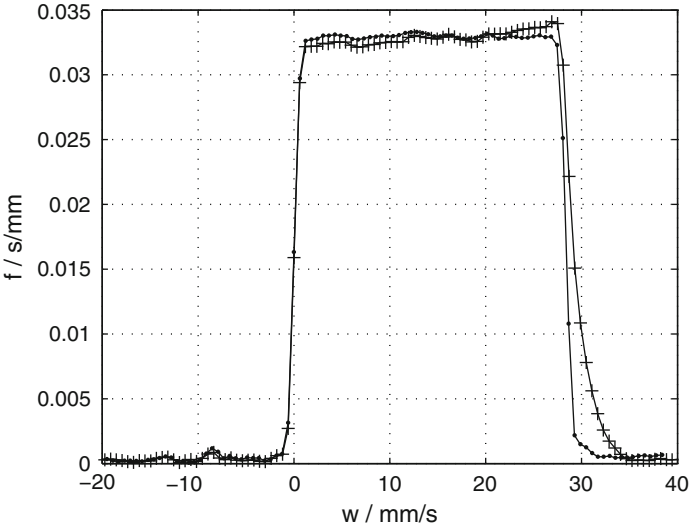

Fig. 2.12 Rectification by post processing of the VPDF measured with sampling-point shifts. Crosses represent the result of inverse Fourier transformation of data measured with the sequence shown in Fig. 4.11. Regriding of the experimental data to equidistant sampling points prior to inverse transformation leads to the improved result displayed as points. Knowledge of the permanent-gradient hysteresis in the experiment is required for regriding

Regriding requires the permanent-gradient hysteresis to be known to calculate the sampling-point positions according to (2.86). In order to obtain a stable inversion of 2.90 the number of sampled points was chosen as twice the number of calculated points for the inverse transform [51]. Thus the experimental time is doubled. The considerable improvement achieved by regriding is obvious in Fig. 2.12 showing experimental results for a Newton fluid with and without post processing, respectively.

2.1.8.5 Alternative NMR Methods

As alternative to phase encoding velocities can be measured by NMR time of flight methods. One method is to generate a line pattern of saturated magnetization that is imaged after a time which is insufficient for complete longitudinal relaxation [41]. An early method used two distinct coils for saturation and detection [30]. Another possibility is to monitor the signal decay due to outflow of excited spins from the detection volume. In contrast, a signal enhancement is obtained for unsaturated spins flowing into the observed slice (inflow) if the repetition time of an imaging sequence is short compared to the longitudinal relaxation time. An application is presented in Sect. 4.8. Phase encoding is considered to be the most accurate method of NMR velocimetry [15]. However, it has to be assured that inflow and outflow effects do

not lead to errors. In the context of inhomogeneous fields this is discussed in the following Sect. 2.1.9.

2.1.9 Relaxation for Flowing Liquids

Also relaxometry experiments without magnetic-field gradients are influenced if the sample flows through the NMR system. Early applications used the effects to monitor blood flow [57]. Considerations in the context of HPLC-NMR hyphenation can be found e.g. in [4]. However, frequently plug flow is assumed [63] and inhomogeneities of the magnetic fields are neglected or drastically simplified [66]. On the other hand, very general statements are formulated by Stepisnik [62]. In the following, expressions for quantitative description in the case of laminar pipe flow presented in Sect. 4.5 are derived. The aim is to correct the relaxometry experiment for the flow-induced effects.

The standard CPMG sequence is considered, see detection part after t_R in Fig. 2.6. It is assumed that:

1. The sample is macroscopically homogeneous
2. Diffusion and thus Taylor dispersion can be neglected
3. The signal is not attenuated by $\boldsymbol{B_0}$ inhomogeneities, i.e., homogeneous $\boldsymbol{B_0}$ or effective refocusing pulses

Due to the timing, echoes from signal excited by imperfect refocusing pulses occur at the time of subsequent refocusing pulses. First the simple case of signal decay by outflow of excited spins is treated using further assumptions. This is followed by calculations including inhomogeneous $\boldsymbol{B_0}$ and $\boldsymbol{B_1}$.

2.1.9.1 Simplest Model: Outflow of Excited Spins

In the simplest model additionally a rectangular $\boldsymbol{B_1}$ profile and homogeneously polarized spins are assumed. Immediately after ideal excitation transverse magnetization is maximum within a cylindrical pipe section of length L and zero outside. For a flow rate Q, the fraction of excited spins in the section of volume V initially decreases linearly by $(1 - Qt/V)$. The fraction decreases less than linear when also non excited spins flow out of the pipe section. With the maximum velocity $w_{\max}$ this occurs at times larger than $t = L/w_{\max}$. This is illustrated in Fig. 2.13.

Considering outflow as well as transverse relaxation with rate R_2 the signal is described by

$$M^+(t) = \int_0^\infty \int_0^{L/t} \rho_{w,R_2}(w, R_2)(1 - wt/L) \exp(-R_2 t)\, \mathrm{d}w\, \mathrm{d}R_2. \qquad (2.91)$$

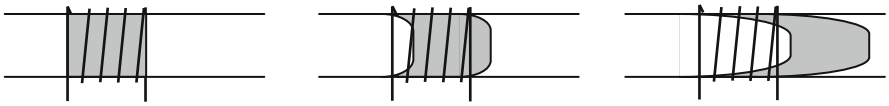

Fig. 2.13 Outflow of excited spins from a cylindrical pipe section of length L. *Left*: Excitation at time $t = 0$. *Middle*: reduction of the volume of excited spins in the pipe section linear in time for $t \leq L/w_{\max}$. *Right*: Reduction less than linear in time for $t > L/w_{\max}$

The velocity integral only extends to L/t. For higher velocities all excited spins have left the pipe section. If velocity and relaxation are not independent, the relation has to be determined for further evaluation. If however relaxation and velocity or shear rate are independent the joint distribution can be factorized into the marginal distributions and the integral into

$$M^+(t) = \int_0^{L/t} \rho_w(w)(1 - wt/L)\,\mathrm{d}w \int_0^{\infty} \rho_{R_2}(R_2)\exp(-R_2 t)\,\mathrm{d}R_2. \tag{2.92}$$

The second integral is the Laplace transform of the relaxation-rate distribution.

For velocities exceeding the maximum velocity the first integral yields one for the velocity distribution and the average velocity for its first moment:

$$M^+(t < L/w_{\max}) = (1 - \langle w\rangle t/L) \int_0^{\infty} \rho_{R_2}(R_2)\exp(-R_2 t)\,\mathrm{d}R_2. \tag{2.93}$$

The slope of the initial decrease of the signal ratio with and without flow is determined by the mean residence time $L/\langle w\rangle$. Calculations for times $t > L/w_{\max}$ require knowledge of the velocity probability-density function (VPDF). For the special case of a Newton fluid with $\rho_w(w) = 1/w_{\max}$ the integral for later times yields a hyperbolic decrease of the ratio:

$$M^+(t > L/w_{\max}) = \frac{L}{2w_{\max}} \frac{1}{t} \int_0^{\infty} \rho_{R_2}(R_2)\exp(-R_2 t)\,\mathrm{d}R_2. \tag{2.94}$$

Expanding the exponential in (2.93) for the case of a single relaxation rate R_2 leads to

$$M^+(t < L/w_{\max}) = 1 - \left(\frac{\langle w\rangle}{L} + R_2\right) t + \ldots. \tag{2.95}$$

Thus a monoexponential decay with the sum of the relaxation rate and the inverse mean residence time can be approximated for short times. This common approximation [4, 57]

$$\left(1 - \frac{\langle w\rangle}{L}\, t\right) \exp(-R_2 t) \approx \exp\left(-\left(R_2 + \frac{\langle w\rangle}{L}\right) t\right) \tag{2.96}$$

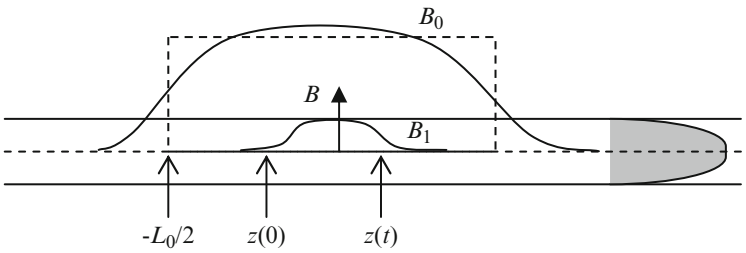

Fig. 2.14 Schematic representation of B_0 and B_1 profile and relevant z coordinates

can be transformed into $(1 - \langle w \rangle t/L) \exp(\langle w \rangle t/L) \approx 1$ to evaluate its validity. The deviation amounts e.g. to -10% for $t = 0.4\, L/\langle w \rangle$.

2.1.9.2 Calculations Including Inhomogeneous Magnetic Fields

Experimental results show that the initial decay of signal ratio is slower than predicted by (2.93). Indeed the assumption of a rectangular B_1 profile in Fig. 2.13 is a crude approximation. In the following signal calculation, the more realistic assumption is that the spatial distribution of the B_1 amplitude only depends on the z coordinate in direction of the tube axis.

According to the reciprocity theorem, see p. 68 the signal contribution of spins at coordinate z is proportional to the rf amplitude $B_1(z)$. If t is the time after excitation, spins with velocity $w(r)$ that are located at coordinate z at time t have been excited at coordinate $z - w(r)t$. Thus, in the calculation of the corresponding excited transverse magnetization, the rf field $B_1(z - w(r)t)$ has to be inserted into the expression for the nutation frequency in (2.24). Besides on the nutation angle, the excited transverse magnetization depends on the polarization of the spins at coordinate $z - w(r)t$. It is obtained by integration of (2.16) with the right-hand side consisting only of the second term. However, the equilibrium magnetization depends on $B_0(z)$ according to (2.11). In general, the relaxation time T_1 also depends on the polarizing field. As simplification it is assumed that the polarizing field has a rectangular profile from $-L_0/2$ to $L_0/2$, see schematic representation in Fig. 2.14. The duration of polarization with constant relaxation rate R_1 then amounts to $(z - w(r)t + L_0/2)/w(r)$.[25] This results in the following equation for the signal:

[25] For the case of spins with velocity w and arbitrary profiles of relaxation rate and equilibrium magnetization, the solution of the differential equation $\dot{M}_z = w(\partial M_z/\partial y) = -R_1(y)(M_z - M_z^{\mathrm{eq}}(y))$ is $M_z(y) = (1/w) \int_{-\infty}^{y} R_1(y') M_z^{\mathrm{eq}}(y') \exp\{-(1/w) \int_{y'}^{y} R_1(y'')\mathrm{d}y''\}\mathrm{d}y'$. This is obtained by solution of the homogeneous differential equation by separation of the variables and variation of the constant for the particular integral. For a constant relaxation rate R_0 and piecewise constant equilibrium magnetization, the integrals yield $M_z(y) = \exp\{-R_0 y/w\}[\sum_{i=1}^{n} M_i(\exp\{R_0 y_i/w\}$

$$M^+(t) = \int_0^\infty \int_0^\infty \int_{-\infty}^\infty \int_0^{2\pi} \int_0^\infty \rho_{r,\phi,z,R_1,R_2}(r,\phi,z,R_1,R_2)$$
$$\underbrace{(1-\exp(-R_1(z-w(r)t+L_0/2)/w(r)))}_{\text{polarization}}\ \underbrace{\sin(-\gamma B_1(z-w(r)t)\tau)}_{\text{Nutation}}$$
$$\underbrace{\exp(-R_2 t)}_{\text{relaxation}}\ \underbrace{B_1(z)/B_1(0)}_{\text{detection}}\ r\,\mathrm{d}r\,\mathrm{d}\phi\,\mathrm{d}z\,\mathrm{d}R_1\,\mathrm{d}R_2. \tag{2.97}$$

The pulse duration is denoted as τ. It is assumed that the repetition time is sufficiently long to avoid saturation effects. If as in (2.92) it is assumed that transverse relaxation is independent of velocity and the remaining variables and that this also holds for longitudinal relaxation, the signal after integration over ϕ reads

$$M^+(t) = \int_0^\infty \rho_{R_1}(R_1) \int_{-\infty}^\infty \int_0^\infty \rho_{r,z}(r,z)$$
$$(1-\exp(-R_1(z-w(r)t+L_0/2)/w(r)))\ \sin(-\gamma B_1(z-w(r)t)\tau)$$
$$B_1(z)/B_1(0)\,2\pi\,r\mathrm{d}r\,\mathrm{d}z\,\mathrm{d}R_1 \int_0^\infty \rho_{R_2}\exp(-R_2 t)\,\mathrm{d}R_2. \tag{2.98}$$

As velocity is independent of z the distribution $\rho_{r,z}(r,z)$ can also be factorized. The integration over r can be replaced by the corresponding integral over the VPDF. For a constant spin density $1/L_0$ in z direction the expression

$$M^+(t) = \int_0^\infty \rho_{R_1}(R_1) \int_0^{w_{\max}} \rho_w(w) \int_{-L_0/2}^{L_0/2} 1/L_0$$
$$(1-\exp(-R_1(z-wt+L_0/2)/w))\ \sin(-\gamma B_1(z-wt)\tau)$$
$$B_1(z)/B_1(0)\,\mathrm{d}z\,\mathrm{d}w\,\mathrm{d}R_1 \int_0^\infty \rho_{R_2}\exp(-R_2 t)\,\mathrm{d}R_2. \tag{2.99}$$

is obtained. In the case of complete polarization, $R_1(z-wt+L_0/2)/w \gg 1$, the z integral simplifies to the cross-correlation integral of $\sin(-\gamma B_1(z)\tau)$ and $B_1(z)$ with the shift $-wt$:

$$M^+(t) = \int_0^{w_{\max}} \rho_w(w)\frac{1}{L_0 B_1(0)} \int_{-L_0/2}^{L_0/2} \sin(-\gamma B_1(z-wt)\tau)\ B_1(z)\,\mathrm{d}z\,\mathrm{d}w$$
$$\int_0^\infty \rho_{R_2}(R_2)\exp(-R_2 t)\,\mathrm{d}R_2. \tag{2.100}$$

$-\exp\{R_0 y_{i-1}/w\}) + M_{n+1}(\exp\{R_0 y/w\} - \exp\{R_0 y_n/w\})]$. With a relaxation profile, numerical integration by simple time slicing yields good results.

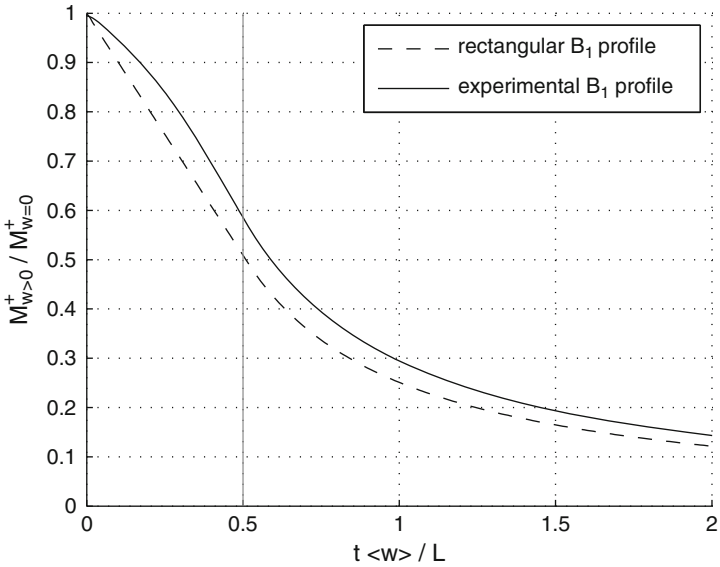

Fig. 2.15 CPMG signal with flow relative to the signal without flow for a Newton fluid according to (2.100). *Dashed line*: result for rectangular B_1 profile with a linear and a hyperbolic part. *Solid line*: Calculation with experimentally determined B_1 profile. L denotes the length of the rectangular profile and a characteristic length of the experimental profile, respectively. The CPMG signal measured with flow can be corrected by this function prior to further analysis. For non-Newtonian flow, the corresponding correction function has to be calculated with (2.100) using the actual VPDF, to be determined as described in Sect. 2.1.8

The cross-correlation integral can be calculated numerically if the B_1 profile is determined experimentally. For different velocities, the results as a function of time differ by a scaling of the abscissa. In order to perform the velocity integral numerically, the different results are interpolated to a common discretization of the time axis. For a rectangular B_1 profile triangles are obtained for the cross-correlation integral. For short times the superposition of triangles yields the previous result of (2.93). Of course also the long-time behavior of (2.94) is obtained if the constant VPDF of a Newton fluid is used in the integration. This can be seen in Fig. 2.15 where the signal calculated numerically according to (2.100) is shown for a Newton fluid and a rectangular B_1 profile. The result with an experimentally determined B_1 profile is plotted in comparison. As observed experimentally, a slower initial signal decay is obtained. This can be understood by the fact that the excitation profile with the sine function is broader than the detection profile. Thus the integrand of the cross correlation stays almost constant for small shifts. The B_1 profile was determined using frequency encoding with 128 discretization points, see discussion in Sect. 4.5. For the VPDF 64 grid points were used.

Without complete polarization the z integral in (2.99) still is a cross-correlation integral. However, the first function has the additional factor $(1 - \exp(-R_1$

$(z + L_0/2)/w)$). In this case the cross correlation not only depends on a property of the NMR system, namely the B_1 profile, but also on the longitudinal relaxation properties of the sample and the B_0 profile. If the distribution $\rho_{R_2}(R_2)$ for transverse relaxation is to be measured, it is likely that the distribution $\rho_{R_1}(R_1)$ is also unknown. Thus if possible complete polarization should be realized. For this purpose only a moderately homogeneous magnetic field is required. Alternatively a sufficient residence time of the flowing liquid in the NMR system before entry in the probe head can be realized. First experimental results are described in Sect. 4.5 on p. 125ff.

2.2 Problems

2.1. NMR Master Equation
For a magnet generating a field of $B_0 = 4.7\,\mathrm{T}$, the proton resonance frequency is indicated as $\nu = 200.13\,\mathrm{MHz}$. Calculate the gyromagnetic ratio of the proton.

2.2. Curie's Law
Show the validity of the evaluation of the sums in (2.11).

2.3. NMR Master Equation in the Context of Precession
Show that the precession with angular frequency $\boldsymbol{\omega_0} = -\gamma \boldsymbol{B_0}$ in (2.13) solves the equation of motion $\mathrm{d}\boldsymbol{M}/\mathrm{d}t = \gamma \boldsymbol{M} \times \boldsymbol{B}$ in (2.12) for a constant field $\boldsymbol{B_0}$ in z direction.

2.4. Rabi Nutation
For a micro-imaging probe connected to a 100 W RF amplifier, a realistic duration of the $\pi/2$ pulse is 12.5 μs. Calculate the Rabi frequency of nutation around $\boldsymbol{B_1}$ and the magnitude of $\boldsymbol{B_1}$.

2.5. Fourier Imaging: Example of k-Space Point for Discrete Sample
A sample is composed of twelve small water droplets at positions $(x, y) = (-25, 0)$, $(-25, 25)$, $(0, -25)$, $(0, 0)$, $(0, 25)$, $(0, 50)$, $(25, -25)$, $(25, 0)$, $(25, 25)$, $(25, 50)$, $(50, 0)$, and $(50, 25)$. Coordinates are given in mm. The four droplets in the center of the sample have twice the volume of the surrounding eight ones.

(a) Sketch the arrangement of the droplets with their initial magnetization as considered in Sect. 2.1.3, i.e., all magnetization along the x axis of the rotating frame.
(b) A gradient along x with $\gamma G_x = 3.142 \times 10^6\,\mathrm{rad\,s^{-1}m^{-1}}$ is switched on for 10 microseconds. Sketch the new rotating-frame magnetization for each droplet after this time period.
(c) Calculate the total transverse magnetization for both situations (a) and (b) in units of the small-droplet magnetization.

2.6. Fourier Imaging: Analytical Expression for a Simple Sample
Consider a cubic sample with edge length a and homogeneous spin density ρ_0.

Calculate the ideal Fourier-imaging signal according to (2.38) for the centered sample with its edges parallel to the gradient-system axes.

2.7. Slice Selection

(a) A slice of 1 mm thickness is to be selected. As in Fig. 2.5, a soft rf pulse with sinc3 amplitude shape and 1 ms duration is used. Calculate the required gradient amplitude according to the linear-response relation (2.50) using the bandwidth of the infinite sinc pulse.
(b) A parallel slice with equal thickness and a gap of 1 mm is to be selected. Calculate the corresponding shift in the rf-pulse carrier frequency if the same gradient amplitude is used.
(c) Estimate the maximum value of the B_1 amplitude for a nutation angle of $\pi/2$. How to perform the numerically exact calculation according to (2.52)?

2.8. Diffusometry vs. Velocimetry
The root-mean-square displacement by diffusion amounts to $\sqrt{2D\Delta}$ in any direction.

(a) Which result is obtained for water at ambient temperature and an observation time of $\Delta = 10\,\text{ms}$?
(b) How does this compare to the displacement during the same time in the absence of diffusion given a velocity of 1 mm/s?

2.3 Image Analysis

NMR measurements often yield huge mounds of data. Reducing this data to relevant, quantitative information can be challenging. As example, consider simple 3D spin-density imaging without sampling of further contrast dimensions. Sampling of 256 points in each dimension of reciprocal position space produces a comparatively high resolution. Discrete inverse Fourier transformation approximately yields the spin density for 256^3 grid points in real space, see (2.46). The volume element around each grid point is called voxel, in analogy to picture elements or pixels in the 2D case. If the signal magnitude at each point is mapped to 16 bits, the 16 megavoxels require 32 megabytes of memory.[26] The same amount of data is obtained for 64 points for each direction of 3D position space and 64 echoes for sampling of transverse relaxation.

In some applications the sample consists of areas with constant observable spin density and areas where no signal is observed. Nevertheless, a more or less broad

[26]The raw data before transformation requires more memory, as it consists of a real and an imaginary part. The spectrometer used always saves raw data with 32 bits, resulting in 128 megabytes in the present example.

signal-intensity distribution is observed also in these cases. One source for the distribution is signal noise. Another cause is the inhomogeneity of the B_1 field, increasing toward the boarders of the FOV. However, depending on the number of points sampled in reciprocal space, a substantial contribution to the intensity distribution results from artifacts of the discrete inverse Fourier transform, see Sect. 2.1.3, p. 14ff. In the ideal NMR image generated numerically in Fig. 2.16b only the last contribution is present. In the following, first the reduction to a binary image is discussed along with the resulting porosity as one elementary information.

2.3.1 Thresholds, Porosity, Filters

2.3.1.1 Threshold

Figure 2.16a shows a quasi continuous binary spin density $\rho(x, y)$. Insertion into (2.38) allows to calculate the ideal NMR signal $M^+(k_x, k_y)$ numerically. The resulting complex matrix is denoted as $(M^+)_{kl}$.[27] Finally, the ideal NMR image $(\tilde{\rho})_{nm}$ is calculated according to (2.40). As usual in experiments, Fig. 2.16b represents the magnitude of the complex image matrix. Concerning the benefits and challenges of phase correction, see Sect. 2.3.5. The absolute-intensity frequency distribution is obviously asymmetric around zero, see Fig. 2.16c, in contrast to the situation for a phase-corrected real-part image.

In this example without noise or experimental artifacts the spatial resolution is relatively high, about ten grid points per disc diameter. Accordingly, the frequency peaks at low and high intensities are well separated. Choosing a threshold ρ_s between the peaks, a binary image with the attributes "signal" or "no signal" is derived according to

$$\tilde{\rho}'_{nm} = \begin{cases} 1 & : \quad |\tilde{\rho}_{nm}| \geq \rho_s \\ 0 & : \quad |\tilde{\rho}_{nm}| < \rho_s \end{cases} . \tag{2.101}$$

2.3.1.2 Porosity and Threshold

If "signal" signifies pore space filled with some liquid and "no signal" solid with fast signal relaxation compared to the echo time, the porosity is calculated from the binary $N \times M$ matrix $\tilde{\rho}'_{nm}$ as

$$\varepsilon(\rho_s) = \left(\sum_n \sum_m \tilde{\rho}'_{nm} \right) (NM)^{-1}. \tag{2.102}$$

[27] There are several common notations for matrices. Here the notation $(a)_{nm}$ is used, see e.g., http://mathworld.wolfram.com/Matrix.html. More detailed notations are $(a_{nm})_{nm}$ as well as $a_{n=1\ldots N, m=1\ldots M}$. Introduction of a new symbol, such as A or $\underline{\underline{a}}$ is avoided.

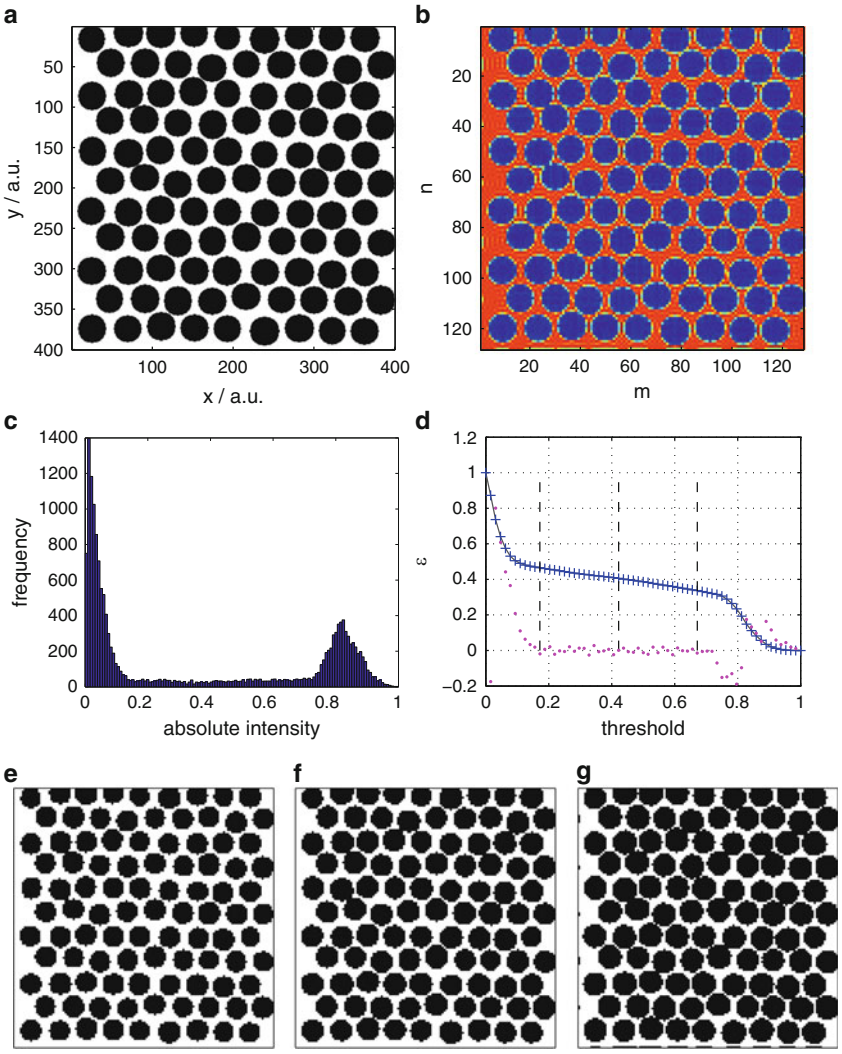

Fig. 2.16 (**a**) Two-dimensional porous structure $\rho(x, y)$ with surface porosity $\varepsilon = 0.41$. Pore space is represented by *white, solid as black*. (**b**) Numerically calculated ideal NMR image $(|\tilde{\rho}|)_{nm}$. (**c**) Frequency distribution of signal magnitude, normalized to one. (**d**) Porosity as function of threshold. Points show the discrete second derivative. The two outer broken vertical lines comprise half the intensity range, centered around the threshold corresponding to the input porosity (*broken line* in between). Binary images obtained with this three values as threshold are shown in (**e**) ($\varepsilon = 0.47$) to (**g**) ($\varepsilon = 0.34$)

This function of the threshold is shown in Fig. 2.16d for the numerically calculated ideal NMR image. Due to transformation artifacts, intensity values between the peaks occur in the intensity frequency distribution and there is no porosity plateau

between the peak intensities. If the actual porosity is known, e.g., by gravimetry, the threshold can be set such that this value is obtained. In Fig. 2.16d the surface porosity of the input structure is indicated as horizontal line and the corresponding threshold as central broken line. The binary image derived with this threshold is shown in Fig. 2.16f. However, Fig. 2.16e, g demonstrate that plausible images are also obtained with a significantly smaller respectively higher threshold, as intensities between the peaks correspond to grid points at the disc boarders. The porosities obtained are 0.47 and 0.34, respectively. One strategy for the determination of the threshold without previous knowledge is to detect the inflection point in the middle of the porosity function $\epsilon(\rho_s)$. The discrete second derivative is shown in Fig. 2.16d as points. Obviously, the strategy yields no sharp criterion in this particular example.

Applications requiring thresholds are presented in Sects. 4.6, 4.7, and 4.8. In the special case of fiber filters, see Sect. 4.1, an alternative method was adopted.

2.3.1.3 Noise

In the experiment, noise is always present in addition to transformation artifacts. Accordingly, normally distributed noise was added to the real and imaginary part of the calculated ideal NMR signal before transformation (the origin of noise and its relation to the signal is discussed in Sect. 2.3.4). Figure 2.17a shows the magnitude image for the noisy data. The impact on the signal frequency distribution can be seen in Fig. 2.17c.

As Fourier transformation is linear and white noise was added, the real and imaginary part of the transformed image also have normally distributed noise superimposed:

$$\begin{aligned} \mathrm{Re}(\tilde{\rho}_{nm}) &\to \mathrm{Re}(\tilde{\rho}_{nm}) + n_{i,nm} \\ \mathrm{Im}(\tilde{\rho}_{nm}) &\to \mathrm{Im}(\tilde{\rho}_{nm}) + n_{q,nm}. \end{aligned} \tag{2.103}$$

The normal distribution

$$P_{\mathrm{N}}(n) = \frac{1}{s\sqrt{2\pi}} \exp\left(-\frac{(n-\mu)^2}{2s^2}\right) \tag{2.104}$$

of noise has average $\mu = 0$ and a variance s^2. Index i for the real-part stands for "in-phase noise" and q for the imaginary part stands for "quadrature noise." In the following it is assumed that the signal distribution due to transformation artifacts can be neglected compared to the distribution caused by noise. In this case the signal magnitude $\sqrt{(\rho_c + n_{i,nm})^2 + n_{q,nm}^2}$ in areas with constant spin density ρ_c is distributed according to the Rice distribution,[28]

[28] Named after Stephen O. Rice.

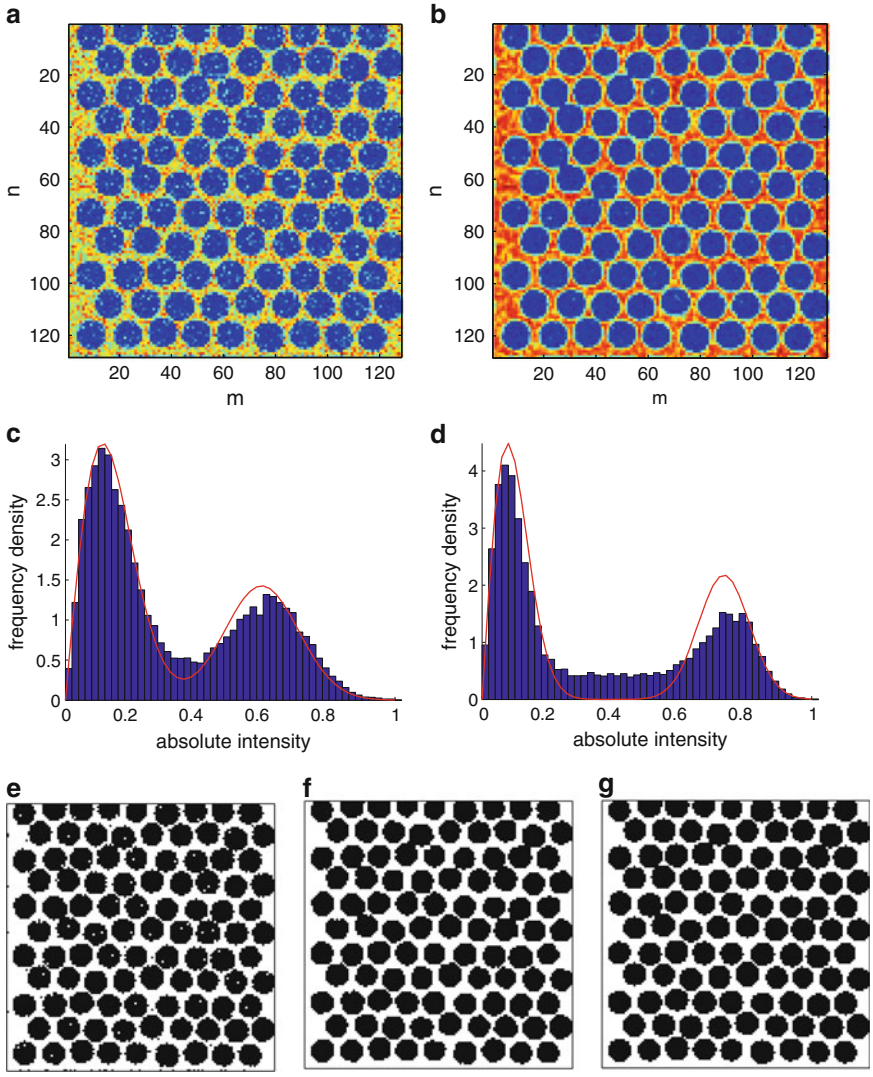

Fig. 2.17 (**a**) NMR image $(|\tilde{\rho}|)_{nm}$ for signal with superimposed noise. (**b**) NMR image $(|\tilde{\rho}_f|)_{nm}$ with low-pass filter, see (2.112). (**c**) Frequency distribution density for image (**a**) and fit of (2.107) resulting in $\varepsilon = 0.40$. (**d**) Frequency distribution density for image (**b**) and fit of (2.107) resulting in $\varepsilon = 0.42$. (**e**) Binary image derived from (**b**) with input porosity (0.41). (**f**) Application of filters (2.108) and (2.109) to image (**e**). (**g**) Binary image derived from (**b**) with input porosity (0.41)

$$P_{\mathrm{Ri}}(\tilde{\rho}) = \frac{\tilde{\rho}}{s^2} \exp\left(-\frac{\tilde{\rho}^2 + \rho_c^2}{2s^2}\right) I_0\left(\frac{\tilde{\rho}\rho_c}{s^2}\right), \tag{2.105}$$

with the modified Bessel function of the first kind and order zero I_0. In areas without observable spin density there is only statistically independent normally distributed noise in the real and imaginary part. In this case the magnitude is distributed according to the Rayleigh distribution

$$P_{\mathrm{Ra}}(\tilde{\rho}) = \frac{\tilde{\rho}}{s^2} \exp\left(-\frac{\tilde{\rho}^2}{2s^2}\right) \tag{2.106}$$

as special case of the Rice distribution. Thus in the simple case of a binary spin density and neglecting transformation artifacts, the total magnitude-signal distribution is the weighted sum of a Rayleigh and Rice distribution with the porosity as weight:

$$P_{\mathrm{ges}}(\tilde{\rho}) = \varepsilon P_{\mathrm{Ri}}(\tilde{\rho}, s, \rho_c) + (1-\varepsilon) P_{\mathrm{Ra}}(\tilde{\rho}, s). \tag{2.107}$$

Under these assumptions (2.107) can be fitted to the signal-magnitude distribution to obtain the porosity without prior knowledge.[29] The result is shown in Fig. 2.17c as solid line. The agreement for the peak at low intensity is good. Larger deviations are observed for the peak at high intensity, showing the influence of transformation artifacts. The porosity value $\varepsilon = 0.40$ obtained is in close agreement with the input value of 0.41.

2.3.1.4 Filter

Due to transformation artifacts and noise, assignments according to 2.101 can be incorrect, i.e., grid points in the pore space are set to zero instead of one and conversely grid points in the solid are set to one instead of zero. Both kinds of errors are observed in the binary image in Fig. 2.17e derived from Fig. 2.17a. If both errors compensate each other, the porosity can be correct. In Fig. 2.17e the threshold is chosen in the way that the input porosity is obtained. However, the specific surface, to be treated in Sect. 2.3.2, is heavily exaggerated for the image with erroneous spots. Likewise pore-space characteristics such as the pore-volume distribution discussed in Sect. 2.3.3 are grossly falsified.

With some prior knowledge of the imaged structures, erroneous assignments can be corrected by inspection of the surrounding grid points. If the imaged structures are known to consist of at least some connected grid points, more or less isolated grid points can be converted to the value of the surrounding grid points. Corresponding rules for a corrected copy $\tilde{\rho}''_{nm}$ of the original image, to be applied

[29] Note that for the Rice or Rayleigh distribution the parameter s^2 is not the variance of the distribution.

for each grid point, are[30]

$$\tilde{\rho}''_{nm} = 0 \quad \text{if} \quad \tilde{\rho}'_{nm} = 1 \quad \text{and} \quad \sum_{k=-1}^{1} \sum_{l=-1}^{1} \tilde{\rho}'_{n+k,m+l} \leq d_{ls}, \tag{2.108}$$

$$\tilde{\rho}''_{nm} = 1 \quad \text{if} \quad \tilde{\rho}'_{nm} = 0 \quad \text{and} \quad \sum_{k=-1}^{1} \sum_{l=-1}^{1} \tilde{\rho}'_{n+k,m+l} \geq d_{sl}. \tag{2.109}$$

In the 2D case the double sum considers the 8-neighborhood of each grid point, in the concept of pixels the four pixels with a common edge and the four pixels with just a common vertex. The filter (2.108) converts isolated liquid pixels (i.e., pore space pixels) to solid pixels if less than d_{ls} neighbors are liquid pixels. Strictly isolated liquid pixels correspond to $d_{ls} = 1$ as the considered pixel is included in the sum. For the filtered image shown in Fig. 2.17f $d_{ls} = 2$ was chosen. Conversely (2.109) converts isolated solid pixels to the liquid pixels if more than d_{sl} neighbors are liquid pixels. Strictly isolated solid corresponds to $d_{sl} = 8$. For the image in Fig. 2.17f $d_{sl} = 5$ was applied. The parameters are chosen by visual inspection of the result.

In the 3D case the corresponding triple sum considers the 26-neighborhood of each grid point, in the concept of voxels six neighbors at faces, twelve neighbors at edges and eight at vertices. Thus totally isolated solid corresponds to $d_{sl} = 26$ whereas for totally isolated liquid $d_{ls} = 1$ still holds. Applications of these filter are described in Sects. 4.6 and 4.7 on p. 132f and 135ff, respectively.

Another possibility is to reduce noise by application of a low-pass filter. The price is a blurring of fine structures. As example the cosine square filter is chosen. For a quadratic matrix with $N = M$ the components at highest frequencies in reciprocal k space are set to zero with the filter definition

$$L_{kl} = \cos^2 \frac{\pi \sqrt{(k - 1 - N/2)^2 + (l - 1 - N/2)^2}}{N\sqrt{2}}, \tag{2.110}$$

$$M^+{}_{kl} \to M^+{}_{kl} L_{kl}. \tag{2.111}$$

The effect of this filter on the numerically calculated data with noise is shown in Fig. 2.17b. As the resolution is quite high and the structures are well resolved, the blurring is not very pronounced. The binary image derived with (2.101) and the threshold giving the input porosity is shown in Fig. 2.17g. Erroneous assignments are avoided, but contacts of the actually separated discs are more frequent than with the filter pair (2.108) and (2.109), see Fig. 2.17f. The signal-magnitude distribution

[30] If the original image is corrected grid point by grid point, it gets modified during the process of correction and the rules would apply to the modified image. Thus it is necessary to apply the corrections to a copy by inspection of the original image.

with low-pass filter is narrower at the peaks compared to the distribution without filter but more intensities are present between the peaks. The fit of (2.107) in Fig. 2.17d for the low-pass filtered image is less adequate. However, the obtained porosity of $\epsilon = 0.42$ still agrees well with the input value of 0.41.

A low-pass filter can also be characterized by its point spread function (PSF). The filtered image $(\tilde{\rho}_f)_{nm}$ is the convolution of the unfiltered image $(\tilde{\rho})_{nm}$ with the PSF:

$$(\tilde{\rho}_f)_{nm} = (\tilde{\rho})_{nm} \otimes \text{PSF}. \tag{2.112}$$

According to the convolution theorem this corresponds to a multiplication in Fourier space, in the discrete case

$$\mathscr{F}\{(\tilde{\rho}_f)_{nm}\}_{kl} = M^{+}{}_{kl} L_{kl}, \tag{2.113}$$

with $\mathscr{F}\{(\tilde{\rho}_f)_{nm}\}_{kl}$ being the k, l component of the discrete Fourier transform of the filtered image. Thus the PSF is the Fourier transform of the filter:

$$\text{PSF} = \mathscr{F}\{(L)_{kl}\}. \tag{2.114}$$

The PSF of the rather broad filter in (2.110) is correspondingly narrow. An example with a Gauß filter can be seen in Fig. 4.25 on p. 136.

The choice of filter or combination of filters depends on the image characteristics, the SNR and the application. For images with outliers, a moving median filter can be appropriate. The influence of experimental artifacts and the case of varying spin density will be discussed in Sect. 2.3.4.

2.3.2 Specific Surface

Besides the porosity, the specific surface is an important information in many applications, see e.g., Sect. 4.7, p. 135ff. In the following, two methods of obtaining the surface from a volume image $(\tilde{\rho})_{nmo}$ on a rectangular grid [29] are briefly described.

2.3.2.1 Reconstruction of the Surface

Surface reconstruction is a common procedure, also used to visualize a volume image. The isosurface for a chosen isovalue is meshed, e.g., by triangulation. It is the 3D analog of a contour or isoline of a 2D data set. The isovalue can equal the threshold used to generate the binary image. In Figs. 2.18a–d results for simple structures are shown. The spin density $(\tilde{\rho})_{nmo}$ is set to one for the grid points in an inner cube of edge length l in units of the lattice spacing. Surface meshing by

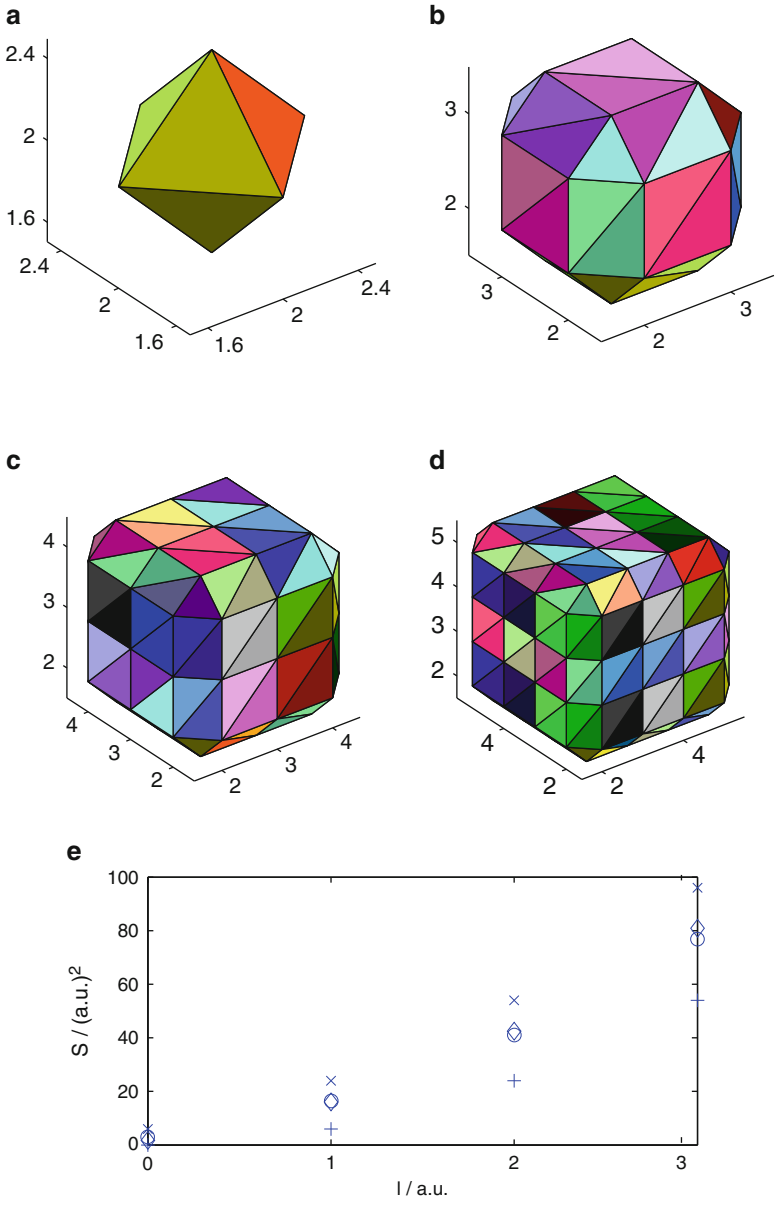

Fig. 2.18 Surface calculations for simple volume images consisting of homogeneous inner cubes with increasing edge length l in units of the lattice spacing. (**a**)–(**d**) Triangulation of the isosurface. (**a**) One inner grid point, i.e., $l = 0$. (**b**) Eight points, $l = 1$. (**c**) 27 points, $l = 2$. (**d**) 64 points, $l = 3$. (**e**) Surface $6l^2$ of the inner cube (*plus*), surface by the Crofton formula (*circle*), surface by triangulation (*diamond*), surface $6(l + 1)^2$ of the outer cube (*times*)

triangulation was performed with a commercial program MATLAB®.[31] The total area of the triangles S_D was calculated from the obtained mesh with the program listed in Sect. 6.2. The mesh is returned as a list of coordinates $\boldsymbol{r}_i$ of vertices and a list of point triples forming each face. If points $(\boldsymbol{r}_1, \boldsymbol{r}_2, \boldsymbol{r}_3)$ form a triangle with vectors $(\boldsymbol{r}_{12} = \boldsymbol{r}_2 - \boldsymbol{r}_1, \boldsymbol{r}_{13} = \boldsymbol{r}_3 - \boldsymbol{r}_1)$ along two edges, the surface S_k of this triangle amounts to

$$S_k = \frac{1}{2} |\boldsymbol{r}_{12} \times \boldsymbol{r}_{13}|. \tag{2.115}$$

With $S_\mathrm{D}(X)$ as total surface of phase X in the total volume V, the specific surface is calculated as

$$S_{V,\mathrm{D}} = S_\mathrm{D}(X)/V = \frac{1}{V} \sum_k S_k. \tag{2.116}$$

2.3.2.2 Indirect Evaluation

An efficient evaluation of the surface without reconstruction is described in [48]. Here first a binary image $(\tilde{\rho}')_{nmo}$ has to be generated from the volume image using a suitable threshold. The method of computation is based on one of the Crofton formulas for the calculation of the surface:

$$S_\mathrm{C}(X) = \frac{1}{\pi} \int \sin\theta \mathrm{d}\theta \int \mathrm{d}\varphi \iint \mathrm{d}\boldsymbol{y}\ \chi(X \cap \boldsymbol{e}_{y,\theta,\varphi}). \tag{2.117}$$

In (2.117) $\boldsymbol{e}_{y,\theta,\varphi}$ designates the line with direction (θ, φ) (polar and azimuth angle) through point $\boldsymbol{y}$ in a plane perpendicular to $\boldsymbol{e}_{y,\theta,\varphi}$. The 1D Euler number $\chi(X \cap \boldsymbol{e}_{y,\theta,\varphi})$ specifies how often the line intersects with X. The inner integral $\iint \mathrm{d}\boldsymbol{y}$ thus yields the weighted shadow area for a light source at infinite distance above the considered plane. The weight at point $\boldsymbol{y}$ is the number of object parts above this point that would cast a shadow independently. For the simple case in Fig. 2.19a the weight is 2. The inner integral is also denoted as "area of the total projection" or "rose of intersections." In this context (2.117) is also denoted as Cauchy formula. For the simple case of a sphere it is easily verified that the integration over the unit sphere and division by π yields the correct value for the sphere surface.

In the case of discrete grid points in three dimensions the evaluation of the Crofton formula (2.117) in [48] is based on the 8-neighborhood of each grid point. As indicated in Fig. 2.19b it can be encoded with eight bits or one byte. The grid point whose neighborhood is to be encoded is associated with the least significant bit 2^0, the neighboring grid points with 2^1 to 2^7. A bit is set only if it belongs to the phase X. If grid points plotted in black in Fig. 2.19b belong to X encoding yields 10101001 as binary number or $1 + 8 + 32 + 128 = 169$ as decimal number. For the evaluation of the surface only the histogram of these numbers is required,

[31] The MathWorks™, Inc.

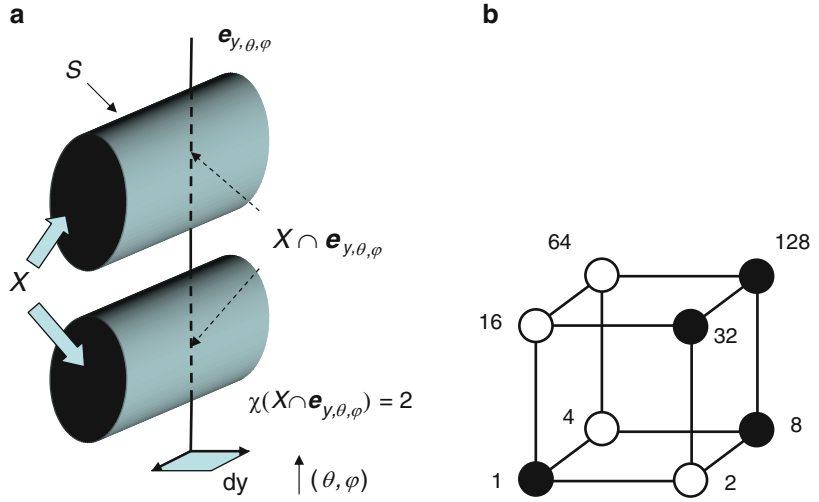

Fig. 2.19 Quantities used in the Crofton formula (**a**) and encoding of the 8-neighborhood of a grid point in the discrete case (**b**)

not the eight-bit gray-tone image itself. In [48] a program written in language "C" is presented that performs encoding using bit-shift operations and compiles the histogram very efficiently in a single triple loop.[32] A literal translation of the required C programs presented in [48] into MATLAB® language can be found in Sect. 6.1. The integration in 2.117 is replaced by a double sum over all 256 possible configurations with the gray-tone histogram as weight and over the 13 directions occurring in the 8-neighborhood (three edge directions, $3 \times 2 = 6$ face diagonals, four body diagonals). The Euler number is obtained very compactly and efficiently as sum of two products of results from logical comparisons involving "bit-wise OR" and "bitwise AND" operations, see Sect. 6.1. In the sum over directions in space weights accounting for the associated solid angle occur. Note that the figures appearing in [48] and Sect. 6.1 only hold for the common case of isotropic spatial resolution.

2.3.2.3 Comparison of the Methods

First the surfaces calculated with both methods are compared for the simple cubic geometries shown in Fig. 2.18. The smallest cube shown in Fig. 2.18a consists of a single grid point and has edge length $l = 0$. Triangulation yields an octahedron with edge length $1/\sqrt{2}$ in units of the lattice spacing. Its surface S_D, indicated in the following in units of the squared lattice distance, amounts to $\sqrt{3}$. According to (2.46) $\tilde{\rho}_{nmo}$ approximates in each direction the integral of the spin density in

[32] A free download as file ghist.c is available at http://www.materialography.net/.

the range of one lattice spacing. A sphere with the lattice spacing as diameter has surface $\pi/6$. A cube with the lattice spacing as edge length (cubical voxel) has surface 6. Computation according to [48] yields $S_C = 3$. In this simplest case the considered results increase in the order $6l^2 < \pi/6 < S_D < S_C < 6(l+1)^2$. In Fig. 2.18e the surfaces for the limiting cases "inner" and "outer" cube as well as S_D and S_C are plotted for the four cubes depicted above. For the cube consisting of eight grid points with $l = 1$ S_D and S_C yield almost the same surface. For larger cubes (verified up to 1,000 points and $l = 10$) the order changes to $S_C < S_D$. In the case of $l = 10$ the mesh consists of 1,448 triangles with total surface 686, the inner cube has surface 600, the outer 726, and the calculation based on the Crofton formula [48] yields a surface of 638. Thus the results obtained with both methods are in line with the limiting cases.

For large data sets the computing time can be relevant, especially if several volume images are to be processed. Both methods were applied to ten data sets of varying size for bead packings and one data set for a ceramic sponge [29], see Sect. 4.7. At first the implementation of both methods in MATLAB®, see Sects. 6.1 and 6.2, were tested with respect to computing time on one computer. As described in [48] the time required for S_C scales with the number of data points. It is about half of the computation time required for S_D, in which the latter obviously depends on the details of the structure under investigation. In addition the literal translation of the optimized C program in [48] into MATLAB® was compared with the original version. For 60 million data points the implementation in MATLAB® ran for 15 min on a PC with P4 processor, 3.2 GHz clock frequency, 1 GB RAM and a XP SP3 operating system. On a Linux PC with P4 processor and only 2.4 GHz clock frequency, 512 MB RAM, the program compiled with the free gcc compiler processed the same data set in only 15 s. This impressively demonstrates the efficiency of the optimized C code compared to the obviously non optimal literal translation in Sect. 6.1.

2.3.2.4 Remarks

Figure 2.18e shows that both methods yield reasonable results for simple test data. However, it is difficult to evaluate the uncertainty for images of complex structures with experimental artifacts.

Moreover the specific surface depends more or less on the observed length scale. Beads of packed bed can appear smooth on a coarse length scale and coarse on a fine length scale. On a molecular length scale the observed specific surface can increase drastically as, e.g., for zeolites. A dependence of the specific surface on the length scale in the accessible range of length scales can be studied by variation of the spatial resolution.

For structures with various relevant length scales obtaining a statistically meaningful volume image is difficult. The data set should contain enough representative coarse structures. The spatial resolution cannot be made arbitrarily small compared to the total image size, for experimental reasons or simply because of the maximum

amount of manageable data. Thus fine structures might not be sufficiently resolved. For coarse structures, edge effects at the borders of the volume image become noticeable.

As already discussed in Sect. 2.3 the choice of the isovalue or threshold also influences the specific surface. Erroneous assignments of grid points are absolutely to be avoided.

To study the inner specific surface NMR measurements of diffusion within the porous structure can be used, see e.g., [3, 44] and also Sect. 4.10.

2.3.3 Segmentation and Frequency Distributions

The porosity and specific surface is clearly defined for a porous system, apart from the length-scale problem. For an open porous system it can be interesting to segment the pore space into virtual individual pores with windows at the necks between connected pores. If this is accomplished, e.g., pore-size distributions can be constructed also for open pore structures like ceramic sponges. In favorable cases segmentation can be performed using existing methods. However, for the volume images studied the results obtained using MATLAB® and MAVI[33] were not satisfying. A method was thus worked out and implemented that allowed a successful segmentation. It is partially described in [26, 55]. However, the program used in these papers is not available from the authors. In the following the commercially available watershed transformation is briefly described. The new method is presented in more detail. Both methods for 3D segmentation are compared using again artificially generated 2D images.

2.3.3.1 Watershed Transformation

Both methods require a binary image $(\tilde{\rho}')_{nm}$. In Fig. 2.20 black areas signify discs in a loose packing. The regular structure in Fig. 2.20a has porosity $\epsilon = 0.55$, the irregular structure in Fig. 2.20b has a slightly lower porosity $\epsilon = 0.53$. Both methods start with a distance transformation, see Fig. 2.20c. Each grid point in the pore space is encoded with the closest distance to a solid grid point. In MATLAB® the Euclidean distance is used by default. A slightly different definition of the distance is obtained using a kind of "morphological thinning." It was used in [26] and was also implemented for the analysis presented in [24]. Here, the Euclidean distance provided by MATLAB® was used for both methods for the sake of comparability:

$$a_{nm} = \min_{op} \sqrt{(o-n)^2 + (p-m)^2} \quad \text{with} \quad \tilde{\rho}'_{nm} = 1 \quad \text{and} \quad \tilde{\rho}'_{op} = 0. \quad (2.118)$$

[33] MAVI – Modular Algorithms for Volume Images, Copyright © 2006 Fraunhofer Institut für Techno- und Wirtschaftsmathematik.

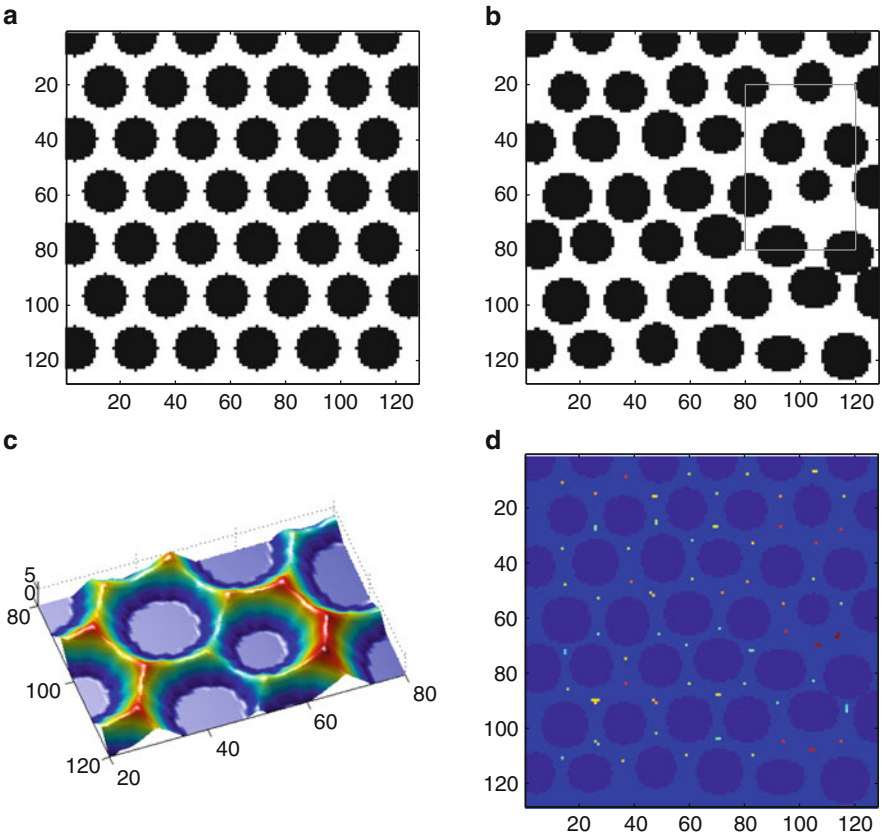

Fig. 2.20 Simple 2D geometries used to test pore-space segmentation. (**a**) Regular structure. (**b**) Irregular structure. (**c**) Distance transformation (2.118) for the cut-out indicated in (**b**). (**d**) Local maxima for the irregular structure (**b**). The average in the neighborhood of local maxima (2.121) is superimposed on the structure

For the watershed transformation, the "distance hills" $(a)_{nm}$ are inverted to the "valleys" $(-a)_{nm}$. Infinite depth is assigned to the solid phase. This matrix is segmented by the watershed transformation [68],[34] in analogy with the catchment basins in hydrology. In Fig. 2.21a the successful segmentation of the regular structure is shown. Each disc is surrounded by six regions in the pore space (catchment basins) that are identified as individual pores. The pixel line separating the basins is labeled separately by the program. In the 3D case, the separation surface is the window in the neck between two pores. At low resolution, a significant portion of grid points is assigned to the separation and not to pores, which is

[34]Concerning the algorithm, MATLAB® refers to [46], where several watershed algorithms are described.

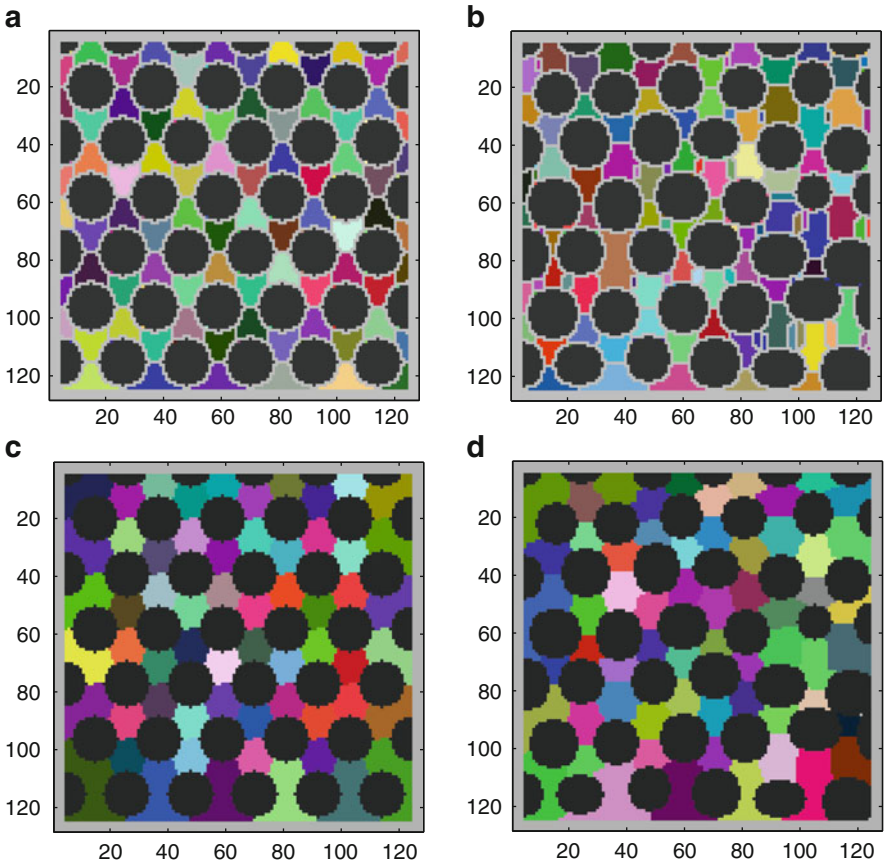

Fig. 2.21 Segmentation of the 2D structures shown in Fig. 2.20. (**a**, **b**) Results obtained with the commercial program. (**c**, **d**) Results obtained with the developed program. (**a**) Successful segmentation by watershed transformation for the regular structure. (**b**) Over-segmentation by watershed transformation for the irregular structure. (**c**) Successful segmentation by stratus transformation for the regular structure. (**d**) Successful segmentation by stratus transformation for the irregular structure

problematic. Discs are also segmented. However, the area associated with a disc can be larger than the disc itself. In Fig. 2.21a the grid points of the discs are plotted in black. Colored spots on the disc borders indicate this artifact. In addition, grid points at the border of discs are again not counted as part of an individual pore.

For the irregular structure in Fig. 2.21b the standard watershed transformation leads to an over segmentation, i.e., some discs are surrounded by many small areas identified as individual pores. Modified versions allow to solve this problem by user intervention, e.g., setting of starting points or collection of areas. However, user intervention introduces a subjective component and is impracticable for large 3D data sets. The problem can also be tackled by preflooding.

2.3.3.2 "Stratus" Transformation

For the procedure partially described in [26, 55][35] the distance matrix $(a)_{nm}$ is not inverted. In the 2D case this matrix can be represented as hilly landscape. The procedure is analog for the 3D case, although more difficult to visualize. Segmentation of the pore space amounts to the assignment of grid points to individual hilltops. The gradual process can be compared to the spectacle that can be seen from a hilltop in the situation of meteorological inversion. The observer can enjoy the sunshine, while everything only some meters below is covered by above-ground fog, an even stratus cloud.[36] Hilltops are the pore centers. As the stratus gradually descends, more and more grid points become visible and are associated with the adjacent hill. Eventually grid points on a saddle border on two hills. The saddle is the virtual boundary between the pores. The stratus is gradually lowered until all grid points are assigned to hills representing pores.

For the search of hilltops or local maxima, first the pairs of indices (n, m) fulfilling

$$a_{nm} = \max_{(o,p) \in O \times P} a_{op} \tag{2.119}$$

are determined. Here $O \times P$ is a moving product set of natural numbers around (n, m). It covers a quadratic (3D: cubic) range with edge length $2l$ and $2l + 1$ points along the edges:

$$\begin{aligned} O &= \{a \,|\, a \in N \text{ and } n - l \leq a \leq n + l\} \\ P &= \{a \,|\, a \in N \text{ and } m - l \leq a \leq m + l\}. \end{aligned} \tag{2.120}$$

Hereby a first list of length K with index pairs of local maxima $\boldsymbol{r}_k = (n_k, m_k)$ is obtained. Additionally a list of the associated averages

$$\bar{a}_k = \frac{1}{(2l+1)^2} \sum_{o=n_k-l}^{n_k+l} \sum_{p=m_k-l}^{m_k+l} a_{op} \tag{2.121}$$

is established. Grid points in the border area of the image matrix are to be treated separately. Alternatively points at the border can be excluded as potential pore centers, as it was done in the presented analysis. The value of l should be

[35] Generation of the distance matrix by a kind of "morphological thinning" is explained in detail, the following steps are only mentioned. However, a straight-forward search for local maxima in the next step leads to an over segmentation. Also in the subsequent association of adjacent grid points to the maxima, care must be taken to avoid distorted pores. Therefore details of the developed procedure are described and in Sect. 6.3 the implementation in MATLAB® is listed.

[36] In Zrich, a tablet on the tramway bearing the inscription "Uetliberg hell" (Uetliberg bright) indicates this situation.

smaller than the smallest considered distance between two pore centers. For the segmentation shown in Fig. 2.21c, d, $l = 4$ was chosen.

As the indices are natural numbers only discrete values are obtained as distances by (2.118). Thus it can occur for an irregular structure as shown in Fig. 2.20b that a ridge or small plateau is obtained instead of a crest, see Fig. 2.20d. Each point of the line contributes to the list $\boldsymbol{r}_k$. In the following association of grid points this would lead to an over-segmentation. Therefore a second parameter c is introduced as minimum distance between two pore centers. In the decision which point $\boldsymbol{r}_k$ is to be retained form a set of local maxima with distances smaller than c the averages $\bar{a}_k$ are compared. For a grid point at the end of a ridge the average is smaller than for a point in the middle of the ridge. Thus, starting with the first local maximum in the list, each local maximum is tested against the following ones with respect to their distance. If the inequality

$$|\boldsymbol{r}_k - \boldsymbol{r}_{k+l}| < c \quad \text{with} \quad l \in \{a \,|\, a \in \boldsymbol{N} \text{ and } k + l \leq K\} \tag{2.122}$$

is false for a $\boldsymbol{r}_k$ and all l this local maximum is incorporated in the final list of local maxima $(\boldsymbol{r})_j$. As soon as the inequality (2.122) is fulfilled for one l the comparison is stopped for this k. If the following local maximum has a higher average, i.e., if

$$\bar{a}_k < \bar{a}_{k+l} \tag{2.123}$$

is fulfilled, $\boldsymbol{r}_k$ is discarded. If this is not the case, $\bar{a}_{k+l}$ and $\boldsymbol{r}_{k+l}$ are replaced by $\bar{a}_k$ and $\boldsymbol{r}_k$, respectively. Thus the decision if the local maximum is to incorporated in the final list is postponed to following tests. In the example of the regular structure shown in Fig. 2.21c the final list has the same length J as the original list, namely $K = 60$. For the irregular structure of Fig. 2.21d however $K = 81$ and $J = 60$. The minimum distance was chosen as $c = 6$.

In the gradual association of grid points in the pore space to bordering points already assigned to pore centers two points have to be considered. For large data sets the implementation has to be numerically efficient and all grid points in the pore space have to be covered. Furthermore it has to be avoided that pores get distorted by an unsuitable systematic procedure (e.g., growth of pores into neighboring pores). First "gradually" has to be defined. Distances calculated by (2.118) extend from one to several lattice spacings. For the structure shown in Fig. 2.21d, e.g., the maximum distance amounts to $\sqrt{7^2 + 1}$ and for the structure in Fig. 2.21c 5 is obtained (with two possibilities: $\sqrt{5^2}$ and $\sqrt{3^2 + 4^2}$). In the first step the lattice points with a distance between the rounded off maximum distance h_1 and the maximum distance are considered. These grid points fulfill the inequality

$$a_{nm} > h_1 \text{ with } h_1 = a_{\max} - (a_{\max} \bmod 1) \text{ and } a_{\max} = \max_j a(\boldsymbol{r}_j). \tag{2.124}$$

Grid points already assigned have to be excluded. These are collected in the matrix $(z)_{nm}$ of the segmented image and are set to the value j of the corresponding pore

center. Initially the segmented image is only non-zero at the local maxima:

$$z_{nm} = \begin{cases} j & : \quad (n,m) = \boldsymbol{r}_j \\ 0 & : \quad \text{else} \end{cases} . \tag{2.125}$$

When all grid points above the highest level are assigned new points are considered applying (2.124) with a lower level h_i reduced, e.g., by one.[37] Both conditions for the points to be considered can be combined in a compact matrix notation and are thus efficiently evaluated in MATLAB® :

$$(\Theta)_{nm} = ((a)_{nm} > h_i) \ \wedge \ (\neg(z)_{nm}). \tag{2.126}$$

The negation is implemented such that $\neg z_{nm} = 0$ for $z_{nm} \neq 0$. The matrix notation in (2.126) signifies for the components

$$\Theta_{nm} = \begin{cases} 1 & : \quad a_{nm} > h_i \text{ and } z_{nm} = 0 \\ 0 & : \quad \text{else} \end{cases} . \tag{2.127}$$

Thus (2.126) is a binary matrix with ones at the positions of grid points to be considered and zeros elsewhere. The neighborhood of points under consideration to points already assigned is established by comparison of $(\Theta)_{nm}$ with a cyclical shifted version of matrix $(z)_{nm}$. In the 2D case a shift by one is executed either to the left, to the right, to the bottom, or to the top. For the indices the shift is either the addition or subtraction of one in either the first or the second index:

$$(n,m) \to (n,m) + \xi \quad \text{with} \quad \xi \in \{(-1,0),(1,0),(0,-1),(0,1)\}. \tag{2.128}$$

As $(\Theta)_{nm}$ is a binary matrix the shift amounts to a bit-shift operation. For $n > 0$ a shift by n bits to the left or to the top is denoted by $<< n$. A shift to the right or bottom is denoted by $>> n$. For $n < 0$ directions are inverted. Thus the matrix-oriented logical operation

$$(\Lambda)_{nm} = (\Theta)_{nm} \ \wedge \ ((z)_{nm} << \xi) \tag{2.129}$$

yields the binary matrix $(\Lambda)_{nm}$ with ones at the positions of points under consideration that are adjacent with already assigned points in direction ξ and zeros elsewhere. At the positions where $(\Lambda)_{nm}$ contains ones the matrix $(z)_{nm}$ should be assigned with the value of the neighboring assigned point. This can be done again very efficiently by indexing of the matrix $(z)_{nm}$ with the binary matrix $(\Lambda)_{nm}$ and

[37] The distance matrix generated in [26, 55] contains only natural numbers so that a reduction of the levels by less than one is not meaningful in this case.

with the version cyclical shifted in the opposite direction, respectively[38]:

$$(z)_\Lambda = (z)_{\Lambda>>\xi}. \tag{2.130}$$

Indexing with the (shifted) matrix signifies for the components

$$z_{nm} = \begin{cases} z_{op} & : \quad \Lambda_{nm} = 1 \text{ with } (o,p) = (n,m) - \xi \\ z_{nm} & : \quad \text{else} \end{cases}. \tag{2.131}$$

Thus the gradual assignment can be described as follows:

1. Determine the grid points to be assigned at a given level and state of assignment using (2.126).
2. Generate a random permutation of the shift-vectors ξ in the set given in (2.128).
3. Determine consecutively for the four (3D: six) permuted shifts the neighboring pixel (3D: voxels) according to (2.129) and assign those grid points according to (2.130).
4. Repeat steps 1 to 3 until all grid points above the actual level are assigned.
5. Lower the level and repeat steps 1 to 4 until level zero is reached and all grid points are assigned to individual pores.

The implementation in a computer program is listed in Sect. 6.3. Without random permutations the oblique borders between pores seen in Fig. 2.21c, d are not obtained. If the random element is not desired a list of suitable permutations can be fixed, leading to an exactly reproducible segmentation. Without the gradual lowering of levels small pores grow into large pores.

2.3.3.3 Comparison of Methods and Example of Analysis

Figure 2.21c, d shows that the implemented stratus transformation produces meaningful results not only for the regular but also for the irregular structure. All grid points in the pore space are associated to separate pores. Only one point at $(x, y) \approx (120, 90)$ remains. However, it is surrounded by discs and is not part of the open pore space. At variance with the commercial method areas at the border of the data set are not assigned to new pores as on the left, bottom, and right border of Fig. 2.21a. Indeed the distance matrix has local maxima at the borders, but borders were not included in the search for local maxima using (2.119). If pore centers at the border are to be allowed, these regions have to be treated separately.

Examples of geometrical characteristics whose distribution can be analyzed are the pore volume, pore surface, coordination number (i.e., number of pores directly

[38]Equivalent and more intuitive is the assignment of new values with the equation $(z)_\Lambda = (z << \xi)_\Lambda$. Due to the syntax of MATLAB® this version requires an additional step as the cyclical shifted matrix cannot be indexed with a matrix in the same expression.

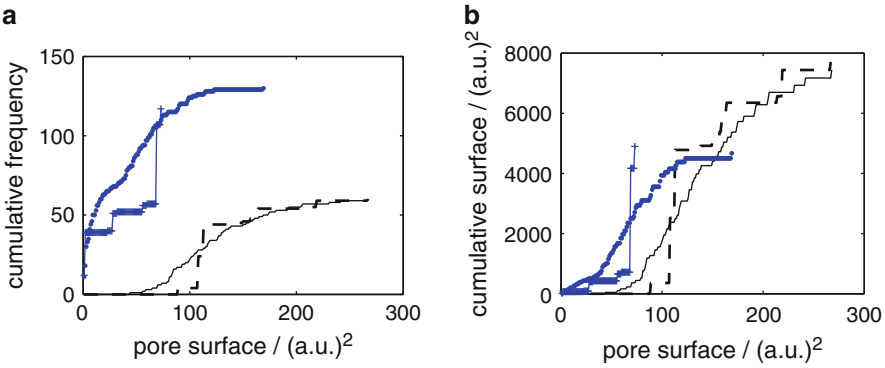

Fig. 2.22 Cumulative pore-surface distribution for both structures and methods shown in Fig. 2.21. The distributions are not normalized in order to emphasize the differences for the two methods. (**a**) Cumulative distribution by number or frequency Q_0. (**b**) Cumulative distribution by surface Q_2. *Crosses* correspond to Fig. 2.21a, *points* to Fig. 2.21b, the *broken line* to Fig. 2.21c, and the *solid line* to Fig. 2.21d

connected to one pore) or the cross-section area of the windows between pores. The total number of pores J is obtained immediately. Whereas the stratus transformation yields 60 pores for both examples, watershed transformation results in 121 pores for the regular structure in Fig. 2.21a and 147 for irregular structure in Fig. 2.21b. For the regular structure the difference is mainly due to pores assigned to the discs that are larger than the discs. The rest is due to 19 additional pores at the left, bottom, and right border. For the irregular structure the number is increased by over-segmentation.

As example the cumulative pore-surface distribution for both structures and methods is shown in Fig. 2.22, see figure caption. Cumulative distribution signifies that at an abscissa value for the considered kind of quantity the total amount of parts with quantity less or equal to that value are given as ordinate value. In Fig. 2.22a the number of parts was chosen as amount, the corresponding cumulative distribution is denoted as Q_0. In Fig. 2.22b the surface of the parts was chosen as amount, corresponding to Q_2. The parts are the virtually separated pores. In the 3D case Q_2 can also be used. More common is the volume or mass as amount with the corresponding symbol Q_3. The kind of quantity is the pore size, here as pore surface in units of the pixel numbers. In order to emphasize the differences between both methods the distributions are not normalized as usual to the total amount. A discrete derivative to a distribution density is noisy due to the small number of pores.

The total number of pores is given in Fig. 2.22a at the end points of the curves. Due to the reasons discussed above it is significantly higher for the watershed transformation. Some over-segmented pores for the irregular structure do not contribute as part of the border was excluded from the analysis for both structures and methods. Endpoints in Fig. 2.22b indicate the total pore surface. As discussed above it is markedly smaller for the watershed transformation as grid points of

the watershed line are counted separately and not as part of the pore space. Both methods reproduce the slightly higher porosity of the regular structure.

Due to the difficulties of the watershed transformation the resulting distributions are not very significant. At least the 60 correctly assigned pores of the regular structure have a narrow surface distribution. With the surface as amount, small over-segmented areas or isolated grid points around the discs contribute less than in the frequency distribution.

The surface distribution for the regular structure is somewhat less narrow using the stratus transformation. At higher surfaces this is due to the larger pores at the left, bottom, and right border. For the irregular structure the median of the distribution by frequency Q_0 amounts to 115 grid points, for the distribution by surface Q_2 to 133. For the regular structure the median of the distribution by frequency and by surface amounts to 111 grid points.

A different application of the stratus transformation to the segmentation of a poorly resolved 3D structure can be found in [24] and Sect. 4.6, p. 132.

2.3.4 Signal, Noise, and Variance

In the preceding it has been assumed that the sample solely consists of areas with constant observable spin density and areas that give no signal. In this section the general case of a continuously distributed observable spin density is considered. In some applications the variance of the spin density is of interest, such as in the characterization of the uniformity of mixtures, see Sect. 4.3, p. 111ff and [32]. Therefore the influence of artifacts on the signal amplitude and variance in the measured NMR image is analyzed.

According to (2.38) the nondimensionalized total transverse magnetization M^+ in ideal Fourier imaging is the Fourier transform of the spin density ρ. In Sect. 2.3.1 it was shown in an example how already artifacts due to the inverse transform (2.40) lead to a distortion of the amplitude in the result $(\tilde{\rho})_{nmo}$. In the following this artifact is neglected compared to artifacts resulting from the inhomogeneity of the rf field $\boldsymbol{B_1}$ and noise. First the generation of the signal and the consequence of rf inhomogeneity is treated in some detail. Then the origin of noise and its impact on the magnitude image is discussed on p. 70f. The influence of inhomogeneities and noise on the observed signal variance is finally treated on p. 71f.

2.3.4.1 Signal Amplitude

To begin with the spatial variation of $\boldsymbol{B_1}$ leads to a spatial dependence of the angular velocity of the Rabi nutation (2.24). For $\omega_1\tau = -\gamma B_1(\boldsymbol{r})\tau \neq \pi/2$ the local transverse magnetization is scaled with $\sin(\omega_1\tau) < 1$. Frequently a second π rf pulse is used for refocusing, see e.g., Fig. 2.8. Due to the deviance $2\omega_1\tau \neq \pi$ in average a total scaling with $\sin^3(\omega_1\tau)$ is obtained [27]. For $\omega_1\tau \approx \pi/2$ this

second-order attenuation of the signal is neglected against the linear dependence of the signal on $\boldsymbol{B_1}$ discussed in the following.

In [37] the voltage U induced in the reception coil is derived using the reciprocity theorem [39]. It relates this voltage to the field $\boldsymbol{B}_1^{\mathrm{dc}}$ generated by the coil when driven with the direct current I^{dc}:

$$U = -\iiint_V \frac{\mathrm{d}}{\mathrm{d}t}\frac{1}{I^{\mathrm{dc}}}\boldsymbol{B}_1^{\mathrm{dc}}(\boldsymbol{r})\boldsymbol{M}(\boldsymbol{r},t)\,\mathrm{d}x\mathrm{d}y\mathrm{d}z. \tag{2.132}$$

The relation of this voltage to the measured spin-density image is derived with consideration of an inhomogeneous $\boldsymbol{B}_1^{\mathrm{dc}}(\boldsymbol{r})$ field. To this the transverse magnetization expressed in (2.32) and (2.37) in the rotating frame of reference has to be expressed in the laboratory frame:

$$\boldsymbol{M}(\boldsymbol{r},t) = \rho(\boldsymbol{r})\langle\mu_z\rangle\left[\cos(\omega_0 t - \boldsymbol{k}\boldsymbol{r})\,\boldsymbol{e_x} + \sin(\omega_0 t - \boldsymbol{k}\boldsymbol{r})\,\boldsymbol{e_y}\right]. \tag{2.133}$$

Insertion into (2.132) and execution of the time derivative yields

$$\begin{aligned} U = &-\frac{\langle\mu_z\rangle}{I^{\mathrm{dc}}}\iiint_V \rho(\boldsymbol{r}) \\ &[-\sin(\omega_0 t - \boldsymbol{k}\boldsymbol{r})\,B_{1,x}^{\mathrm{dc}}(\boldsymbol{r}) + \cos(\omega_0 t - \boldsymbol{k}\boldsymbol{r})\,B_{1,y}^{\mathrm{dc}}(\boldsymbol{r})] \\ &(\omega_0 - \gamma\boldsymbol{G}\boldsymbol{r})\,\mathrm{d}x\mathrm{d}y\mathrm{d}z. \end{aligned} \tag{2.134}$$

In the time derivative of the phase $\boldsymbol{k}\boldsymbol{r}$ due to gradients definition (2.36) was used. However, the contribution $|\gamma\boldsymbol{G}\boldsymbol{r}| \ll |\omega_0|$ on the signal amplitude is neglected. It is assumed that $B_{1,x}^{\mathrm{dc}}(\boldsymbol{r}) = 0$, i.e., $\phi_1 = -\pi/2$ in (2.22). Denoting the remaining transverse component as $B_{1,y}^{\mathrm{dc}}(\boldsymbol{r}) = -B_1^{\mathrm{dc}}(\boldsymbol{r})$ the induced voltage is expressed as

$$U = \frac{\langle\mu_z\rangle}{I^{\mathrm{dc}}}\omega_0\iiint_V \rho(\boldsymbol{r})\cos(\omega_0 t - \boldsymbol{k}\boldsymbol{r})\,B_1^{\mathrm{dc}}(\boldsymbol{r})\,\mathrm{d}x\mathrm{d}y\mathrm{d}z. \tag{2.135}$$

Before digitization the induced high-frequency voltage in the megahertz range is mixed with the resonance frequency, assumed to be equal to the rf frequency. This corresponds to the transformation in the rotating frame, see (2.18). As for the excitation here the common case is considered that a linear polarized field is detected. To obtain the circular polarized average magnetization the voltage is mixed in quadrature detection with two reference signals phase-shifted by $\pi/2$. Multiplication of the time-dependent term with $\cos(\omega_0 t)$ respectively $\sin(-\omega_0 t)$ yields

$$\begin{aligned} \cos(\omega_0 t - \boldsymbol{k}\boldsymbol{r})\cos(\omega_0 t) &= \frac{1}{2}[\cos(2\omega_0 t - \boldsymbol{k}\boldsymbol{r}) + \cos(-\boldsymbol{k}\boldsymbol{r})] \\ \cos(\omega_0 t - \boldsymbol{k}\boldsymbol{r})\sin(-\omega_0 t) &= \frac{1}{2}[-\sin(2\omega_0 t - \boldsymbol{k}\boldsymbol{r}) + \sin(-\boldsymbol{k}\boldsymbol{r})]. \end{aligned} \tag{2.136}$$

The high-frequency component at about twice the resonance frequency is eliminated by a low-pass filter. The field averaged over the sample is denoted as $\langle B_1^{\mathrm{dc}} \rangle$ and relative errors compared to a homogeneous field as $e(\boldsymbol{r})$. The result of mixing and filtering then reads

$$U\cos(\omega_0 t) \rightarrow \frac{\langle \mu_z \rangle \langle B_1^{\mathrm{dc}} \rangle}{2I^{\mathrm{dc}}} \omega_0 \iiint_V \rho(\boldsymbol{r}) e(\boldsymbol{r}) \cos(-\boldsymbol{k}\boldsymbol{r})\, \mathrm{d}x\mathrm{d}y\mathrm{d}z$$

$$U\sin(-\omega_0 t) \rightarrow \frac{\langle \mu_z \rangle \langle B_1^{\mathrm{dc}} \rangle}{2I^{\mathrm{dc}}} \omega_0 \iiint_V \rho(\boldsymbol{r}) e(\boldsymbol{r}) \sin(-\boldsymbol{k}\boldsymbol{r})\, \mathrm{d}x\mathrm{d}y\mathrm{d}z. \quad (2.137)$$

In analogy to (2.38) the second contribution is multiplied by i and added to the first contribution. Nondimensionalization with $\langle \mu_z \rangle \langle B_1^{\mathrm{dc}} \rangle \omega_0 / (2I^{\mathrm{dc}})$ yields as final result

$$U^+(\boldsymbol{k}) = \iiint_V \rho(\boldsymbol{r}) e(\boldsymbol{r}) \exp(-i\boldsymbol{k}\boldsymbol{r})\, \mathrm{d}x\mathrm{d}y\mathrm{d}z. \quad (2.138)$$

Thus the nondimensionalized complex voltage is the Fourier transform of the spin density weighted with relative errors of the rf-field amplitude. Whereas this weighting can already be recognized in (2.132) the factor used above for nondimensionalization shows the dependencies of the signal amplitude:

$$U \propto \langle \mu_z \rangle \frac{\langle B_1^{\mathrm{dc}} \rangle}{I^{\mathrm{dc}}} \omega_0 = \frac{\gamma I(I+1)\hbar^2}{3kT} \frac{\langle B_1^{\mathrm{dc}} \rangle}{I^{\mathrm{dc}}} \omega_0^2, \quad (2.139)$$

In the expression of the Boltzmann averaged z component of the observed nuclear magnetic dipoles, see (2.30), γB_0 was replaced by the resonance frequency ω_0. The signal is thus proportional to the square of the resonance frequency. This motivates the efforts to generate the highest possible homogeneous field, as in many NMR applications the SNR is critical. The signal is further proportional to the B_1 field per current in the sample volume. Optimization of this factor along with other characteristics of the rf probe is the object of continuous research. The factors I and γ are properties of the kind of nucleus under investigation. Although the signal increases with the spin quantum number, nuclei with $I > 1/2$ are used less frequently. They possess an electric quadrupole moment. In the presence of fluctuating gradients of the electric field this leads to a very rapid signal decay. Isotopes with high magnetogyric ratio γ, spin 1/2, and large natural abundance are ^{1}H and ^{19}F. Hydrogen nuclei are studied most frequently. The sample temperature T is usually predetermined by the application. However, when measuring at different temperatures, the inverse proportionality of the signal amplitude on the temperature has to be included in a quantitative analysis.

2.3.4.2 Noise

Perturbation of the signal by noise was already introduced as additive contribution in (2.103). It has to be minimized in order to increase SNR. The noise voltage U_n is expressed in [37] as

$$U_n = (F 4kT_c \, \Delta f \, R_c)^{1/2}. \tag{2.140}$$

Whereas T in (2.139) denotes the sample temperature T_c signifies the temperature of the conductors in the rf coil. In order to reduce noise, cryogenic rf probes are established in sophisticated NMR systems. This is also beneficial for the coil resistance R_c. The noise figure of the preamplifier and the spectral width are denoted by F and Δf, respectively. Due to the skin effect the coil resistance is frequency dependent. For a wire of length l_c and radius $r_c \ll l_c$ it is given by

$$R_c = \frac{l_c}{2\pi r_c} \sqrt{\frac{\mu_r \mu_0 \omega_0}{2\sigma_c(T_c)}}, \tag{2.141}$$

s. also (3.4). The temperature-dependent electrical conductivity is denoted as σ_c and the relative permeability as μ_r. From (2.139) to (2.141) it follows that SNR scales with $\omega_0^{7/4}$. In [20] a noise contribution due to losses in the sample which is quadratic in the frequency is considered. In this case SNR is only proportional to ω_0 respectively B_0. The effectively attainable SNR depends on many factors, see e.g., [1, 13, 20, 22, 37].

As a result of the measurement the discrete inverse Fourier transform of (2.138) including B_1 inhomogeneities with additional in-phase and quadrature-phase noise is considered. In the common case of magnitude images it is expressed as

$$\begin{aligned} \hat{\rho}_{nmo} &= \sqrt{[\mathrm{Re}(\tilde{\rho}_{nmo})\, \hat{e}_{nmo} + n_{i,nmo}]^2 + [\mathrm{Im}(\tilde{\rho}_{nmo})\, \hat{e}_{nmo} + n_{q,nmo}]^2} \\ &\approx \tilde{\rho}_{nmo}\, \hat{e}_{nmo} + n_{i,nmo}. \end{aligned} \tag{2.142}$$

For the discrete inverse Fourier transform of the ideal measurement the notation $(\tilde{\rho})_{nmo}$ was already used to indicate the presence of transformation artifacts. In analogy the outcome of an ideal measurement of $e(\boldsymbol{r})$, i.e., with constant ρ in (2.138) would be denoted as $(\tilde{e})_{nmo}$. However, the multiplicative relation between ρ and e in (2.138) does not strictly transform into a multiplicative relation between $(\tilde{\rho})_{nmo}$ and $(\tilde{e})_{nmo}$, as can be seen by inspection of (2.46). In fact transformation artifacts depend on the details of the new product function. Nevertheless the notation $(\tilde{\rho})_{nmo}$ is used in (2.142). Deviations from the multiplicative relation, which are small for a smoothly varying e are accounted for by introduction of the new symbol $\hat{e}$. The simplification in (2.142) assumes that the imaginary part of the measurement can be neglected against the real part (without phase errors, see Sect. 2.3.5) and that the real part including in-phase noise is always positive. This is the case of high SNR.

2.3.4.3 Variance

The variance of the measured spin density is calculated as

$$\hat{s}^2 = \frac{1}{NMO-1} \sum_{n=1}^{N} \sum_{m=1}^{M} \sum_{o=1}^{O} (\hat{\rho}_{nmo} - \langle \hat{\rho} \rangle)^2. \tag{2.143}$$

Accepting the simplified expression in (2.142) the relation to the variance $\tilde{s}^2$ of the ideally measured spin density $(\tilde{\rho})_{nmo}$ and the variances of the inhomogeneity $(\hat{e})_{nmo}$ and noise $(n_i)_{nmo}$ can be approximated as [32, 42]:

$$\hat{s}^2 \approx \tilde{s}^2 + \langle \tilde{\rho} \rangle^2 s_e^2 + \frac{1}{N_A} s_n^2. \tag{2.144}$$

The variance of the ideally measured spin density has a factor of $\langle \hat{e} \rangle^2$ which is neglected as by definition $\langle e \rangle = 1$. The variance of the inhomogeneity is denoted by s_e^2. Its contribution scales with the square of the average spin density. In the last term s_n^2 signifies the noise variance for one scan or average, $N_A = 1$. In (2.144) it is assumed that there is no covariance between the ideally measured spin density, the inhomogeneity of the rf field and noise. The relation is formulated for the case that the accumulated nondimensionalized voltage is divided by the number of averages. Otherwise the variance of the ideally measured signal would increase with N_A^2. Therefore the scaled noise variance decreases with the inverse of N_A as factor.

If the contributions of artifacts can be determined, (2.144) can be used to correct the variance calculated from the experimental data by subtraction of these contributions. To this end measurements on a sample of same size and similar, but homogeneous spin density can be performed. For the usual case of ^{1}H such a sample can be realized by a mixture of normal and heavy water (D_2O). For a homogeneous sample the variance of the ideally measured spin density is assumed to be zero. The two remaining contributions can be separated by measuring with variable number of scans and fitting of (2.144) to the results, see Fig. 2.23.

2.3.5 Phase Correction

Deviations of the measured spin density $(\tilde{\rho})_{nmo}$ from the true spin density $\rho(\boldsymbol{r})$ due to transformation and discretization artifacts have been treated in Sect. 2.1.3, p. 14ff. The impact of noise on the signal and magnitude image as well as the application of filters were discussed on p. 50ff in Sect. 2.3.1. Systematic errors originating from inhomogeneities of the $\boldsymbol{B_1}$ field were considered in Sect. 2.3.4. In the following the influence of nonlinear phase errors on the measured spin density and their correction will be presented.

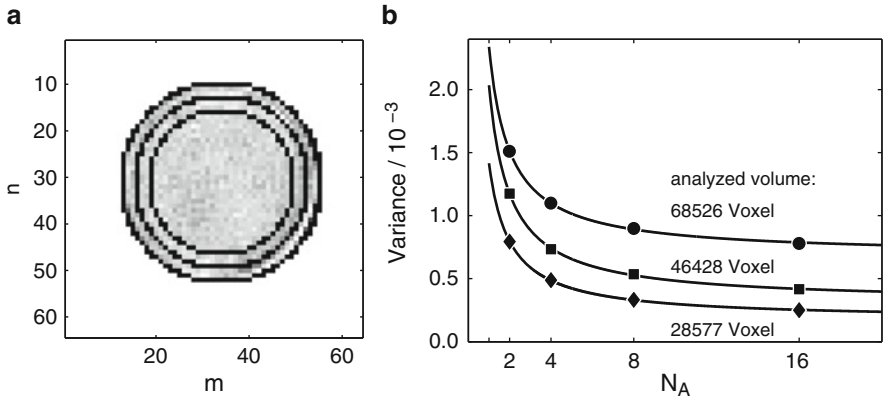

Fig. 2.23 Experimental determination of contributions to the variance by artifacts. (**a**) Slice of a 3D image of a homogeneous sample (i.e., $\tilde{s}^2 = 0$) with analyzed areas of different size. (**b**) Variance of the measured spin density (in the units used $\langle\tilde{\rho}\rangle = 0.41$) for the different areas as a function of the number of averages. *Solid lines* show fits of (2.144) to the data, allowing to separate the contributions. For white noise s_n^2 shows no systematic dependence on the area analyzed. For decreasing size, 0.0017, 0.0017, and 0.0012 are obtained, respectively. As expected, the contribution by inhomogeneities s_e^2 decreases with size: 0.0041, 0.0018, and 0.0010. Reprinted from [32] © 2007, with permission from Elsevier

2.3.5.1 Influence of Phase Errors

The influence of phase errors increases with decreasing SNR. Therefore noise is considered in the complex image. For the sake of simplicity, inhomogeneities of the $\boldsymbol{B_1}$ field are neglected. In addition it is assumed that the imaginary part of the transformed spin density can be neglected, $\tilde{\rho}_{nmo} = \mathrm{Re}(\tilde{\rho}_{nmo})$. Experimentally, a phase error $(\phi_e)_{nmo}$ is observed, so that the measured spin density is expressed as

$$\hat{\rho}_{nmo} = (\tilde{\rho}_{nmo} + n_{i,nmo} + i\, n_{q,nmo})\, \exp(i\, \phi_{e,nmo}). \tag{2.145}$$

Phase errors originate e.g. from off-resonance effects, pulse-phase errors, relaxation, transformation artifacts, or effects of electronic signal processing. If the experimental image is expressed as a magnitude image and a phase image, the relation to the unknown quantities in (2.145) is

$$|\hat{\rho}_{nmo}| = \sqrt{(\tilde{\rho}_{nmo} + n_{i,nmo})^2 + n_{q,nmo}^2} \tag{2.146}$$

$$\phi_{nmo} = \phi_{n,nmo} + \phi_{e,nmo}. \tag{2.147}$$

The noise contribution to the image phase is the four-quadrant inverse tangent

$$\phi_{n,nmo} = \tan^{-1}(n_{q,nmo}/(\tilde{\rho}_{nmo} + n_{i,nmo})). \tag{2.148}$$

For uncorrelated noise the average of $\phi_{n,nmo}$ is zero. The standard deviation of the phase resulting from noise is approximately $s_n/\tilde{\rho}_{nmo}$, the inverse of SNR [42]. According to (2.146) noise in the imaginary part also contributes to the magnitude image. In addition, normal distribution of noise leads to a Rice respectively Rayleigh distribution in the magnitude image, see (2.105) and (2.106). This does not only decrease SNR but also leads to a systematic, signal-dependent bias of signal amplitude.

2.3.5.2 Intention and Method of Phase Correction

The intention of phase correction is to determine the phase error $(\phi_e)_{nmo}$, to correct the complex image for the phase error and to use the real part of the result [2, 5, 11, 17, 45, 47, 53, 64]:

$$\mathrm{Re}\{\hat{\rho}_{nmo}\,\exp(-i\,\phi_{e,nmo})\} = \tilde{\rho}_{nmo} + n_{i,nmo} \tag{2.149}$$

$$= |\hat{\rho}_{nmo}|\cos(\phi_{n,nmo}). \tag{2.150}$$

The experimental phase consists of the more or less smooth phase error with additional noise. It can be attempted to fit a parametrized function $(\phi_o)_{nmo}$ to the experimental phase $(\phi)_{nmo}$. This requires that the phase image can be first corrected for 2π jumps, as the experimental phase is contained in an interval of width 2π. However, this procedure called phase unwrapping fails if the image consists of several unconnected regions with low SNR. Another method circumvents the ambiguity of the phase. The procedure is to minimize the magnitude or square of the imaginary part, e.g.,

$$\min_{\boldsymbol{k}_o} \sum_{nmo} |\hat{\rho}_{nmo}|^2 \sin(\phi_{nmo} - \phi_{o,nmo})^2 \tag{2.151}$$

with the parameter vector $\boldsymbol{k}_o$ of the phase fit function. The index o signifies order if the fit function represents a series expansion. Differences between the fitted and experimental phase of multiples of 2π have no influence on the sine function producing the imaginary part. For unconnected regions in the image it was observed that this method can lead to areas with positive as well as areas with negative signal (with superimposed in-phase noise). In the areas with negative signal a phase error of π remains. In order to solve also this problem, a new method was developed [33]. It consists of the maximization of the real-part sum:

$$\max_{\boldsymbol{k}_o} \sum_{nmo} |\hat{\rho}_{nmo}|\cos(\phi_{nmo} - \phi_{o,nmo}). \tag{2.152}$$

Taylor expansion of the cosine to second order shows that in this approximation and without 2π jumps the procedure corresponds to a least-square fit of the phase

function with the signal magnitude as weight. Fitting without weight yields similar results. Using the squared signal magnitude as weight leads to a chi-square fit, as the standard deviation of the phase is inversely proportional to the signal intensity. A fundamentally different method uses the phase of a filtered image as approximation for phase correction, see [47] and Fig. 4.4.

2.3.5.3 Implementation

The implementation of the new method is shown schematically in Fig. 2.24. A third-order 3D polynomial is used as fit function, corresponding to 20 fit parameters. The magnitude and phase images are read by the program. Only points with intensities above a chosen threshold are retained so that the fit is not loaded by points containing only noise. If the remaining number still exceeds a chosen limit points are discarded from the list at regular intervals. Typically 10^5 points are used for the fit, corresponding to over 45 points per direction in space. Identification of the global first-order optimum turned out to be essential for successful phase correction. To this end the starting points for the first-order fits in the parameter vectors $\boldsymbol{k}_1$ are first taken from a suitable lattice. For the constant term only a 2π interval has to be considered, values of -1.5, 0, 1.5, and 3 rad are chosen, respectively. The linear component for each spatial direction is chosen such that the change in phase along the image extension amounts to 0, ± 1, ± 2, or ± 4 rad, respectively. The 4D lattice vectors are sorted by increasing magnitude and used one by one in this order. For each starting point the maximum obtained according to expression (2.152) is saved along with the parameter vector. Optimizations starting from lattice points is aborted if the attained real-part sum exceeds a chosen fraction of the magnitude sum. If this criterion is not fulfilled for all of the 1,372 lattice points, a chosen number of optimizations with random starting points from a larger domain are executed and the parameter vector resulting from the most successful optimization is retained. If desired second- and third-order fits are executed with parameters from the lower-order fit as starting point. The new parameters are randomly chosen for each of the optimizations. Typically, two second-order and one third-order optimization is added. A lattice with six dimensions for the additional second-order terms or even ten dimensions for the additional third-order terms would be very large. Addition of the second- and third-order was observed to lead to a comparatively small increase of the sum in expression (2.152).

Optimization was performed in MATLAB® R2007a with a quasi-Newton method. It yielded better results in shorter times than a simplex method. For the first-order optimization the analytical gradients were provided. The computation time on a simple personal computer (Intel P4 3.2 GHz processors, 1 GB RAM, Microsoft Windows XP Pro SP2 operating system) is of the order of minutes. In order to investigate computation times results for several runs on a more efficient multi-core computer were averaged (Intel Xeon CPU 5130@2.00 GHz processor, 14 GB RAM, XP Pro x64 Edition SP2 operating system). The computation time as a function of number of points included and order is compiled in Table 2.1 (all first-order

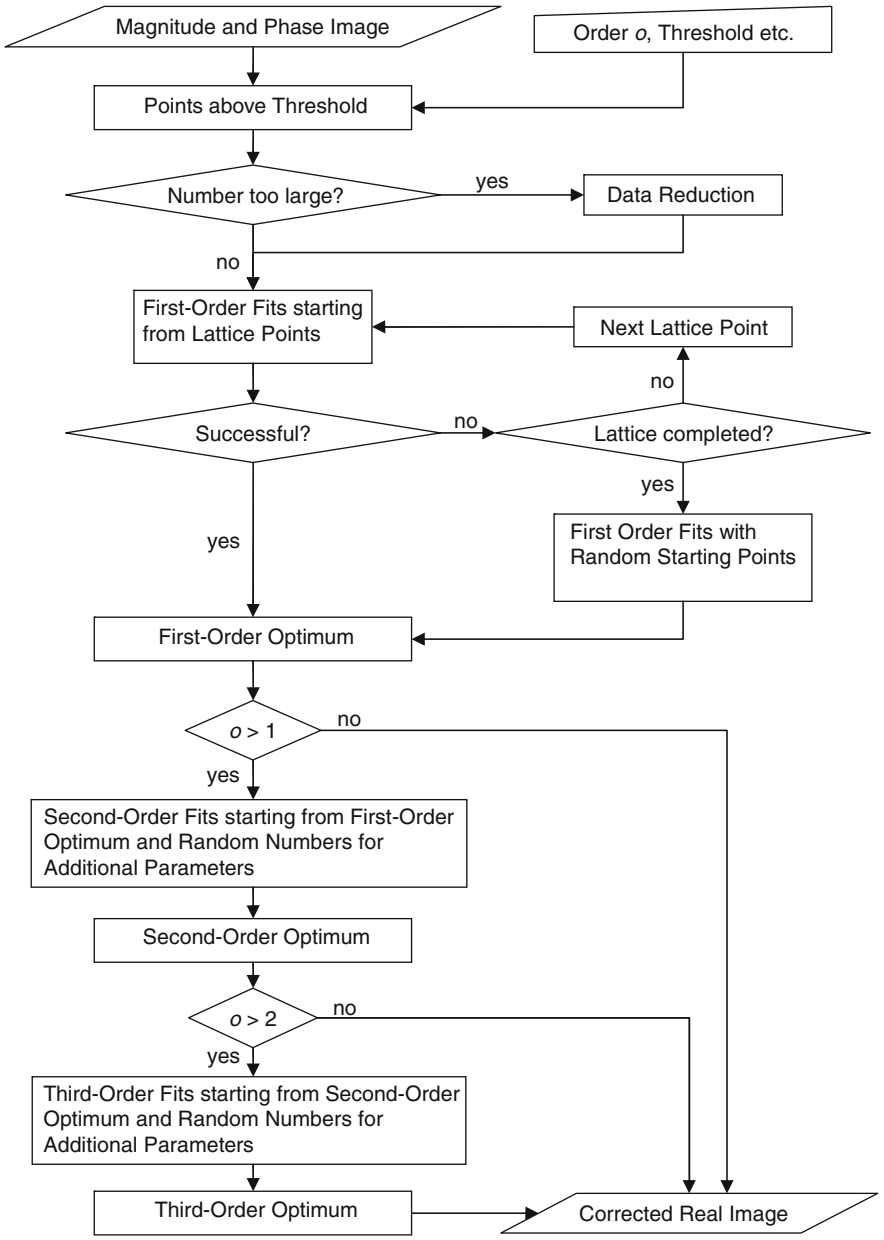

Fig. 2.24 Procedure of phase correction. Reprinted from [33] © 2009, with permission from Elsevier

Table 2.1 Computation time for phase correction in seconds

Number of points	13,351	26,922	53,836	107,263	214,514
Second order	4	8	16	40	121
Third order	39	78	157	377	1,005

calculations took less than 2 s). For the first three numbers of points computation time scales with the number of points, then the increase is over proportional. At a given number of points third-order optimization takes about ten times longer than the second-order optimization. Including all fourth-order terms would probably lead to hardly acceptable computation times. Concerning the number of points included, satisfactory results were already obtained with the lowest value corresponding to about 23 points per spatial dimension.

2.3.5.4 Application of the Method to Test Cases

The method was developed to investigate the deposition of small particle masses in fibrous filters in situ, see Sect. 4.1. Here it is first examined and discussed for several test cases.

First it was investigated if the polynomial series is suitable and sufficiently flexible to map phase errors that occur experimentally. A 3D gradient-echo was used as test image. Here inhomogeneities of the static field are not refocused as it is the case for a SE image. A sample tube was filled with an aqueous Gadovist solution (relaxation agent, 2.5 mmol/l). The entire available sample volume was filled in order to assess the performance of the method in the border areas. Within the sample SNR is so high that according to (2.146) or (2.148) and (2.150) the magnitude and phase-corrected real-part image should be nearly identical. Deviations indicate an insufficient phase correction. Outside the sample there should be only noise. Figure 2.25 shows four out of 64 horizontal slices through the sample in four columns. In the first three rows the difference of the magnitude image shown in the last row and the corrected real-part image is represented for a first, second, and third-order polynomial, respectively. Black represents full correction, white a difference of 10% of the maximum intensity in the magnitude image. The first row shows that for slices near the center already the first-order polynomial leads to a high degree of correction. For slices near the border, however, errors of up to 10% remain. These errors are markedly reduced in second order, see second row, and no longer observable in third order in the third row. The presence of pattern outside the sample indicates experimental artifacts. In general a bright border at the rim of the sample shows that at the interface phase errors occur that are not described by a smooth function. Apart from this, correction with the new method is successful for this data set and a third-order polynomial is suitable and sufficiently flexible.

Next the ability of the method to correct the phase in the case of low SNR and isolated regions was investigated. To this end known masses of oil-filled microcapsules with different spatial distributions were imaged with a fast SE

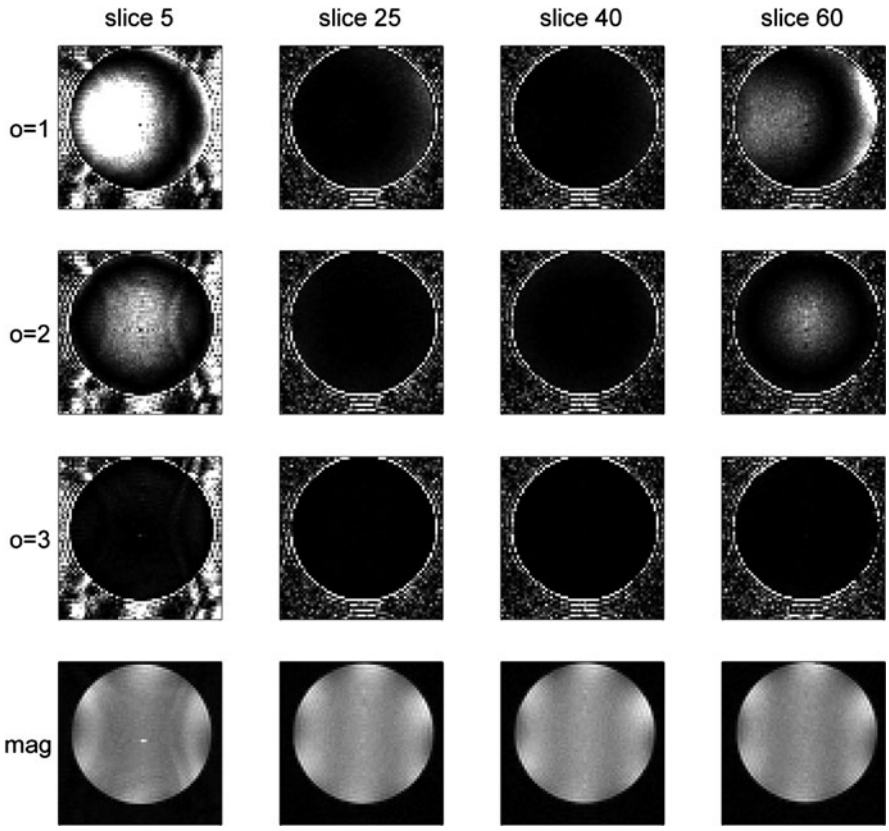

Fig. 2.25 Convergence of phase correction with order of polynomial (1–3) for two slices close to the border of the sample (5 and 60) as well as two slices in the middle (25 and 40). The first three rows show the difference of the magnitude and real-part image. For this data set with high SNR the difference should approach zero (*black*). *Last row*: magnitude image. Reprinted from [33] © 2009, with permission from Elsevier

sequence. The total signal with and without phase correction is plotted against the total mass in Fig. 2.26. The linear relation for the phase-corrected data in the double-logarithmic plot shows the expected proportionality (note that a linear dependence with positive ordinate intersection does not appear linear in a double-logarithmic plot). For the magnitude data the calibration curve deviates at low masses toward the plateau of the sum of magnitude noise.

The applicability of the method to large data sets was tested for the image of a fibrous filter immersed in an aqueous Gadovist solution with tenside. The data set acquired with a fast SE sequence comprises 256^3 points. Phase correction was successful. However, marked intensity distortions occur in the phase-corrected real-part image in the vicinity of small air bubbles which remain in the sample in spite of thorough degassing. In the magnitude image, air bubbles are not easily distinguished for fibers and lead to errors in the determination of fiber structure.

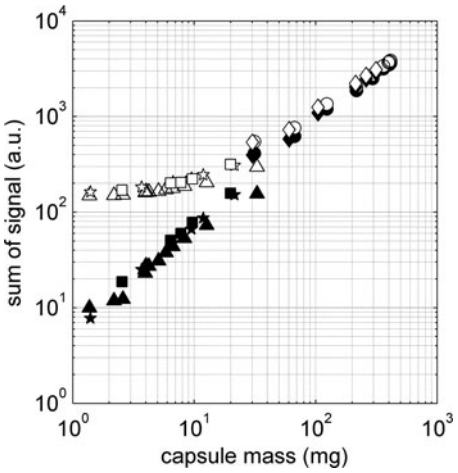

Fig. 2.26 Signal calibration with (filled symbols) and without (open symbols) phase correction. Reprinted from [33] © 2009, with permission from Elsevier

Phase correction could thus be useful also for images with high SNR in the automatic detection of air bubbles or interfaces between different susceptibilities in general.

The method was also applied successfully to a series of volume images with increasing signal decay by transverse relaxation. For early high SNR images noise has almost the same influence in the magnitude and phase-corrected real-part image. However, magnitude images with strong decay and low SNR approach the limit of magnitude noise. This leads to errors, e.g., in the fit of the transverse relaxation time T_2.

Finally it is noted that the method can also be used for data in which the spin density can appear with negative sign, e.g., images with inversion-recovery or fat-water filter. To this end the complex image is squared and the fit function is used to approximate the double of the phase error. This was shown for simulated data.

References

1. Abragam, A (1961) Principles of nuclear magnetism. Clarendon Press, Oxford
2. Ahn C, Cho Z (1987) A new phase correction method in NMR imaging based on autocorrelation and histogram analysis. IEEE Trans Med Imaging 6(1):32–36
3. Bardakci M, Tillich JE, Holz M (2006) Characterization of structure and transport in porous media by pulsed field gradient (PFG) NMR technique – Part I: Master curve and characteristic inner length. Chem Eng Technol 29(7):847–853. DOI 10.1002/ceat.200600043
4. Behnke B, Schlotterbeck G, Tallarek U, Strohschein S, Tseng LH, Keller T, Albert K, Bayer E (1996) Capillary HPLC-NMR coupling high-resolution NMR spectroscopy in the nanoliter scale. Anal Chem 68(7):1110–1115
5. Bernstein M, Thomasson D, Perman W (1989) Improved detectability in low signal-to-noise ratio magnetic-resonance images by means of a phase-corrected real reconstruction. Med Phys 16(5):813–817

6. Bloch, F (1946) Nuclear induction. Phys Rev 70:460–474
7. Bloch F, Siegert A (1940) Magnetic resonance for nonrotating fields. Phys Rev 57(6):522–527. DOI 10.1103/PhysRev.57.522
8. Bloembergen N, Purcell EM, Pound RV (1948) Relaxation effects in nuclear magnetic resonance absorption. Phys Rev 73:679–712
9. Blümich, B (2000) NMR imaging of materials. Clarendon Press, Oxford
10. Braun S, Kalinowski HO, Berger S (1998) 150 and more basic NMR experiments. Wiley-VCH, Weinheim
11. Bretthorst, GL (2008) Automatic phasing of MR images. Part I: Linearly varying phase. J Magn Reson 191(2):184–192. DOI 10.1016/j.jmr.2007.12.010
12. Callaghan PT (1990) PGSE MASSEY, a sequence for overcoming phase instability in very-high-gradient spin-echo NMR. J Magn Reson 88(3):493–500
13. Callaghan PT (1991) Principles of nuclear magnetic resonance microscopy. Clarendon Press, Oxford
14. Canet D (1996) Nuclear magnetic resonance: Concepts and methods. Wiley, Chichester
15. Caprihan A, Fukushima E (1990) Flow measurements by NMR. Phys Rep 198(4):195–235
16. Cavanagh J, Fairbrother WJ, Palmer AG III, Skelton NJ (1996) Protein NMR spectroscopy. Academic Press, San Diego
17. Chang Z, Xiang, Q (2005) Nonlinear phase correction with an extended statistical algorithm. IEEE Trans Med Imaging 24(6):791–798. DOI 10.1109/TMI.2005.848375
18. Chen CN, Hoult DI, Sank VJ (1983) Quadrature detection coils – A further square-root2 improvement in sensitivity. J Magn Reson 54(2):324–327
19. Cotts RM, Hoch MJR, Sun T, Markert JT (1989) Pulsed field gradient stimulated echo methods for improved NMR diffusion measurements in heterogeneous systems. J Magn Reson 83(2):252–266
20. Edelstein WA, Glover GH, Hardy CJ, Redington RW (1986)The intrinsic signal-to-noise ratio in NMR imaging. Magn Reson Med 3(4):604–618
21. Engelke F (2010) Virtual photons in magnetic resonance. Concept Magn Res A 36A(5):266–339. DOI 10.1002/cmr.a.20166
22. Ernst RR, Bodenhausen G, Wokaun A (1987) Principles of nuclear magnetic resonance in one and two dimensions. Clarendon Press, Oxford
23. Feynman RP (1985) QED : The strange theory of light and matter. Alix G. Mautner memorial lectures. University Press, Princeton, NJ
24. von Garnier A, Hardy EH, Schweitzer JM, Reimert R (2007) Differentiation of catalyst and catalyst support in a fixed bed by magnetic resonance imaging. Chem Eng Sci 62(18–20, Sp. Iss. SI):5330–5334. DOI 10.1016/j.ces.2007.03.034
25. Geen H, Freeman R (1991) Band-selective radiofrequency pulses. J Magn Reson 93(1):93–141
26. Gladden LF, Alexander P (1996) Applications of nuclear magnetic resonance imaging in process engineering. Meas Sci Technol 7(3):423–435
27. Glover GH, Hayes CE, Pelc NJ, Edelstein WA, Muller OM, Hart H, Hardy CJ, ODonnell M, Barber W (1985) Comparison of linear and circular-polarization for magnetic-resonance imaging. J Magn Reson 64(2):255–270
28. Goldman M (1991) Quantum description of high-resolution NMR in liquids. Oxford University Press, Oxford
29. Grosse J, Dietrich B, Martin H, Kind M, Vicente J, Hardy EH (2008) Volume image analysis of ceramic sponges. Chem Eng Technol 31(2):307–314. DOI 10.1002/ceat.200700403
30. Halbach RE, Battocletti JH, Sances A, Bowman RL, Kudravcev V (1979) Cylindrical crossed-coil NMR limb blood flowmeter. Rev Sci Instrum 50(4):428–434
31. Hardy EH (2006) Magnetic resonance imaging in chemical engineering: Basics and practical aspects. Chem Eng Technol 29(7):785–795. DOI 10.1002/ceat.200600046
32. Hardy EH, Hoferer J, Kasper G (2007) The mixing state of fine powders measured by magnetic resonance imaging. Powder Technol 177(1):12–22. DOI 10.1016/j.powtee.2007.02.042
33. Hardy EH, Hoferer J, Mertens D, Kasper G (2009) Automated phase correction via maximization of the real signal. Magn Reson Imaging 27(3):393–400. DOI 10.1016/j.mri.2008.07.009

34. Harris RK (1986) Nuclear magnetic resonance spectroscopy. Longman Scientific and Technical, Essex
35. Hoult D, Ginsberg N (2001) The quantum origins of the free induction decay signal and spin noise. J Magn Reson 148(1):182–199
36. Hoult DI (2009) The origins and present status of the radio wave controversy in NMR. Concept Magn Res A 34A(4):193–216. DOI 10.1002/cmr.a.20142
37. Hoult DI, Richards RE (1976) Signal-to-noise ratio of nuclear magnetic-resonance experiment. J Magn Reson 24(1):71–85
38. Hurlimann MD, Burcaw L, Song YQ (2006) Quantitative characterization of food products by two-dimensional D-T-2 and T-1-T-2 distribution functions in a static gradient. J Colloid Interface Sci 297(1):303–311. DOI 10.1016/j.jcis.2005.10.047
39. Jin J (1999) Electromagnetic analysis and design in magnetic resonance imaging. CRC Press, Boca Raton
40. Karlicek RF, Lowe IJ (1980) Modified pulsed gradient technique for measuring diffusion in the presence of large background gradients. J Magn Reson 37(1):75–91
41. Kimmich R (1997) NMR tomography, diffusometry, relaxometry. Springer-Verlag, Berlin, Heidelberg, New York
42. Kreyszig E (1970) Introductory mathematical statistics. Wiley, New York
43. Kriesten E, Alsmeyer F, Bardow A, Marquardt W (2008) Fully automated indirect hard modeling of mixture spectra. Chemom Intell Lab Syst 91(2):181–193. DOI 10.1016/j.chemolab.2007.11.004
44. Latour L, Mitra P, Kleinberg R, Sotak C (1993) Time-dependent diffusion-coefficient of fluids in porous-media as a probe of surface-to-volume ratio. J Magn Reson Ser A 101(3):342–346
45. Liu J, Koenig J (1990) An automatic phase correction method in nuclear-magnetic-resonance imaging. J Magn Reson 86(3):593–604
46. Meyer F (1994) Topographic distance and watershed lines. Signal Process 38(1):113–125
47. Noll DC, Nishimura DG, Macovski A (1991) Homodyne detection in magnetic-resonance-imaging. IEEE Trans Med Imaging 10(2):154–163
48. Ohser J, Mcklich, F (2000) Statistical analysis of microstructures in materials science. Wiley, Chichester, England
49. Pople JA, Schneider WG, Bernstein HJ (1959) High-resolution nuclear magnetic resonance. McGraw-Hill Book Co, New York
50. Redpath TW, Norris DG, Jones RA, Hutchison JMS (1984)A new method of NMR flow imaging. Phys Med Biol 29(7):891–895
51. Rosenfeld D (1998) An optimal and efficient new gridding algorithm using singular value decomposition. Magn Reson Med 40(1):14–23
52. Sankey MH, Holland DJ, Sederman AJ, Gladden LF (2009) Magnetic resonance velocity imaging of liquid and gas two-phase flow in packed beds. J Magn Reson 196(2):142–148. DOI 10.1016/j.jmr.2008.10.021
53. Sarkar S, Heberlein K, Metzger G, Zhang X, Hu X (1999) Applications of high-resolution echoplanar spectroscopic imaging for structural imaging. J Magn Reson Imaging 10(1):1–7
54. Sedarat H, Nishimura DG (2000) On the optimality of the gridding reconstruction algorithm. IEEE Trans Med Imaging 19(4):306–317
55. Sederman AJ, Alexander P, Gladden LF (2001) Structure of packed beds probed by magnetic resonance imaging. Powder Technol 117(3):255–269
56. Shankar R (1980) Principles of quantum mechanics. Plenum Press, New York
57. Singer JR (1959) Blood flow rates by nuclear magnetic resonance measurements. Science 130(3389):1652–1653
58. Slichter CP (1980) Principles of magnetic resonance. Springer-Verlag, Berlin
59. Song YQ, Venkataramanan L, Hurlimann MD, Flaum M, Frulla P, Straley C (2002) T-1-T-2 correlation spectra obtained using a fast two-dimensional Laplace inversion. J Magn Reson 154(2):261–268. DOI 10.1006/jmre.2001.2474
60. Stejskal EO (1965) Use of spin echoes in a pulsed magnetic-field gradient to study anisotropic restricted diffusion and flow. J Chem Phys 43(10P1):3597–3603

61. Stejskal EO, Tanner JE (1965) Spin diffusion measurements – Spin echoes in presence of a time-dependent field gradient. J Chem Phys 42(1):288–292
62. Stepisnik J (1985) Measuring and imaging of flow by NMR. Prog Nucl Magn Reson Spectrosc 17(Part 3):187–209
63. Sudmeier JL, Gunther UL, Albert K, Bachovchin WW (1996) Sensitivity optimization in continuous-flow FTNMR. J Magn Reson Ser A 118(2):145–156
64. Tisdall D, Atkins M (2005) MRI denoising via phase error estimation. In: Fitzpatrick JM, Reinhardt JM (eds) Medical imaging 2005: Image processing, Pt 1–3, *Proceedings of the society of photo-optical instrumentation engineers (spie)*, vol 5747. Medical Imaging 2005 Conference, San Diego, CA, 15–17 February 2005, pp 646–654. DOI 10.1117/12.595677
65. Torrey HC (1956) Bloch equations with diffusion terms. Phys Rev 104(3):563–565
66. VanAs H, Schaafsma TJ (1987) Measurement of flow by the NMR repetitive pulse method. J Magn Reson 74(3):526–534
67. van de Ven FJM (1995) Multidimensional NMR in liquids: Basic principles and experimental methods. VCH Publishers, Inc, New York, Weinheim, Cambridge
68. Vincent L, Soille P (1991) Watersheds in digital spaces – An efficient algorithm based on immersion simulations. IEEE Trans Pattern Anal Mach Intell 13(6):583–598

Chapter 3
Hardware

3.1 Micro-Imaging System

All high-field experiments were conducted in a micro-imaging system provided by Bruker, Rheinstetten, Germany.

The super-wide-bore (SWB) magnet, see Fig. 3.1a, has a continuous vertical room-temperature bore with 150 mm diameter. A superconducting coil at 4.2 K generates a static field B_0 of 4.7 T. This value represents a suitable compromise between sufficient polarization of the sample and avoiding of susceptibility artifacts which both increase with magnetic field. For hydrogen nuclei, the resulting resonance frequency according to (2.13) amounts to 200 MHz.

A set of resistive coils denoted as shim system is mounted in the room-temperature bore. Adjusting the current in these coils allows to reduce the inhomogeneity of B_0 across the individual sample to values that are typically significantly below 1 ppm (parts per million).

Within the shim system the three-axis (xyz) gradient system used for spatial resolution and displacement encoding is mounted. For the largest sample diameter the mini0.36 gradient system shown on the left in Fig. 3.1b is used. The sensitivity in each spatial direction amounts to 3.6 mT $m^{-1}A^{-1}$. A stronger gradient for smaller sample diameters can be generated with the micro2.5 gradient system depicted on the right in Fig. 3.1b. Its sensitivity amounts to 25 mT $m^{-1}A^{-1}$. The gradient amplifier used (BAFPA 40) supplies a maximum current of 40 A, resulting in maximum gradients $\boldsymbol{G}$ of 0.144 and 1 T/m, respectively.

Finally, the probe head is mounted into the gradient system. The setup with the largest continuous inner diameter of 64 mm is shown in Fig. 3.2a. An electrical resonator formed by capacitors and vertical legs, denoted as birdcage resonator generates the transverse rf field. To achieve this, the current distribution on the legs approximates the surface current density on a cylinder according to a sine function. The same probe head is shown on the left in Fig. 3.2b with the resonator separated from the corresponding holder. On the right further holders and resonators to be used with the smaller gradient system are shown. In order to generate hard, i.e., short and

E.H. Hardy, *NMR Methods for the Investigation of Structure and Transport*,
DOI 10.1007/978-3-642-21628-2_3,

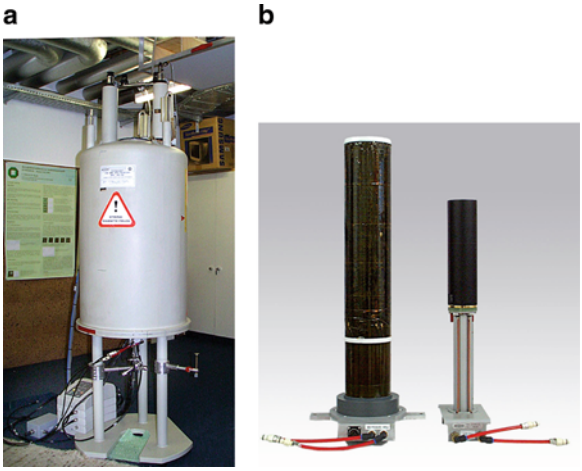

Fig. 3.1 Magnet and gradient systems of the micro-imaging system: (**a**) shows the superconducting super-wide-bore (SWB) magnet. In the vertical room-temperature bore with 150 mm diameter a magnetic field of 4.7 T is generated. The height of the magnet from the floor to the upper end of the bore amounts to 1.95 m. (**b**) shows on the left the mini0.36 gradient system with a maximum gradient of 0.144 T/m, used for larger samples. For smaller samples, the micro2.5 gradient system shown on the right generates a maximum gradient of 1 T/m

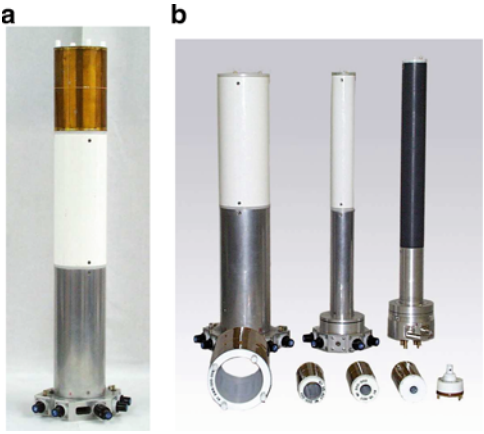

Fig. 3.2 High field probe heads: (**a**) shows the probe head with a continuous inner diameter of 64 mm; (**b**) shows further probe heads with varying inner diameter

intense rf pulses, the resonators are fed with a rf power of about 30 W (BLARH 100 amplifier at 0 dB). The resulting amplitude of the usable circular polarized magnetic field component B_1 decreases with the inner diameter of the resonator. For 64 mm, about 50 μT are achieved, for 15 mm about 280 μT. For protons this corresponds according to (2.24) to a Rabi nutation frequency of 2 and 12 kHz, respectively.

The set of electronic components is denoted as "Avance DRX console." In Fig. 3.3 the three bays are shown with open doors. The three gradient amplifiers

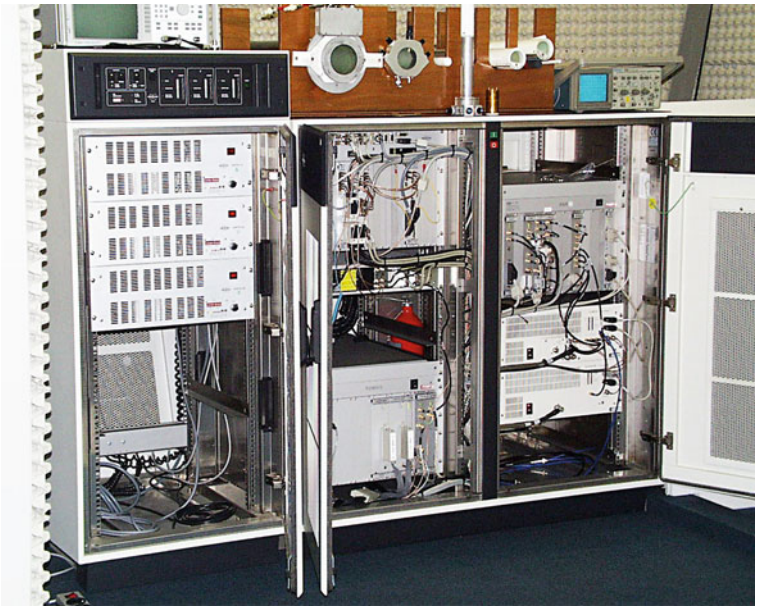

Fig. 3.3 High-field console with open doors. *Left*: Imaging bay with preemphasis unit and three gradient amplifiers; *Middle*: Module with predominantly digital boards, frequency synthesizer, and magnet- and shim-control module; *Right*: Module with boards for signal processing and rf amplifiers

are located in the bay on the left. On top of the bay is a preemphasis unit (BGU II), used to compensate eddy-current effects. The bay in the middle contains, from top to bottom, the module with predominantly digital boards (AQX), the frequency synthesizer (PTS), and the module for magnet and shim control (BSMS/2). In the right bay, from top to bottom, the module containing the boards for signal processing (AQR), the 100-W 200-MHz amplifier for protons (BLARH 100), and the 300-W broadband amplifier for other nuclei (BLAX 300RS) are located. The preamplifier module (HPPR) is placed close to the probehead and can be seen left to the magnet base in Fig. 3.1a.

A schematic representation of a micro-imaging system as well as further explanations and figures can be found, e.g., in [7] or [1].

If possible pulse and gradient programs provided by Bruker in the software package ParaVision 3 were used. This allows to set high-level parameters such as FOV or slice thickness and position. The corresponding low-level parameters such as gradient amplitudes, pulse duration, and frequency offset are calculated by the software. Only in special cases programing of customized pulse- and gradient programs in XWinNMR (stand-alone part of ParaVision) was necessary (see Sect. 4.2 and 4.6).

Fig. 3.4 Compact and mobile low-field system for the NMR-based capillary rheometer. The height of the magnet box on the left of the table amounts to 0.32 m without the aluminum parts at the ends of the flow loop, see Sect. 3.4. In the middle of the table the electronic box can be seen. A cryostat used for thermostatting of the flow loop is placed on the right. The 60-A gradient amplifier and the electronics for pressure-difference and temperature recording are located on the lower board

3.2 Low-Field System

A low-field NMR system was provided by Bruker, Rheinstetten, Germany, see Fig. 3.4. It was used for the development of a compact and mobile NMR-based capillary rheometer, see Sect. 4.4. The AlNiCo permanent magnets are mounted on a yoke and generate a static field B_0 of 0.23 T between the pole faces with 125 mm diameter, separated by 50 mm. According to (2.13), this corresponds to a resonance frequency of 10 MHz for protons.

The instrument is based on the mq10 benchtop analyzer. It was additionally equipped by Bruker with a one-axis gradient system in flow direction. Its sensitivity amounts to 50 mT $m^{-1}A^{-1}$. Driven by a modified GREAT 1/60 amplifier with 60 A maximum current gradients $\boldsymbol{G}$ of up to 3 T/m can be applied. In contrast to the three-axis gradient system for the high-field tomograph, there is no active shielding. As marked artifacts resulting from interactions of pulsed gradients with the permanent-magnet system were observed, an actively shielded gradient system was developed, see Sect. 3.3.1.

The probe head with a solenoid coil has an inner diameter of 10 mm. With an attenuation of 20 dB of the 300 W amplifier, the rf field B_1 has an amplitude of 735 μT. For protons this results in a nutation frequency of 31 kHz according to (2.24).

All pulse and gradient programs were written with the ExSpel software provided by Bruker.

3.2.1 Properties of Magnet Materials

Several parameters of the magnet material are of relevance for the application in NMR experiments. The Curie temperature (complete loss of magnetization) or rather maximum operating temperature (irreversible loss of magnetization) have to be higher than the working temperature. A reversible linear dependence of magnetization on temperature is described by the temperature coefficient, which should be as small as possible. The coercive field strength (opposing field required for demagnetization) indicates if the material is magnetically hard or soft. A high remanence (residual induction after magnetization) and energy product (density of energy) are desired to produce high fields. Also the mechanical workability and resistance against corrosion as well as the price are of interest.

Exact values of the parameters depend on details of the material and production. In the following, typical values for commercially available magnets are indicated. A high maximum operating temperature (700 K) and low temperature coefficient (−0.02%/K) can be obtained using AlNiCo. The remanence is also high (1.1 T), however the energy product (40 kJ/m^3) and coercivity (250 kA/m) are low. A favorable compromise of parameters is given for SmCo. At a somewhat lower remanence (0.9 T) the energy product (above 150 kJ/m^3) and coercivity (630 kA/m) are considerably higher. The maximum operating temperature (550 K) is not as high as for AlNiCo and the temperature coefficient is doubled (−0.04%/K). However, the price for SmCo is significantly higher than for AlNiCo or also NdFeB. The highest energy product, remanence, and coercivity is achieved with NdFeB (above 300 kJ/m^3, 1.2 T, and 900 kA/m respectively). On the other hand, the maximum operating temperature and temperature coefficient (400 K and −0.1%/K, respectively) are disadvantageous.

The inside-out setup shown in Fig. 3.8 requires compact and strong magnets. As temperature can vary and the price of the magnet material is not decisive,

SmCo magnets are used. For the simple, compact, and efficient NMR magnet shown in Fig. 3.9, temperature variations are not critical and NdFeB magnets are employed. Ongoing developments are expected to yield magnet materials with further improved properties.

Due to inhomogeneities of the permanent-magnet material, a homogeneity of the static B_0 field below 10 ppm can be hardly achieved by mechanical adjustments only. Commercial systems usually cannot be provided with resistive shim coils, so chemical resolution is not achieved for proton NMR. Standard applications are restricted to relaxometry and diffusometry. However, a number of compact systems based on permanent magnets capable of chemical resolution for protons have been developed by now, see e.g., [4, 8, 9, 19, 24]. Medium resolution NMR with compact, maintenance free, and cost-efficient devices certainly is an emerging field.

3.3 Design of Specific NMR Parts

3.3.1 Actively Screened Gradient Coils

The low-field system described in Sect. 3.2 has a gradient system generating the desired field profile in flow direction between two parallel plates. However, without active shielding a magnetic field is also generated outside the plates inside the permanent-magnet system. Application of gradient pulses leads to transient as well as remanent effects. Both effects can be described approximately as transient and remanent *gradients* with an amplitude of the order of one per mill of the amplitude of the switched gradient. Depending on the experiment, such gradient imperfections can exclude the use of standard pulse and gradient sequences, see also p. 34ff. As remedy, an actively shielded gradient system fitting in the available magnet gap was developed.

Common permanent magnet systems as the one shown in Fig. 3.4 as well as more recent yokeless setups as the Halbach array shown in Fig. 3.9 have their main field direction transverse to the sample axis. This is at variance with the situation in superconducting magnets, see Fig. 3.1 with main field direction parallel to the sample axis. Thus gradient systems developed for the prevailing superconducting magnets cannot be used. However, permanent magnet setups have the transverse field orientation in common with electromagnets that were used for NMR before the propagation of superconducting magnets. Bowtell and Mansfield published a method for the design of actively shielded gradient coils for transverse field geometry. It was used for fast chemical shift imaging in an electromagnet with 0.7 T and 127 mm pole gap [6]. The method allows the calculation of surface current densities on two coaxial cylinders such that no field is produced outside the outer cylinder. Defining an appropriate target field on a fictitious coaxial cylinder inside the inner cylinder, the current densities are determined. In practice, the current densities are approximated by discrete conducting paths. The inner coil with radius

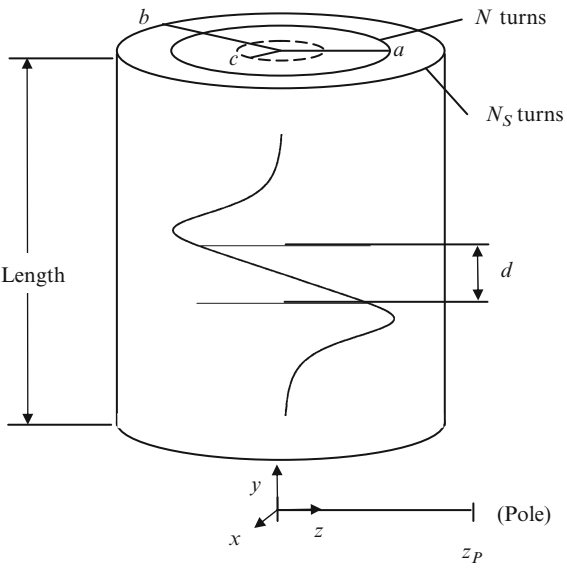

Fig. 3.5 Parameters of the actively shielded gradient system

a and N turns is denoted as primary coil, the outer coil with radius b and N_S turns as screen coil, respectively. The target field on a cylinder with radius c has one parameter d:

$$B_z = G_y y/(1 + (y/d)^6). \tag{3.1}$$

As usual the z axis is in direction of the polarizing field which is horizontal. The y axis is pointing upward in direction of flow. A sketch with the parameters and the target field according to (3.1) can be seen in Fig. 3.5. The radius b of the screen coil is determined by the pole gap. As the current density is approximated by discrete conducting paths, a distance of the order of the typical path separation should be left between the screen coil and the pole faces. Reducing the radius a of the primary coil increases the gradient sensitivity. However, the rf coil and rf shield have to fit into the primary coil, requiring a compromise. The parameters c (radius of the target field cylinder) and d (length of region with homogeneous gradient) can be varied in order to optimize the gradient characteristics. As constraint, the inequality $c+d/2 > a$ has to be fulfilled. Increasing the number of turns increases the gradient sensitivity, however also the inductance. This can result in gradient rise times which are too long. In addition, the number of turns is limited by the minimum separation of the calculated current paths and the width of the conducting elements. The overall length of the cylinders is limited by constructive considerations so that some current paths might have to be compressed.

In a preliminary study the parameters are varied and the resulting current paths are saved. Using Biot–Savart calculations, field maps are determined for the planes $z = 0$, $z = z_{\mathrm{Pol}}$, and $x = 0$. The screening efficiency is given by the field in the

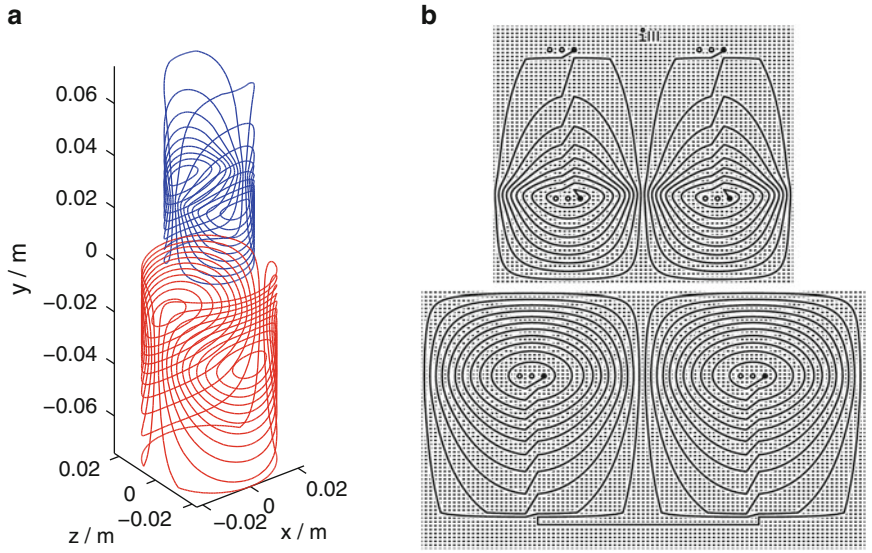

Fig. 3.6 Conductive path for the gradient in flow direction. The upper and lower halves of each coil are identical. Only the lower half of the screen coil and the upper half of the primary coil are shown, respectively. (**a**) 3D representation of the conductive paths without connections as used for the Biot–Savart calculations. The surface current density was previously calculated up to fifth order of the Fourier–Bessel expansion. A grid with 128 points for the polar angle and 256 points for the z axis was used. (**b**) Inner layers with connections as used for the production of the conducting paths. They are connected in series with a similar outer layer. In total three double-sided layers were connected in parallel for the primary and screen coil, respectively, reducing the resistance to one-third. In order to maximize the sensitivity the connections could be done in series

plane $z = z_{\mathrm{Pol}}$. In the planes at $z = 0$ and $x = 0$ the deviation from a homogeneous gradient G is evaluated. Finally the parameters $a = 15\,\mathrm{mm}$, $b = 22.5\,\mathrm{mm}$, $c = 2\,\mathrm{mm}$, $d = 35\,\mathrm{mm}$, $N = 9$, and $N_S = 11$ were chosen. The total length of the cylinders is 150 mm. A representation of the current paths without connections is given in Fig. 3.6a. In the construction double-sided layers were used and connected in series, see Fig. 3.6b. Thus the sensitivity per double-sided layer is twice the value obtained for the paths represented in Fig. 3.6a. The sensitivity was determined experimentally to 23 mT/m/A, in good agreement with the theoretical calculation. Per coil three double-sided layers were superimposed and connected in parallel. A serial connection would triple not only the sensitivity but also the dissipated power. The required current ratio between the screen coil and the primary coil was calculated to 0.39. For DC this is realized by connecting the primary coil in series to the screen coil which has a resistance in parallel. An alternative circuit and provision for the frequency dependence are explained in [6].

The conductive paths consist of copper layers with $70\,\mu$m thickness. For the width 0.6 mm was chosen. This results in a cross section of $0,08\,\mathrm{mm}^2$. For a given current I the dissipated power depends on the cross section A of the conductor

with length l according to $P = RI^2 = \rho_e(l/A)I^2$. The electrical resistivity (or specific electrical resistance) is denoted as ρ_e. Assuming adiabatic heating, the temperature increase ΔT of the conductor during time t also depends on the cross section according to $Pt = cm\Delta T = c\rho_m Al\Delta T$. The mass density is denoted as ρ_m and the specific heat capacity as c. A realistic assumption is that the maximum current $I = 60\,\mathrm{A}$ is switched on for at maximum $t = 10\,\mathrm{ms}$. The condition that the maximum temperature increase amounts to $\Delta T = 50\,\mathrm{K}$ leads to a minimum cross section of

$$A \approx I\sqrt{\frac{\rho_e t}{c\rho_m \Delta T}} = 0.065\,\mathrm{mm}^2\,.$$

After heating the conductor cools down by radiation, heat conduction, and convection. For the mass density of copper $8.9\,10^3\,\mathrm{kg\,m^{-3}}$ was used, for the specific resistance $0.017\,(1 + 0.0039(T - 293\,\mathrm{K}))\,\Omega\,\mathrm{mm}^2/\mathrm{m}$ with $T = 343\,\mathrm{K}$, and for the specific heat capacity $380\,\mathrm{J/(kg\,K)}$. The temperature dependence of these parameters was not included in the calculation of the temperature increase. According to this evaluation each double-sided layer has a sufficient cross section to carry the maximum current. However, the duty cycle (total gradient-pulse duration relative to the total experimental time) and the efficiency of cooling have to be considered. As in the presented setup three double-sided layers were connected in parallel and as no high duty cycles were used, a gradient cooling by air or liquid was not required.

The rf part of the probe head as well as the fabrication of the three double-sided layers was realized by Bruker, Karlsruhe. Construction of the mechanical part was carried out by E. Oliver, Karlsruhe.

Two additional radial gradients are needed to measure directly the flow profile in a slice or to perform 3D imaging experiments. The case of a radial gradient was also treated using the method developed by Bowtell and Mansfield [6]. In Fig. 3.7 a primary coil with five turns and a screen coil with seven turns for the same dimensions as for the flow gradient are shown. For a double-sided layer the sensitivity was calculated to 52 mT/m/A.

3.3.2 Magnet Setup and Probes

3.3.2.1 Inside-Out NMR

One of the early engineering applications of NMR which is still applied and further developed is well logging in oil industries. Mobile NMR devices are lowered in the borehole to inspect the properties of the surrounding wall. An axially symmetric inside-out NMR setup is realized by the opposing-dipole configuration of Jackson et al. [14]. The static field is pushed radially outward the narrow gap between

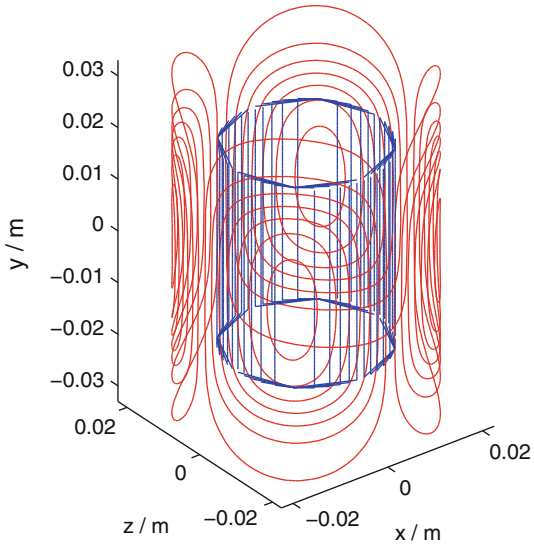

Fig. 3.7 Conductive paths for a gradient in radial direction. The gradient for the perpendicular radial gradient is obtained by a rotation of the paths by $\pi/2$ around the cylinder axis

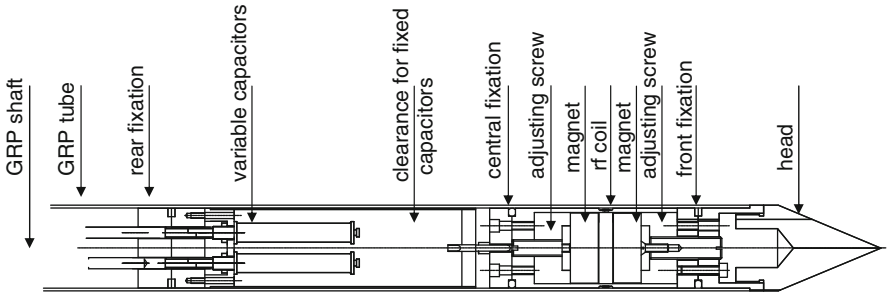

Fig. 3.8 Schematic representation of a miniaturized inside-out NMR device as suggested by Jackson et al. [14], e.g., for well logging. The two SmCo permanent-magnet discs have a diameter of 25 mm and magnetization in opposing directions. Between the magnets a coil with 28 mm diameter is located outside the rf shield and inside the protecting GRP tube. The sensitive volume for 8.4 MHz proton resonance frequency is a toroidal region close to the tube surface

magnetic disks mounted in a tube. A perpendicular rf field is generated by a single-turn coil or a solenoid with few turns which is located between the magnets. This results in a toroidal sensitive volume close to the tube surface where the resonance condition is fulfilled. Such a miniaturized NMR sensor was developed at the institute for mechanical process engineering and mechanics by D. Mertens, see Fig. 3.8. A possible application is presented in Sect. 4.3 on p. 115. An alternative configuration and further applications are described, e.g., in [5].

Single-sided NMR is a special case of inside-out NMR where a sensor producing a more or less thin and flat sensitive volume is placed on the surface of the object under investigation. In a basic configuration the static field can be generated by a

u-shaped magnet or a bar magnet [2, 3]. For the former the field lines leaving the magnet close parallel to the surface of the magnet. As perpendicular rf field the stray field of a solenoid located inside the u-shaped magnet can be used [3]. For a bar magnet, the field lines leaving the middle of the surface are perpendicular to the surface. A perpendicular rf field can be produced by a double-D coil [2]. For other configurations, see e.g., [17, 18]. Although generation of homogeneous static and rf fields in single-sided NMR is challenging, spectroscopic and spatial resolution have been achieved [22, 23].

3.3.2.2 Simple, Compact, and Efficient NMR Magnet

As already mentioned in Sect. 3.2 on p. 88 important progress has also been achieved in the development of permanent-magnet systems surrounding the sample as in conventional NMR, see e.g., [4,8,9,19,24]. Frequently the concept of yokeless dipolar Halbach arrays realized by identical bar magnets is employed. In the simplest case with four adjacent bar magnets a strong and relatively homogeneous field is obtained [24]. However, the magnet volume is four times the volume inside the magnet, resulting in a large volume and mass of magnet material. Increasing the distance between the magnets reduces the relative magnet volume and offers additional access to the sample [13]. However, field strength and homogeneity are drastically reduced. Optimized arrays with multiple magnets can yield good field strength and homogeneity. Due to the strong forces and inhomogeneity of the magnetic material, mechanical construction and precise positioning are challenging. A very simple Halbach array has been derived from the Halbach with four adjacent magnets by removal of the outside half of each magnet. In practice each rectangular magnet is realized by two identical bar magnets, see Fig. 3.9a. The relatively small NdFeB-52 magnets ($10 \times 10 \times 25$ mm) can still be handled with due care (protective glasses and gloves) without tools. They are placed between two sections of off-the-shelf square aluminum pipes in a plug-and-play fashion. A screw driver is needed only to fix the end plates (brass) to the aluminum bars in the corners. Distance pieces can be used to slightly shift the positions of the magnet. Two-dimensional finite-element calculations (free software: FEMM 4.2, David Meeker, Foster-Miller, Inc., Waltham, MA.) predict that for optimized small in-plane displacements the field homogeneity is even improved compared to the arrangement with four adjacent identical bar magnets. With 4/9th of the footprint and half of the magnet mass, 70% of the field strength is retained. For the first prototype two sets of 4×2 magnets are stacked in order to improve the axial homogeneity. Screws allow to move each magnet individually in axial direction. Accordingly 70 mm was chosen as length of the square pipes instead of the 50 mm required for contiguous sets. Four slots were cut in the middle of the outer pipe faces (and if applicable in the distance pieces) to enable a visual inspection of the magnet positions, see Fig. 3.9b.

The 16 magnets of the prototype have a total volume and mass of 40 ml and 300 g, respectively. The proton resonance frequency is 22 MHz, which is already relatively high for a yokeless permanent-magnet system. A six-turn solenoid of silver plated

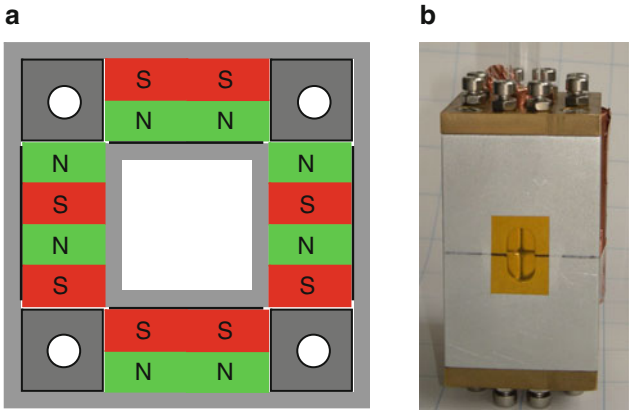

Fig. 3.9 Simple, compact, and efficient NMR magnet. Its design is derived from the dipolar Halbach array with four identical magnets by omission of the outer half of each magnet. In practice a "half magnet" is realized by two bar magnets (**a**). The eight magnets (NdFeB-52 10×10×25 mm) of a set can be mounted in a plug and play manner (with due care) between sections of off-the-shelf square aluminum pipe. The outer pipe has 45 mm outside edge length in the cross section, the inner pipe 20 mm. Slight in-plane shifts can be realized by distance pieces. The prototype shown in (**b**) has two sets in order to improve axial homogeneity and screws to adjust the axial magnet positions individually. Four magnets are seen through a slot in the pipe. In NMR experiments, contiguous sets were used resulting in a field of 0.52 T. The coil is wound on a 10 mm NMR tube, samples with 9 mm diameter can be studied

AWG 18 copper wire with PTFE insulation is wound on a 10-mm NMR tube. Alternatively, a circular pipe could be used as coil carrier. The connection to the impedance matching network outside the magnet is realized by a short parallel-wire transmission line. Without damping a dead time of 15 μs is required.

A single-shot spin echo for an aqueous Gadovist solution (Schering, Berlin), 1 mmol/l in a 7.5-mm NMR tube is shown in 3.10a. The pulse lengths were 3 and 6 μs, respectively. For the phase-corrected real-part signal a SNR of 228 is obtained (286 if the magnitude data is evaluated). A minispec instrument was used.

A CPMG measurement for the same sample is shown in Fig. 3.10b. The echo time is 246 μs. Individual echoes were sampled with 1 μs DW and 7 points at the echo top are averaged. With eight scans, the intensity of the first point divided by the standard deviation of fit residuals (SNR) amounts to 750. These results were obtained without distance between the two sets of 4 × 2 magnets. A significant improvement of the results could not be observed for shifts of the magnets in axial direction.

The magnet is suited for online relaxometry measurements, provided a setup of sufficient length for complete polarization is assembled. For the purpose of prepolarization individual elements with one set and the end plates formed as thin flanges were built. Pipes with up to 10 elements are used. Given the simple construction and low cost, the setup could also be used for applications requiring disposable magnets. The magnet can also be used for educational purposes. Students in a practical course could even assemble the magnet before executing

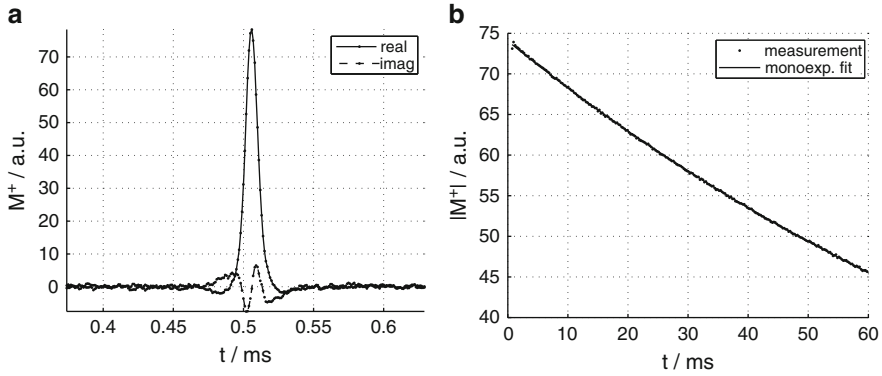

Fig. 3.10 NMR measurements executed in the magnet shown in Fig. 3.9. (**a**) Single-scan spin echo of an aqueous solution in a 7.5-mm NMR tube. (**b**) CPMG of the same sample with eight scans. Noise or deviations for the monoexponential fit are hardly discernible on the scale of the plot

and analyzing NMR relaxometry experiments. In principle the design can be scaled up to accommodate larger samples and coils for spatial resolution and shimming. However, more sophisticated designs are probably preferable for such applications.

3.3.2.3 Probe-Impedance Matching

Several probes were constructed for various applications at high field and low field. As the voltage induced by the precessing nuclear magnetization is very small, usually electrical resonators with suitable bandwidth are used as probes. Probes can be designed to create a homogeneous rf field, like a Helmholtz coil, or a heterogeneous field, as a surface coil. Depending on the design, the field is in direction of the symmetry axis, as for solenoids, or transverse to the symmetry axis, as for birdcage resonators. These types of probes and the issues of, e.g., electrical balancing, quadrature driving, or multiple frequency tuning are treated in [21]. At low NMR frequencies, the probe can usually be treated as lumped circuit. For permanent-magnet systems, frequently solenoids are used as receiving elements. An example of solenoid probe is presented in [10]. In superconducting magnets, birdcage resonators are widely used, see Fig. 3.2. An analysis of these electrical resonators can be found in [15]. In the following, the task of probe-impedance matching will be treated in an intuitive representation used in electrical engineering.

The spectrometer operates with a system impedance of $Z_0 = 50\,\Omega$. In order to avoid reflection, the probe is matched to the spectrometer by transformation of the impedance Z_c of the receiving element to the value Z_0 at the NMR frequency. A solenoid coil of length b_c with radius a_c and n_c turns mainly presents an inductive reactance $i\omega L_c$ that is proportional to frequency. If length and radius are inserted in centimeters, the inductance L_c in microhenry can be approximated by

$$L_c \approx a_c^2 n_c^2/(23a_c + 25b_c) \,, \tag{3.2}$$

see [10]. However, the presence of a rf shield can considerably reduce the inductance of the receiving element. If available, a network analyzer should be used to determine the impedance of the receiving element mounted inside the grounded rf shield.[1] The resistance of the wire R_c is considered as a small contribution in series. A frequency dependence of R_c follows from the frequency dependence of the skin depth:

$$\delta_s = \sqrt{\frac{2}{\sigma_c \mu_0 \mu_r \omega}} \,. \tag{3.3}$$

Instead of the cross-sectional area of the wire with radius r_c only the area of the outer ring of width δ_s is inserted in the calculation of the wire resistance. Estimating the wire length from the solenoid radius and the number of turns finally yields

$$R_c = \frac{2\pi a_c n_c}{\pi(r_c^2 - (r_c - \delta_s)^2))\sigma_c} \,. \tag{3.4}$$

If the skin depth is small compared to the wire radius its quadratic contribution can be neglected in (3.4). Insertion of (3.3) then leads to (2.141). As the coil impedance $Z_c = R_c + i\omega L_c$ has a resistance as well as a reactance it can be transformed to any impedance by a suitable parallel and series connection with two reactances. In the design of NMR probes frequently two fixed capacitors and two variable capacitors are used. A common circuit is shown in Fig. 3.11. In electrical engineering the transformation is intuitively represented by a resistance diagram in the impedance plane. The resistance is represented on the positive horizontal axis and the reactance on the vertical axis. Series connection of an inductive reactance moves the impedance vertically upward, with a capacitive reactance vertically downward. Parallel connection of an inductive reactance moves the impedance on a circle in positive sense, i.e., counterclockwise, of a capacitive reactance in negative sense, i.e., clockwise. This circle with constant conductance has its origin on the resistance axis and passes through the origin. The position of the origin and the radius have the value $1/(2G_c)$ with the conductance G_c, defined by $Y_c = 1/Z_c = G_c + iB_c$.

As example matching of a solenoid for 10 MHz with the circuit of Fig. 3.11 is represented in Fig. 3.12. The solenoid has a length of $b_c = 2\,\text{cm}$ and $n_c = 10$ turns with a radius of $a_c = 0.6\,\text{cm}$. According to (3.2) the inductance amounts to $L_c = 0.52\,\mu\text{H}$. For a brass wire with a radius $r_c = 0.43\,\text{mm}$ and a conductivity of $\sigma_c = 14.3 \times 10^6\,\Omega^{-1}\text{m}^{-1}$ (3.3) and (3.4) result in a skin depth of $\delta_s = 0.042\,\text{mm}$

[1] A network analyzer capable of measuring the S_{11} parameter including phase is sufficient. The impedance of the device under test is conveniently represented in a Smith chart. A cable must be used to connect the analyzer to the receiving element. Its influence on the measured impedance can be corrected automatically if the analyzer has an "extended port" option.

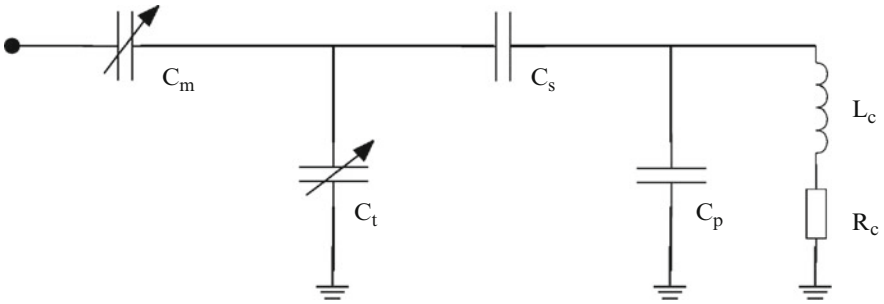

Fig. 3.11 Tank circuit and transformation circuit for the matching of the coil impedance $Z_c = R_c + i\omega L_c$ to the system impedance $Z_0 = 50\,\Omega$

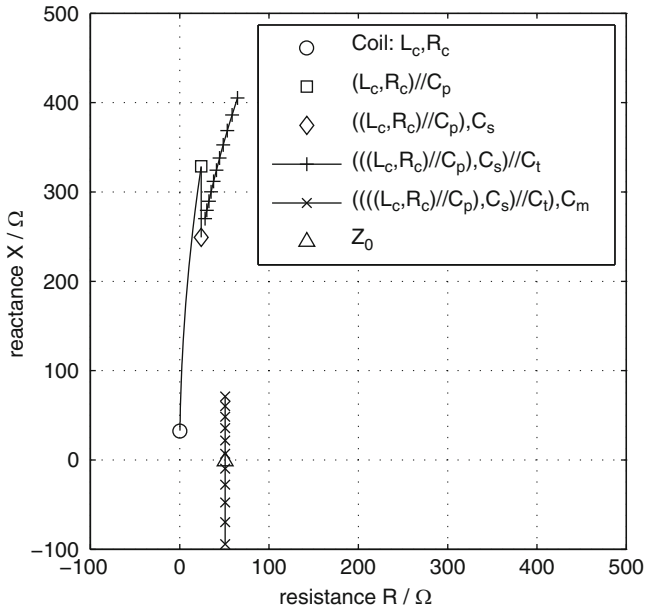

Fig. 3.12 Transformation of the probe impedance for the circuit shown in Fig. 3.11 as resistance diagram in the impedance plane

and a resistance of $R_c = 0.24\,\Omega$. As the reactance of the coil impedance

$$Z_c = 0.24\,\Omega + i\,32.6\,\Omega$$

is much larger than the resistance a large radius of 2.3 kΩ is obtained for the circle with constant G_c. A first increase of the resistance toward Z_0 is achieved by parallel connection of the fixed capacitor with capacitance C_p and reactance $1/(i\omega C_p)$. The resulting additional increase of reactance is partially compensated

Table 3.1 Capacitances and reactances of the capacitors in the transformation circuit represented in Figs. 3.11 and 3.12

Capacitor	C_p	C_s	C_t	C_m
Capacitance / pF	440	200	20	44
Reactance / Ω	−36	−80	−796	−362

by series connection of a fixed capacitor with capacitance C_s. With the values given in Table 3.1 the resulting circle with constant (partly transformed) conductance has a smaller radius of 1.3 kΩ. Moving on this circle by parallel connection of a variable capacitor with conductance C_t the resistance can be adjusted to 50 Ω. The resulting reactance can be finally compensated by a variable capacitor with conductance C_m. Non-magnetic variable capacitors with small size and high quality factor are available for different ranges of capacitance. A typical range is 1.5–55 pF (NMAT55HVE, Voltronics, Denville, NJ, USA). In Fig. 3.12 the discrete values represented for C_t range from 5 to 25 pF and for C_m from 35 bis 55 pF in steps of 2 pF, respectively.

Already for one solenoid and four capacitors the analytical calculation for the impedance transformation is quite complex. The representation as resistance diagram makes it comprehensible and easier to plan. It becomes clear how the impedance changes if, e.g., the coil impedance gets closer to the reactance axis if a different wire material is used (aluminum: $\sigma_c = 36.0 \times 10^6\,\Omega^{-1}\mathrm{m}^{-1}$, copper: $\sigma_c = 56.2 \times 10^6\,\Omega^{-1}\mathrm{m}^{-1}$, silver: $\sigma_c = 62.5 \times 10^6\,\Omega^{-1}\mathrm{m}^{-1}$). The analytical calculation of the transformed impedance Z can be used to calculate the frequency dependence of the coefficient $|(Z - Z_0)/(Z + Z_0)|^2$ that determines the ratio of the reflected and incident power. Important characteristics are the magnetic field per unit current and the spatial distribution of the field. They can be estimated by Biot–Savart calculations. Further relevant parameters are the dead time and the degree of probe detuning due to varying sample properties. Besides capacitive coupling of the receiving element, inductive coupling is used, see e.g., [16].

Finally an interesting possibility is mentioned. The homogeneous polarizing field and imaging capabilities of a high-field tomographic NMR instrument can be used to develop low-field probes. Thus a magnet for 200 MHz proton frequency can be used to test a probe at 30.7 MHz using a sample of heavy water, as deuterium has a correspondingly smaller gyromagnetic ratio, see (2.8). Note that not only the precession but also the nutation frequency is reduced by the same factor.

3.4 Flow Loop

Online measurements are estimated to be an important future application of low-field NMR, e.g., in the context of process analytics. For the NMR-based capillary rheometer presented in Sect. 4.4 on p. 115ff the low-field instrument shown in Fig. 3.4 was equipped with the flow loop represented schematically in Fig. 3.13

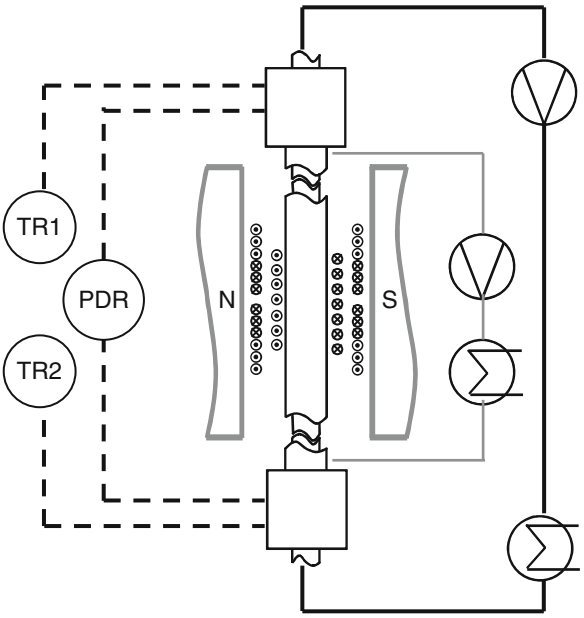

Fig. 3.13 Schematic representation of the flow loop for NMR-based capillary rheometry. The sample is pumped through a heat exchanger into the inner capillary. A temperature-control liquid is pumped through a coaxial outer tube. The tubes are surrounded by the rf coil, the gradient system, and the permanent magnet. Above and below the magnet system the temperatures (TR1/TR2) and the pressure difference (PDR) are measured and recorded

[11, 12, 20]. In order to use the highest filling factor the outer diameter of the flow loop should just fit inside the receiving element and the ratio of the outer and inner diameter should be as close to one as possible. Thus connection of tubes by a flange or threaded ends is disadvantageous. Instead tubes are fixed in turned parts with o-ring sealings at the top and bottom of the magnet system. Two coaxial tubes are used. The inner has an outer diameter of 7 mm. Its inner diameter is either 4.7 mm for a PMMA tube or 4 mm for a glass capillary with 1.5 mm wall thickness. The outer PVC tube has an inner diameter of 9 mm and 0.5 mm wall thickness. In the annular gap a liquid is circulated for temperature control. In this application initially only the velocity measured by an echo experiment was evaluated. In this case water with sufficient relaxation agent (e.g., Gadovist, Schering, Berlin, Germany) can be used so that the water signal does not contribute to the echo. In extension the NMR relaxation behavior of the sample was also measured, see Sect. 2.1.9, p. 41ff and Sect. 4.5, p. 125ff. In order to avoid superposition of signal from the temperature control liquid a perfluorinated liquid was used (Galden, Solvay Solexis, Bruxelles). The turned parts also contain the connections for the temperature-control liquid and the access points for temperature and pressure measurement. A version for elevated pressure and temperature has an outer tube with 18 mm outer and 14.4 mm inner diameter and an inner tube with 12 mm outer and 7.6 mm inner diameter.

For rheological applications or online measurements of NMR relaxation a constant and low-pulsation flow of the sample has to be realized. Further requests concerning the pump can be that the sample viscosity is elevated, that particles are suspended, or that the sample is altered by high shear rates. As suitable device a rotor-stator pump with special geometry was identified (ViscoTec, Töging a. Inn). For viscosities up to a few Pa s a syringe pump (KD Scientific, Holliston, MA, USA) with disposable syringes (100 ml) can be used. The pressure and temperature measurements should have only negligible influence on the flow field. Miniaturized pressure transducers with temperature compensation for the required pressure range are available with a diameter of 3 mm (FGP sensors, Les Clayes-sous-Bois, France). Alternatively small radial boreholes (2 mm diameter) in the turned parts can allow the sample to enter into horizontal PTFE tubings that are connected further away with a pressure-difference sensor. While this method is simpler to realize, it can yield erroneous results if the sample exhibits a yield stress.

References

1. Blümich B (2000) NMR imaging of materials. Clarendon Press, Oxford
2. Blümich B, Anferov V, Anferova S, Klein M, Fechete R, Adams M, Casanova F (2002) Simple NMR-MOUSE with a bar magnet. Concept Magnetic Res 15(4):255–261. DOI 10.1002/cmr.10046
3. Blümich B, Blümler P, Eidmann G, Guthausen A, Haken R, Schmitz U, Saito K, Zimmer G (1998) The NMR-mouse: Construction, excitation, and applications. Magn Reson Imaging 16(5–6):479–484
4. Blümich B, Casanova F, Appelt S (2009) NMR at low magnetic fields. Chem Phys Lett 477(4–6):231–240. DOI 10.1016/j.cplett.2009.06.096
5. Blümich B, Mauler J, Haber A, Perlo J, Danieli E, Casanova F (2009) Mobile NMR for geophysical analysis and materials testing. Pet Sci 6(1):1–7. DOI 10.1007/s12182-009-0001-4
6. Bowtell R, Mansfield P (1990) Screened coil designs for NMR imaging in magnets with transverse field geometry. Meas Sci Technol 1(5):431–439
7. Callaghan PT (1991) Principles of nuclear magnetic resonance microscopy. Clarendon Press, Oxford
8. Danieli E, Mauler J, Perlo J, Blümich B, Casanova F (2009) Mobile sensor for high resolution NMR spectroscopy and imaging. J Magn Reson 198(1):80–87. DOI 10.1016/j.jmr.2009.01.022
9. Danieli E, Perlo J, Bluemich B, Casanova F (2010) Small magnets for portable NMR spectrometers. Angew Chem Int Edit 49(24):4133–4135. DOI 10.1002/anie.201000221
10. Fukushima E, Roeder SBW (1981) Experimental pulse NMR: A nuts and bolts approach. Addison-Wesley, Reading, MA
11. Hardy EH, Mertens D, Hochstein B, Nirschl H (2009) Compact NMR-based capillary rheometer. In: Fischer P, Pollard M, Windhab EJ (eds) Proceedings of the 5th ISFRS, pp 94–97. http://www.isfrs.ethz.ch/proc/2009_proc. 5th International symposium on food rheology and structure, ETH Zrich, Zrich, 15–18 June 2009
12. Hardy EH, Mertens D, Hochstein B, Nirschl H (2009) Kompaktes, NMR-gesttztes Kapillar-rheometer. Chem Ing Tech 81(8):1100–1101
13. Hills B, Wright K, Gillies D (2005) A low-field, low-cost Halbach magnet array for open-access NMR. J Magn Reson 175(2):336–339. DOI 10.1016/j.jmr.2005.04.015

14. Jackson JA, Burnett LJ, Harmon JF (1980) Remote (inside-out) NMR.3. Detection of nuclear magnetic-resonance in a remotely produced region of homogeneous magnetic-field. J Magn Reson 41(3):411–421
15. Jin J (1999) Electromagnetic analysis and design in magnetic resonance imaging. CRC Press, Boca Raton
16. Kuhns PL, Lizak MJ, Lee SH, Conradi MS (1988) Inductive coupling and tuning in NMR probes – Applications. J Magn Reson 78(1):69–76
17. Manz B, Coy A, Dykstra R, Eccles CD, Hunter MW, Parkinson BJ, Callaghan PT (2006) A mobile one-sided NMR sensor with a homogeneous magnetic field: The NMR-MOLE. J Magn Reson 183(1):25–31. DOI 10.1016/j.jmr.2006.07.017
18. McDonald PJ, Aptaker PS, Mitchell J, Mulheron M (2007) A unilateral NMR magnet for sub-structure analysis in the built environment: The surface GARField. J Magn Reson 185(1):1–11. DOI 10.1016/j.jmr.2006.11.001
19. McDowell A, Fukushima E (2008) Ultracompact NMR: H-1 spectroscopy in a subkilogram magnet. Appl Magn Reson 35(1):185–195. DOI 10.1007/s00723-008-0151-3
20. Mertens D, Hardy EH, Hochstein B, Guthausen G (2009) A low-field-NMR capillary rheometer. In: Guojonsdottir M, Belton P, Webb G (eds) Magnetic resonance in food science: Challenges in a changing world, pp 81–88. 9th International conference on applications of magnetic resonance in food science, Reykjavik, Iceland, 15–17 September 2008
21. Mispelter J, Lupu M, Briguet A (2006) NMR probeheads for biophysical and biomedical experiments : Theoretical principles and practical guidelines. Imperial College Press, London
22. Perlo J, Casanova F, Blümich B (2004) 3D imaging with a single-sided sensor: An open tomograph. J Magn Reson 166(2):228–235. DOI 10.1016/j.jmr.2003.10.018
23. Perlo J, Casanova F, Blümich B (2007) Ex situ NMR in highly homogeneous fields: H-1 spectroscopy. Science 315(5815):1110–1112. DOI 10.1126/science.1135499
24. Raich H, Blumler P (2004) Design and construction of a dipolar Halbach array with a homogeneous field from identical bar magnets: NMR mandhalas. Concept Magn Res B 23B(1):16–25. DOI 10.1002/cmr.b.20018

Chapter 4
Applications

4.1 Gas Filtration

4.1.1 Introduction

Filtration is a wide spread method for the removal of particles from gas streams. For low particle concentrations deep-bed filters consisting of natural or synthetic fibers with high porosity are used [90]. Relevant parameters are the particle caption efficiency and the pressure drop. As a consequence of particle deposition these parameters change during filtration until the filter is clogged and has to be replaced. An accurate prediction of the filtration process during filter service life is desired in order to optimize filters and their application. It is observed that theoretical calculations with a homogeneous porosity do not accurately reproduce experimental results. Some filters are already designed with a porosity gradient in direction of mean flow. Even for a homogeneous initial porosity, particle deposition can lead to a markedly heterogeneous porosity. A cell-based filter model was developed in order to improve the theoretical description of the filtration process [91]. The challenge for an experimental method is the non-invasive determination of initial fiber distribution as well as the in line monitoring of particle deposition during filtration. In the following it is summarized how this can be achieved using MRI [37, 45, 63, 64].

4.1.2 Results and Discussion

4.1.2.1 Filter Structure

The cell-based filter model requires the average packing density per cell as input. Attempts to measure the packing density directly with sufficient resolution and SNR were not successful. Instead the inverse filter structure was imaged. The filter was immersed in a suitable liquid, here water with relaxation agent (Gadovist, Schering,

E.H. Hardy, *NMR Methods for the Investigation of Structure and Transport*,
DOI 10.1007/978-3-642-21628-2_4, © Springer-Verlag Berlin Heidelberg 2012

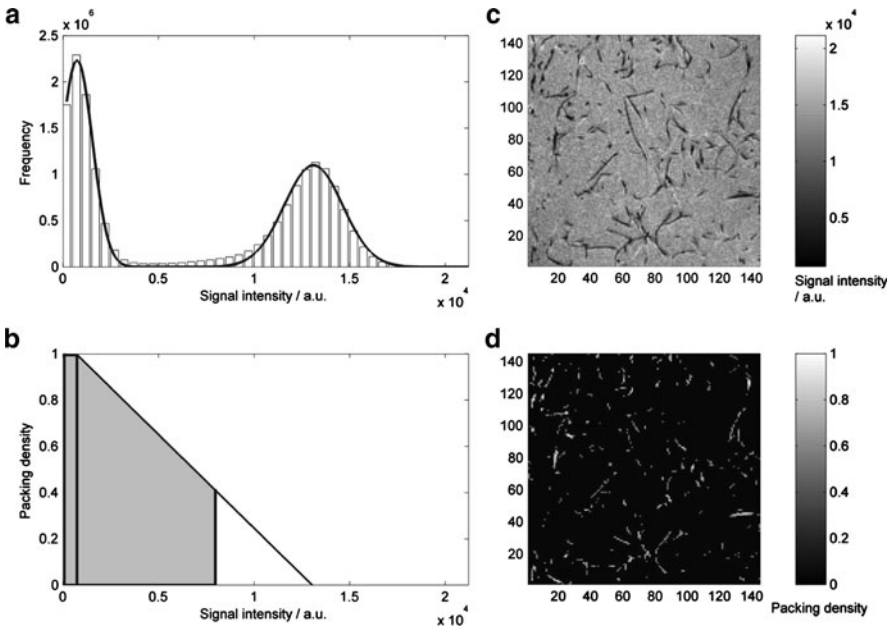

Fig. 4.1 Initial structure of a deep-bed filter. (**a**) Intensity-distribution function. (**b**) Procedure for the assignment of packing density to intensity. (**c**) Measured intensities for a cut-out of a slice through the 3D data set. (**d**) Calculated packing density in the same cut-out. Data were acquired using a 3D RARE, see Fig. 2.7. An echo time of 4.6 ms was used. The RARE factor was $r = 8$, the repetition time 225 ms, and the number of averages $N_A = 8$. This results in an experimental time of 8 h. [45] © Wiley-VCH Verlag GmbH & Co. KGaA. Reproduced with permission

Berlin, Germany). A vacuum was applied to remove gas bubbles. Addition of a surfactant can help to avoid gas bubbles.

The investigated sample should be large compared to the length scales of the structure to represent the filter and minimize edge effects. A filter holder with 12 mm inner diameter was constructed and the FOV was set to $(15\,\text{mm})^3$. With 256^3 grid points the isotropic resolution amounts to 59 μm. The fiber diameter is of the same order of magnitude, even for the investigated rather coarse filter. Consequently the situation is different from that described in Sect. 2.3.1, where a disc diameter is sampled by several grid points. Therefore the signal-intensity distribution shown in Fig. 4.1a is also characterized by partially filled voxels, not only by noise and transformation artifacts. Instead of a single threshold, a linear relation between signal intensity and packing density was established. First a bimodal distribution is fitted to the signal-intensity distribution, here a sum of two normal distributions. The intensity of the peak at lower intensity is denoted as P_1, at high signal intensity as P_2. Packing density 1 is assigned to grid points with intensity P_1 or lower. The packing density assigned to grid points with higher intensity decreases linearly with slope $-1/(P_2 - P_1)$. However, above a threshold T the packing density is set to zero:

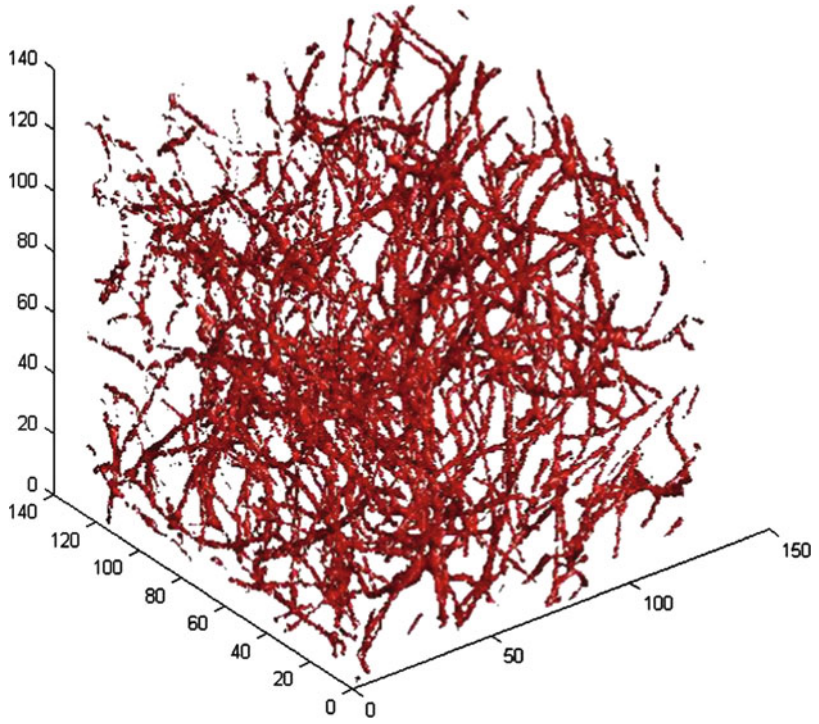

Fig. 4.2 Surface reconstruction (cut-out) of a deep-bed filter imaged at a high isotropic resolution of 29 μm

$$\alpha_{\mathrm{MRI},nmo} = \begin{cases} 1 & : \quad \tilde{\rho}_{nmo} \leq P_1 \\ (P_2 - \tilde{\rho}_{nmo})/(P_2 - P_1) & : \quad P_1 < \tilde{\rho}_{nmo} < T \\ 0 & : \quad \tilde{\rho}_{nmo} \geq T \end{cases} . \tag{4.1}$$

The threshold is chosen such that the averaged packing density equals the gravimetric packing density:

$$\overline{\alpha_{\mathrm{MRI}}} = \overline{\alpha_{\mathrm{grav}}}. \tag{4.2}$$

The procedure and the result for one slice is illustrated in Fig. 4.1.

At cut-out of a data set with $256 \times 512 \times 512$ grid points and 29 μm isotropic resolution is shown in Fig. 4.2. Attaining a usable SNR at this high resolution requires an accurate optimization of experimental parameters.

4.1.2.2 Particle Deposition

After characterization of the filter structure the filter is dried in the tomograph and the deposition of particles during filtration is monitored in situ. Using oil-filled

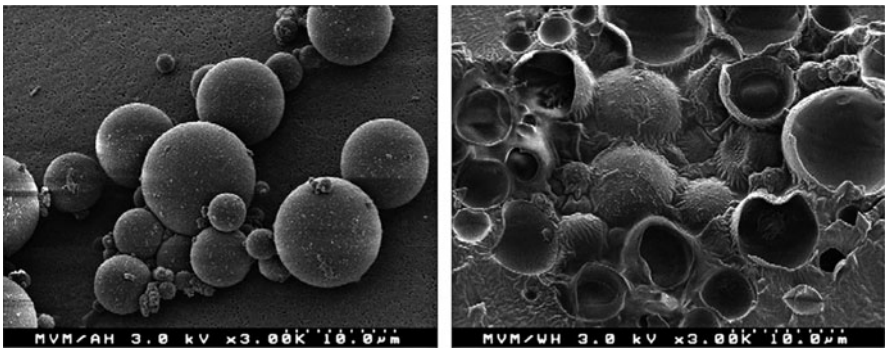

Fig. 4.3 Oil-filled melamine microcapsules imaged with a scanning electron microscope. In the right image some capsules are sliced open. Reprinted from [36] © 2007, with permission from Elsevier

melamine microcapsules (Schubert International, Utting, Germany), see Fig. 4.3, the deposited particles can be imaged directly. The mass related median diameter of the used particles amounts to 6 μm. Their size distribution is similar to that of a common test dust (ISO-12103-1, A1, ultra fine).

Particle deposition was imaged with 64^3 grid points, corresponding to an isotropic resolution of 234 μm. During the MRI experiment the filtration process was interrupted. Results for 2 h and 8.5 h are shown on the left and right of Fig. 4.4, respectively. Already after 2 h of filtration a heterogeneous particle deposition is observed. The deposited mass increases behind the leading edge and reaches a maximum close to the edge. It subsequently decreases smoothly toward the end of the filter. Particle deposition reduces porosity which increases gas-flow velocity. This promotes inertia deposition. In addition, the particle concentration within the filter decreases along flow direction as particles are deposited. However, the slice perpendicular to the mean flow direction after 8.5 h also reveals a considerable heterogeneity within this slice. At this time, the filter is largely clogged.

In the case of particle-deposition profiles as shown in Fig. 4.4 the improved quantifiability using the phase-correction method described in Sect. 2.3.5 [37] is obvious.

4.1.3 Conclusion

The presented work represents the first 3D determination of fiber packing density in a filter with subsequent 3D in situ monitoring of particle deposition during filtration. Distinct heterogeneities are observed for the deposited mass, in direction of mean flow as well as in perpendicular slices. This successful experimental investigation of filtration kinetics can support the development of improved filtration models.

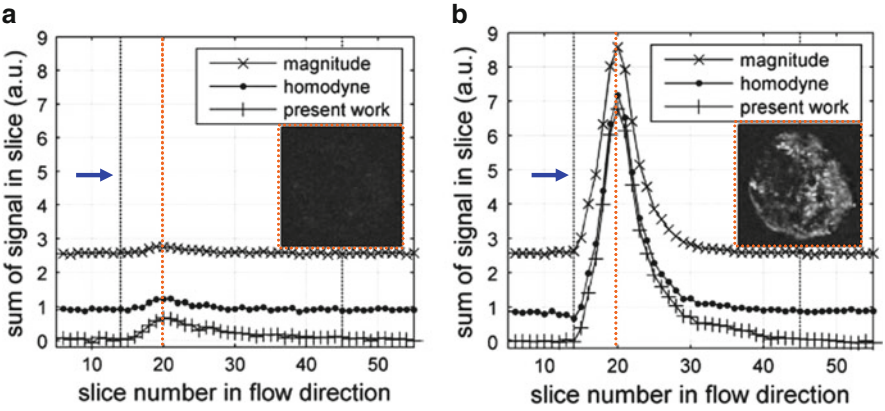

Fig. 4.4 MRI images of the in situ deposition of dust particles in a filter. *Left*: after 2 h of filtration. *Right*: after 8.5 h of filtration. The large images show the deposition profiles along the direction of mean flow (arrow). The embedded small images show the deposited mass in slice 20 with maximum deposition. Slice number 14 is the leading edge of the filter that ends in slice 45. Obviously the phase-correction method presented in Sect. 2.3.5 ("present work," [37]) improves the quantifiability compared to the usual magnitude reconstruction. In addition, results obtained with an alternative phase-correction method are shown ("homodyne," [76]). A 3D RARE was employed, see Fig. 2.7, with 3.2 ms echo time, a RARE factor of $r = 4$, a repetition time of 1.6 ms and $N_A = 8$ averages. This results in an experimental time of 3.6 h. Reprinted from [37] © 2009, with permission from Elsevier

Examinations with smaller fiber diameters and lower average packing density are expected to be challenging. Here high-resolution X-ray tomography (μ-CT) is an alternative. The oil-filled melamine microcapsules can be used also for other types for MRI experiments, see, e.g., Sect. 4.3.

4.2 Solid–Liquid Separation

4.2.1 Introduction

Removal of particles from a suspension is a common operation, e.g., in the production of pigments or ceramics, in the processing of food, or in the treatment of waste water. Possible solid–liquid separation mechanisms are filtration and sedimentation in the gravitational or centrifugal field. In order to achieve short processing times models describing separation as a function of product properties and process parameters are in demand. Detailed experimental investigations by means of MRI can guide modeling and validate predictions of models. Volume images with high resolution revealed a fine ramified network of drainage channels for a sediment produced in a bowl centrifuge. Modeling in such detail is challenging.

Primarily a 1D porosity gradient is observed and included in models. Already 20 years ago NMR measurements have been used in this context [49]. In the following the application of fast profile measurements for the validation of a filtration model for sub micron particles is presented [23]. Also mentioned are investigations on thin-layer filtration [42] and on separation in a tubular centrifuge [95].

4.2.2 Results and Discussion

4.2.2.1 Surface Filtration

The setup for in situ MRI investigation of filtration of a suspension is shown in Fig. 4.5. In the presented measurements alumina particles with a mean particle diameter of 0.6 μm were used (CT 3000 SG, Alcoa, now Almatis GmbH, Ludwigshafen, Germany). The microporous membrane filter had a pore diameter of 0.2 μm (Pall Corporation, Port Washington, NY, USA). As filtration processes can be quite fast, depending on experimental parameters, a high temporal resolution was desired. A SE sequence with frequency encoding without slice selection and the shortest possible echo time was implemented. At each single shot measurement of less than three milliseconds the signal profile was acquired with a spatial resolution of 230 μm. Distortions due, e.g., to the inhomogeneity of the B_1 field were accounted for by normalization to a measurement with the filter cell filled with water. As the signal for the suspension and filter cake is weighted by transverse relaxation, the relation between the signal and porosity was established by preliminary measurements on samples with known homogeneous porosity.

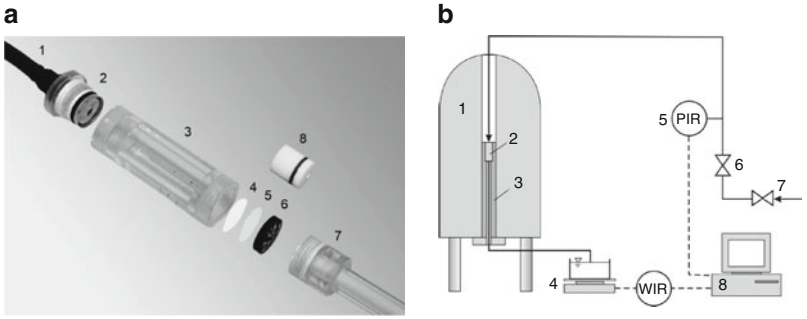

Fig. 4.5 Setup for in situ filtration. (**a**) Filter cell with 25 mm outer diameter. (1) inlet for pressurized gas, (2) screw cap, (3) PMMA cylinder with suspension, (4) filter medium, (5) supporting mesh, (6) drainage system (PVC), (7) drain outlet, (8) piston (PTFE, optional). (**b**) Overall setup. (1) NMR tomograph, (2) filter cell, (3) probe head, (4) balance, (5) manometer, (6) pressure valve, (7) inlet for pressurized gas, (8) data acquisition. [23]

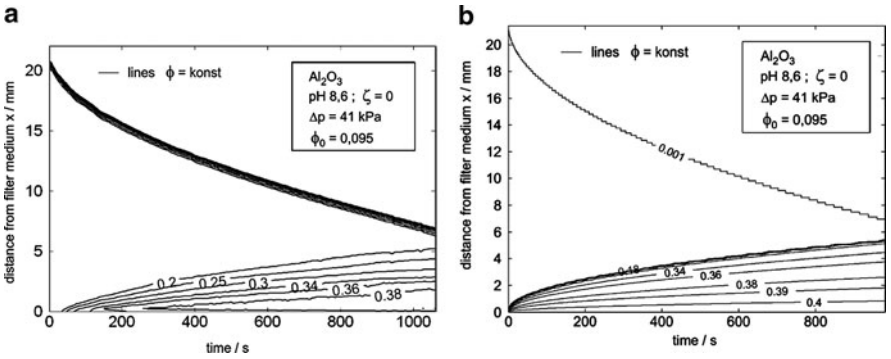

Fig. 4.6 Measurement and simulation of filtration. (**a**) Measurement of the solid volume fraction as a function of distance from the filter medium and time. (**b**) Simulation using the model of Bürger et al. [12]. A good agreement between experiment and simulation is observed. [23] © Wiley-VCH Verlag GmbH & Co. KGaA. Reproduced with permission

In Fig. 4.6a an example of measured solid volume fraction as a function of distance from the filter medium and time is represented as isolines. The initial height of the suspension with a solid volume fraction of 0.095 is about 20 mm. As the signal is projected on the symmetry axis of the filter cell which is in direction of gravity, the meniscus of the suspension leads to a signal gradient at the interface. The decreasing signal at the meniscus is transformed by the calibration into an increase in solid volume fraction. While this artifact is not problematic, the method requires that the filter cake is horizontal on the length scale of the spatial resolution. This can be verified by volume images if filtration is stopped. The filter cake builds up during filtration and the height of the suspension decreases. As can be seen in the presented example the filter cake can exhibit a strong porosity gradient. For longer filtration times, the suspension level can reach the filter cake which can be consolidated to a constant porosity. The results of a simulation based on the model of Bürger et al. is shown in Fig. 4.6b [12]. For the investigated systems, a close agreement of experiment and simulation was observed. In the presented example the pH was adjusted to 8.6 by addition of NaOH. This corresponds to zeta potential 0, measured using an Acoustosizer II (Colloidal Dynamics, North Attleboro, MA, USA). At the isoelectric point attractive forces between the particles prevail. Particles aggregate and form a porous and permeable network. Experiments at a pH of 4, realized by addition of HCl, occur at $\zeta = 62$ mV. In spite of a higher pressure difference (PDR) of 111 kPa the filter cake builds up markedly slower. Repulsive interactions prevail and lead to a more regular and dense filter cake buildup.

In [42] filtration of particles with smaller size was investigated. Alumina particles with volume-related mean diameter of 100 nm were used (Disperal 20, Sasol, Hamburg, Germany), in which an increase of the measured particle diameter with pH was observed. As the resistance during filtration is high, only thin filter cakes with 0.5–3 mm thickness were generated. In these systems determination of the

porosity from the signal intensity was not accurate. Instead a strong correlation of porosity and transverse relaxation time T_2 was observed and used for an accurate determination of porosity. In order to achieve a high spatial resolution of 65 μm, slice images were acquired with the sequence shown in Fig. 2.7. In the inner part of the filter, the signal of pixels with equal distance to the filter medium was averaged. Acquisition of several signal averages was performed to increase SNR, resulting in an experimental time of 40 min. Accordingly, the filtration process had to be interrupted during the MRI measurement. Experiments under varying conditions generate a consistent image of the course of filtration in these systems.

4.2.2.2 Centrifugation

Investigations of solid–liquid separation in a tubular centrifuge by means of MRI are presented in [95]. The profile of sediment build-up during centrifugation was determined. As the steel tube of the centrifuge was not appropriate for MRI measurements, a GRP tube was fitted into the steel tube. It could be removed after centrifuging and inserted into the tomograph. In order to mark the surface of the sediment at different times of centrifugation, tracers were injected into the suspension at the desired times. The sediment consists of titania particles (Rutil Sachtleben R 611, Sachtleben Chemie GmbH, Duisburg, Germany) with an average particle diameter of 0.61 μm. Carbon black was added as tracer. Due to a T_2 contrast, see Sect. 2.1.6, the sediment with carbon black produces a stronger signal than the sediment with titan dioxide. As the sediment in the tube was longer than the height of the maximum FOV, the GRP tube was moved stepwise through the tomograph and the overall view was assembled from five slice images with 256×200 pixels. The isotropic spatial resolution was 200 μm and the experimental time per slice 25 min. In another experiment the centrifuging of cells was investigated with carbon black as tracer, too. Again the signal from the sediment with tracer was stronger, in this case due to a T_1 contrast.

4.2.3 Conclusion

The presented results demonstrate that MRI allows a nondestructive and quantitative investigation of solid–liquid separation with spatial and temporal resolution. In the case of in situ filtration the porosity was either derived from signal intensity or transverse relaxation time. In the case of centrifuging tracers were employed for a subsequent MRI experiment. Such measurement can assist the modeling and optimization of solid–liquid separation processes. A study of the separation of small amounts of particles using paramagnetic iron(III) oxide is presented in [20].

4.3 Powder Mixing

4.3.1 Introduction

As reversal of separation with examples treated in Sects. 4.1 and 4.2, mixing is a further unit operation in mechanical process engineering [93]. Typically, a uniform mixture is to be attained quickly and with low energy input. For example pharmaceutical tablets formed from a mixture should all contain the same amount of active agent. In this case one tablet is the natural sample size. The variance of the amount of the considered component from sample to sample is a common measure for the uniformity of the mixture. Extreme cases are total segregation and the ideal random mixture. Consider N samples containing the same number of particles. Particles are either of type A or type B. The composition can be defined by the number fraction p of particles A. Let $\langle p \rangle$ be the average fraction of particles A over all samples. In case of total segregation $\langle p \rangle N$ samples have composition 1 and $(1 - \langle p \rangle)N$ samples have composition 0. Calculation of the variance of the composition in this case yields

$$\begin{aligned} s_p^2 &= \left[\langle p \rangle N(1 - \langle p \rangle)^2 + (1 - \langle p \rangle)N(0 - \langle p \rangle)^2\right]/N \\ &= \langle p \rangle \left(1 - \langle p \rangle\right). \end{aligned} \tag{4.3}$$

In the calculation of the variance N was used as denominator and not $N - 1$ as the average composition $\langle p \rangle$ is known. For the ideal random mixture it is assumed that samples consist of M particles that are drawn at random. In the urn model the number of particles A in a sample exhibits a binomial distribution[1] with variance $M \langle p \rangle (1 - \langle p \rangle)$. This results for the variance of the number-fraction distribution in

$$s_p^2 = \left[\langle p \rangle (1 - \langle p \rangle)\right]/M. \tag{4.4}$$

Thus the variance of the ideal random mixture (4.4) equals the variance in the case of total segregation (4.3) divided by the number of particles in the sample. Both variances are symmetric with respect to the average composition $\langle p \rangle = 0.5$. More complex expressions are obtained if, e.g., mass fractions are used instead of number fractions. Potentially already the mass of particles of type A can exhibit a distribution instead of a single value, further complicating the situation.

Several investigations of mixing or demixing of granular mixtures have been performed using MRI, see e.g., [43, 72, 84, 85]. In the presented work the mixing of two powders was analyzed for the first time [36]. First stepwise mixing in a simple mixing device is studied. Then mixtures with varying average composition

[1]The binomial distribution applies to the basic urn model where particles are returned after being drawn. Without replacement a hypergeometric distribution is obtained. If K is the total number of particles the variances differ by the factor $(K - M)/(K - 1)$ which is close to one for $K \gg M$.

are produced and the uniformity of the mixtures is compared with the limiting cases discussed above.

4.3.2 Results and Discussion

4.3.2.1 Stepwise Mixing in a Simple Device

In a MRI volume image the mixture is represented by a number of grid points. The intensity at a grid point originates mainly from spins inside the volume element around the grid point.[2] Thus voxels are the samples in an MRI investigation of a mixture. As the entire mixture is imaged, errors originating form the analysis of a limited number of samples are absent. The fraction of one component is derived from the MRI signal in the voxel. In the simplest case one component produces a signal in the chosen experiment and the other component is invisible. Experimentally more demanding is the differentiation of components based on their NMR spectrum or relaxation properties. In the presented measurements the oil-filled melamine microcapsules introduced in Sect. 4.1 (Schubert International, Utting) were used as component producing a signal. As second component with similar properties but without signal contribution solid melamine spheres were used. The density and volume averaged diameter of the microcapsules are $1.08\,\mathrm{g/cm^3}$ and $6\,\mu$m, respectively. For the solid spheres, $1.44\,\mathrm{g/cm^3}$ and $9\,\mu$m are obtained, respectively. The MRI signal indicates the volume fraction of capsules in the voxel volume. It should be noted that already for a powder consisting only of capsules and an ideal measurement the signal would exhibit a variance due to the variance of packing density [36]. Contributions to the measured variance by noise and artifacts were treated as described in Sect. 2.3.4, p. 71ff.

The simple mixing device represented schematically in Fig. 4.7 consists of a cylinder with symmetry axis in direction of gravity. The cylinder can be rotated around an axis perpendicular to the symmetry axis. Rotations were performed slowly and stepwise so that mixing occurs as the content of the partially filled cylinder falls from one end to the other. The volume of the mixture was $1\,\mathrm{cm^3}$. With a FOV of $(15\,\mathrm{mm})^3$ and 64^3 grid points the voxel edge length is $235\,\mu$m. Images for increasing the number of mixing steps reveal the formation of fine structures. The initial variance before mixing is slightly below the value of 0.24 for $\langle p \rangle = 0.6$ and total segregation. An explanation for this is the presence of voxels including the interface between capsules and spheres. Upon mixing, the variance decreases roughly exponentially with the number of turns, see Fig. 4.8. The last point is still slightly above the variance contribution by noise and experimental artifacts.

[2] Concerning the significance of a voxel, see Sect. 2.1.3, p. 14ff.

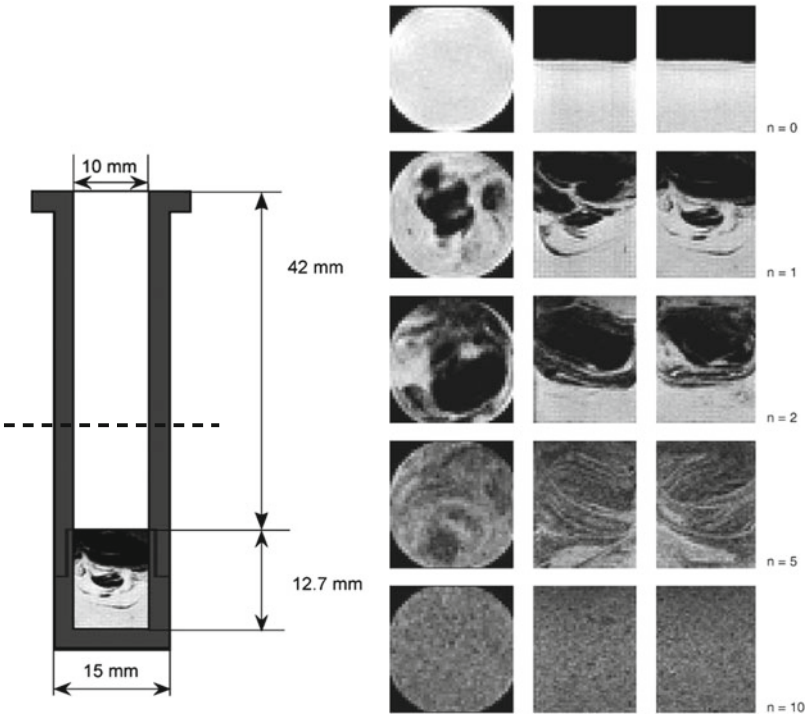

Fig. 4.7 Investigation of powder mixing by MRI. *Left*: schematic representation of the simple mixing device. *Right*: in each row three mutually perpendicular slices through the 3D images of the mixture. Oil-filled microcapsules appear white, solid spheres black. The first row shows the initial superposition of capsules and spheres. Following rows represent the mixture after increasing the number of mixing steps. A 3D RARE was used, see Fig. 2.7. The echo time was 3.2 ms, the RARE factor $r = 4$, and the repetition time 1.6 s. In order to improve SNR $N_A = 8$ averages were acquired. With 64^3 grid points, the experimental time per volume image was 3 h and 38 min. Reprinted from [36] © 2007, with permission from Elsevier

4.3.2.2 Influence of Average Composition

As further application the same measurements were repeated with mixtures of varying composition. In order to achieve comparable mixtures with a high degree of uniformity the powders were mixed outside the tomograph by repeated passage through a sample divider (Retsch, PT100 with DR100). As the samples were mixed outside the tomograph in a device different from the cylinder used for the measurement, the analyzed region was limited to the smallest volume indicated in Fig. 2.23a. This reduces the contribution by experimental artifacts that increases toward the border of the FOV. At the low variance of the reasonably uniform mixtures the influence of corrections of contributions by noise and experimental artifacts according to (2.144) is noticeable, see Fig. 4.9 left. In the semilogarithmic plot on the right hand side of Fig. 4.9 the variances for the limiting cases of an

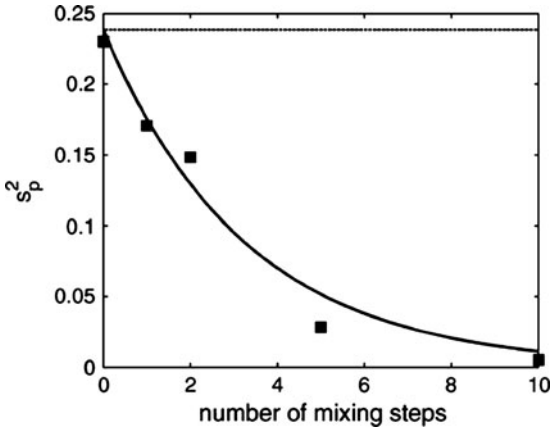

Fig. 4.8 Variance of composition as function of mixing steps for the steps shown in Fig. 4.7. The *solid line* shows an exponential fit, the broken line the value corresponding to total segregation. On this scale the variances with and without correction of contributions from noise and experimental artifacts cannot be distinguished, in contrast to the case in Fig. 4.9. Reprinted from [36] © 2007, with permission from Elsevier

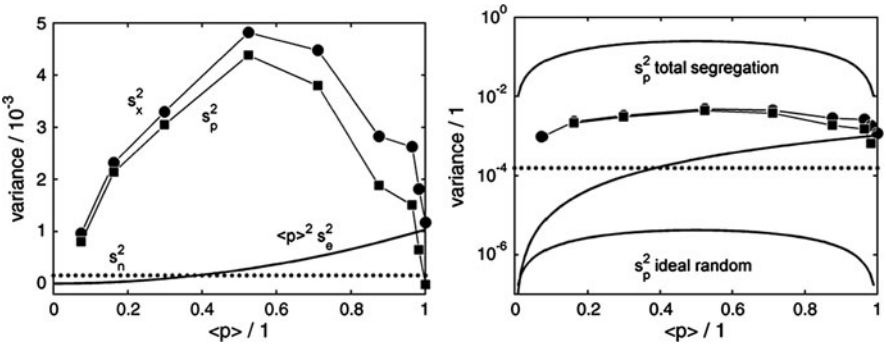

Fig. 4.9 Variance for mixtures of varying composition with (s_x^2) and without (s_p^2) corrections of contributions from the measuring method, respectively. *Left*: linear plot. The broken line indicates the noise contribution, the *solid line* with increasing slope indicates the contribution by experimental artifacts. *Right*: semilogarithmic plot including the limiting cases of total segregation (upper parabola) and ideal random mixture (lower parabola). Reprinted from [36] © 2007, with permission from Elsevier

ideal random mixture (4.4) and total segregation (4.3) are also added. Due to the huge number of particles in a voxel the variance for the ideal random mixture is about two orders of magnitude smaller than the contributions by noise and experimental artifacts. For voxel edge length of 235 μm, a particle diameter of 6 μm, and a packing density of 0.5 about 6×10^4 particles are contained in a voxel. The uncorrected variances are significantly above the contributions of the experimental method. Only for the case of pure capsules $\langle p \rangle = 1$ the result is even slightly

smaller than these contributions. The corrected variance for all compositions is about 50 times smaller than the value for total segregation. On the one hand these results allow to appraise the mixture uniformity achieved with the used device and procedure. On the other hand they point out that experimental contributions can limit the applicability of the method to highly uniform mixtures of fine powders.

4.3.3 Conclusion

The presented results demonstrate the ability of MRI methods to analyze mixture uniformity. Statistical uncertainties due to a limited number of samples are absent. The entire mixture volume is analyzed with over 10^4 samples. Investigations with the simple mixing device revealed that only a few mixing steps are required to achieve a good uniformity. In the study of highly uniform mixtures variance contributions due to the experimental method were shown to be significant and were corrected. The contribution by artifacts depends on the composition of the mixture. Special oil-filled microcapsules were used in order to realize ideal conditions for the MRI experiment. Systems of practical relevance can be treated as long as a MRI contrast between the components can be observed. However, the variance contributions by noise and systematic errors in the system have to be evaluated and must be smaller than the variance of the composition. In solid systems achieving images with high resolution and SNR by MRI is challenging. Here μ-CT can be an alternative. In the preceding the uniformity of the entire mixture was analyzed. With the high number of samples, it is possible to determine, e.g., the profile of uniformity per slice [36].

For bulky mixtures, as in stationary concrete mixers, uniformity analysis using a mobile inside-out NMR device is conceivable. The principle challenge is to realize a setup with sufficient SNR. An example is the miniaturized and rugged construction shown in Fig. 3.8 which is based on the principle presented in [52]. Encouraging results were obtained with this apparatus developed by D. Mertens and E. Oliver at the Institut fr Mechanische Verfahrenstechnik und Mechanik. However, for demanding mixtures of practical relevance, the SNR has to be further improved.

4.4 Rheometry

4.4.1 Introduction

The application of NMR in the domain of rheometry is another example from the field of mechanical process engineering. Here the capability of NMR to measure displacements is exploited. An experimentally demanding procedure is to combine velocity imaging in a slice by MRI with rotational rheometry, e.g., to observe

the occurrence of shear banding [13, 14]. The principle of capillary rheometry is suited for online applications. A drawback of standard capillary rheometry is that measurements at several flow rates and iterative corrections have to be performed to determine the flow function for non Newtonian fluids. However, if it is possible to determine the flow profile in addition to the pressure gradient the flow function can be determined for all shear rates occurring at a constant flow rate without corrections. One possibility to measure flow profiles is to evaluate the Doppler shift and echo time of back scattered ultrasound pulses [7, 10, 41, 60, 70, 79, 80, 101]. Also velocity imaging by MRI in superconducting magnets has been applied by several groups to perform capillary rheometry at only one flow rate, see e.g., [2, 3, 18, 26–28, 97]. However, superconducting magnets are difficult to use in an industrial environment. Therefore the NMR-based capillary rheometer described in the following was developed [38, 39, 68]. It uses the permanent-magnet system presented in Sect. 3.2. This required not only the construction of the adapted flow loop described in Sect. 3.4 but also the elucidation, quantification, and compensation of the effects occurring if unshielded pulsed gradients are used for velocity measurements in a permanent-magnet system. The measurement of pulsed-gradient effects is described in Chap. 8. Influences on velocity measurements are treated in Sect. 2.1.8 on p. 34ff. The results demonstrate that precise and reliable results can be obtained using a standard low-field magnet. For the measurement of flow profiles in pipes adapted magnet systems based on Halbach arrays are promising, see [9] and p. 93ff. Even single-sided devices can be used [16, 83].

4.4.2 Results and Discussion

4.4.2.1 Velocity Probability Density Function and Velocity Profile

In the presented work the velocity profile $v(r)$ was not measured directly.[3] Instead the velocity profile is derived from the measured VPDF $f(v)$, see Sect. 2.1.8, p. 32 [104]. Experimentally this is a simplification as only one gradient system, amplifier, and control is required for the direction of flow. In addition, the VPDF is measured for the entire capillary instead of the profile in a thin slice, which is beneficial with respect to SNR.

For the relation between the VPDF and the inverse flow profile $r(v)$ a simple derivation considering the cumulative probability density function $F(v)$ was found. A fully developed laminar isothermal capillary flow and a macroscopically homogeneous fluid is assumed. In this case velocity v is a monotonous function of radius r. Consequently the cumulative VPDF for velocities up to $v(r)$ equals the surface

[3] As usual in standard low-field systems, the y axis is chosen vertically (the z axis is in direction of the polarizing field, i.e., horizontal). Accordingly the velocity component of interest is denoted by v in this section instead of w.

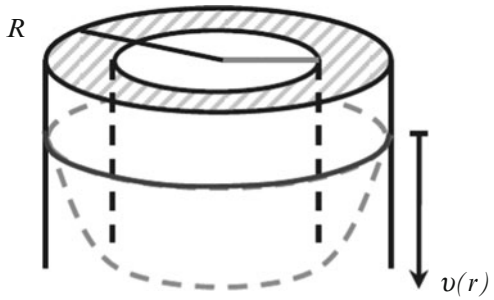

Fig. 4.10 Capillary flow and rheometry. Fully developed laminar isothermal capillary flow of a homogeneous fluid is assumed. Then fluid with velocity between zero and $v(r)$ is located in a hollow cylinder with inner radius $r(v)$ and the capillary radius R as outer radius. This allows to establish the relation between the velocity probability density function and the velocity or shear-rate profile. The shear-stress profile follows from the balance of forces acting on the inner cylinder with radius $r(v)$

fraction of the ring shown in Fig. 4.10 in relation to the total cross section of the capillary πR^2:

$$F(v) = \int_0^v f(v')\,\mathrm{d}v' = \frac{\pi R^2 - \pi r(v)^2}{\pi R^2}. \tag{4.5}$$

This equation can be solved for the inverse profile:

$$r(v) = R\sqrt{1 - F(v)}. \tag{4.6}$$

Differentiation finally yields the shear-rate profile:

$$\kappa(v) = -\frac{\mathrm{d}v}{\mathrm{d}r} = \frac{2\sqrt{1 - F(v)}}{R\,f(v)}. \tag{4.7}$$

For the VPDF measurements shown in Figs. 4.12–4.14 the sequence depicted in Fig. 4.11 and described in Sect. 2.1.8 on p. 34ff was used. Velocity encoding was performed with $N_\mathrm{G} = 128$ increments of gradient pulses of duration $\delta = 3$ ms and time separation $\Delta = 14$ ms. This results in an echo time of $t_\mathrm{SE} = 28$ ms. In order to achieve a steady state for the transient and remanent permanent gradient effects (see App. 8) $N_d = 10$ prepulses were applied. Magnitude data of the Fourier transformed echo amplitudes are shown without further data processing. As exception olive-oil data represented in Fig. 4.12 were measured with $N_\mathrm{G} = 256$ encoding steps and "uniform resampling" to 128 steps, see p. 39f. In addition here a Hamming filter and a linear outflow correction by at maximum 2.7% was applied, see Sect. 2.1.9, p. 41f.

The starch powder was heated in water to 358 K with a mass fraction of 0.60. It was kept at this temperature while stirring for 10 min. All other food samples were

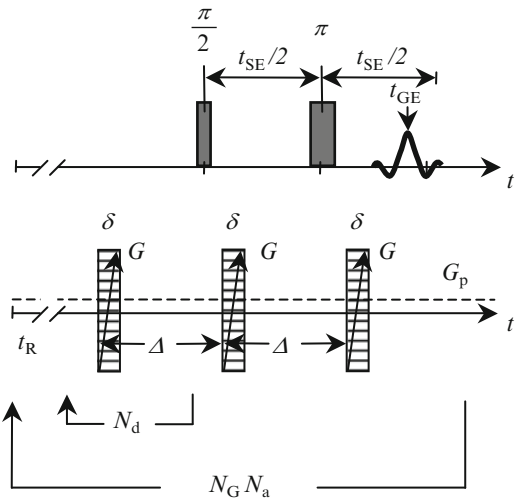

Fig. 4.11 Steady-state pulsed-gradient spin-echo (PGSE) sequence. The upper row represents the sequence of rf pulses in the SE experiment. In the lower row the timing of $N_d + 2$ gradient pulses of amplitude G and duration δ is shown. The simple PGSE experiment has only the two last gradient pulses. In order to achieve a steady state the time separation Δ of all pulses must be equal. For a sufficiently big number N_d the required equality $t_{GE} = t_{SE}$ is fulfilled. The remanent permanent gradient G_p exhibits a marked hysteresis with respect to G

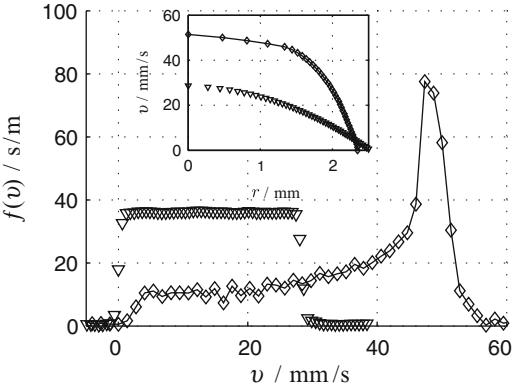

Fig. 4.12 VPDF and flow profile (small embedded plot) for olive oil at 298 K (▽) and mayonnaise at 303 K (*diamond*), respectively. For olive oil the capillary diameter was 5 mm, the flow rate 0.3 ml/s, the first gradient amplitude −0.47 T/m, and the repetition time 1 s. Eight averages and 256 encoding steps for uniform resampling were used, resulting in an experimental time of 40 min. For mayonnaise the capillary diameter was 4.7 mm, the flow rate 0.6 ml/s, the first gradient amplitude −0.21 T/m, and the repetition time 1.4 s. With eight averages and 128 encoding steps an experimental time of 30 min is obtained

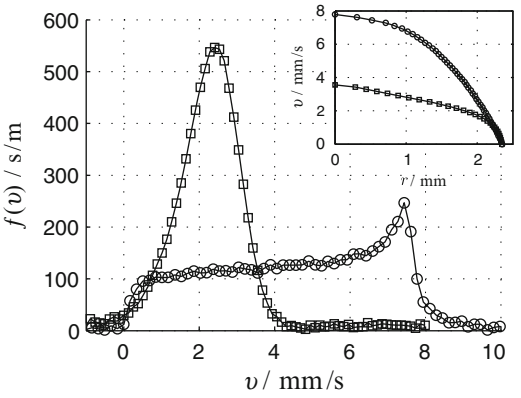

Fig. 4.13 VPDF and flow profile (small embedded plot) for cake batter (*circle*) and starch gel (*square*), respectively. Measurements were performed at 303 K in a capillary with 4.7 mm diameter. For cake batter the flow rate was 0.075 ml/s, the first gradient amplitude −1.65 T/m, and the repetition time 1 s. With eight averages an experimental time of 22 min is obtained. For starch gel the flow rate was 0.038 ml/s, the first gradient amplitude −2.20 T/m, and the repetition time 8 s. Only four averages were used, still leading to an experimental time of 70 min

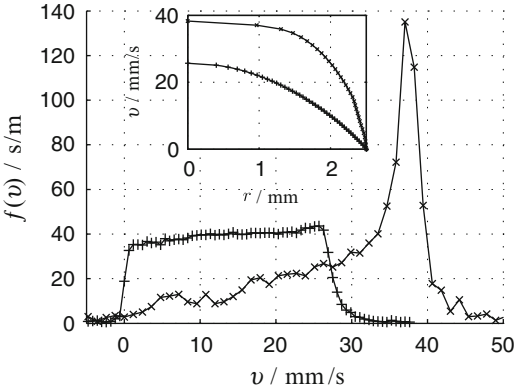

Fig. 4.14 VPDF and flow profile (small embedded plot) for a technical PVP solution (*plus*) and a polymer dispersion (*times*), respectively. Measurements were performed at 298 K in a capillary with 5 mm diameter. For the PVP solution the flow rate was 0.3 ml/s, the first gradient amplitude −0.47 T/m, and the repetition time 3.5 s. With four averages this results in an experimental time of 33 min. For the polymer dispersion the flow rate was 0.6 ml/s, the first gradient amplitude −0.233 T/m, and the repetition time 1.5 s. Sixteen averages were accumulated, leading to an experimental time of 1 h

measured without preparation. This also holds for the technical PVP solution and the polymer dispersion.

For olive oil a neat rectangular VPDF is obtained. It corresponds to the expected Newtonian flow behavior. This can be seen by comparison of the expression $v(r) = v_{\max}(1 - r^2/R^2)$ for the parabolic flow profile of a Newton fluid with maximum

velocity v_{max} with the general expression (4.5) for the cumulative VPDF. It shows that the cumulative VPDF of a Newton fluid is $F(v) = v(r)/v_{max}$. It follows that the VPDF, i.e., the derivative with respect to velocity is constant: $f(v) = 1/v_{max}$. Mayonnaise exhibits a pronounced shear-thinning behavior. For the VPDF this results in a peak at the maximum velocity. The flow profile is flattened compared to the parabolic profile. For velocities close to zero only a small frequency is observed, indicating a zone of slippage at the capillary wall.

The VPDF obtained for cake batter appears like a superposition of a Newtonian and a shear-thinning VPDF. For starch gel the VPDF resembles a normal distribution centered around the average velocity. Possibly the assumption of a macroscopically homogeneous fluid was not good for this sample. At such low velocities Taylor dispersion can be significant. The influence of experimental artifacts can be increased for the high gradients used. Determination of the cumulative VPDF by integration beyond the maximum (up to approx. 4 mm/s), leads in (4.6) to a velocity profile with an inflection point. As shown below, this also leads to questionable results for the viscosity function. The profile depicted in Fig. 4.13 was derived by integrating only to the VPDF maximum.

The VPDF of the technical PVP solution is approximately rectangular with a slight increase toward high velocities. Later measurements revealed that the first measurement of longitudinal relaxation underestimated the relevant relaxation times and the 3.5 s of repetition time lead to partial saturation for low velocities. Thus the increase of the VPDF probably results rather from an inflow effect than from shear-thinning behavior. For the polymer dispersion the VPDF of a shear-thinning fluid is obtained. Due to the high content of polymer with fast transverse relaxation, SNR is lower than for mayonnaise.

4.4.2.2 Viscosity Function

Frequently the flow curve or flow function $\tau(\kappa)$ is used to characterize the flow behavior of a fluid. It is defined as the shear stress τ as function of the shear rate κ for simple stationary shear. In practice users often prefer the viscosity function $\eta(\kappa)$, i.e., the ratio of shear stress to shear rate under steady shear:

$$\eta(\kappa) = \tau/\kappa. \tag{4.8}$$

This is the secant slope of the flow function. Further definitions are the differential viscosity as slope of the flow function or the kinematic viscosity as ratio of viscosity to density. Calculation of the inverse velocity profile and thereby of the shear-rate profile from the VPDF was derived in (4.5)–(4.7). As is well-known the shear-stress profile is determined by the pressure gradient p':

$$\tau\,(r(v)) = p'r(v)/2. \tag{4.9}$$

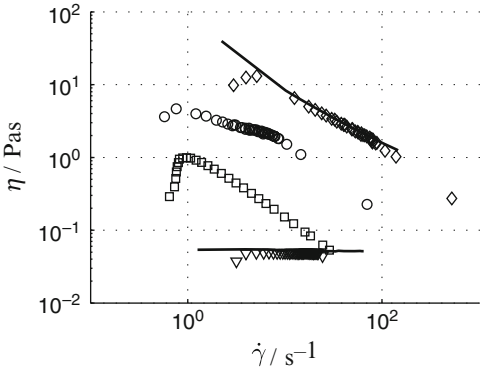

Fig. 4.15 Viscosity function for food stuff, calculated from the VPDF represented in Figs. 4.12 and 4.13 and the measured pressure gradients. For mayonnaise (*diamond*) and olive oil ($\bigtriangledown$) *solid lines* show reference measurements with rotational rheometry. Starch gel: *square*. Cake batter: *circle*

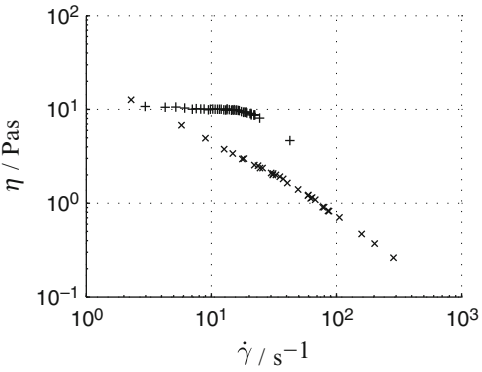

Fig. 4.16 Viscosity functions calculated from the VPDF represented in Fig. 4.14 and the measured pressure gradients. Technical PVP solution: (*plus*). Polymer dispersion: (*times*)

This can be shown by equating the pressure forces on the face surfaces of an imaginary fluid cylinder (see Fig. 4.10) with the shear force on the lateral surface.

In the presented indirect measurement the shear rate (4.7) and shear stress (4.9) are obtained for equally spaced grid points on the velocity axis. If the velocity profile is measured directly by NMR using three gradient axis, the shear rate is obtained with a regular spacing on the radius axis. For both methods, in general the shear-rate grid points in the flow function are not equidistant.

Viscosity functions for food stuff calculated using the above equations are represented in Fig. 4.15 and for samples with polymer in Fig. 4.16, respectively. The integral in (4.5) was calculated with the trapezoidal rule. As already noticeable in the VPDF the measured viscosity for olive oil is shear-rate independent, corresponding to a Newtonian fluid. Reference measurements in a rotational rheometer performed for olive oil as well as mayonnaise are in excellent agreement with the results obtained by low-field NMR-based capillary rheometry. Only at low shear rates, i.e., high velocities in the pipe center deviations are obvious. These result from a broadening of the VPDF noticeably predominantly at the high-velocity edge.

Broadening is due to transformation artifacts and imperfections, e.g., remanent permanent gradients, see Fig. 2.12, p. 40. Apart from this the viscosity function for mayonnaise is well described by a power law. As stated above the viscosity function for starch gel was obtained by integrating the VPDF only up to its maximum and is therefore questionable. Integration beyond the maximum leads to an inflexion point in the velocity profile and as a consequence to more than one shear stress (proportional to the radius) associated with one shear rate. Possible causes for the unexpected VPDF shape are given above. Cake batter also shows a decrease in viscosity with increasing shear rate. A power law is less suited to represent the viscosity function, compared to the case of mayonnaise.

The observed slight decrease of the viscosity function for the PVP solution can be an artifact resulting from an insufficient relaxation delay as discussed in the context of the corresponding VPDF. For the polymer dispersion, at the constant flow rate shear-thinning behavior over two decades of viscosity can be measured.

4.4.3 Conclusion

NMR-based capillary rheometry allows the determination of the viscosity function at constant flow rate for the range of occurring shear rates. Slippage or yield stress can be observed in the velocity profile, depending on the resolution. With the adaptation of the method for a compact and mobile low-field system with permanent magnets applications in industrial environment are possible.

Depending on the application, the use of the VPDF to derive the shear-rate profile is unfavorable due to the rather long experimental times. The presented measurements were conducted acquiring several averages to increase SNR and 128 velocity-encoding steps in order to achieve good velocity resolution. If less precision is required the number of averages or encoding steps can be reduced. In the latter case however not only velocity resolution is decreased but also the influence of transformation artifacts is increased. To circumvent this problem, e.g., a power-law behavior could be assumed for the viscosity function and the correspondingly parametrized velocity profile calculated. Its representation in reciprocal space could be fitted to the measured data without Fourier transformation.

Whereas low-field NMR measurements usually require the presence of mobile hydrogen nuclei investigations with ultrasound are only possible if there is sufficient transparency for ultrasound as well as back-scattering amplitude. In general the velocities typically measured by ultrasound experiments are one to two orders of magnitude higher compared to the ones measured in NMR experiments. However, shear rates are comparable, as larger tube diameters are employed. Time resolution is in the range of seconds to minutes.

If NMR methods that measure the velocity profile directly are used, experimental times are also reduced to some seconds, see Fig. 4.17. Another advantage is that radial heterogeneities of the spin density or other influencing parameters are

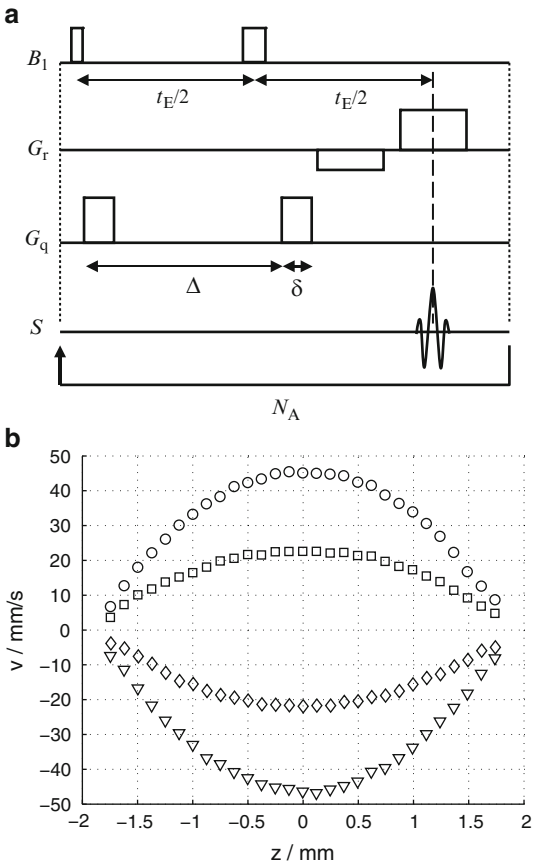

Fig. 4.17 Preliminary experiments with a direct measurement of the velocity profile. (**a**) Pulse sequence, here without slice selection. As an audio amplifier with coupling capacitor was used for frequency encoding (no DC output) a pair of bipolar gradients (G_r) was applied after the rf refocusing pulse. Of the 13.5 V output voltage 11 V were dissipated in a 2.2 Ω resistor in series to the gradient coil. The corresponding current of 5 A generates a gradient of about 0.1 T/m. At a spectral width of 64 kHz this results in a FOV of 16 mm. With 128 digitized points this yields a spatial resolution (here in z direction) of 125 μm. The half echo time $t_E/2$ and the gradient-pulse separation Δ were 7.5 ms, the duration of the flow-encoding gradient δ 1 ms. A GREAT 1/60 amplifier was used to generate the unipolar gradient pulses for flow encoding, in which the second gradient G_q was chosen slightly higher than the first in order to obtain complete refocusing (25.0 and 25.3 mT/m). (**b**) Results for olive oil in a capillary with 2 mm radius. Average velocities were ± 16 and ± 32 mm/s. The reference measurement was performed without flow. With 32 averages and a repetition time of 1 s the experimental time for one profile measurement with flow encoding amounts to 32 s. The influence of missing slice selection is discussed in the text. Bruker, Rheinstetten, is gratefully acknowledged for providing a three-axis gradient system

detected, macroscopical homogeneity is no longer required as in the evaluation of the VPDF. However additional hardware components are required for radial frequency encoding of position as well as slice selection. Selection of a thin slice

containing a radius and the direction of flow reduces SNR. Possible interactions of additional gradient pulses with the permanent-magnet system have to be considered.

Higher shear rates can be realized at a given flow rate if the capillary radius is reduced. In order to maintain a high filling factor at a given coil radius bundles of capillaries can be used. In this case the VPDF method is adapted. As also the sign of the velocity is obtained in the VPDF, capillaries can form loops that enter the magnet from both sides. At higher velocities more care has to be taken in order to avoid artifacts by outflow or incomplete thermal polarization. This applies also if the magnet and coil size are reduced.

Already NMR-based capillary rheometry is an interesting method for the purpose of process analytics. The information content can be significantly increased if it is combined with online NMR relaxation measurements. As worked out in Sect. 2.1.9 on p. 41ff complex effects occur in relaxation measurements on fluids flowing through inhomogeneous polarizing and rf fields. Correction of these effects requires knowledge of the VPDF. A first simple example is presented in Sect. 4.5.

Finally the properties of the measurement without slice selection shown in Fig. 4.17 are discussed. For a 2D spatial resolution perpendicular to the flow direction (y) and a Newtonian fluid, the velocity at $(x, z) = (0, 0)$ should be twice the average velocity. In Fig. 4.17 a lower velocity is obtained at $z = 0$ as the projection along x contains velocities between 0 and $v_{\max}$ that contribute to the local magnetization phase $\phi(x, 0) = -q_v v(x, 0)$. The cumulative VPDF restricted to the plane $z = 0$ can be generally expressed as $F(v) = 1 - x/R$, with a similar argumentation as for (4.5). For a Newton fluid with flow profile $v(x) = v_{\max}(1 - x^2/R^2)$ in this plane the profile can be solved for x. Insertion into F and performing the derivative to obtain the VPDF yields

$$f(v) = \frac{1}{2v_{\max}\sqrt{1 - v/v_{\max}}}. \tag{4.10}$$

The average velocity $\langle v \rangle$ at $z = 0$, i.e., $\int f(v) v \mathrm{d}v$, amounts to $2v_{\max}/3$. However, it is important to note the phase of the projected magnetization in general is not $-q_v \langle v \rangle$. Instead the phase has to be calculated from

$$M^+ = \int_0^{v_{\max}} f(v) \exp(-i q_v v)\, \mathrm{d}v = \int_0^{v_{\max}} \frac{\exp(-i q_v v)}{2v_{\max}\sqrt{1 - v/v_{\max}}}\, \mathrm{d}v. \tag{4.11}$$

Again the last expression applies to the case of a Newtonian fluid. For the experiment shown in Fig. 4.17 with $q_v = 50.2\,\mathrm{s/m}$ and $v_{\max} = 64\,\mathrm{mm/s}$ the integral was calculated numerically.[4] Division of the resulting magnetization phase by q_v leads to 45.1 mm/s, in good agreement with the result shown in Fig. 4.17b. In comparison, the average velocity $\langle v \rangle = 42.\bar{6}\,\mathrm{mm/s}$ is lower. Instead of applying slice selection with negative effect on SNR, the radial symmetry of the flow profile

[4] With http://integrals.wolfram.com.

and spin density can be used in the data evaluation. For a radially symmetric sample the projection on one axis is the Abel transform. As the Abel transformed complex magnetization is only sampled on a discrete number of grid points, the challenge is to perform a reliable discrete inverse Abel transform (DIAT) [26,35,47,51,65,100] respectively a discrete Hankel transform [1,2].

4.5 Relaxometry for a Flowing Liquid

4.5.1 Introduction

Low-field NMR devices with permanent magnets are frequently used to perform NMR relaxometry. In quality control this allows, e.g., to monitor the fractions of different phases. A typical example is the determination of solid fat content. The progress of a polymerization reaction influences strongly the NMR signal decay. In most applications a sample is extracted from the process for the NMR analysis. This requires an intervention and a time interval during which the sample properties can change. The results obviously only have a statistical meaning and usually the samples have to be discarded. For these reasons it is desirable to perform inline measurements of the product or at least online analysis of a bypass. In addition to the NMR-based capillary rheometry presented in Sect. 4.4 online relaxometry is a valuable method for process analytics. As discussed in Sect. 2.1.9 on p. 41ff in general determination of the VPDF is a prerequisite for the analysis of relaxometry measurements on a flowing liquid. It is therefore natural to combine both methods and the expression rheo-TD-NMR is suggested.[5]

In the following first results for a simple system are presented. Longitudinal relaxation was enhanced so that even at the highest velocity the assumption of complete thermal polarization is reasonable. A Newton fluid with parabolic flow profile was used. Transverse relaxation is monoexponential. A direct influence of shear on NMR relaxation is not expected.

4.5.2 Results and Discussion

For the experiments represented in Fig. 4.18 the low-field NMR setup presented in Sect. 3.2 operating at 10 MHz was used with the probe head described in Sect. 3.3.1. The echo time was 0.5 ms, reference measurements with 2 ms showed similar results. With 64 averages and a repetition time of 1.6 s the duration of one measurement is less than 2 min.

[5]E. H. Hardy, D. Mertens, K. H. Wassmer, N. Nestle, Low-field integrated rheo-TD-NMR on industrial media – experiences and challenges, poster presented on the ICMRM 10 in Montana.

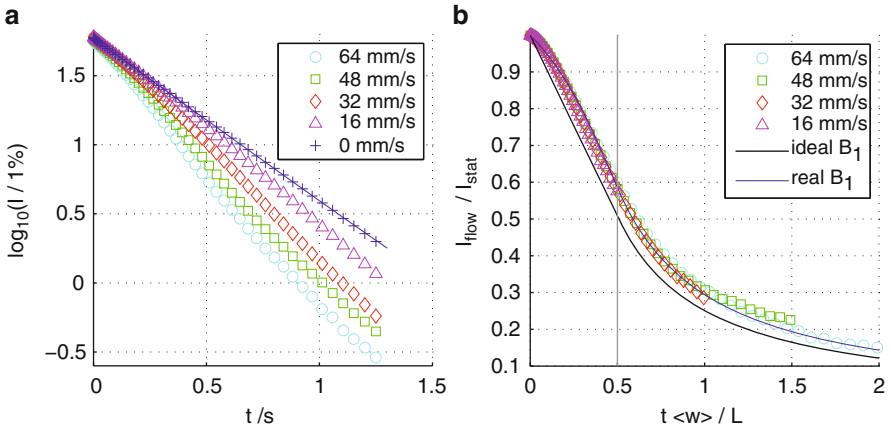

Fig. 4.18 Relaxometry experiment using the CPMG sequence for the fully developed laminar pipe flow of an aqueous Gadovist solution (0.33 mmol/l, $T_1 = 0.39$ s) at 303 K. The capillary radius was 2 mm. With the flow rates set on the syringe pump this results in the average flow velocities indicated in the legend. (**a**) Without flow the signal decay is monoexponential. With increasing flow rate the decay of the observed signal is increased in a non-exponential manner. (**b**) Ratio of the decay curves with flow to the decay curve for the stationary liquid. The *solid lines* show the theoretical result calculated by (2.100) using the measured B_1 profile and an ideal rectangular profile, respectively (see also Fig. 2.15)

As can be seen from Fig. 4.18a the measured signal decays by more than two orders of magnitude. Accordingly, SNR is low for long decay times. In order to obtain smooth curves for the signal ratios, three additional kinds of averaging were employed. By experimental artifacts odd and even echoes scatter systematically around the relaxation curve. This is effectively reduced by averaging each neighboring pair of odd and even echo. At each flow rate measurements were conducted with flow velocity parallel and antiparallel to gravity. As expected, no systematic difference was observed, so results for both flow orientations were also averaged. Finally it is noted that intensity changes at higher rate for the first points and at low rate toward long decay times. Therefore several methods were tested that average over an increasing number of points with increasing decay time. In Fig. 4.18 results for a simple procedure are shown. It conserves the shape of the decay curve and reduces effectively noise for long decay times. The first data point is accepted without modification (apart from the averaging steps explained above). Next the average of the two following points is used. Then the following three points are averaged and so on. Thus the nth filtered data point is obtained by averaging the original points $(n-1)n/2+1$ to $n(n+1)/2$. In the experiment initially 4,096 data points were acquired and 2,600 were retained for further analysis. Averaging over odd and even echoes reduces data to 1,300 points separated by 1 ms. Applying the last kind of variable averaging described above, the averaged 1,300 data points for both flow directions are reduced to 50 values. This is the integer part of

$(\sqrt{1 + 8 \times 1{,}300} - 1)/2$, i.e., the positive root for n when the last original point for n is set to 1,300.

In order to determine the B_1 profile for the analysis according to (2.100) a reliable experimental method is to measure the Rabi nutation frequency as a function of position of a small sample. As this is time consuming, frequently the maximum time-domain intensity (FID or echo) profile is recorded for a small sample instead. While this is a valid characterization of the probe head, the result is qualitatively and more or less quantitatively different from the B_1 profile. According to (2.100) the intensity profile is related to the B_1 profile by

$$M^+(B_1(z), \tau) \propto \sin(-\gamma B_1(z)\tau)\, B_1(z). \tag{4.12}$$

Obviously the intensity profile also depends on the pulse length τ. The B_1 profile can be approximately inferred from the intensity profile if small flip angles are used. Expansion of the sine then yields

$$M^+(z) \propto B_1^2(z), \quad |\gamma B_1(z)\tau| \ll 1 \quad \text{for all } B_1(z). \tag{4.13}$$

The proportionality constant can be determined if the nutation frequency is measured at one sample position. For the presented results the B_1 profile was obtained approximately from the intensity profile of a homogeneous sample measured by frequency encoding with small flip angle. This is the fastest method as no variation of sample position is required. However, it is additionally assumed that the read gradient is homogeneous in the region with non-zero B_1 profile and that the bandwidth of the receiving chain is larger than the bandwidth of the signal. An additional advantage of the 1D projection by frequency encoding is that the B_1 profile can be determined for each sample in situ.

As predicted by (2.100) nondimensionalization with average velocity $\langle w \rangle$ and a characteristic length L results in a master curve for the signal ratios, see Fig. 4.18b. If the average length of the rf field is chosen as characteristic length the ratio $L/\langle w \rangle$ corresponds to the mean residence time. Usually its inverse is used to correct the apparent relaxation rates, see Sect. 2.1.9. The data shown in Fig. 4.18a were analyzed with three different procedures, summarized in Fig. 4.19. Without corrections a monoexponential fit yields apparent relaxation times that decrease with increasing flow rate. Correction by the inverse mean residence time results in a better agreement with the relaxation rate for the static sample. The quality of this correction depends on the extent to which the decay is analyzed and on the chosen length L. Division of the decay curves by the scaled theoretical master curve (2.100) prior to a monoexponential fit results in the best agreement with the reference relaxation rate of the static sample. However, deviations beyond the estimated uncertainties remain. Further experimental investigations and possibly an extension of the effects considered in the theory are required. Correction of CPMG relaxation data with a theoretically predicted intensity ratio is also applicable to multi-exponential relaxation that occurs in mixtures. In this case the usual subtraction of the inverse mean residence time cannot be applied.

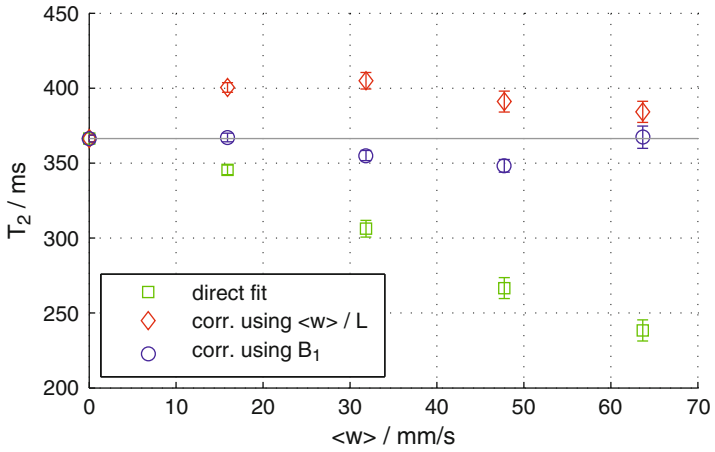

Fig. 4.19 Analysis of the CPMG data shown in Fig. 4.18a in order to obtain relaxation rates respectively times. Direct monoexponential fit without correction: *square*. Correction of the rates by the inverse mean residence time: *diamond*. Monoexponential fit after correction of the decay curves based on (2.100): *circle*

4.5.3 Conclusion

First experimental results on a simple sample agree with the physical model presented in Sect. 2.1.9. Extensive investigations on samples of practical relevance are planned. In general the simplifications of complete thermal polarization, parabolic flow profile, or monoexponential relaxation will not be applicable. Relaxometry then has to be combined with VPDF measurement. As for NMR-based capillary rheometry other magnet geometries can be of interest for rheo-TD NMR [9]. It is conceivable that for complex fluids, not only viscosity but also NMR relaxation shows a shear-rate dependence. Whereas rheology characterizes the macroscopic flow behavior NMR relaxation is governed by microscopic structure and dynamics [8]. Also for such investigations an additional gradient axis is advantageous.

4.6 Trickle-Bed Reactor

4.6.1 Introduction

A further example of MRI application in chemical engineering are investigations of fixed-bed reactors, see e.g., [29, 59, 89]. Without MRI integral quantities such as porosity of the bed, residence-time distribution, or chemical conversion can be measured. However, simple models considering only integral parameters cannot be expected to allow a reliable upscale from bench scale to large scale reactors.

Models with spatial resolution are desired in order to provide more accurate predictions in the process of upscaling. Again, MRI can provide input data for such models and validate the results. In the simplest case the structure of the solid phase is characterized, e.g., by a radial porosity distribution or the specific surface. Obtaining the liquid distribution in two-phase flow can be more demanding, depending on the details of the system under investigation. Quantification of velocity or concentration fields under reaction conditions is challenging. In this section studies in the context of hydration reactions are presented [25, 74, 75]. Finally, it is shown that in a mixture of catalyst and support particles, individual particles can be identified and differentiated into catalyst and support by MRI.

4.6.2 Results and Discussion

4.6.2.1 Setup for In Situ Investigations

A sketch of the experimental setup for in situ investigations on fixed-bed reactors is shown in Fig. 4.20. Gas, hydrogen or nitrogen, is obtained from a gas cylinder.

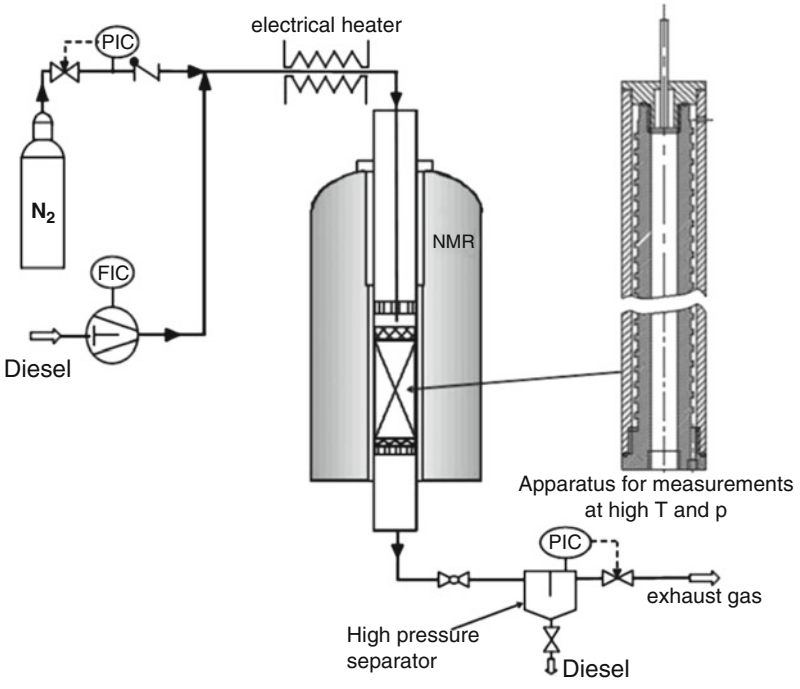

Fig. 4.20 Setup with fixed-bed reactor for in situ investigations by means of MRI. The reactor has an inner diameter of 19 mm. Reprinted from [74] © 2005, with permission from Elsevier

Liquid hydrocarbons are fed by a pump and the mixture is electrically heated before entering the tomograph. Within the tomograph temperature control is realized using the hydrogen-free liquid that was also used in the NMR-based capillary rheometer, see p. 99. The temperature-control jacket is thermally decoupled from the tomograph by an annular gap with air circulation. Suitable non-metallic materials have to be used inside the measuring zone that resist simultaneously elevated temperature and pressure (473 K and 2 MPa). Either plastics or glass were employed. After passage of the fixed bed in the tomograph the mixture is fed in a high-pressure separator.

4.6.2.2 Structure of the Solid Phase

Wall effects cause a porosity heterogeneity in the reactor. Due to the small contact area between the reactor wall and the particles the porosity is high at the wall. Evaluation of the MRI data reveals how far the ordering effect of the wall reaches inside the reactor. In Fig. 4.21 the radial porosity distributions for spherical glass beads and trilobe support particles in a cylindrical reactor are shown, respectively. For the glass beads the distance to the wall is nondimensionalized with the sphere diameter. For the trilobe particles, the equivalent diameter of a sphere with identical volume was used. The glass beads were chosen such that both diameters are identical so that both porosity-distribution function extend over the same range of reduced wall distance. If the radial porosity distribution is calculated for one slice by averaging over the circumference, in general an irregular pattern is observed. The smooth distributions shown in Fig. 4.21e are only obtained after averaging over the bed height. For the spheres with narrow diameter distribution five decaying oscillations are clearly discerned. The wavelength is somewhat smaller than the sphere diameter. A fit of the model by Martin [66] is shown as solid line. The high porosity at the wall is also present for trilobe support particles. However, systematic variations of the porosity extend only to one equivalent particle diameter from the wall. The decaying porosity function was fitted with a monoexponential decay. Although the shape of both types of particles is quite different, a similar average porosity is obtained. The porosity depends however noticeably on the filling procedure of the reactor. Instructions exist, e.g., regarding the number of steps in which a bench-scale reactor has to be filled and how the bed has to be agitated after each filling steps.

4.6.2.3 Distribution of the Liquid Phase

Distribution of the liquid phase has an important impact on chemical conversion. It depends on the volume flow rates and the viscosity of the gas and liquid, respectively, the surface tension as well as on the structure of the solid phase. Characteristic properties of the liquid phase are the saturation, i.e., the volume fraction with respect to the pore volume and the wetting efficiency. In Fig. 4.22 top

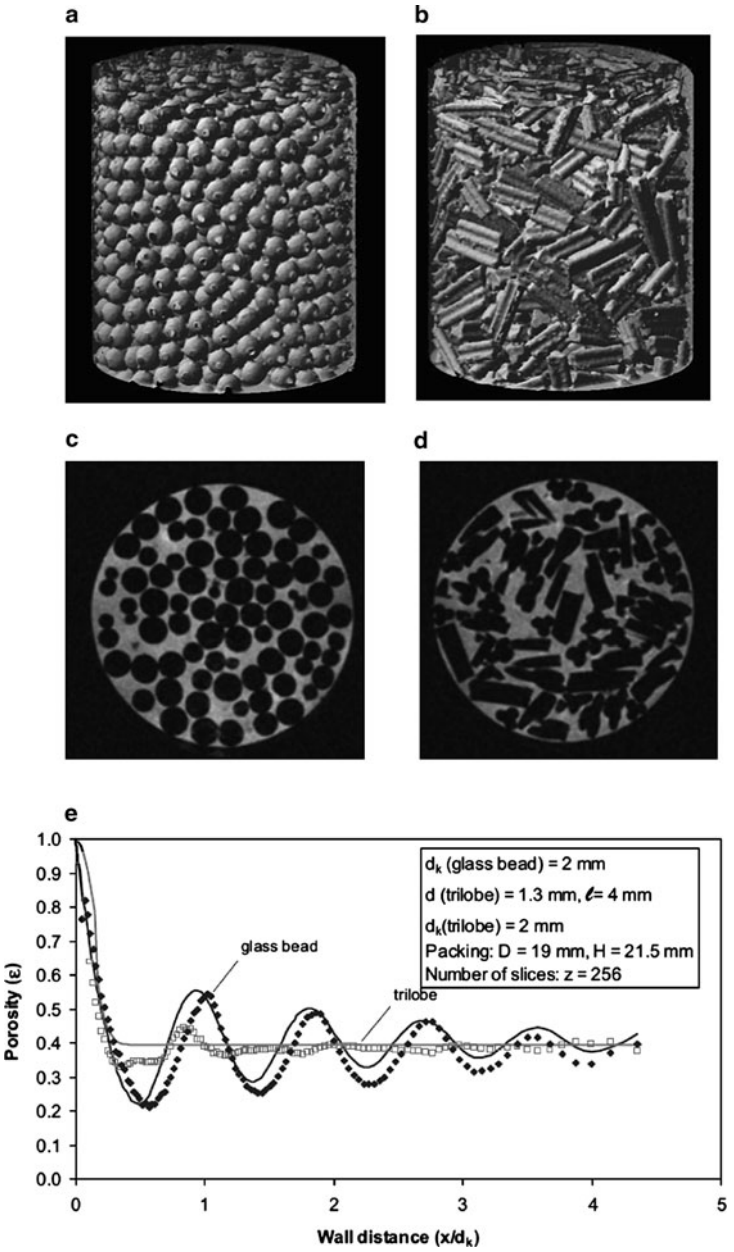

Fig. 4.21 Radial porosity distribution for glass beads with narrow size distribution and for trilobe support particles. (**a**) Surface reconstruction of the volume image for glass beads. (**c**) Slice through the volume image. Filled symbols in (**e**) radial porosity gradient averaged over the circumference and height. (**b**), (**d**), and open symbols in (**e**) corresponding results for trilobe support particles. [75] © Wiley-VCH Verlag GmbH & Co. KGaA. Reproduced with permission

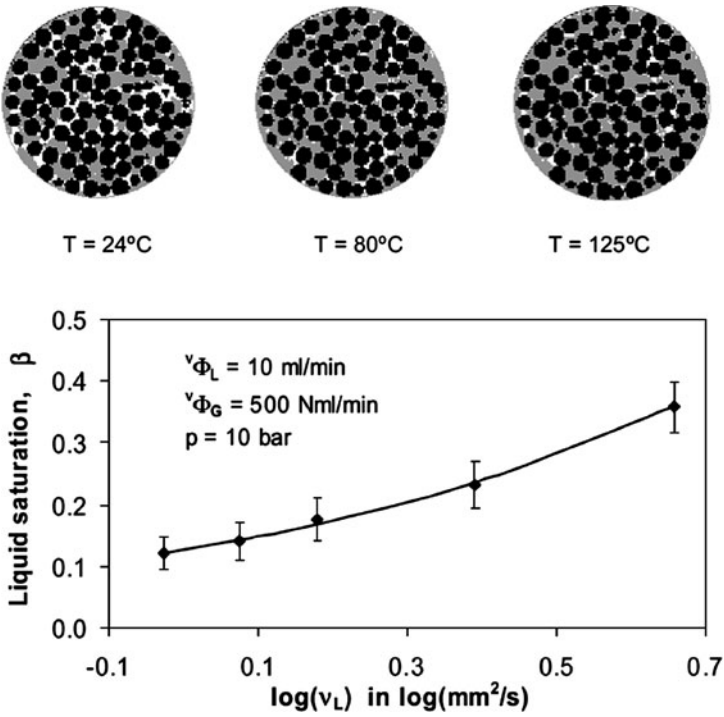

Fig. 4.22 Liquid saturation. *Top*: slice from a volume image. As obtained form the application of thresholds and the combination of images, solid is represented in black, liquid in white, and gas in gray. The gas and liquid flow rate is unchanged. *Bottom*: correlation of liquid saturation obtained from the images with kinematic viscosity of the liquid. [75]

the influence of temperature on liquid distribution is represented for one slice of the volume image and three temperatures. In Fig. 4.22 bottom the kinematic viscosity of the liquid, here diesel is used as abscissa instead of temperature.

4.6.2.4 Segmentation of the Solid Phase

On the left of Fig. 4.23 the surface reconstruction of a volume image of a bed consisting of catalyst and support particles is shown. Due to the coarse spatial resolution the particles are not separated at the contact area and appear as a continuous volume. In order to characterize the bed structure, e.g., by the distributions of particle volume, particle surface, or number of contacts, the continuous volume has to be separated into individual particles. This was achieved using the method described in Sect. 2.3.3 on p. 62ff that was initially developed for the segmentation of a continuous pore space. In the presented application, segmentation

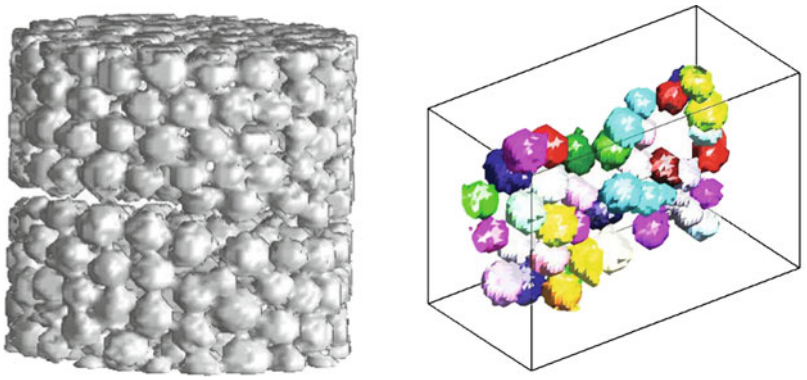

Fig. 4.23 Segmentation of a connected solid. *Left*: Surface reconstruction. Due to the coarse spatial resolution solid particles are not separated in the volume image. *Right*: Set of arbitrarily chosen and colored particles after successful segmentation. Reprinted from [25] © 2007, with permission from Elsevier

into individual particles was a prerequisite for the differentiation of catalyst and support particles by T_2 imaging. In order to simplify the differentiation described below, catalyst and support particles were superimposed and separated by a PTFE sheet. Its position can be discerned in Fig. 4.23 left as there the separation of the particles is increased. The bed was immersed with n-heptane that fills also the pore space in the particles. Therefore the signal-intensity distribution has three peaks. The peak at low intensities results from noise in the areas outside the sample, in the PTFE sheet, and in gas bubbles. Liquid inside the particles contributes to a peak at medium signal intensity. High intensities result from liquid in the outer pore space between the particles. Thus the binary image of the solid phase was gained from the application of two thresholds. The thresholds were determined for a volume image averaged suitably over several echoes, see below. In addition the filter described in Sect. 2.3.1, p. 52f was applied in order to correct for erroneous assignments of grid points to solid or void. For the entire volume image the success of segmentation was verified. Successively, groups of some particles are picked arbitrarily from the bed and colored, so that particles can be identified by their color. An example is shown in Fig. 4.23 on the right. With only a few exceptions, separation into individual particles was successful, i.e., neither under segmentation, over segmentation, or distortion of contact areas was observed.

4.6.2.5 Differentiation of Catalyst and Support Particles

In some experiments beds with catalyst are diluted with support particles. This allows to reduce the reaction rate, e.g., of strongly exothermic reactions or to reduce the costs for expensive catalysts without changing the geometric properties. In this case, the detailed interpretation of investigations with spatial resolution requires the

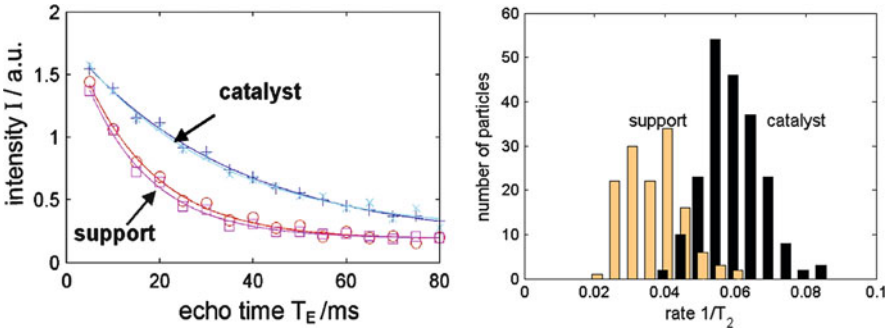

Fig. 4.24 Relaxation of n-heptane in catalyst and support particles. *Left*: signal decay and monoexponential fit for two voxels in catalyst and two voxels in support particles, respectively. *Right*: histogram of relaxation rates for the individual catalyst and support particles, respectively. Reprinted from [25] © 2007, with permission from Elsevier

ability to differentiate between catalyst and support particles. It is already known that metal deposition on the support particles can lead to a modified relaxation behavior of the liquid inside to porous catalyst, see e.g., [59]. In order to assess the applicability of relaxation imaging a 4D measurement with echo time as fourth dimension was applied to the bed described above, see Sect. 2.1.6, p. 28, Fig. 2.7. Plots of the signal decay for two points in the catalyst and two points in the support particles, respectively, in Fig. 4.24 on the left show also a clear influence of metal deposition on transverse relaxation in this system. For each of the segmented particles the signal intensity as a function of echo time was averaged over all voxels of the particle. After a monoexponential fit a transverse relaxation time was assigned to each particle. Due to the superposition of catalyst and support particles the kind of particle can be inferred from the vertical coordinate. Thus relaxation-rate histograms can be established for catalyst and support particles separately. As some degree of overlap exists, a differentiation based on transverse relaxation leaves an uncertainty. However, if the threshold for differentiation is set to 0.05 / ms, the assignment of particles is correct to 95%.

4.6.3 Conclusion

The presented results show possible applications of MRI in the field of fixed bed reactors. A further application is the determination of the velocity field for single-phase liquid flow, see also Fig. 4.27. For two-phase gas–liquid flow no results could be obtained with the required accuracy. If liquid is flowing in a thin film only, low SNR and effects by partially filled voxels limit accuracy. In addition, large susceptibility gradients interfere with phase encoding of velocity. Attempts to measure the flow field using inflow or outflow effects also did not yield an accuracy

in the lower percent range. Comprehensive investigations on model systems could clarify the applicability of various methods in such a system. Possibly accurate measurements of the VPDF with a coarse axial resolution can be performed. A question of relevance for the application is if the liquid-phase flow is evenly distributed over the cross section. The presence of stagnant liquid as well as areas with preferential flow is disadvantageous. As alternative method, positron-emission tomography (PET) can yield velocity information with tomographic resolution. However, it requires radioactive tracers and is not commonly employed.

The spatially resolved determination of chemical conversion from NMR spectra under two-phase flow could equally not been achieved with sufficient accuracy for various methods. Inhomogeneities of the magnetic field lead to distorted spectra with broad lines. This hampers spectra analysis by direct integration. Gradient imperfections also influence the measured spectra. As alternative method for spectra analysis "Indirect Hard Modeling" was employed [61], see also Sect. 2.1.5, p. 23f and App. 7. Finally multivariate statistical or chemometric data analysis was applied, namely "Principal Component Regression" and "Partial Least Squares Regression." As for the case of velocity fields in two-phase flow, comprehensive investigations on model systems are required to evaluate the applicability of different NMR methods to determine chemical composition in such complex systems.

Another quantity of interest is the gas–liquid mass transfer. Investigations by MRI using isotopically labeled substances can be conceived. However, this would be rather expensive if large quantities are required.

In this section stationary trickle flow in a fixed-bed reactor was treated. Fast MRI methods allow to study the onset of pulsating flow. However, most of the presented methods cannot be applied in the regime of pulsating flow. An application similar to the one presented above is the investigation of droplet separation in a fixed bed filter, see [74].

4.7 Ceramic Sponges

4.7.1 Introduction

The applicability of ceramic sponges in chemical and process engineering is studied by a research group at Karlsruhe Institute of Technology (KIT) (DFG FOR 583). Compared to fixed beds ceramic sponges possess a significantly higher porosity from about 0.7 to 0.95. Besides porosity the specific surface is of relevance. However, determination of the specific surface is more challenging. Different types of alumina sponges have been imaged by MRI. Various image-analysis methods were applied to investigate the influence of the method on the result obtained [31].

4.7.2 Results and Discussion

In Sect. 2.3.2 on p. 54ff two methods for the determination of the specific surface from binary volume images have been presented. Results were compared for model systems. In the presented study also different methods of preliminary data treatment were applied to obtain the binary image. At KIT the equations derived in Chap. 2 were used. Alternative methods were applied by a partner within a collaboration [99]. For one slice the different steps of the two preliminary data-treatment methods are compared in Fig. 4.25 a–d and e–h, respectively. The removal of isolated solid voxels in Fig. 4.25g was performed according to (2.108) with consideration of the face neighbors only and $d_{ls} = 2$. On p. 53f the application of the equations to the removal of isolated liquid voxels was described, but here the matrix was inverted as it was done by the partner. Filling of the inner void space, see Fig. 4.25h was achieved by application of (2.109) with $d_{sl} = 14$ and three iterations.

Besides two methods of preliminary data treatment and of specific-surface evaluation results for two different types of sponges are presented. Of one type

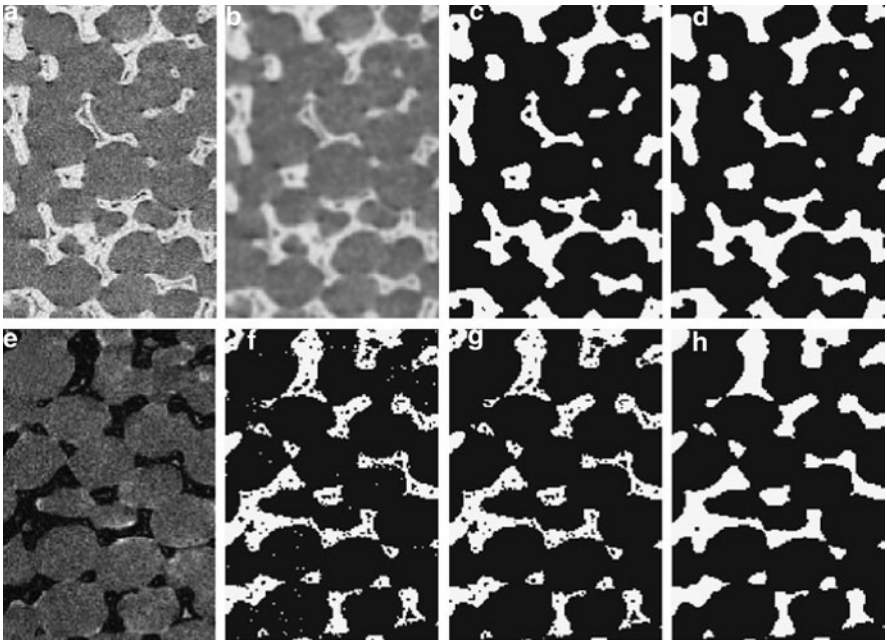

Fig. 4.25 Ceramic sponge, sample 2. (**a**) Cut-out of a slice from the volume image. The intensity is inverted. (**b**) Application of a Gauss filter, see (2.112)–(2.114). (**c**) Binary image after automatic slice-wise application of a threshold. (**d**) Removal of isolated solid voxels and morphological filling of inner void spaces. (**e**) Cut-out of a slice from the volume image. (**f**) Inverted binary image after application of a global threshold, chosen as minimum in the histogram, see (2.101). (**g**) Removal of isolated solid voxels according to (2.108). (**h**) Filling of inner void space according to (2.109). [31]

two samples are chosen. Finally in one case the number of averages was varied. According to the producer all samples had a porosity of 0.8. For samples 1 and 2 the pore density was indicated as 20 ppi (pores per inch), for sample 3 45 ppi. In order to analyze a similar number of pores the FOV for samples 1 and 2 was set to 22 mm in each dimension and for sample 3 the FOV was set to 12.8 mm. Accordingly the adapted probe heads with 25 and 15 mm inner diameter were used, respectively, see Fig. 3.2b. In all cases a data matrix with 256^3 grid points was chosen. This results in an isotropic resolution of 86 and 50 μm, respectively. The strut diameters are about 350 and 130 μm and the average face diameter 1.2 and 0.75 mm, respectively. Consequently the resolution is sufficiently high to image the structures on these length scales. A resolution of surface roughness is not possible and is also not considered in the specific surface here. The representations of the reconstructed surface in Fig. 4.26 allow to appraise the range of details resolved. For sample 2 $N_\mathrm{A} = 2$ as well as 8 averages were acquired. As it turned out that SNR did not have a decisive influence on the determined specific surface all other measurements were performed with two averages. For a RARE sequence with a RARE factor of $r = 16$ and a repetition time of 1.2 s the resulting experimental time per image is 2 h and 45 min. In order to avoid saturation at this repetition time the demineralized water was doped with 1 g/l copper sulfate. The samples were immersed in the solution and a vacuum was applied to remove air bubbles. As experimental results show, the solution enters also in inner void space inside the struts, see Fig. 4.25.

Some results are summarized in Table 4.1. Even without filling of the void space inside the struts (line with ϵ total) the porosity obtained is significantly below the value of 0.8 indicated by the producer. Possibly the number refers to the total porosity including the inner porosity of the solid alumina material that

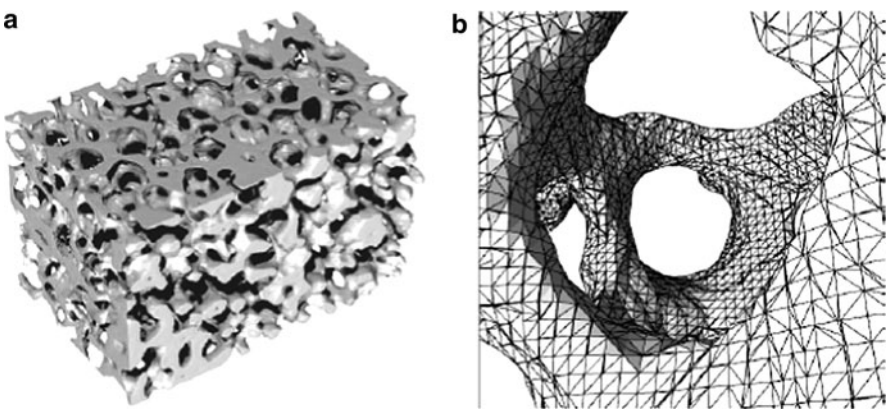

Fig. 4.26 Determination of specific surface by surface reconstruction for ceramic-sponge sample 1. (**a**) Overview with smoothed surface and simulated light effects. (**b**) Small cut-out with representation of the individual triangles. [31]

Table 4.1 Porosity including and excluding inner void space as well as specific surface. The indications "a–d" and "e–h" refer to Fig. 4.25. Details are explained in the text. [31] © Wiley-VCH Verlag GmbH & Co. KGaA. Reproduced with permission

	Sample 1	Sample 2 $N_A = 2$	Sample 2 $N_A = 8$	Sample 3
Pore density / ppi	20	20	20	45
ϵ (total, a–d)	0.741	0.721	0.750	0.730
ϵ (total, e–h)	0.781	0.775	0.768	0.781
ϵ (outer, a–d)	0.736	0.718	0.737	0.727
ϵ (outer, e–h)	0.757	0.745	0.747	0.760
S_V (2.115f, a–d) / m^{-1}	1,244	1,268	1,430	1,982
S_V (2.117, a–d) / m^{-1}	1,229	1,247	1,389	1,974
S_V (2.117, e–h) / m^{-1}	1,187	1,213	1,204	1,917
S_V (4.14) / m^{-1}	1,458	1,362	1,362	2,119

is not resolved in the binary NMR image. The preliminary data treatment applied by the partner results in a porosity for $N_\mathrm{A} = 2$ that is about 5% lower than the one determined with the methods presented above. This can be a consequence of broadened solid structures due to the applied Gauss filter and the threshold applied. For the measurement with $N_\mathrm{A} = 8$ no Gauss filter was applied and the difference between the two porosities is smaller. Filling of void space inside the struts decreases the porosity by about 3%.

Also for the specific surface the largest values are obtained with the preliminary data treatment used by the partner and the method of surface reconstruction, see (2.115) and (2.116). Application of the Crofton formula (2.117) to the matrix resulting from pre-processing by the partner reduces the specific surface slightly by about 1%. With the preliminary data-treatment described in this book the Crofton formula leads to results lower by about 3%. Only for the measurement with high SNR the difference is larger (9%). The influence of different pre-processing on specific surface is consistent with the influence on porosity. In the range of high porosity a reduction of porosity due to an increase of strut thickness results in an increase of surface. Only in the low-porosity range with thick struts porosity and surface decrease together.

Rather than a detailed tomographic analysis of each kind of ceramic sponge ultimately a model correlating, e.g., the specific surface with easily measurable quantities is desired. The applicability of the relation

$$S_V = 4.82 \frac{1}{d_f + t_\mathrm{S}} \sqrt{1 - \epsilon} \tag{4.14}$$

for a dense packing of tetrakaidecahedra is discussed in [11]. As the pore diameter is not easily accessible by optical methods, the average face diameter d_f and the strut diameter t_S are utilized. The specific surface calculated using this model is also listed in Table 4.1. It is somewhat higher than the one derived from MRI data. A dependence of the absolute difference on the pore density is not observed. For

some samples an overall heterogeneity of the structure was observed, probably due to the fabrication process. Thus, the experimental results depend on which part of the sponge is analyzed.

4.7.3 Conclusion

For structures with length scales in the range of millimeters MRI measurements and suitable methods for data analysis allow to determine the specific surface. If the solid material itself is porous, smaller values are obtained compared, e.g., to BET, as the inner surface is not resolved by MRI. Which surface is of relevance for which process depends on the application. As alternative method, μ-CT can be used if porosity and specific surface only are required. With suitable hardware, higher resolution can be obtained in less experimental time. The advantage of MRI

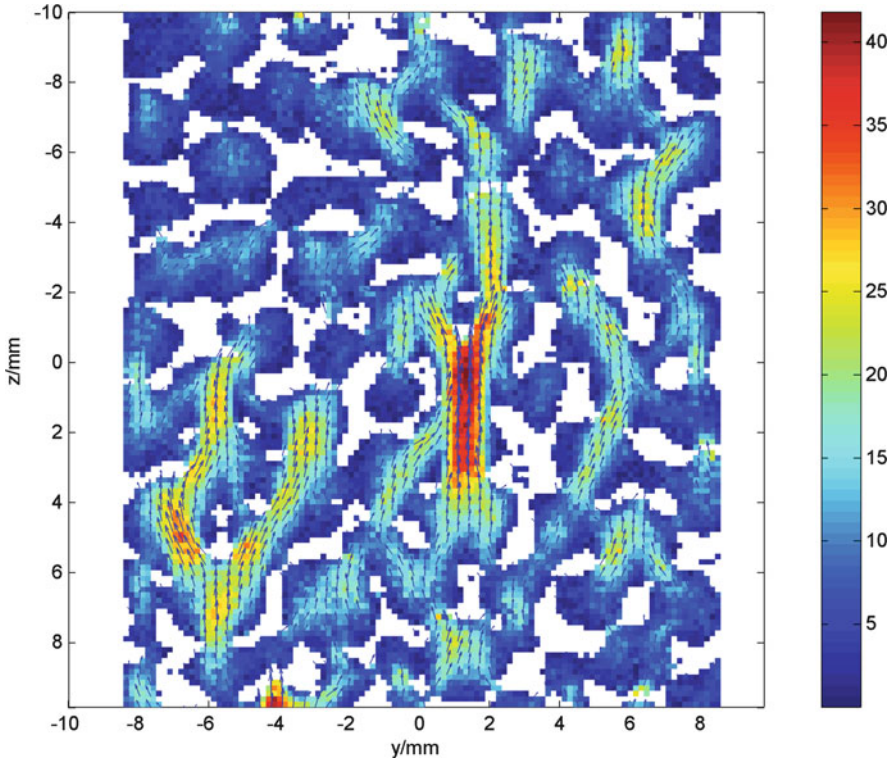

Fig. 4.27 Flow through a ceramic sponge. A slice of the measured 3D vector field is shown. The solid phase is represented in white. Arrows correspond to the two velocity components within the slice. Colors represent the magnitude of the velocity and the colorbar is labeled with velocities in mm/s. For the sake of clarity, only one arrow with average velocity is plotted for four voxels

is that a multitude of additional parameters can be measured. As example, Fig. 4.27 shows results for single-phase liquid flow through a ceramic sponge, see Sect. 2.1.8, p. 32ff. As pores are larger compared to the situation in the fixed bed presented in Sect. 4.6 accurate experiments with chemical and spatial resolution should be possible, at least for single-phase liquid flow.

4.8 Biofilm

4.8.1 Introduction

In this section studies on another fixed bed by MRI are presented, here in the context of bio process engineering. In the bead-packed reactor, biofilm grows on glass beads. Bioreactors are applied, e.g., in waste-water treatment or for the monitoring of waste-water toxicity. The efficiency and service life of a reactor depends on its structure and the resulting transport properties that evolve with time. The aim of the presented work was to image biofilm growth and flow with appropriate resolution in space and time without the addition of contrast agents. Taking advantage of inflow contrast, this could be achieved, at least qualitatively [69].

4.8.2 Results and Discussion

Before the MRI measurement the biofilm reactor was operated outside the tomograph for a first time until approximately half of the pore space was occupied by biofilm. In this state preliminary MRI experiments were performed in order to optimize parameters of the measurement. For the longitudinal relaxation time T_1 1.8 s were obtained. No indications were found that longitudinal relaxation is enhanced inside the biofilm.

Transverse relaxation was described adequately as biexponential decay. The fast relaxing component with $T_2 = 0.1\,\mathrm{s}$ and a weight of 66% was assigned to water inside the biofilm. For the 34% assigned to bulk water in the remaining pore space a longer relaxation time of $T_2 = 0.44\,\mathrm{s}$ was measured. These results agree with previously published ones [50], namely 0.05–0.11 s for water inside the biofilm and 0.12–0.40 s for bulk water inside the remaining pore space. In [50] and also in the presented work it was concluded that this difference in T_2 is not well suited for the monitoring of biofilm growth in a porous system.

In the diffusion experiment also two components were observed. The major component has a translational self-diffusion coefficient $D = 1.9 \times 10^{-9}\,\mathrm{m^2/s}$ close to that of bulk water at the same temperature. Indeed, a noticeable restriction by the biofilm matrix is not expected. Additionally, a small contribution with less than 5% exhibits a markedly slower diffusion with about $D = 2 \times 10^{-10}\,\mathrm{m^2/s}$. It is attributed

to hydrogen atoms in the biofilm and to water closely associated with the biofilm. The latter contribution is too small for observation of biofilm growth in diffusion-weighted images with high spatial and temporal resolution.

As contrast by relaxation and diffusion are not well suited for the observation of the chosen biofilm inflow contrast was used in a second experiment with the reactor operating inside the tomograph from the beginning. At a comparatively short repetition time of 1 s static spins are markedly saturated. The effective echo time of the RARE sequence was 21 ms. Given the range of flow velocities present and the slice thickness of 1 mm outflow contrast is neglected. During one repetition time four slices perpendicular to the reactor axis were observed. The distance of 6 mm between centers of neighboring slices was sufficient to avoid interference of measurements between slices at the occurring flow velocities. Given the isotropic FOV of 25.6 mm and the matrix size of 128^2 the isotropic resolution was 200 μm. The experimental time for the measurement of four slices amounted to 512 s. During 18 h one set of four images was acquired every 30 min.

The polycarbonate reactor had an inner diameter of 22 mm and a length of 500 mm. A random packing of glass beads with 3 mm diameter was used. Feed medium was pumped with a peristaltic pump at a flow rate of 880 ml/h against gravity. At the end of the investigations by MRI the biomass was determined additionally by gravimetry.

Results for slice 3 without flow and for three later times with flow are shown in Fig. 4.28. In Fig. 4.28a without flow all spins are equally saturated. Apart from noise and artifacts, intensity differences result only from beads that occupy only partially voxels in the slice. In the following images acquired under flow areas with high flow velocity are recognized at a high intensity. It is obvious that the area with high flow velocity decreases as biofilm grows with time.

A binary version of each image with distinction between glass beads and pore space was generated. Volume elements for which the assignment changed during the investigation were excluded from the analysis. The fraction of these voxels in

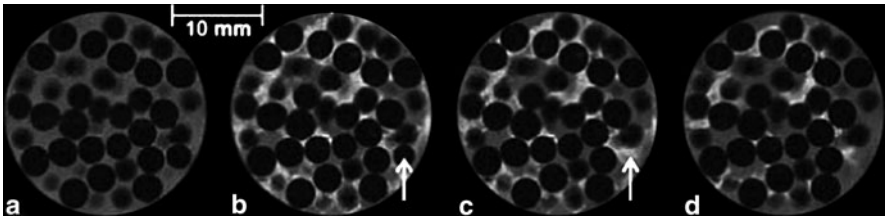

Fig. 4.28 Parameter-weighted spin-density image of slice 3. (**a**) First image without flow. A spatially homogeneous weighting results from partial saturation of magnetization due to a short relaxation delay. The following images are acquired with flow. Weighting by inflow contrast increases the image intensities with increasing flow velocity. (**b**) After additional growth for a time $t = 0.5$ h. (**c**) $t = 9$ h. (**d**) $t = 18$ h. Glass beads are represented in black. The arrow indicates a bead that moved during the measurement. With kind permission from Springer Science+Business Media © 2006 [69]

Table 4.2 Porosity for different slices in the biofilm reactor, mean value, and total porosity as obtained from the gravimetric measurement. Standard deviation from the mean is indicated in parentheses in units of the last digit. With kind permission from Springer Science+Business Media © 2006 [69]

Slice	1	2	3	4	Average	Gravimetry
ϵ	0.41	0.45	0.41	0.34	0.40(4)	0.40

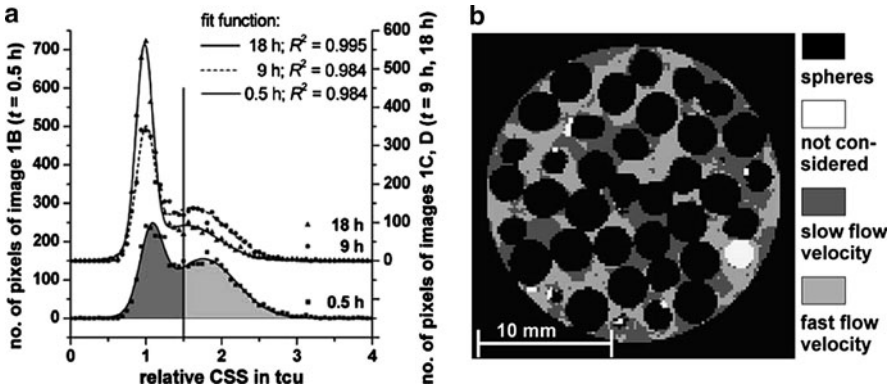

Fig. 4.29 Frequency of relative image intensity under flow referred to the intensity in the image without flow for slice 3 shown in Fig. 4.28 and the growth times represented in this figure. Normalization of voxel intensity by the intensity in the static case removes the contribution of varying spin density. (**a**) Histogram and fit of two normal distributions for the three growth times. With increasing growth of biofilm the fraction of volume elements with high flow rate and image intensities decreases. In the analysis, a binary distinction into areas without or with slow flow and areas with high velocities was preformed. In this, the threshold was set to 1.5. (**b**) Representation of the procedure for the slice shown in Fig. 4.28b. Glass beads are represented in black. Stagnant areas are shown in dark gray. Voxels with high flow velocity appear in light gray. White indicates grid points that are excluded from the analysis. With kind permission from Springer Science+Business Media © 2006 [69]

the four slices amounts to 1.4%. Inside the reactor, the binary images directly yield the porosity. The results are listed in Table 4.2.

Partial volume effects visible in Fig. 4.28a were corrected in the images acquired under flow by division of the intensities with flow by the intensities in the static case. The histograms of relative image intensity shown in Fig. 4.29a are markedly bimodal. This is interpreted as a distinction into stagnant and flowing areas in the pore space. In the analysis, a threshold of 1.5 was chosen to assign voxels to the stagnant or flowing case. The result for the raw image shown in Fig. 4.28b is represented in Fig. 4.29b.

The decay of area with fast flow A_{ff} was used as indicator for biofilm growth. It is represented as fraction of total porous area A_{p} in Fig. 4.30. Experimental data are well described with an exponential fit. However, it has to be noted that stagnant or slow-flow area A_{sf} is also observed in the bead packing without biofilm. Thus the increase of slow-flow area cannot be simply set equal to the area A_{Bf} occupied by biofilm. In order to enable a quantitative analysis, it was assumed that the growing

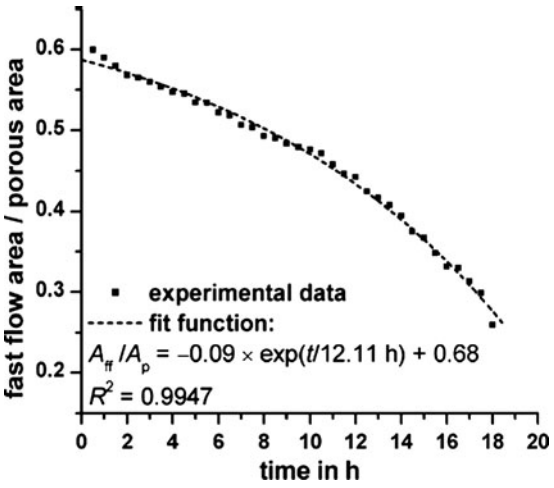

Fig. 4.30 Impact of biofilm growth on flow field. For the four slices the decaying fraction of area with fast flow or equivalently the increasing fraction of voxels with slow flow is shown. The latter increase is well described by an exponential growth. With kind permission from Springer Science+Business Media © 2006 [69]

biofilm does not change the initial ratio of slow-flow area A_{sf} to fast-flow area A_{ff} observed in the reactor without biofilm:

$$A_p = A_{ff}(t) + A_{ff}(t)\frac{A_{sf}(0)}{A_{ff}(0)} + A_{Bf}(t). \tag{4.15}$$

Inserting the values for the initial ratio, obtained form the data shown in Fig. 4.30 extrapolated to $t = 0$ the following equation is obtained for the fraction of biofilm with respect to the total porous area:

$$\frac{A_{Bf}(t)}{A_p} = 1 - \frac{A_{ff}(t)}{A_p}(1 + 0.70). \tag{4.16}$$

Thus also the extreme case of unit biofilm fraction for no flow is correctly reproduced by the assumption. After 18 h evaluation of the data shown in Fig. 4.30 with (4.16) yields a biofilm fraction of 53%. This is significantly lower than the result of 64% obtained by gravimetry. Simply setting the biofilm area equal to the increase in slow-flow area yields an even lower value. Also unit biofilm faction cannot be obtained in this case. Larger fractions are obtained if instead of the initial value used in (4.15) a time-dependent ratio A_{sf}/A_{ff} is inserted that decreases as biofilm grows. This is consistent with the picture that due to the various processes occurring during operation flow predominantly occurs in a few rather straight channels.

4.8.3 Conclusion

The results presented above were obtained in situ and without addition of a contrast agent that could interfere with the microbial metabolism. Using inflow contrast

allows high spatial and temporal resolution. However, velocity is obtained rather qualitatively than quantitatively. Formation of flow channels as observed at later times is unfavorable for the efficiency of the reactor. The presented methods can be applied to study if a fixed bed with differently shaped particles or solid structures as presented in Sect. 4.7 exhibit improved flow properties. For MRI investigations on the deposition of paramagnetic metal ions in a biofilm, see [78]. Flow inside a capillary biofilm reactor as studied by MRI is described in [92].

4.9 Microwave Heating

4.9.1 Introduction

The two final application examples stem from the domain of food process engineering. In this section in situ measurements of temperature fields by MRI during microwave heating are presented. They were performed in the context of studies on microwave-assisted drying of food [58]. Similar methods are used in medical applications in the context of therapeutic hyperthermia [62, 82, 102].

Advantages of microwave heating are that heating occurs directly inside the product and that heating can be switched on and off immediately. As drawback, heating by microwaves is rather inhomogeneous. The distribution of deposited power does not only depend on material properties but also on the shape of the object. Inhomogeneous heating can affect the quality of the product. Worse, safety can be compromised if minimum temperatures are locally not reached for the required time. In preliminary investigations, water distribution during microwave drying of food was monitored by MRI. Additional temperature mapping by MRI as described here is possible as chemical shift of hydrogen in water depends on temperature. Experimental results were compared to simulations that are intended to replace measurements in future applications. If the spatial and temporal dependence of microwave absorption and heat transport properties are included a close agreement between experiment and simulation is obtained. In the following it is explained by which MRI method a good spatial and temporal resolution can be achieved for in situ investigations and the impact of artifacts due to the fast measurement is discussed.

4.9.2 Results and Discussion

4.9.2.1 Setup for In Situ Investigations

The setup for in situ investigations of microwave heating by MRI is depicted in Fig. 4.31. In cooperation with GIGATHERM AG (Grub, Switzerland) a microwave

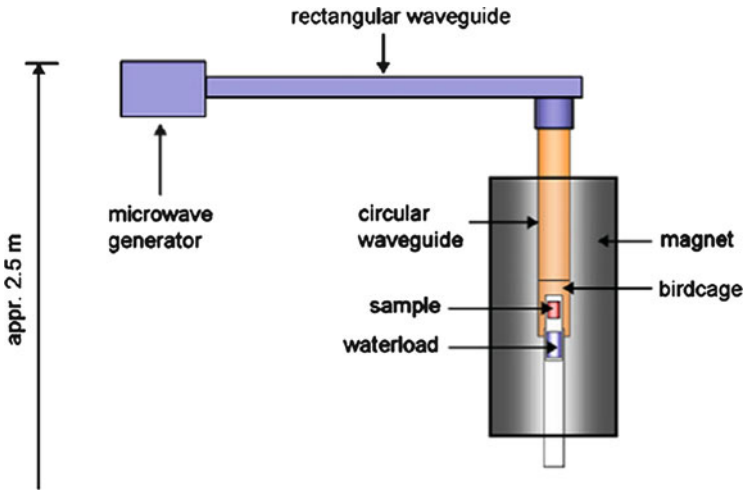

Fig. 4.31 Setup with a microwave device that transmits microwaves to the food sample through wave guides for in situ investigations by MRI. Reprinted from [58] © 2009, with permission from Elsevier

device was developed that transmits microwaves through wave guides directly into the shielded birdcage resonator enclosing the food sample. Below the sample a water load absorbs the power that is not absorbed by the sample.[6]

The model food had a height of 32 mm and a diameter of 33 mm.[7] In order to verify the accuracy of the MRI measurements at least locally a fiber-optic thermometer was inserted into the model-food cylinder. Besides cylindrical samples also spherical samples and real food samples were investigated.

4.9.2.2 MRI Method and Numerical Investigation

Thermography by MRI is based on the fact that the chemical shift, see Sect. 2.1.5 p. 23f of hydrogen atoms in hydrogen bonds depends on temperature. For water in the temperature range of interest a linear relation with slope $\alpha_T = 0.01\,\text{ppm/K}$ can be used [44, 77]. In preliminary investigations it was verified that this relation is also valid for water in the environment of model food. The small difference in

[6] In the first experiment no water load was present. Although only low power was applied for short time damaging of the birdcage resonator by local overheating was impressive. Fortunately care was taken to build a resonator especially for the tests.

[7] For measurements on larger samples a third variable capacitor was added to the birdcage resonator. At high salt content matching to the system impedance is not possible with the standard capacitances.

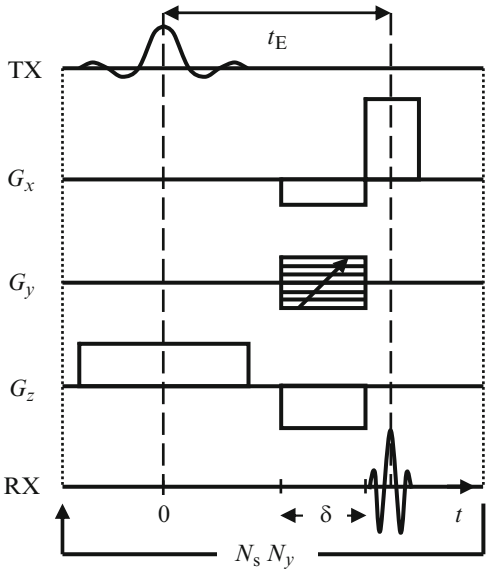

Fig. 4.32 Pulse sequence for thermography. The sequence is repeated for $N_y = 64$ phase-encoding steps and up to $N_s = 50$ slices. Reprinted from [58] © 2009, with permission from Elsevier

chemical shift can be measured with suitable imaging methods in which it leads to a measurable change in the magnetization phase during the echo time t_E, see [77].

The pulse sequence is represented in Fig. 4.32 with time intervals approximately at the same scale. In order to allow selection of a 1-mm thin slice using the less sensitive mini036 gradient system a longer HF pulse with 2 ms duration and a bandwidth of 3 kHz was used (see Sect. 2.1.3, p. 19ff). The duration δ for slice refocusing, phase encoding, and the read-dephase gradient was set to 1 ms. Data acquisition with 64 points and a spectral width of 101 kHz requires only 640 μs. The echo time between the maximum of the excitation pulse and the maximum of the gradient echo amounts to $t_E = 2.7$ ms, the total duration for one pass of the sequence is less than 4 ms. During the repetition time of 200 ms up to 50 contiguous slices could be measured. With 64 phase-encoding steps and without averaging the total experimental time for one pseudo 3D measurement of spin density and magnetization phase is 12.8 s. At an isotropic resolution of 1 mm and the highest duty cycle the temperature measured in the water-cooled gradient system increased to 323 K. This is still below the temperature of automatic gradient-amplifier shutdown for protection of the gradient coils.

In the gradient-echo-fast-imaging (GEFI) sequence shown in Fig. 4.32 the phase evolution due to inhomogeneities of the magnetic field and chemical shift are not refocused at the echo time as no rf refocusing pulse is applied. Including phase-encoding for spatial resolution according to [1] the expression for the signal in (2.55) is replaced by

$$M^+(k_x, k_y, t) = \int\int \rho(x, y) \exp(i(\Omega_i(x, y) + \Omega_T(x, y))t) \exp(-i k_x x) \exp(-i k_y y)\, \mathrm{d}x\, \mathrm{d}y. \tag{4.17}$$

Compared to (2.55) the situation is similar to the one in (2.79) where at each point in position space only one velocity is considered. A local distribution of chemical shifts is not included. The expression in (4.17) appears as Fourier transform of the spin density with a complex phase factor resulting from the spatially varying angular frequency due to inhomogeneities of the magnetic field $\Omega_i(x, y)$ and chemical shift resulting from temperature variation $\Omega_T(x, y)$ in the rotating frame of reference. Concerning the phase-encoding dimension, here y, this is correct. However, in the frequency-encoding dimension, here x, the wave vector k_x depends on time as well as the additional phase factor, see (2.36) for the case of constant gradient amplitude and varying time. The interference of frequency encoding of position and chemical shift in the GEFI experiment results, after simple inverse Fourier transformation, in distortions of image geometry and intensity. In [1] this is treated theoretically and a possible post processing for correction of distortions is discussed. Here, instead the validity of the approximate result

$$\mathcal{F}^{-1}\{M^+(k_x, k_y, t)\} \approx \rho(x, y) \exp(i(\Omega_i(x, y) + \Omega_T(x, y))t_E) \tag{4.18}$$

is assumed and the magnitude of resulting artifacts is calculated numerically for typical experimental conditions. This procedure also includes the influence of usual transformation artifacts that cannot be neglected at the rather coarse spatial resolution of 64^2 points, see Sect. 2.1.3, p. 14ff. If spatial resolution for both directions within the slice is achieved by phase encoding the interference with inhomogeneities of the magnetic field and chemical shift (due to temperature variations) is absent. This chemical-shift-imaging (CSI) experiment contains the transformation artifacts only. However, as the experimental time is increased by the number of phase-encoding steps, here 64, it was not used in the experiment requiring high temporal resolution. In the numerical calculation it is included for comparison.

Assuming the validity of (4.18), first a reference image at known homogeneous temperature is acquired. At reference temperature, the temperature-dependent chemical shift is zero, i.e., the spectrometer is set "on resonance" in the experiment. Further images are acquired with unknown temperature distribution. The temperature shift is then calculated from the difference of the phase image and the reference phase image to

$$\Delta T(x, y) = -\Omega_T(x, y)/(\gamma B_0 \alpha_T), \tag{4.19}$$

see p. 23. The angular frequency Ω_T is obtained by division of the phase difference by the echo time t_E. In (4.19) it is assumed that a temperature dependence of the magnetic-field inhomogeneities can be neglected.

For the numerical calculation of the signal according to (4.17), on the one hand the discrete wave-vectors and times used in the experiment are needed. They can be calculated for the sequence shown in Fig. 4.32 from the times and the spatial resolution indicated above. On the other hand realistic distributions for the spin density and the frequency contributions by inhomogeneities of the magnetic field and temperature variations are required. For the spin density simply a constant value inside a circular region is assumed, corresponding to a cross section through the

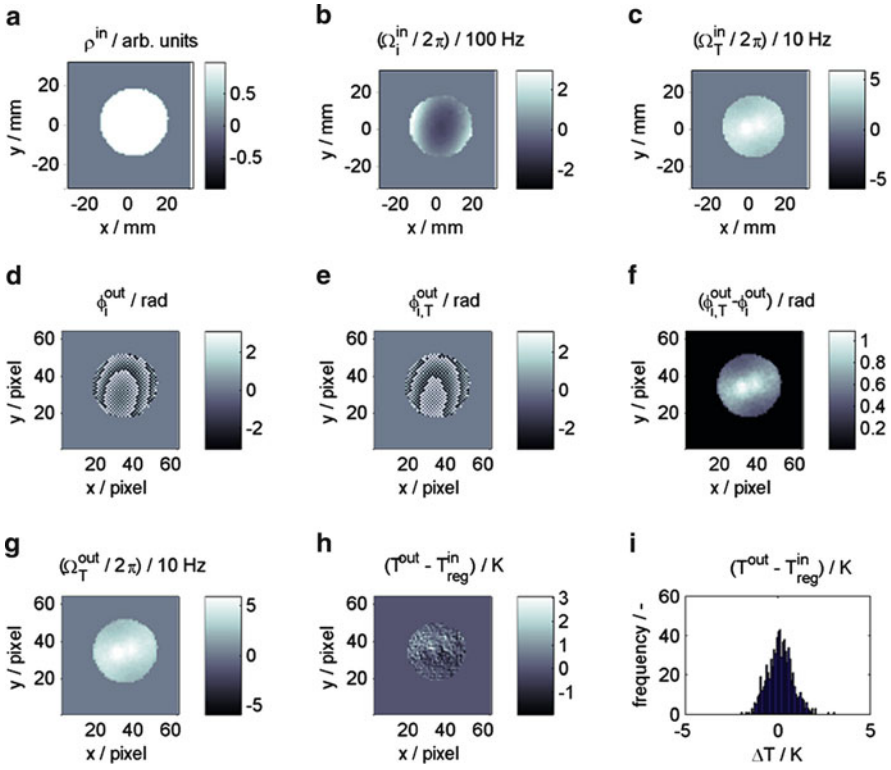

Fig. 4.33 Numerical calculation of artifacts in NMR thermography. (**a**) Homogeneous spin density in a circular area. (**b**) Field inhomogeneity in the considered area, expressed in Hz. (**c**) Input temperature map, expressed in Hz. (**d**) Calculated phase image at reference temperature. (**e**) Calculated phase image including temperature distribution. (**f**) Phase-difference image. (**g**) Output temperature map, expressed in Hz. (**h**) Temperature-difference image. (**i**) Histogram of temperature differences. Reprinted from [58] © 2009, with permission from Elsevier

model-food cylinder, see Fig. 4.33a. In the calculation the double integral in (4.17) is replaced by a double sum assuming piecewise constant functions. Thus the spin density is defined on a N by N matrix. The integration converges for high values of N. This numerical discretization of real space is not to be confused with the necessary discretization of reciprocal k space, here 64 by 64. The latter is also the discretization of the spin density in real space as obtained by inverse Fourier transformation of the calculated signal. According to (4.18), the phase image at reference temperature yields the frequency contribution by inhomogeneities. As also transformation artifacts are included in the phase image, a phase image at reference temperature with homogeneous magnetic field was calculated and subtracted to obtain the corrected inhomogeneity map on the experimental 64 by 64 grid. A linear interpolation was applied to define the inhomogeneity map on the numerical N by N grid, see Fig. 4.33b. Also for the temperature map a typical experimental

result on the 64 by 64 grid was interpolated on the numerical grid and used as true temperature distribution $\Omega_T^{\text{in}}(x, y)$, see Fig. 4.33c. Concerning the proportionality between temperature shift and frequency at the experimental B_0 field the value of 2 Hz/K was used. As can be seen in Fig. 4.33 the contribution by inhomogeneities extends over about 300 Hz whereas the contribution by temperature shift is only in the range of 50 Hz for temperature shifts in the range of 25 K (note the different scaling of the color bars indicated above the figures).

Having defined the input spin density, inhomogeneity, and temperature map the signal can be calculated. After inverse Fourier transformation, the output can be compared to the input. The accuracy of the artifacts determined by this procedure depends on the numerical discretization with N^2 grid points. For a homogeneous field at reference temperature, i.e., transformation artifacts only, no artifacts at all are observed in the special case of identical grids for the numerical calculation and the result of the experiment. In this situation merely a pair of discrete Fourier transforms is performed numerically, verifying the analytical treatment indicated on p. 14ff. Obviously the convergence of the calculation for increasing N has to be checked. Besides the number of numerical grid points N also the number of experimental grid points N_x and N_y was varied. Implemented in MATLAB® R2008a (Mathworks, Natick, MA, USA) under Windows XP SP3 on a Pentium 4 processor with 3.2 GHz clock frequency and 1 GB RAM runs for a single experiment took between some seconds and some hours.

Fourier transformation of the calculation at reference temperature yields a first phase image $\phi_i^{\text{out}}(x, y)$, see Fig. 4.33d. Index i indicates "inhomogeneity." The checkerboard pattern results from the interpretation of the echo in the discrete Fourier transform and is explained by the shift theorem, see also (2.46). The oval superstructures result from the field inhomogeneity. Including the temperature-shift map the phase image $\phi_{i,T}^{\text{out}}(x, y)$ is similar, with a shift of the superstructures, see Fig. 4.33e. The phase resulting from the temperature map with artifacts from transformation and interference of frequency encoding and frequency shifts is contained in the phase-difference image $\phi_{i,T}^{\text{out}} - \phi_i^{\text{out}}$. It is shown in Fig. 4.33e after automatic correction of phase jumps by 2π. In the last row of Fig. 4.33 this final result of the calculated experiments is represented as frequency map, as temperature-difference map with respect to the input temperature, and as histogram of temperature differences. The latter reveals an unimodal distribution which is approximately symmetric with respect to zero, corresponding to no error. In the temperature-difference map Fig. 4.33h no clear patterns are present.

The calculated artifacts and their convergence with N are summarized in Table 4.3 as mean of the absolute error. It increases with increasing N. The only exception is the case where the experimental discretization is smaller than the one in the experiment. For each equal step in N the change decreases. It is assumed that the results do converge and are close to convergence for $N = 1{,}000$. Numbers in parentheses are the calculated results for the CSI experiment with otherwise equal parameters reflecting the transformation artifacts only. For the experimental case of $N_x = N_y = 64$ the mean absolute error with artifacts by transformation as well as interfering frequency encoding and frequency shifts is only slightly above the CSI

Table 4.3 Mean absolute error of the temperature map for the calculated GEFI experiment with respect to the input temperature map in millikelvin, $\langle|\Delta T|\rangle/m\mathrm{K}$. Results are assumed to converge with increasing numerical discretization N. Increasing the experimental resolution N_x, N_y reduces transformation and discretization artifacts. Numbers in parentheses show the mean absolute error for the CSI experiment where artifacts resulting form interfering frequency encoding of position and frequency shift are absent. Reprinted from [58] © 2009, with permission from Elsevier

N_x, N_y	$N = 200$	$N = 400$	$N = 600$	$N = 800$	$N = 1{,}000$
16	916 (936)	949 (973)	956 (980)	962 (986)	967 (990)
32	581 (556)	627 (604)	642 (620)	649 (627)	654 (632)
64	430 (390)	531 (499)	557 (526)	576 (546)	587 (558)
128	222 (113)	275 (197)	296 (225)	306 (239)	313 (245)
256	214 (67)	212 (58)	222 (90)	229 (107)	234 (117)

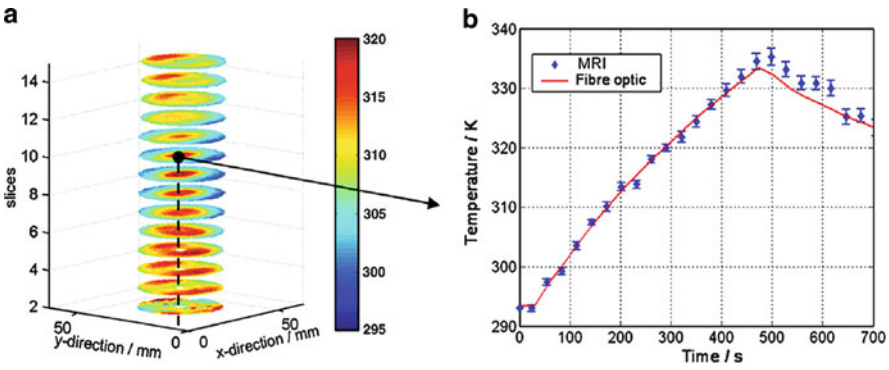

Fig. 4.34 Comparison of NMR thermometry and fiber-optic temperature measurement. In the left image the position of the fiber-optic sensor is indicated. Reprinted from [58] © 2009, with permission from Elsevier

result. Thus in the studied situation artifacts due to the fast imaging method can be neglected compared to transformation artifacts. At a rather high spatial resolution of $N_x = N_y = 256$ the error calculated for CSI is exactly half the GEFI result which is already reduced by more than a factor of two compared to the experimental resolution. For a very coarse resolution of $N_x = N_y = 16$ the order is even inverted, but measurements at such a resolution are probably useless.

4.9.2.3 Comparison with Fiber-Optic Thermometer

In order to test the accuracy of the MRI temperature measurement a fiber-optic thermometer was placed inside the sample within the FOV. Temperature was measured by both methods during microwave heating and were compared for the position of the sensor. The sample was heated using 19 W microwave power during 8 min. Subsequently cooling without microwave heating was observed. In Fig. 4.34a

the 3D temperature field measured by MRI after 130 s is shown. The position of the fiber-optic sensor is indicated by the black line with a circle for the position of the sensitive spot. Results from both methods at this spot are plotted in Fig. 4.34b as function of time. During heating a good agreement of the values is observed. However, during the cooling period MRI temperatures are higher by 2 K than the results of the fiber-optic measurement.

4.9.3 Conclusion

The presented MRI thermography produces results with an uncertainty of about one K with good spatial and temporal resolution during in situ microwave heating. Numerical calculations show that artifacts resulting from the fast imaging method can be neglected compared to the transformation artifacts at this resolution. An impact of the simultaneous microwave irradiation on the MRI temperature measurement was not observed.

No other experimental method offers a comparable space, time, and temperature resolution. Thermocouples allow fast and accurate local measurements at low cost. However, they distort the microwave field significantly. Distortion of the microwave field by fiber-optic thermometers is feeble. However, the price is rather high. Infrared thermography is only applicable for the surface temperature and installation inside a microwave oven is not straightforward. Also microwave radiometry yields results only for areas close to the surface. The surface temperature distribution can also be measured with thermo paper or liquid-crystal foils with coarse temperature resolution. Finally, model substances can be employed that indicate temperature by a color change.

The advantages of MRI thermography were also used in the in situ investigation of convective drying [88]. As further application of MRI in food process engineering, structure and transport properties in porous products were studied [87]. Volume images acquired by MRI as well as 2D images obtained by simple scanning of dyed samples were analyzed. In particular, segmentation as described in Sect. 2.3.3 on p. 59ff was performed.

4.10 Emulsions

4.10.1 Introduction

Nuclear magnetic resonance with pulsed field gradients (PFG NMR) is a standard method for the determination of droplet-size distributions in food emulsions such as mayonnaise (oil in water, O/W) or margarine (water in oil, W/O), see e.g., [32, 46–48, 54, 81, 96] for recent developments. As measurable effect the restriction

of translational self-diffusion inside the confining droplets is exploited. In contrast to light-scattering methods dilution of the sample is not required. In the following investigations on double emulsions of type W/O/W are presented [103]. Water droplets in the phase W1 reside inside larger oil droplets forming phase O that is surrounded by the outer water phase W2. The situation is much more complex than in a simple emulsion and standard methods cannot be used for data analysis. Routine measurements are performed in low-field instruments. Here the high-field tomograph was chosen for the first measurements. The higher field improves SNR and the better field homogeneity allows for spectral separation of water and oil, see Sect. 2.1.5, p. 23f. In the large room-temperature bore a sensitive and actively shielded one-axis gradient system can be used (Bruker diff30, 300 mT/m/A and up to 12 T/m using the 40 A gradient amplifier).

4.10.2 Results and Discussion

As raw data the decaying signal for increasing diffusion encoding in a PFG experiment is acquired. Generally diffusion encoding can be varied via the gradient-pulse amplitude G_q, duration δ, or the time separation of the rising (or falling) gradient edges Δ. For large droplet sizes long observation times Δ are required. In the standard PGSE the observation time equals half the echo time. The latter is limited by the shortest relevant transverse relaxation time T_2. Frequently longitudinal relaxation times are significantly longer than transverse relaxation times. In order to increase the maximum observation time to the order of the shortest relevant T_1 the PGSTE can be employed, see Fig. 4.35. It is the simplest PFG variant of the stimulated echo (STE) experiment that is explained in the following.

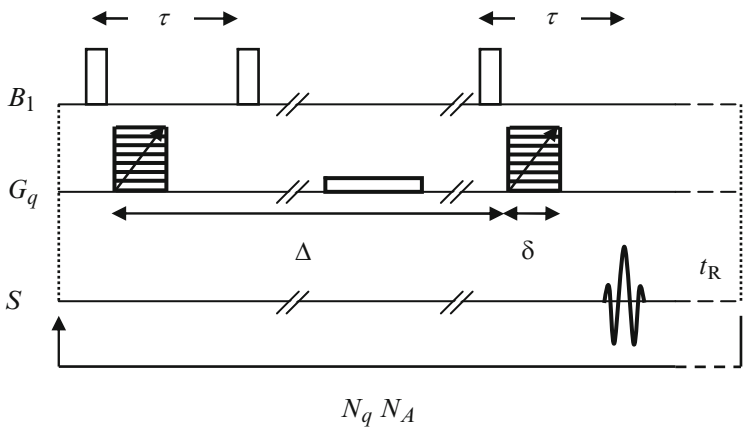

Fig. 4.35 PGSTE pulse sequence. In the storage time between the second and third $\pi/2 - B_1$ pulse a spoiler gradient is included. It additionally dephases transverse magnetization

In the standard SE experiment the decay of transverse magnetization due to dephasing in an inhomogeneous field is totally refocused by a rf pulse with nutation angle π. The echo time amounts to twice the separation of the rf pulses. In the stimulated-echo pulse sequence three rf pulses with nutation angle $\pi/2$ are employed. The separation of the first two rf pulses is denoted as τ. Magnetization components perpendicular to B_1 are rotated on the z axis by the second $\pi/2$ pulse. Components parallel to B_1 remain unchanged by the second rf pulse. Simple classical calculations of the magnetization dynamics show that in an inhomogeneous field and in the absence of gradient pulses the first two rf pulses lead to a first echo at time 2τ. The echo amplitude is half that of the spin echo with a π pulse for refocusing. Magnetization components that are "stored" on the z axis do not decay by T_2 processes or by dephasing in an inhomogeneous field. Longitudinal magnetization relaxes by T_1 processes only. Before the third $\pi/2$ pulse a spoiler gradient can be applied to dephase transverse components that might not have decayed. The third rf pulse rotates the longitudinal components again in the transverse plane. As the classical calculations show a so-called STE is formed at time τ after the last rf pulse. Again, the echo amplitude is half that of the spin echo. As in the PGSE experiment, gradient pulses can be included between the first two rf pulses and after the last rf pulse in order to obtain displacement encoding. After the last gradient pulse, a stabilization time has to be provided before acquisition of the SE. Otherwise spectroscopic resolution is compromised by field fluctuations due to eddy currents.

For the PGSE sequence and unrestricted diffusion the signal as function of G_q, δ and Δ is given in (2.71) on p. 30. If only one diffusion coefficient D is present and for fixed δ and Δ a monoexponential decay is obtained as function of G_q^2. For restricted diffusion in a spherical geometry with radius R the signal is expressed in [71] as

$$\ln(M^+/M_0^+) = -\frac{2(\gamma G_q)^2}{D} \sum_{m=1}^{\infty} \frac{\alpha_m^{-4}}{(\alpha_m R)^2 - 2} S_m \tag{4.20}$$

with

$$\begin{aligned} S_m = 2\delta - \frac{1}{\alpha_m^2 D}[2 + \exp(-\alpha_m^2 D(\Delta - \delta)) - 2\exp(-\alpha_m^2 D\delta) \\ -2\exp(-\alpha_m^2 D\Delta) + \exp(-\alpha_m^2 D(\Delta + \delta))]. \end{aligned} \tag{4.21}$$

In (4.20) the ratio M^+/M_0^+ is the ratio of the echo maximum with non-zero gradient to the echo maximum without gradient. It is frequently abbreviated as E. The α_m are the mth roots of the equation

$$\frac{1}{\alpha R} J_{3/2}(\alpha R) = J_{5/2}(\alpha R) \tag{4.22}$$

with the Bessel functions of the first kind J. The required number of roots was determined to the desired accuracy in MATLAB® by a simple nested-intervals

search. It also holds for the rather complex expressions in (4.20) and (4.21) that for only one diffusion coefficient D and fixed δ and Δ as well as monodisperse droplets a monoexponential decay as function of G_q^2 is obtained. Deviations from the monoexponential decay observed in experiments on emulsions are not assigned to a different dependency on G_q, δ, and Δ but to a distribution of droplet sizes. Usually a log-normal distribution is assumed:

$$P(R) = \frac{1}{\sqrt{2\pi}R\sigma} \exp\left\{-\frac{(\ln(2R/d_{50,3}))^2}{2\sigma^2}\right\}. \tag{4.23}$$

The two parameters of the distribution are the standard deviation σ of the associated normal distribution and in the above formulation the volume-related mean droplet diameter $d_{50,3}$.

The log-normal distribution (4.23) and the expressions in (4.20) and (4.21) were implemented in MATLAB® for a discrete R axis. Thus the signal decay can be calculated for the experimental G_q, δ, and Δ as well as the known unrestricted diffusion coefficient D for water at the experimental temperature as a function of the parameters σ and $d_{50,3}$ by weighting of (4.20) and (4.21) with (4.23). The parameters σ and $d_{50,3}$ of the inner water droplets of the investigated emulsion were obtained by a fit of the calculated signal to the experimental signal using the curve-fitting tools provided by MATLAB®.

In principle the signal decay with diffusion encoding can result not only from restricted diffusion within the droplets but also from a contribution of the overall diffusion of the entire droplet in the outer phase. This contribution was estimated using the Stokes–Einstein equation:

$$D = \frac{kT}{6\pi\eta R_d}. \tag{4.24}$$

Given a typical droplets radius R_d and the viscosity η of the surrounding oil phase the signal decay due to diffusion of the entire droplet can be neglected. Taking the droplets volume fraction ϕ into account, e.g., by a factor $1 - 2\phi$ further reduces the contribution of overall droplet diffusion.

For a double emulsion with large volume fraction of the outer droplets and long observation times restriction of diffusion in the outside phase can be noticeable. A treatment of restricted diffusion in a packing of spheres can be found, e.g., in [4]. In the presented measurements it is assumed that the tortuosity limit is already attained. In this case an effective diffusion coefficient is predicted that amounts to 55% of the value for unrestricted diffusion. Experimentally this has been verified for an O/W emulsion and 65% were obtained.

Indications regarding the composition of the components of the double emulsion as well as their unrestricted diffusion coefficients and relaxation times are collected in Table 4.4. Further details, in particular concerning the production of the double emulsions, can be found in [103]. For the duration of each gradient pulse $\delta = 4$ ms was chosen. Six different observation times were employed, namely $\Delta = 50, 100,$

Table 4.4 NMR measurements on the separate components of the emulsion before the double emulsion is produced. Measurements were performed at 290 K. For the oil phase the most intense peak was evaluated. Water diffusion in the W2 phase is comparable to pure water. [103] © Wiley-VCH Verlag GmbH & Co. KGaA. Reproduced with permission

Component	T_1 / ms	T_2 / ms	D / m^2s^{-1}
Vegetable oil (O phase)	510	50	7.94×10^{-12}
Water with 0.6 wt-% NaCl and 5 wt-% gelatin (W1 phase)	2,280	890	1.68×10^{-9}
Water with 2 wt-% Tween 20 (W2 phase)	2,450	1,620	1.88×10^{-9}

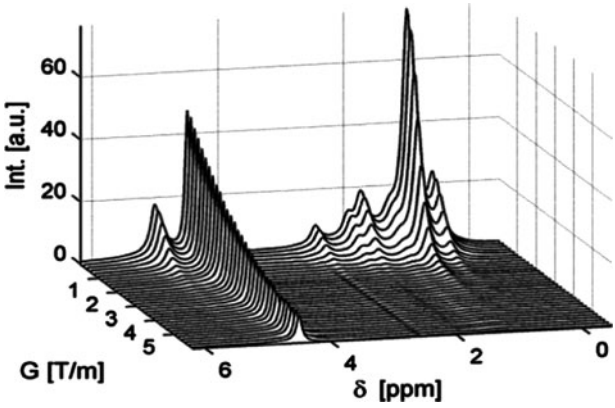

Fig. 4.36 Investigation of diffusion in a W/O emulsion using a PGSTE measurement with spectral resolution. The content of the inner phase with composition of W1 (see Table 4.4) was 10 wt-% and the observation time 150 ms. Although unrestricted diffusion in phase W1 is much faster than in oil, the W1 water signal at 4.6 ppm decays significantly less with diffusion encoding than the remaining signal from the surrounding vegetable oil. [103] © Wiley-VCH Verlag GmbH & Co. KGaA. Reproduced with permission

150, 200, 300, and 500 ms. Results for 150 ms gradient-pulse separation are shown in Fig. 4.36. Further parameters of the pulse sequence represented in Fig. 4.35 are $\tau = 6$ ms, $t_R = 8$ s, $N_q = 32$ (linear steps from 3.5 mT/m to 6 T/m), and $N_A = 2$. Before each measurement two "dummy scans" were performed in order to establish a steady state. The spoiler gradient with 200 mT/m had a duration of 5 ms.

Spectra with diffusion encoding in a PGSTE sequence for a simple W/O emulsion are shown in Fig. 4.36. The effect of restriction in a spherical droplet is obvious from the strongly reduced water-signal decay with increasing diffusion encoding. Note that the water content cannot be directly deduced from the peak integrals in the first spectrum as the oil signals decay faster during τ due to the shorter T_2 time and also during the gradient-pulse separation due to the shorter T_1 time.

For the separated components, the W1/O simple emulsion, and the W1/O/W2 double emulsion experimental results for water are shown in Fig. 4.37a and for oil in Fig. 4.37b, respectively. In the case of the separated components signal decay

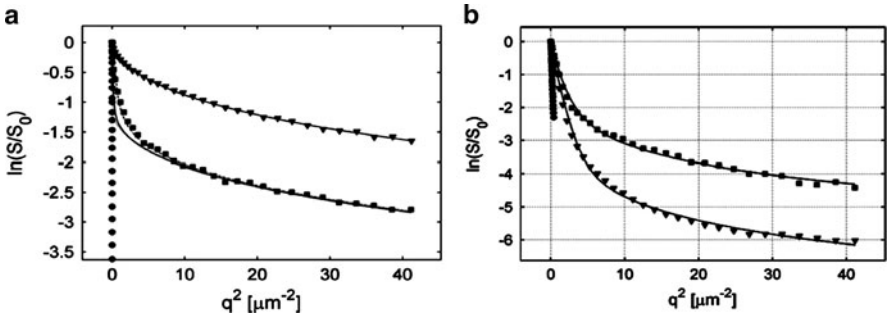

Fig. 4.37 Investigation of diffusion using PGSTE measurements with an observation time of 150 ms at a temperature of 299 K. The ratio of the peak amplitude with diffusion encoding to the amplitude without gradient is denoted as S/S_0. As usual the abbreviation $q = \gamma G_q \delta$ is used. (**a**) Results for the water phase. (**b**) Results for the oil phase. *Filled circles* are used to represent experiments on the separated components (W1 resp. O). *Filled triangles* reflect the results of the measurement on the simple emulsion shown in Fig. 4.36. *Filled squares* correspond to the signal ratios in the double emulsion. For the separated components the expression for unrestricted diffusion (2.71) was fitted (*solid lines*). For the inner phase W1 in the simple emulsion (4.20) and (4.21) with (4.23) could be fitted to the data. This was not the case for the double emulsion. The *solid line* represents the fit of an exchange model. Fit curves plotted for the oil signal in emulsions do not correspond to a particular model. [103] © Wiley-VCH Verlag GmbH & Co. KGaA. Reproduced with permission

is well described by expression (2.71) for unrestricted diffusion. The water signal in the W1/O simple emulsion is a typical case for the description using (4.20) and (4.21) with (4.23). As a result of the fit to the represented data $d_{50,3} = 3.60(3)\ \mu$m and $\sigma = 0.47(2)$ were obtained. Investigations by light scattering yielded a smaller value of $d_{50,3} = 2.28(24)\ \mu$m. However, such a discrepancy is not unusual if droplet-size distributions are studied by different methods.

For the W1/O/W2 double emulsion with mass fractions of 6%/54%/40% the W1 water signal is not well described by (4.20), (4.21), and (4.23). Several observations indicate that some exchange between the inner and outer water phase occurs during the observation time, see discussion in [103]. In the double emulsion, oil diffusion is restricted to within the oil droplet as well as by the presence of inner W1 droplets. The signal decay in this situation was not modeled.

4.10.3 Conclusion

Although further research is required, PFG-NMR is a promising tool for the characterization of multiple emulsions. Light scattering is not well suited as at least the inner phases cannot be diluted and data analysis is difficult for the case of multiple scattering. Investigation by microscopy methods cover only parts of the sample. The resolution of optical microscopy is limited and performing electron

microscopy without modification of the properties of the multiple emulsion is difficult.

As multiple emulsions are of major interest, e.g., in food science or for the encapsulation of active agents suitable PFG-NMR methods would be valuable. For a wide-spread application, implementation on low-field instruments would be advantageous.

4.11 Concluding Remarks

The presented results summarize various applications of NMR and MRI in the field of chemical and process engineering at the KIT. Suitable methods assist the formulation of improved models, provide input data for modeling, and are used to validate the models. Measurements on realistic systems frequently require adaptation and development of the experimental method and data analysis. Although the technique is complex and experimentally demanding, especially as tomographic method, a continued increase of research activities in this area is expected. In many opaque systems, no other non-invasive method can provide comparable results with 3D spatial resolution.

In the domain of low-field NMR, further activities concerning the development and application of online methods are expected, especially in the context of process analytics [55]. Also here, valuable results can be obtained that are complementary to information typically obtained by optical methods.

The vast field of NMR in microporous media is equally of relevance in engineering sciences and was briefly discussed in the context of emulsions, see Sect. 4.10. Methods for the characterization of rocks or investigations using NMR cryoporosimetry and diffusometry can be found, e.g., in [94], [56], and [98], respectively.

Building materials are a special case of porous media in the domain of construction engineering. Numerous investigations using superconducting NMR instruments have been reported, see e.g., [5, 17, 34] for the measurement of longitudinal relaxation and [30] for transverse relaxation . Subjects studied cover, e.g., hydration with [24] and without [30] additives, specific surface[34], the influence of low [86] and high temperatures [19, 40], aging [17], moisture transport [5, 6, 19], as well as molecular structure and proton exchange [21].

As susceptibility artifacts are less pronounced at low field, measurements on building materials are also frequently performed in permanent-magnet systems. For studies of transverse relaxation, see e.g., [24, 33, 53, 73]. As in high-field NMR, hydration with [24, 73] and without [15, 33, 53] additives is investigated. Of interest are, e.g., the pore-size distribution[33, 53, 67] and the effect of low temperatures [53].

In heterogeneous building materials with high specific surface and paramagnetic components decay of transverse magnetization is usually very fast. Unless special materials such as white cement with low iron content are used imaging sequences

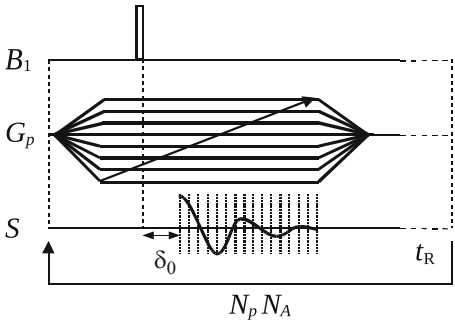

Fig. 4.38 Pulse sequence for 1D single-point imaging (SPI) of solids with acquisition of multiple data points at each phase-encoding gradient. As phase-encoding time increases from point to point, images with increasing relaxation weighting and spatial resolution are obtained

with long encoding times cannot be applied or produce results with strong relaxation weighting. In order to obtain reliable results imaging methods for solids such as single point imaging (SPI) [22] can be employed.

As outlook first measurements showing the applicability of SPI at low field on samples of ordinary gray portland cement paste[8] in the permanent-magnet instrument described in Sect. 3.2 are presented. The pulse sequence is depicted in Fig. 4.38. Space encoding is performed by pure phase encoding. The phase gradient G_p is switched on before the rf pulse so that no delay for gradient stabilization has to be provided after excitation. Consequently a broad-banded rf pulse has to be used, otherwise sample excitation is restricted by slice selection.

Instead of acquiring a single phase-encoded data point per gradient amplitude, several points sampling the decaying signal were recorded. For each encoding time a relaxation weighted spin-density profile is obtained. With increasing encoding time relaxation weighting as well as spatial resolution increase. As example, results for a geometry test sample are shown in Fig. 4.39. It consisted of two water saturated[9] cement-paste cylinders separated by a PTFE spacer. At each of the 128 phase-encoding steps 16 data points were acquired. Using a rather long excitation pulse of 10.5 μs slice selection at the highest gradients was accepted to some extent ($|G_{\mathrm{p,max}}| = 342\,\mathrm{mT/m}$). In order to improve SNR 64 scans were averaged with a repetition delay of 500 ms. The result of inverse Fourier transform in phase-encoding direction is represented in Fig. 4.39a as function of grid point number. In Fig. 4.39b the abscissa is converted into the space axis by multiplication with the spatial resolution depending on the gradient-amplitude increment as well as phase-encoding time. In addition the signal intensity is corrected by the spatial resolution as the signal is distributed over more grid points at higher resolution. The position of the spacer from about 0 mm to 1 mm is clearly observed. Signal decay toward the edges of the FOV results from the rf profile. Already at the shortest encoding time $\delta_0 = 100\,\mu$s the signal originates predominantly from evaporable

[8]CEM I 42,5 HS samples were kindly prepared and provided by Z. Djuric and M. Haist, KIT, CS, IMB.

[9]Saturated at 150 bar after evacuation and stored in water for 20 days.

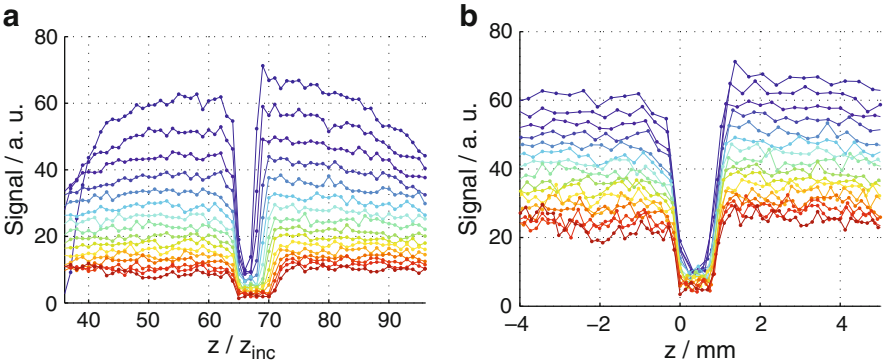

Fig. 4.39 Relaxation weighted spin-density profiles of two water saturated cement-paste cylinders separated by a PTFE spacer. Ordinary gray portland cement was used. Blue points: phase-encoding time $\delta_0 = 100\,\mu$s, resulting in a spatial resolution of $z_{inc} = 344\,\mu$m; red points: $\delta = 250\,\mu$s resulting in $z_{inc} = 138\,\mu$m. (**a**) Result after inverse Fourier transform in phase-encoding direction. With increasing resolution the spin density is distributed on an increasing number of grid points. This effect leads to an additional decrease of the obtained signal intensity. (**b**) Results represented over the individual spatial grid points after correction of the effect of resolution on signal intensity

water. The dead time of the probe is 50 μs. In order to investigate also, e.g., crystal water or hydroxyl protons of portlandite a dead time of about 10 μs is required. Here further developments and investigations are planned.

References

1. Arola D, Barrall G, Powell R, McCarthy K, McCarthy M (1997) Use of nuclear magnetic resonance imaging as a viscometer for process monitoring. Chem Eng Sci 52(13):2049–2057
2. Arola DF, Powell RL, Barrall GA, McCarthy MJ (1998) A simplified method for accuracy estimation of nuclear magnetic resonant imaging. Rev Sci Instrum 69(9):3300–3307
3. Arola DF, Powell RL, Barrall GA, McCarthy MJ (1999) Pointwise observations for rheological characterization using nuclear magnetic resonance imaging. J Rheol 43(1):9–30
4. Bardakci M, Tillich JE, Holz M (2006) Characterization of structure and transport in porous media by pulsed field gradient (PFG) NMR technique – Part I: Master curve and characteristic inner length. Chem Eng Technol 29(7):847–853. DOI 10.1002/ceat.200600043
5. Beyea S, Balcom B, Bremner T, Armstrong R, Grattan-Bellew P (2003) Detection of drying-induced microcracking in cementitious materials with space-resolved H-1 nuclear magnetic resonance relaxometry. J Am Ceram Soc 86(5):800–805
6. Beyea S, Balcom B, Bremner T, Prado P, Green D, Armstrong R, Grattan-Bellew P (1998) Magnetic resonance imaging and moisture content profiles of drying concrete. Cement Concrete Res 28(3):453–463
7. Birkhofer BH, Jeelani SAK, Windhab EJ, Ouriev B, Lisner KJ, Braun P, Zeng Y (2008) Monitoring of fat crystallization process using UVP-PD technique. Flow Meas Instrum 19(3–4):163–169. DOI 10.1016/j.flowmeasinst.2007.08.008
8. Bloembergen N, Purcell EM, Pound RV (1948) Relaxation effects in nuclear magnetic resonance absorption. Phys Rev 73:679–712

9. Blümich B, Casanova F, Appelt S (2009) NMR at low magnetic fields. Chem Phys Lett 477(4–6):231–240. DOI 10.1016/j.cplett.2009.06.096
10. Brunn PO, Wunderlich T, Muller M (2004) Ultrasonic rheological studies of a body lotion. Flow Meas Instrum 15(3):139–144
11. Buciuman F, Kraushaar-Czarnetzki B (2003) Ceramic foam monoliths as catalyst carriers. 1. Adjustment and description of the morphology. Ind Eng Chem Res 42(9):1863–1869. DOI 10.1021/ie0204134
12. Bürger R, Concha F, Karlsen KH (2001) Phenomenological model of filtration processes: 1. Cake formation and expression. Chem Eng Sci 56(15):4537–4553
13. Callaghan PT (1999) Rheo-NMR: Nuclear magnetic resonance and the rheology of complex fluids. Rep Prog Phys 62(4):599–670
14. Callaghan PT (2008) Rheo NMR and shear banding. Rheologica Acta 47(3):243–255. DOI 10.1007/s00397-007-0251-2
15. Cano-Barrita PFdJ, Marble AE, Balcom BJ, Garcia JC, Masthikin IV, Thomas MDA, Bremner TW (2009) Embedded NMR sensors to monitor evaporable water loss caused by hydration and drying in Portland cement mortar. Cement Concrete Res 39(4):324–328. DOI 10.1016/j.cemconres.2009.01.011
16. Casanova F, Perlo J, Blümich B (2004) Velocity distributions remotely measured with a single-sided NMR sensor. J Magn Reson 171(1):124–130. DOI 10.1016/j.jmr.2004.08.008
17. Chemmi H, Petit D, Levitz P, Korb JP (2010) NMR control of aging and durability of hardened cement pastes. CR Chim 13(4):405–408. DOI 10.1016/j.crci.2009.09.003
18. Cheung MK, Powell RL, McCarthy MJ (1997) Nuclear-magnetic-resonance-imaging-based capillary rheometer. AICHE J 43(10):2596–2600
19. Dicoi O, Walzel P, Blumich B, Rahse W (2004) Investigation of the drying behavior of solids by nuclear magnetic resonance. Chem Ing Tech 76(1–2):94–99. DOI 10.1002/cite.200403323. Meeting of the GVC committees on drying technology, heat and material transfer, Marburg, Germany, 17–19 March 2003
20. Dirckx C, Clark S, Hall L, Antalek B, Tooma J, Hewitt J, Kawaoka K (2000) Magnetic resonance imaging of the filtration process. AICHE J 46(1):6–14
21. Dolinsek J, Apih T, Lahajnar G, Blinc R, Papavassiliou G, Pintar M (1998) Two-dimensional nuclear magnetic resonance study of a hydrated porous medium: An application to white cement. J Appl Phys 83(7):3535–3540
22. Emid S, Creyghton J (1985) High-resolution NMR imaging in solids. Physica B & C 128(1):81–83
23. Erk A, Hardy EH, Althaus T, Stahl W (2006) Filtration of colloidal suspensions – MRI investigation and numerical simulation. Chem Eng Technol 29(7):828–831. DOI 10.1002/ceat.200600054
24. Friedemann K, Stallmach F, Karger J (2006) NMR diffusion and relaxation studies during cement hydration – A non-destructive approach for clarification of the mechanism of internal post curing of cementitious materials. Cement Concrete Res 36(5):817–826. DOI 10.1016/j.cemconres.2005.12.007
25. von Garnier A, Hardy EH, Schweitzer JM, Reimert R (2007) Differentiation of catalyst and catalyst support in a fixed bed by magnetic resonance imaging. Chem Eng Sci 62(18–20, Sp. Iss. SI):5330–5334. DOI 10.1016/j.ces.2007.03.034
26. Gibbs SJ, Haycock DE, Frith WJ, Ablett S, Hall LD (1997) Strategies for rapid NMR rheometry by magnetic resonance imaging velocimetry. J Magn Reson 125(1):43–51
27. Gibbs SJ, James KL, Hall LD, Haycock DE, Frith WJ, Ablett S (1996) Rheometry and detection of apparent wall slip for Poiseuille flow of polymer solutions and particulate dispersions by nuclear magnetic resonance velocimetry. J Rheol 40(3):425–440
28. Gibbs SJ, Xing D, Carpenter TA, Hall LD, Ablett S, Haycock D, Frith WJ (1994) NMR flow imaging of aqueous polysaccharide solutions. J Rheol 38(6):1757–1767
29. Gladden LF, Alexander P (1996) Applications of nuclear magnetic resonance imaging in process engineering. Meas Sci Technol 7(3):423–435

30. Greener J, Peemoeller H, Choi C, Holly R, Reardon E, Hansson C, Pintar M (2000) Monitoring of hydration of white cement paste with proton NMR spin–spin relaxation. J Am Ceram Soc 83(3):623–627
31. Grosse J, Dietrich B, Martin H, Kind M, Vicente J, Hardy EH (2008) Volume image analysis of ceramic sponges. Chem Eng Technol 31(2):307–314. DOI 10.1002/ceat.200700403
32. Haiduc AM, Trezza EE, van Dusschoten D, Reszka AA, van Duynhoven JPM (2007) Non-invasive 'through-package' assessment of the microstructural quality of a model food emulsion by the NMR MOUSE. LWT Food Sci Technol 40(4):737–743. DOI 10.1016/j.lwt.2006.02.026
33. Halperin W, Jehng J, Song Y (1994) Application of spin–spin relaxation to measurement of surface areo and pore-size distributions in a hydrating cement paste. Magn Reson Imaging 12(2):169–173. 2nd International meeting on recent advances in MR applications to porous media, CANTERBURY, ENGLAND, 14–16 April 1993
34. Hansen E, Gran H, Kvernberg P, Pedersen B (1997) Surface-to-volume ratio of porous materials obtained by a combined use of NMR and MIP. J Phys Chem B 101(45):9206–9214
35. Hansen E, Law P (1985) Recursive methods for computing the Abel transform and its inverse. J Opt Soc Am A 2(4):510–520
36. Hardy EH, Hoferer J, Kasper G (2007) The mixing state of fine powders measured by magnetic resonance imaging. Powder Technol 177(1):12–22. DOI 10.1016/j.powtee.2007.02.042
37. Hardy EH, Hoferer J, Mertens D, Kasper G (2009) Automated phase correction via maximization of the real signal. Magn Reson Imaging 27(3):393–400. DOI 10.1016/j.mri.2008.07.009
38. Hardy EH, Mertens D, Hochstein B, Nirschl H (2009) Compact NMR-based Capillary Rheometer. In: Fischer P, Pollard M, Windhab EJ (eds) Proceedings of the 5th ISFRS, pp 94–97. http://www.isfrs.ethz.ch/proc/2009_proc. 5th International symposium on food rheology and structure, ETH Zrich, Zrich, 15–18 June 2009
39. Hardy EH, Mertens D, Hochstein B, Nirschl H (2009) Kompaktes, NMR-gesttztes Kapillarrheometer. Chem Ing Tech 81(8):1100–1101
40. van der Heijden GHA, van Bijnen RMW, Pel L, Huinink HP (2007) Moisture transport in heated concrete, as studied by NMR, and its consequences for fire spalling. Cement Concrete Res 37(6):894–901. DOI 10.1016/j.cemconres.2007.03.004
41. Herle V, Manneville S, Fischer P (2008) Ultrasound velocimetry in a shear-thickening wormlike micellar solution: Evidence for the coexistence of radial and vorticity shear bands. Eur Phys J E 26(1–2):3–12. DOI 10.1140/epje/i2007-10304-3
42. Hieke M, Ruland J, Anlauf H, Nirschl H (2009) Analysis of the porosity of filter cakes obtained by filtration of colloidal suspensions. Chem Eng Technol 32(7):1095–1101. DOI 10.1002/ceat.200800609
43. Hill KM, Caprihan A, Kakalios J (1997) Bulk segregation in rotated granular material measured by magnetic resonance imaging. Phys Rev Lett 78(1):50–53
44. Hindman J (1966) Proton resonance shift of water in gas and liquid states. J Chem Phys 44(12):4582–4592
45. Hoferer J, Lehmann MJ, Hardy EH, Meyer J, Kasper G (2006) Highly resolved determination of structure and particle deposition in fibrous filters by MRI. Chem Eng Technol 29(7):816–819. DOI 10.1002/ceat.200600047
46. Hollingsworth K, Johns M (2003) Measurement of emulsion droplet sizes using PFG NMR and regularization methods. J Colloid Interface Sci 258(2):383–389. DOI 10.1016/S0021-9797(02)00131-5
47. Hollingsworth K, Johns M (2005) Spatially resolved emulsion droplet sizing using inverse Abel transforms. J Magn Reson 176(1):71–78. DOI 10.1016/j.jmr.2005.05.019
48. Hollingsworth K, Sederman A, Buckley C, Gladden L, Johns M (2004) Fast emulsion droplet sizing using NMR self-diffusion measurements. J Colloid Interface Sci 274(1):244–250. DOI 10.1016/j.jcis.2004.02.074

49. Horsfield MA, Fordham EJ, Hall C, Hall LD (1989) H-1-NMR imaging studies of filtration in colloidal suspensions. J Magn Reson 81(3):593–596
50. Hoskins B, Fevang L, Majors P, Sharma M, Georgiou G (1999) Selective imaging of biofilms in porous media by NMR relaxation. J Magn Reson 139(1):67–73
51. Hutsel MR, Montarou CC, Dachevski AI, Gaylord TK (2008) Algorithm performance in the determination of the refractive-index profile of optical fibers. Appl Optics 47(6):760–767
52. Jackson JA, Burnett LJ, Harmon JF (1980) Remote (inside-out) NMR.3. Detection of nuclear magnetic-resonance in a remotely produced region of homogeneous magnetic-field. J Magn Reson 41(3):411–421
53. Jehng J, Sprague D, Halperin W (1996) Pore structure of hydrating cement paste by magnetic resonance relaxation analysis and freezing. Magn Reson Imaging 14(7–8):785–791. 3rd International meeting on recent advances in MR applications to porous media, Louvian, Belgium, 03–06 September 1995
54. Johns M, Gladden L (2002) Sizing of emulsion droplets under flow using flow-compensating NMR-PFG techniques. J Magn Reson 154(1):142–145. DOI 10.1006/jmre.2001.2469
55. Kessler RWH (ed) (2006) Prozessanalytik : Strategien und Fallbeispiele aus der industriellen Praxis. WILEY-VCH, Weinheim
56. Khokhlov A, Valiullin R, Kaerger J, Steinbach F, Feldhoff A (2007) Freezing and melting transitions of liquids in mesopores with ink-bottle geometry. New J Phys 9:1–9. DOI 10.1088/1367-2630/9/8/272
57. Kimmich R (1997) NMR tomography, diffusometry, relaxometry. Springer-Verlag, Berlin, Heidelberg, New York
58. Knoerzer K, Regier M, Hardy EH, Schuchmann HP, Schubert H (2009) Simultaneous microwave heating and three-dimensional MRI temperature mapping. Innov Food Sci Emerg 10:537–544
59. Koptyug I, Khitrina L, Parmon V, Sagdeev R (2001) NMR imaging of mass transport and related phenomena in porous catalysts and sorbents. Magn Reson Imaging 19(3–4):531–534
60. Kotze R, Haldenwang R, Slatter P (2008) Rheological characterization of highly concentrated mineral suspensions using ultrasound velocity profiling with combined pressure difference method. Appl Rheol 18(6):1–10
61. Kriesten E, Alsmeyer F, Bardow A, Marquardt W (2008) Fully automated indirect hard modeling of mixture spectra. Chemom Intell Lab Syst 91(2):181–193. DOI 10.1016/j.chemolab.2007.11.004
62. Lebihan D, Delannoy J, Levin R (1989) Temperature mapping with MR imaging of molecular-diffusion – Application to hyperthermia. Radiology 171(3):853–857
63. Lehmann MJ, Hardy EH, Meyer J, Kasper G (2003) Determination of fibre structure and packing density distribution in depth filtration media by means of MRI. Chem Ing Tech 75(9):1283–1286. DOI 10.1002/cite.200303229
64. Lehmann MJ, Hardy EH, Meyer J, Kasper G (2005) MRI as a key tool for understanding and modeling the filtration kinetics of fibrous media. Magn Reson Imaging 23(2):341–342. DOI 10.1016/j.mri.2004.11.048
65. Majors P, Caprihan A (1991) Fast radial imaging of circular and spherical objects by NMR. J Magn Reson 94(2):225–233
66. Martin H (1978) Low peclet number particle-to-fluid heat and mass-transfer in packed-beds. Chem Eng Sci 33(7):913–919
67. McDonald PJ, Rodin V, Valori A (2010) Characterisation of intra- and inter-C-S-H gel pore water in white cement based on an analysis of NMR signal amplitudes as a function of water content. Cement Concrete Res 40(12):1656–1663. DOI 10.1016/j.cemconres.2010.08.003
68. Mertens D, Hardy EH, Hochstein B, Guthausen G (2009) A low-field-NMR capillary rheometer. In: Guojonsdottir M, Belton P, Webb G (eds) Magnetic resonance in food science: Challenges in a changing world, pp 81–88. 9th International conference on applications of magnetic resonance in food science, Reykjavik, Iceland, 15–17 September 2008
69. Metzger U, Lankes U, Hardy EH, Gordalla BC, Frimmel FH (2006) Monitoring the formation of an Aureobasidium pullulans biofilm in a bead-packed reactor via flow-weighted magnetic resonance imaging. Biotechnol Lett 28(16):1305–1311. DOI 10.1007/s10529-006-9091-x

70. Muller M, Brunn PO, Wunderlich T (1997) New rheometric technique: The gradient-ultrasound pulse Doppler method. Appl Rheol 7(5):204–210
71. Murday J, Cotts R (1968) Self-diffusion coefficient of liquid lithium. J Chem Phys 48(11):4938–4945
72. Nakagawa M, Altobelli SA, Caprihan A, Fukushima E, Jeong EK (1993) Noninvasive measurements of granular flows by magnetic-resonance-imaging. Exp Fluids 16(1):54–60
73. Nestle N, Kuehn A, Friedemann K, Horch C, Stallmach F, Herth G (2009) Water balance and pore structure development in cementitious materials in internal curing with modified superabsorbent polymer studied by NMR. Micropor Mesopor Mat 125(1–2, Sp. Iss. SI):51–57. DOI 10.1016/j.micromeso.2009.02.024
74. Nguyen NL, van Buren V, von Garnier A, Hardy EH, Reimert R (2005) Application of Magnetic Resonance Imaging (MRI) for investigation of fluid dynamics in trickle bed reactors and of droplet separation kinetics in packed beds. Chem Eng Sci 60(22):6289–6297. DOI 10.1016/j.ces.2005.04.083
75. Nguyen NL, Reimert R, Hardy EH (2006) Application of magnetic resonance imaging (MRI) to determine the influence of fluid dynamics on desulfurization in bench scale reactors. Chem Eng Technol 29(7):820–827. DOI 10.1002/ceat200600058
76. Noll DC, Nishimura DG, Macovski A (1991) Homodyne detection in magnetic-resonance-imaging. IEEE Trans Med Imaging 10(2):154–163
77. Nott K, Hall L, Bows J, Hale M, Patrick M (1999) Three-dimensional MRI mapping of microwave induced heating patterns. Int J Food Sci Technol 34(4):305–315
78. Nott K, Paterson-Beedle M, Macaskie L, Hall L (2001) Visualisation of metal deposition in biofilm reactors by three-dimensional magnetic resonance imaging (MRI). Biotechnol Lett 23(21):1749–1757
79. Ouriev B, Windhab E, Braun P, Birkhofer B (2004) Industrial application of ultrasound based in-line rheometry: From stationary to pulsating pipe flow of chocolate suspension in precrystallization process. Rev Sci Instrum 75(10, Part 1):3164–3168. DOI 10.1063/1.1790585
80. Ouriev B, Windhab EJ (2002) Rheological study of concentrated suspensions in pressure-driven shear flow using a novel in-line ultrasound Doppler method. Exp Fluids 32(2):204–211. DOI 10.1007/s003480100345
81. Pedersen H, Ablett S, Martin D, Mallett M, Engelsen S (2003) Application of the NMR-MOUSE to food emulsions. J Magn Reson 165(1):49–58. DOI 10.1016/S1090-7807(03)00243-X
82. Peller M, Kurze V, Loeffler R, Pahernik S, Dellian M, Goetz A, Issels R, Reiser M (2003) Hyperthermia induces T-1 relaxation and blood flow changes in tumors. A MRI thermometry study in vivo. Magn Reson Imaging 21(5):545–551. DOI 10.1016/S0730-725X(03)00070-5
83. Perlo J, Casanova F, Blümich B (2005) Velocity imaging by ex situ NMR. J Magn Reson 173(2):254–258. DOI 10.1016/j.jmr.2004.12.010
84. Pernenkil L, Cooney CL (2006) A review on the continuous blending of powders. Chem Eng Sci 61(2):720–742. DOI 10.1016/j.ces.2005.06.016
85. Porion P, Sommier N, Faugere AM, Evesque P (2004) Dynamics of size segregation and mixing of granular materials in a 3D-blender by NMR imaging investigation. Powder Technol 141(1–2):55–68. DOI 10.1016/j.powtec.2004.02.015
86. Prado P, Balcom B, Beyea S, Bremner T, Armstrong R, Grattan-Bellew P (1998) Concrete freeze/thaw as studied by magnetic resonance imaging. Cement Concrete Res 28(2):261–270
87. Regier M, Hardy EH, Knoerzer K, Leeb CV, Schuchmann HP (2007) Determination of structural and transport properties of cereal products by optical scanning, magnetic resonance imaging and Monte Carlo simulations. J Food Eng 81(2):485–491. DOI 10.1016/j.jfoodeng.2006.11.025
88. Regier M, Idda P, Knoerzer K, Hardy EH, Schuchmann HR (2006) Temperature- and water distribution in convective drying by means of inline magnetic resonance tomography. Chem Ing Tech 78(8):1112–1115. DOI 10.1002/cite.200600041

89. Ren X, Stapf S, Blümich B (2005) NMR velocimetry of flow in model fixed-bed reactors of low aspect ratio. AICHE J 51(2):392–405
90. Schmidt E (2008) Dust separation. In: Ullmann's Encyclopedia of industrial chemistry. Wiley-VCH, Weinheim, pp 1–37.
91. Schweers E, Loffler F (1994) Realistic modeling of the behavior of fibrous filters through consideration of filter structure. Powder Technol 80(3):191–206
92. Seymour J, Codd S, Gjersing E, Stewart P (2004) Magnetic resonance microscopy of biofilm structure and impact on transport in a capillary bioreactor. J Magn Reson 167(2):322–327. DOI 10.1016/j.jmr.2004.01.009
93. Sommer K (2008) Mixing of solids. In: Ullmann's Encyclopedia of industrial chemistry. Wiley-VCH, Weinheim, pp 1–17.
94. Song Y, Ryu S, Sen P (2000) Determining multiple length scales in rocks. Nature 406(6792):178–181
95. Stahl S, Spelter LE, Nirschl H (2008) Investigations on the separation efficiency of tubular bowl centrifuges. Chem Eng Technol 31(11):1577–1583. DOI 10.1002/ceat.200800300
96. Topgaard D, Malmborg C, Soderman O (2002) Restricted self-diffusion of water in a highly concentrated W/O emulsion studied using modulated gradient spin-echo NMR. J Magn Reson 156(2):195–201. DOI 10.1006/jmre.2002.2556
97. Uludag Y, Powell RL, McCarthy MJ (2004) Effects of periodic flow fluctuations on magnetic resonance flow images. AICHE J 50(8):1662–1671. DOI 10.1002/aic.10152
98. Valiullin R, Kaerger J, Glaeser R (2009) Correlating phase behaviour and diffusion in mesopores: perspectives revealed by pulsed field gradient NMR. Phys Chem Chem Phys 11(16):2833–2853. DOI 10.1039/b822939b
99. Vicente J, Topin F, Daurelle JV (2006) Open celled material structural properties measurement: From morphology to transport properties. Mater Trans 47(9):2195–2202. DOI 10.2320/matertrans.47.2195
100. Vicharelli P, Lapatovich W (1987) Iterative method for computing the inverse Abel transform. Appl Phys Lett 50(10):557–559
101. Wiklund J, Shahram I, Stading M (2007) Methodology for in-line rheology by ultrasound Doppler velocity profiling and pressure difference techniques. Chem Eng Sci 62(16):4277–4293. DOI 10.1016/j.ces.2007.05.007
102. Wlodarczyk W, Boroschewski R, Hentschel M, Wust P, Monich G, Felix R (1998) Three-dimensional monitoring of small temperature changes for therapeutic hyperthermia using MR. J Magn Reson Imaging 8(1):165–174
103. Wolf F, Hecht L, Schuchmann HP, Hardy EH, Guthausen G (2009) Preparation of W-1/O/W-2 emulsions and droplet size distribution measurements by pulsed-field gradient nuclear magnetic resonance (PFG-NMR) technique. Eur J Lipid Sci Tech 111(7):730–742. DOI 10.1002/ejlt.200800272
104. Wu DH, Chen A, Johnson CS (1995) Flow imaging by means of 1D pulsed-field-gradient NMR with application to electroosmotic flow. J Magn Reson Ser A 115(1):123–126

Chapter 5
Solutions

5.1 Problems of Chapter 2

2.1 NMR Master Equation
To apply (2.8) the linear frequency has to be transformed into angular frequency:

$$\gamma = \frac{2\pi\nu}{B_0} = \frac{2\pi\, 200.13 \times 10^6\,\mathrm{Hz}}{4.7\,\mathrm{T}} = 2.675 \times 10^8\,\mathrm{rad\,s^{-1}\,T^{-1}}.$$

For other nuclei see list of constants on p. xviii.

2.2 Curie's law
Rather obviously $\sum_{m=-I}^{I} 1 = (2I+1)$ and $\sum_{m=-I}^{I} m = 0$. The relation

$$\sum_{m=-I}^{I} m^2 = I(I+1)(2I+1)/3$$

can be proved by mathematical induction.

2.3 NMR Master Equation in the Context of Precession
Precession of magnetization around $\boldsymbol{B}$ with angular velocity $-\gamma B_0$ is expressed as

$$\begin{pmatrix} M_x \\ M_y \\ M_z \end{pmatrix} = \begin{pmatrix} M_{xy}\cos(\phi_0 - \gamma B_0 t) \\ M_{xy}\sin(\phi_0 - \gamma B_0 t) \\ M_{z0} \end{pmatrix}.$$

Insertion into (2.12) shows that this is a solution.

It can also be seen from the geometric representation e.g. for the case of magnetization in the transverse plane:

E.H. Hardy, *NMR Methods for the Investigation of Structure and Transport*,
DOI 10.1007/978-3-642-21628-2_5, © Springer-Verlag Berlin Heidelberg 2012

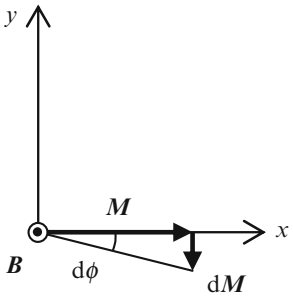

The increment of length $\mathrm{d}M = \gamma M B\,\mathrm{d}t$ is perpendicular to $\boldsymbol{B}$ and $\boldsymbol{M}$. Thus $\boldsymbol{M}$ reorients by an angle $\mathrm{d}\phi$ which for infinitesimal increment equals $\mathrm{d}M/M = \gamma B\,\mathrm{d}t$. This results in the angular velocity with magnitude $\omega_0 = \mathrm{d}\phi/\mathrm{d}t = \gamma B$.

2.4 Rabi Nutation

The period of nutation is $4 \times 12.5\,\mu\mathrm{s} = 50\,\mu\mathrm{s}$ and thus the Rabi frequency 20 kHz. The magnitude of $\boldsymbol{B_1}$ can be calculated from (2.24). As the nutation frequency is 10^{-4} times the precession frequency in problem 2.1 the magnitude of $\boldsymbol{B_1}$ amounts to $4.7\ 10^{-4}$ T. This situation is not suited for a graphical representation as in Fig. 2.2.

2.5 Fourier Imaging: Example of *k*-Space Point for Discrete Sample

Sketch of the magnetization of the droplets in the rotating frame before (a) and after (b) the application of a gradient along x:

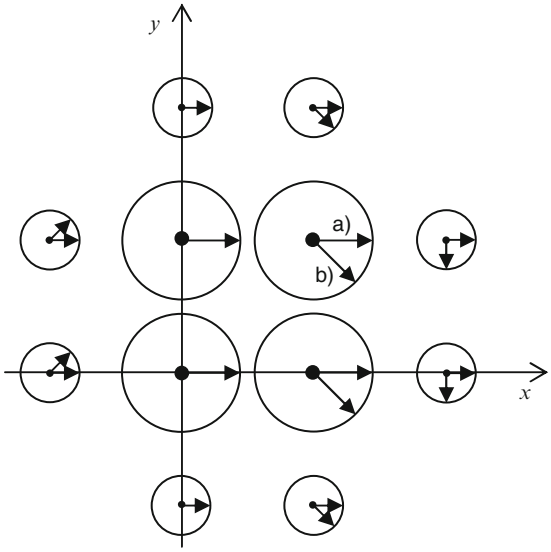

The angle of precession is calculated according to (2.34).

Before the gradient-pulse application the total magnetization only has a non-zero x component. In units of the small-droplet magnetization M_0 it amounts to

$$M_x = (8 + 4 \times 2)M_0 = 16\, M_0 \,.$$

After the gradient pulse the x component of the total magnetization reduces to

$$M_x = \left(2\frac{1}{2}\sqrt{2} + 6 + 6\frac{1}{2}\sqrt{2}\right) M_0 = (6 + 4\sqrt{2})M_0 \,.$$

The y components of the magnetization only partially cancel, leaving

$$M_y = \left(-4\frac{1}{2}\sqrt{2} - 2\right) M_0 = -(2 + 2\sqrt{2})M_0 \,.$$

2.6 Fourier Imaging: Analytical Expression for a Simple Sample
In this special case the integral of the signal (2.38) simplifies to the product of three integrals:

$$M^+(\boldsymbol{k}) = \rho_0 \int_{-a/2}^{a/2} \exp(-ik_x x)\mathrm{d}x \int_{-a/2}^{a/2} \exp(-ik_y y)\mathrm{d}y \int_{-a/2}^{a/2} \exp(-ik_z z)\mathrm{d}z \,.$$

As example the first integral is solved:

$$\begin{aligned}
\int_{-a/2}^{a/2} \exp(-ik_x x)\mathrm{d}x &= \left[\frac{1}{-ik_x} \exp(-ik_x x)\right]_{-a/2}^{a/2} \\
&= \frac{i}{k_x}\left\{\cos\left(-k_x\frac{a}{2}\right) + i\,\sin\left(-k_x\frac{a}{2}\right)\right. \\
&\quad \left. - \cos\left(k_x\frac{a}{2}\right) - i\,\sin\left(k_x\frac{a}{2}\right)\right\} \\
&= \frac{2}{k_x}\sin\left(k_x\frac{a}{2}\right) \\
&= a\,\mathrm{sinc}\left(k_x\frac{a}{2}\right) \,.
\end{aligned}$$

The expression for the ideal signal thus reads

$$M^+(\boldsymbol{k}) = \rho_0 a^3 \mathrm{sinc}\left(k_x\frac{a}{2}\right)\mathrm{sinc}\left(k_y\frac{a}{2}\right)\mathrm{sinc}\left(k_z\frac{a}{2}\right).$$

In this special case the signal is real. Obviously the signal at the center of $\boldsymbol{k}$-space reflects the total number of spins, i.e., the spin density multiplied by the volume.[1] The first positive node of the signal in x direction occurs for $k_x\frac{a}{2} = \pi$. Larger samples correspond to narrower signals in reciprocal space.

[1] sinc(0) = 1 as can be seen from l'Hospital's rule.

2.7 Slice Selection

(a) The bandwidth of an infinite sinc pulse with (1/6) ms between the maximum and the first zero crossing is 6 kHz, see also solution 2.6. Thus the gradient amplitude amounts to

$$G_s = \frac{2\pi\, 6\,\text{kHz}}{\gamma\, 1\,\text{mm}} = 141\,\text{mT}\,.$$

(b) The shift of the carrier frequency is calculated according to (2.50) with $\Delta\omega$ for the shift in angular frequency instead of the bandwidth and Δz for the distance from slice center to slice center instead of the slice thickness. Given the slice thickness of 1 mm and the gap of 1 mm, the distance of slice centers amounts to 2 mm. With the same gradient as in (a) this corresponds to a shift in carrier frequency of 12 kHz.

(c) In the center of the slice (no additional field due to the gradient) magnetization nutates around the $\boldsymbol{B_1}$ field. Changes in sign of B_1 amplitude signify a change in the direction of nutation. The major part of magnetization dynamics occurs around the center of the rf pulse. As estimate, the central part is replaced by a block pulse with the maximum amplitude and other contributions are neglected. Assuming an equivalent duration of the block pulse of somewhat less than (1/6) ms, e.g., 150 μs, the rf amplitude is calculated to 39 μT from $-\gamma B_1 \tau = \pi/2$. For the exact value of the maximum amplitude $\hat{B}_1$ the integral of the normalized amplitude shape has to be calculated. For the sinc3 pulse the relation (2.52) leads to

$$-\gamma \hat{B}_1 \int_0^\tau \text{sinc}\{6\pi(t-\tau/2)/\tau\}\,\text{d}t = \pi/2\,.$$

Denoting the average of the normalized amplitude shape by $\bar{b}_1$ this can also be expressed as

$$-\gamma \hat{B}_1 \bar{b}_1 \tau = \pi/2\,.$$

As can be seen in Fig. 2.5a the exact calculation leads to a slightly smaller value for the maximum value than the above estimation.

2.8 Diffusometry vs. Velocimetry

(a) The diffusion coefficient for water at ambient temperature amounts to $D = 2.3 \times 10^{-9}\,\text{m}^2/\text{s}$. During an observation time of $\Delta = 10\,\text{ms}$ this results in a root-mean-square displacement of 6.8 μm.

(b) At a velocity of $v = 1\,\text{mm/s}$ without diffusion, the displacement during the same time amounts to $l = 10\,\mu\text{m}$. The Peclet number for mass diffusion $\text{Pe} = lv/D$ calculated with this length is $\text{Pe} = (v\Delta)^2/(D\Delta) = 4.3$. In such a situation with rather small velocity and large diffusion coefficient, the signal in NMR velocimetry will be markedly attenuated by diffusion.

Chapter 6
Source Code

6.1 specSurfOM

```
%  specSurfOM calculates the specific surface as in
%  Ohser, J. and Muecklich, F., Statistical Analysis of
%  Microstructures in Materials Science,
%  Wiley & Sons, Chichester, England (2000).
%  Input: binary image as matrix and grid spacing as vector
%============================================================
%
%  Name:        specSurfOM.m
%
%  Author:      EH
%  Date:        2006/12/06
%
%  Modifications on 2006/00/00 by EH:
%
%  Bugs, suggestions, remarks:
%  Runs under MatLab 6.5, not under 7.0
%
%============================================================
function [vf sp surfaceAbs]=specSurfOM(bin_image,Delta)
n = size(bin_image);
h = ghist(n, bin_image);
vf = volfrac(h);
[sp surfaceAbs]=specsurf(h,Delta);
%%%%%%%%%%%%%%%%%%%%%%%%%%%%%%%%%%%%%%%%%%%%%%%%%%%%%%%%%%%%%%
%Subroutines
%------------------------------------------------------------
function h = ghist(n, bin_image)
% Orginal by Ohser and Mcklich in C:
% #include<math.h>
% #include<malloc.h>
% long int *ghist(int *n, int ***bin_image)
% /* given a 3-dimensional binary image bin_image of size
%    n[0..2], the image is convolved with a filter mask F and
%    the gray-tone histogram h[0..255] of the convolved image
```

E.H. Hardy, *NMR Methods for the Investigation of Structure and Transport*,
DOI 10.1007/978-3-642-21628-2_6, © Springer-Verlag Berlin Heidelberg 2012

```
%        is returned
% */
% {  int i, j, k;
%    int l;
%    long int *h;
%    h=(long *)malloc(256*sizeof(long));
%    for(l=0;l<256;l++) h[l]=0L;
%    for(i=0;i<n[0]-1;i++)
%       for(j=0;j<n[1]-1;j++)
%       {  l=bin_image[i][j][0]+(bin_image[i+1][j][0]<<1)
%             +(bin_image[i][j+1][0]<<2)
%             +(bin_image[i+1][j+1][0]<<3);
%          for(k=0;k<n[2]-1;k++)
%          {  l+=(bin_image[i][j][k+1]<<4)
%              +(bin_image[i+1][j][k+1]<<5)
%              +(bin_image[i][j+1][k+1]<<6)
%              +(bin_image[i+1][j+1][k+1]<<7);
%             h[l]++; l>>=4;
%          }
%       }
%    return h;
% }
% Translation into Matlab:
h=zeros(256,1);
for i=0+1:n(0+1)-1
    for j=0+1:n(1+1)-1
        l=bin_image(i,j,0+1)
            + bitshift(bin_image(i+1,j,0+1),1) ...
            + bitshift(bin_image(i,j+1,0+1),2) ...
            + bitshift(bin_image(i+1,j+1,0+1),3);
        for k=0+1:n(2+1)-1
            l=l+ bitshift(bin_image(i,j,k+1),4)...
                +bitshift(bin_image(i+1,j,k+1),5)...
                +bitshift(bin_image(i,j+1,k+1),6)...
                +bitshift(bin_image(i+1,j+1,k+1),7);
            h(l+1)=h(l+1)+1; l=bitshift(l,-4);
        end
    end
end
%-----------------------------------------------------------------
function vf = volfrac(h) %double volfrac(long int *h)
% Orginal by Ohser and Mcklich in C:
% double volfrac(long int *h)
% /* returns an estimate of the volume fraction V_V from the
%    vector h[0..255] of absolute frequencies of neighborhood
%    configurations of a binary image
% */
% {  int l;
%    long int iVol=0L, iVol1=0L;
%    for(l=0;l<256;l++)
%    {  iVol+=h[l];
%       if(l==(l|1)) iVol1+=h[l];
%    }
%    return (double)iVol1/(double)iVol;
```

```
% }
% Translation into Matlab:
iVol=0;iVol1=0;
for l=0+1:256
   iVol=iVol+h(l);
      if (l-1)==bitor((l-1),1); iVol1=iVol1+h(l); end
end
vf=iVol1/iVol;
%-----------------------------------------------------------------
function [sp surfaceAbs]=specsurf(h,Delta)
%double specsurf(long int *h, double *Delta)
% Orginal by Ohser and Mcklich in C:
% #include<math.h>
% double specsurf(long int *h, double *Delta)
% /* returns the specific surface area S_V from the gray-tone
%    histogram h[0..255], the grid spacing Delta[0..2] is input
% */
% {  int kl[13][2]= {{1,2}, {1,4}, {1,16}, {1,8}, {2,4},
%       {1,32}, {2,16},{1,64}, {4,16}, {1,128}, {2,64},
%       {4,32}, {8,16}};
%    double c[13]={0.045778, 0.045778, 0.045778, 0.036981,
%       0.036981, 0.036981, 0.036981, 0.036981, 0.036981,
%       0.035196, 0.035196, 0.035196, 0.035196};
%    double S_V=0.0;
%    int l, ny;
%    long iVol=0L;
%    double r[13];
%    r[0]=Delta[0]; r[1]=Delta[1]; r[2]=Delta[2];
%    r[3]=r[4]=sqrt(Delta[0]*Delta[0]+Delta[1]*Delta[1]);
%    r[5]=r[6]=sqrt(Delta[0]*Delta[0]+Delta[2]*Delta[2]);
%    r[7]=r[8]=sqrt(Delta[1]*Delta[1]+Delta[2]*Delta[2]);
%    r[9]=r[10]=r[11]=r[12]=sqrt(Delta[0]*Delta[0]
%                   +Delta[1]*Delta[1]+Delta[2]*Delta[2]);
%    for(l=0; l<256; l++)
%    {  iVol+=h[l];
%       for(ny=0; ny<13; ny++)
%       S_V+=h[l]*c[ny]/r[ny]
%            *((l==(l|kl[ny][0]))*(0==(l&kl[ny][1]))
%                +(l==(l|kl[ny][1]))*(0==(l&kl[ny][0])));
%    }
%    return 4.0*S_V/(double)iVol;
% }
% Translation into Matlab:
kl= [[1,2]; [1,4]; [1,16]; [1,8]; [2,4]; [1,32]; [2,16]; ...
    [1,64]; [4,16]; [1,128]; [2,64]; [4,32]; [8,16]];
c=[0.045778, 0.045778, 0.045778, 0.036981, 0.036981, ...
    0.036981, 0.036981, 0.036981, 0.036981, 0.035196, ...
    0.035196, 0.035196, 0.035196];
S_V=0;
iVol=0;
r(0+1)=Delta(0+1); r(1+1)=Delta(1+1); r(2+1)=Delta(2+1);
r(3+1)=sqrt(Delta(0+1)^2+Delta(1+1)^2);
r(4+1)=r(3+1);
r(5+1)=sqrt(Delta(0+1)^2+Delta(2+1)^2);
```

```
r(6+1)=r(5+1);
r(7+1)=sqrt(Delta(1+1)^2+Delta(2+1)^2);
r(8+1)=r(7+1);
r(9+1)=sqrt(Delta(0+1)^2+Delta(1+1)^2+Delta(2+1)^2);
r(10+1)=r(9+1);
r(11+1)=r(9+1);
r(12+1)=r(9+1);
for l=1:256
    iVol=iVol+h(l);
    for ny=1:13
        S_V=S_V+h(l)*c(ny)/r(ny)...
            *(((l-1)==bitor((l-1),kl(ny,0+1)))...
            *(0==bitand((l-1),kl(ny,1+1))) ...
            +((l-1)==bitor((l-1),kl(ny,1+1)))...
            *(0==bitand((l-1),kl(ny,0+1))));
    end
end
sp=4.0*S_V/iVol;
surfaceAbs=4.0*S_V*prod(Delta);
%%%%%%%%%%%%%%%%%%%%%%%%%%%%%%%%%%%%%%%%%%%%%%%%%%%%%%%%%%%%%%%%%%%%%%%%%%%
```

6.2 specSurfRec

```
%  specSurfRec
%  calculates the specific surface reconstructed by isosurface
%=============================================================
%
%  Name:        specSurfRec.m
%
%  Author:      EH
%  Date:        2006/12/08
%
%  Modifications on 2006/00/00 by EH:
%
%  Bugs, suggestions, remarks:
%
%=============================================================
function [vf sp solidSurface]=specSurfRec(bin_image,isoRes)
N=numel(bin_image);
%get surface as triangles
fv=isosurface(bin_image);
%extract vertices and "faces" from struct
ecken=fv.vertices;  %vertices of faces
        %first index is number of point (length n)
        %second index is for x, y, z (length 3)
gruppen=fv.faces;   %List of groups of 3 vertices that form
        %faces. First index is number of face (length m)
        %second index for involved points (length 3)
%get number of faces
tmp=size(gruppen,1);  %result = m
solidSurface=0;
for iFace=1:faceMTX
    eckenX=[ecken(gruppen(iFace,1),1) ...
```

```
                    ecken(gruppen(iFace,2),1) ecken(gruppen(iFace,3),1)];
    eckenY=[ecken(gruppen(iFace,1),2) ...
                    ecken(gruppen(iFace,2),2) ecken(gruppen(iFace,3),2)];
    eckenZ=[ecken(gruppen(iFace,1),3) ...
                    ecken(gruppen(iFace,2),3) ecken(gruppen(iFace,3),3)];
    vec1=[eckenX(2)-eckenX(1) eckenY(2)-eckenY(1)...
                    eckenZ(2)-eckenZ(1)]; %one face vector
    vec2=[eckenX(3)-eckenX(1) eckenY(3)-eckenY(1)...
                eckenZ(3)-eckenZ(1)]; %other face vector
    vecProd=cross(vec1,vec2); %vector product
    faceSurf=1/2*norm(vecProd);
    solidSurface=solidSurface+faceSurf;
end
disp(['surface of the solid / m**2 = '...
    num2str(solidSurface*isoRes^2)])
vf=sum(sum(sum(bin_image)))/N;
sp=solidSurface/N/isoRes;
```

6.3 Pore-Space Segmentation

```
%-----------------------------------------------------------------
% generate list of local maxima with average height
%-----------------------------------------------------------------
% d: result of distance transform, size MTX**2, 0 for solid
% discRad: disc radius in pixel units
% ms: search range +/- for local maximum in pixel units
% minDist: minimum Euclidean distance between maxima in p. u.
maxMat=zeros(MTX); %matrix with local maxima,
                   %used for visualization only
nMaxEst=round((MTX/discRad)^2);
%estimation of upper limit for number of local maxima
nMaxCount=0; %counter for local maxima found
maxList=zeros(nMaxEst,3); %list with average height and coordinates
for i1=1+mS:MTX-mS
    for i2=1+mS:MTX-mS
        if d(i1,i2)>0 %if within pore space
                      %(otherwise discs (0) contribute)
            if d(i1,i2)==max(max(d(i1-mS:i1+mS,i2-mS:i2+mS)))
                maxMat(i1,i2)=mean(mean(d(i1-mS:i1+mS,...
                               i2-mS:i2+mS)));
                nMaxCount=nMaxCount+1;
                maxList(nMaxCount,:)=[maxMat(i1,i2),i1,i2];
            end
        end
    end
end
maxList=maxList(1:nMaxCount,:); %truncate list to eff. number
%%% If inter-max distance to small, select highest-av. max %%%
maxListNew=zeros(nMaxCount,3);
toSmall=0;
newCount=0;
for iMax=1:nMaxCount %go through list from beginning
```

```
    for iMaxRest=iMax+1:nMaxCount %compare with rest
        if norm(maxList(iMax,2:3)-maxList(iMaxRest,2:3))...
           <minDist
        %if distance to small
            toSmall=1;
            if maxList(iMax,1)>=maxList(iMaxRest,1)
            %if actual value higher
                maxList(iMaxRest,:)=maxList(iMax,:);
                %shift for later tests
            end
            break %stop comparison with iMax
        end
    end
    if ~toSmall
        newCount=newCount+1;
        maxListNew(newCount,:)=maxList(iMax,:);
        %retain local maximum
    else
        toSmall=0; %reset test variable and proceed
    end
end
maxListNew=maxListNew(1:newCount,:); %truncate to eff. number
clear maxList %no longer used and modified anyway
%-----------------------------------------------------------------
% assign pore space to pore center, descending sucessively in
% height
%-----------------------------------------------------------------
shiftMat=[1 0; -1 0; 0 1; 0 -1]; %matrix with possible shifts
% parallel to axis
nShifts=size(shiftMat,1);
assigned=zeros(MTX);
for iMax=1:newCount %assign a number to each local maximum
    assigned(maxListNew(iMax,2),maxListNew(iMax,3))=iMax;
end
iMaxAv=min(find(maxListNew(:,1)==max(maxListNew(:,1))));
%(first) index with maximum average
level=floor(d(maxListNew(iMaxAv,2),maxListNew(iMaxAv,3)));
%integer part of highest level
daumen=1;
overlappFound=pi*daumen; %set some value > 0
                         %for first while test
%set region not searched for max to zero (otherwise artifacts)
d(1:mS,:)=0;d(:,1:mS)=0;
d(:,MTX-mS+1:MTX)=0;d(MTX-mS+1:MTX,:)=0;
while level>=0 %for all levels
    while overlappFound>0
    %continue if some assignement done in previous pass
    %at given level
        overlappFound=0;
        randShiftVec=randperm(nShifts); %random shift-index
                                        %permutation
        for iShift=1:nShifts %for all shift directions
            shiftDirInd=randShiftVec(iShift);
                %shift-direction index
```

```
            toDo=(d>level)&(~assigned);
            %mask with actual locations to be assigned at
            %given level
            identified=toDo...
                &circshift(assigned,shiftMat(shiftDirInd,:));
            %shift assigned over toDo: overlapp?
            nIdPerShift=sum(sum(identified)); %numver of
                                              %overlapps
            if nIdPerShift>0
            %set region with overlapp to corresponding
            %assigned value
                assigned(identified)=...
                    assigned(circshift(...
                    identified,-shiftMat(shiftDirInd,:)));
                overlappFound=overlappFound+nIdPerShift;
            end
        end
    end
    level=level-1;
    %if no more assignments at given level,
    %decrease level and continue
    overlappFound=pi*daumen;
    %for this, set some value > 0 for first while test
end
assigned(~dens)=-1;
assigned(1:mS,:)=0;
assigned(:,1:mS)=0;
assigned(:,MTX-mS+1:MTX)=0;
assigned(MTX-mS+1:MTX,:)=0;
```

6.4 Slice Selection

```
% program for the simmulation of slice selection through
% integration of Bloch equations in the rotating frame:
% dM/dt=gamma MxB with
% B = (0,-B1(t),G*z), i.e., nutation around y toward x
% in the center of the slice (no field by the gradient)

%
% Usage:      slice_sim_sinc_n
%

%=============================================================
%
% Name:        slice_sim_sinc_n.m
%
% Author:      Dirk Mertens and Edme H. Hardy
% Date:        2003
%
% Modifications 2004 by DM: Translation from PV-Wave to MatLab
```

```
%
% Bugs, suggestions, remarks:
%
%==========================================================

function slice_sim_sinc_n
%%% Parameters for image-file output
bilder=1; %1 for generation of output
figH=5; %figure height in cm
figW=7.5;%figure width in cm
imForm='-deps2'; %output format is eps
imPath='../bilder/';

%%% Experimental parameters
lZ=1E-2; %sample length in m
dSlice=4E-3; %slice thickness in m
refRel=0.52; %relative duration of refocusing gradient,
             %e. g. 0.5 or 0.52
gyrmag=2.6752E8; %gyromagnetic ratio for 1H in rad/s/T
phiP=pi/2; %pulse angle in center of slice
tau=0.001; %pulse duration in s
n=3; %number of sinc roots on each side of the maximum
bw=1/(tau/(2*n)); %bandwidth in Hz
gZ=2*pi*bw/dSlice/gyrmag; %calculate gradient amplitude

%%% Simulation parameters
tStepsInt=20000; %number of time steps for the integration
tStepsFft=1024; %number of time steps for FFT
zMTX=128; %number of grid points in position space
tIncInt=tau/tStepsInt; %time increment in integration
tIncFft=10*tau/tStepsFft; %time increment in FFT
zInc=lZ/zMTX; %separation of space points
tAxPulse=tIncInt*(-tStepsInt/2:tStepsInt/2-1); %time axis for
                                               %pulse shape
tAxPlot=tIncInt*(0:tStepsInt-1); %time axis for plot
tAxFft=tIncFft*(-tStepsFft/2:tStepsFft/2-1); %time axis for FFT
zAx=zInc*(-zMTX/2:zMTX/2-1); %z axis

%%% Definition of B1(t) for the sinc pulse
sincArg=n*pi*tAxPulse/(tau/2); %argument of the sinc pulse
b1=sin(sincArg)./sincArg;
b1(isnan(b1))=1; %set function value for argument 0
sincArgFft=n*pi*tAxFft/(tau/2); %argument of sinc pulse for FFT
b1Fft=sin(sincArgFft)./sincArgFft;
b1Fft(isnan(b1Fft))=1; %set function value for argument 0
iL=find(abs(tAxFft-(-tau/2))==min(abs(tAxFft-(-tau/2))));
  %index of time -tau/2
iR=find(abs(tAxFft-tau/2)==min(abs(tAxFft-tau/2)));
  %index of time tau/2
b1Fft(1:iL)=0; %truncation of sinc before -tau/2
b1Fft(iR:end)=0; %truncation of sinc after tau/2
b1Spec=fftshift(fft(fftshift(b1Fft))); %Fourier transform
```

```
  %of the pulse shape
b1AvIst=mean(b1); %actual average pulse amplitude
b1AvSoll=phiP/(gyrmag*tau); %required average pulse amplitude
b1=-b1*b1AvSoll/b1AvIst; %correction of B1 amplitude

%%%% Pulse representation in time and frequency domain
figure(1)
plot (1e3*[tAxPlot tau 1.52*tau],1e6*[b1 0 0],'k',...
                                    'LineWidth', 1.5)
grid
xlim([0 1.6e3*tau])
xlabel('t / ms')
ylabel('B_1 / \mu T')
if bilder == 1
    set(1,'PaperPosition',[0.63 6.3 figW figH])
    print(imForm, [imPath 'sliceSim1'])
end
figure(2)
plot (1e3*[tAxPlot(1) tau tau (1+refRel)...
    *tau (1+refRel)*tau],...
    1e3*[gZ gZ -gZ -gZ 0],'k','LineWidth', 1.5)
grid
xlim([0 1.6e3*tau])
xlabel('t / ms')
ylabel('G_s / (mT/m)')
if bilder == 1
    set(2,'PaperPosition',[0.63 6.3 figW figH])
    print(imForm, [imPath 'sliceSim2'])
end
figure(3)
fAx=(1/tIncFft/tStepsFft)*(-tStepsFft/2:tStepsFft/2-1);
    %frequency axis
fU=-lZ/2*gZ*gyrmag/2/pi; %lowest frequency in the sample
                         %with slice gradient
fO=-fU; %highest frequency in the sample with slice gradient
iU=find(abs(fAx-fU)==min(abs(fAx-fU))); %corresponding index
                                       %on the frequency axis
iO=find(abs(fAx-fO)==min(abs(fAx-fO))); %corresponding index
                                       %on the frequency axis
plot(fAx(iU:iO)/1e3,real(b1Spec(iU:iO))/max(abs(b1Spec)),...
        'k','LineWidth', 1.5)
axis tight
grid
xlabel('Frequency / kHz')
ylabel('Spectrum / a.u.')
if bilder == 1
    set(3,'PaperPosition',[0.63 6.3 figW figH])
    print(imForm, [imPath 'sliceSim3'])
end

%%% Integration of the Bloch equations
wZ=gyrmag*gZ*zAx; %-angular precession frequency due to gradient
```

```
w1=b1*gyrmag; %-angular nutation frequency due to B1
mMat=zeros(3,zMTX); %magnetic field (Mx,My,Mz for zMTX points)
mMat(3,:)=1; %equilibrium magnetization (Mz = 1)
for k=1:tStepsInt
    mMatAlt=mMat; %save magnetization of previous time step
    mMat(1,:)=mMatAlt(1,:)+(mMatAlt(2,:).*wZ-mMatAlt(3,:)...
              *w1(k))*tIncInt;
    mMat(2,:)=mMatAlt(2,:)+(0-mMatAlt(1,:).*wZ)*tIncInt;
    mMat(3,:)=mMatAlt(3,:)+(mMatAlt(1,:)*w1(k)-0)*tIncInt;
end

%%% Refocusing
ref_phase=-wZ*refRel*tau;      % phase after refocusing for
    % the defined duration. Precession with -omega Z and
    % omegaZ=-wZ
mMatAlt=mMat;
% rotation in the (x,y) plane using the rotation matrix
% ((cosP -sinP)(sinP cosP))
mMat(1,:)=mMatAlt(1,:).*cos(ref_phase)-mMatAlt(2,:)...
    .*sin(ref_phase);
mMat(2,:)=mMatAlt(1,:).*sin(ref_phase)+mMatAlt(2,:)...
    .*cos(ref_phase);
% visualization of refocusing
figure(4)
plot (1e3*zAx,mMat(3,:),'k--','LineWidth', 1.5), hold on
plot (1e3*zAx,mMat(1,:),'k-','LineWidth', 1.5)
plot (1e3*zAx,mMat(2,:),'k.','MarkerSize', 3), hold off
axis ([-1e3*lZ/2 1e3*lZ/2 -.4 1.2]), grid on
xlabel ('z / mm')
ylabel ('M_\alpha / M_0')
if bilder == 1
    set(4,'PaperPosition',[0.63 6.3 figW figH])
    print(imForm, [imPath 'sliceSim4'])
end
```

Chapter 7
NMR Line Shape Parametrization

Due to field inhomogeneities NMR line shapes are frequently asymmetric. This indicates higher order contributions to the inhomogeneity that are more difficult to correct by shimming than the first-order contributions. In view of line shape modeling, a parametrized analytical asymmetric line shape involving a second-order component is derived.

7.1 Assumptions

It is assumed that

1. The signal decay for the considered line in a homogeneous field is monoexponential, corresponding to a Lorentz line shape after Fourier transformation.
2. The actual field has a quadratic dependence along the symmetry axis of the sample, leading to a resonance-frequency distribution ("spectrum") that has to be calculated.
3. The spectral contributions of 1 are broadened by the distribution of 2 or vice versa, corresponding to a convolution, see below.

7.2 Lorentz Line Shape

The Lorentz distribution L centered around frequency $\nu = 0$ is given by (7.1). It has a single parameter γ that equals the full width at half height. The distribution is normalized to one:

$$L(\nu) = \frac{\gamma}{\pi(\nu^2 + \gamma^2)} \,. \tag{7.1}$$

E.H. Hardy, *NMR Methods for the Investigation of Structure and Transport*,
DOI 10.1007/978-3-642-21628-2_7, © Springer-Verlag Berlin Heidelberg 2012

7.3 Field Distribution

A quadratic spatial dependence of the field inhomogeneity results in a quadratic spatial dependence of the NMR resonance-frequency shift with respect to a homogeneous field. Thus the resonance frequency ν in the rotating frame as function of the z coordinate in direction of the symmetry axis of the sample is expressed with constant second derivative ν_{zz} as

$$\nu = \frac{1}{2}\nu_{zz}z^2 \,. \tag{7.2}$$

Next the frequency probability density $f(\nu)$ or "spectrum" has to be calculated for this assumed spatial distribution.[1] The relation is derived considering the cumulative probability density function $F(\nu)$.

It is assumed that frequency is a monotonous function of position along the considered coordinate. This is the case for the spatial dependence of (7.2) if the sample is located on the positive z axis or also if the sample is symmetric around $z = 0$ and the halves are considered separately. Likewise a monotonous function is obtained for a linear, cubic, etc. dependence.

If the sample is homogeneous and has constant cross section the number of observed spins from the coordinate origin to height z is proportional to z. Accordingly the cumulative frequency distribution $F(\nu)$ for resonance-frequency shifts up to ν can be expressed by the corresponding coordinate $z(\nu)$ as:

$$F(\nu) = \frac{z(\nu)}{z_{\text{tot}}} \,. \tag{7.3}$$

Division by the total sample extent z_{tot} along the considered coordinate has the effect that the cumulative frequency distribution is normalized to one. Thus it holds for an infinitesimal change in F

$$\mathrm{d}F(\nu) = \frac{\mathrm{d}z(\nu)}{z_{\text{tot}}} = \frac{1}{z_{\text{tot}}}\frac{\mathrm{d}z}{\mathrm{d}\nu}\,\mathrm{d}\nu \,. \tag{7.4}$$

The probability density f to be calculated is the derivative $\frac{\mathrm{d}F}{\mathrm{d}\nu}$ of the cumulative distribution, yielding

$$f(\nu) = \frac{1}{z_{\text{tot}}}\frac{\mathrm{d}z}{\mathrm{d}\nu} \,. \tag{7.5}$$

To proceed (7.2) is solved for the coordinate,

[1] Usually the situation is opposite, i.e., the spectrum is observed in the experiment and the spatial distribution is unknown, resulting in a rather empirical shimming process.

$$z = \sqrt{\frac{2\nu}{\nu_{zz}}}\,, \tag{7.6}$$

and the derivative is calculated:

$$\frac{\mathrm{d}z}{\mathrm{d}\nu} = \frac{1}{\sqrt{2\nu\nu_{zz}}}\,. \tag{7.7}$$

Denoting the frequency at z_{tot} as ν_{max}, (7.5)–(7.7) finally yield

$$\boxed{f(\nu) = \frac{1}{2\sqrt{\nu_{\mathrm{max}}\nu}}\,.} \tag{7.8}$$

The frequency density f is normalized to one if it is integrated from zero to ν_{max} although it diverges at $z = 0$. It has only the maximum frequency as parameter. The first moment of the distribution is not zero. This corresponds to the experimental observation that second-order shims produce a frequency shift of the line.

7.4 Convolution

At each frequency $\tilde{\nu}$ the Lorentz distribution has a contribution with weight $L(\tilde{\nu})$. Thus in an inhomogeneous field as considered above distributions of type (7.8) shifted by $\tilde{\nu}$, $f(\nu - \tilde{\nu})$ are superimposed with these weights. The total spectrum $S(\nu)$ is obtained by integration over the Lorentz distribution:

$$S(\nu) = \int_{-\infty}^{\infty} L(\tilde{\nu}) f(\nu - \tilde{\nu})\mathrm{d}\tilde{\nu}\,. \tag{7.9}$$

As expressed by (7.9) the total signal is the convolution of the spectrum originating from the sample with the frequency distribution resulting from the instrument. Insertion of (7.1) and (7.8) yields

$$S(\nu) = \int_{\nu-\nu_{\mathrm{max}}}^{\nu} \frac{\gamma}{\pi(\tilde{\nu}^2 + \gamma^2)}\,\frac{1}{2}\,\frac{1}{\sqrt{\nu_{\mathrm{max}}(\nu - \tilde{\nu})}}\,\mathrm{d}\tilde{\nu}\,. \tag{7.10}$$

In the integration limits it has been used that the spectrum due to the inhomogeneous field is zero for frequencies below zero and above ν_{max}.

As convolution is commutative, it can be expressed alternatively as

$$S(\nu) = \int_{-\infty}^{\infty} f(\tilde{\nu}) L(\nu - \tilde{\nu})\mathrm{d}\tilde{\nu}\,. \tag{7.11}$$

This reflects the point of view that at each frequency $\tilde{\nu}$ resulting from the inhomogeneous field the Lorentz distribution $L(\nu - \tilde{\nu})$ from the sample shifted by $\tilde{\nu}$ contributes with weight $f(\tilde{\nu})$. Limiting the integration to the interval with $f(\tilde{\nu}) \neq 0$ yields

$$S(\nu) = \int_0^{\nu_{\max}} \frac{1}{2\sqrt{\nu_{\max}\tilde{\nu}}} \frac{\gamma}{\pi((\nu - \tilde{\nu})^2 + \gamma^2)} \, \mathrm{d}\tilde{\nu} \tag{7.12}$$

$$= \frac{\gamma}{2\pi\sqrt{\nu_{\max}}} \int_0^{\nu_{\max}} \frac{1}{\sqrt{\tilde{\nu}}} \frac{1}{\tilde{\nu}^2 - 2\nu\tilde{\nu} + \nu^2 + \gamma^2} \, \mathrm{d}\tilde{\nu} \, . \tag{7.13}$$

The integral is simplified by the transformation $y = \sqrt{\tilde{\nu}}$:

$$I(\nu) = 2 \int_0^{\sqrt{\nu_{\max}}} \frac{\mathrm{d}y}{y^4 - 2\nu y^2 + \nu^2 + \gamma^2} \, . \tag{7.14}$$

It can be solved analytically.[2] Insertion of the limits and simplification leads to the final result

$$\boxed{S(\nu) = \frac{1}{2\pi i \sqrt{\nu_{\max}}} \left(\frac{\arctan \sqrt{\frac{\nu_{\max}}{-\nu - \gamma i}}}{\sqrt{-\nu - \gamma i}} - \frac{\arctan \sqrt{\frac{\nu_{\max}}{-\nu + \gamma i}}}{\sqrt{-\nu + \gamma i}} \right)} \, . \tag{7.15}$$

Although (7.15) contains the complex unit i the function $S(\nu)$ for the total spectrum is real valued as it should be. The integral is normalized to one and the first moment is not zero. The distribution has two parameters, γ and $\nu_{\max}$, as it is the case for the Voigt function with γ and σ. In contrast to the Voigt distribution, where the convolution cannot be calculated analytically, no approximation of the convolution is necessary. It is suggested to denote the NMR line shape as *Lorentz-z2 profile*.

7.5 Examples

Profiles with different values for γ and $\nu_{\max}$ are shown in Fig. 7.1. Besides the total width the asymmetry varies considerably.

[2] Here using the online program at http://integrals.wolfram.com.

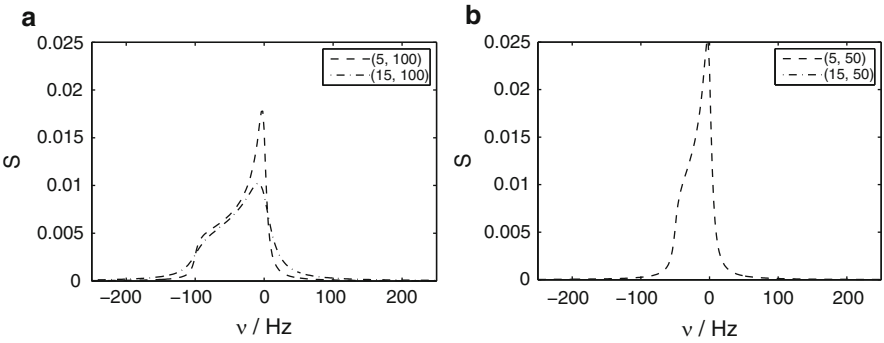

Fig. 7.1 Lorentz-$z2$ profiles. The four combinations of 5 Hz and 15 Hz Lorentz broadening γ with maximum field shift $\nu_{\max}$ of 100 Hz (**a**) and 50 Hz (**b**) are shown

7.6 Conclusion

A new parametrized analytical expression for an asymmetric line shape was derived. It is based on physical considerations as it is the case for the Voigt profile. The new type of line shape can be extended to other spatial field dependencies (cubic etc.). If necessary, several Lorentz-zn lines can be superimposed for an accurate line modeling.

Chapter 8
Gradient Echoes

8.1 Influence of Inhomogeneities on Echo Shifts

The pulse sequence depicted in Fig. 8.1 with gradients (a) represents the situation of a spin–spin echo sequence in which a switched gradient $G(t)$ still rises between excitation ($\pi/2$) and refocusing (π). From refocusing till data acquisition a constant gradient is assumed. As a result, the integral of the corresponding effective gradient $\tilde{G}(t)$ has its zero crossing already before the SE time t_{SE}. Calculation of the time t_{GE} at which an echo occurs is of interest in different applications.[1] In a simple situation where only a permanent gradient G_{p} in the same direction as $G(t)$ is present derivation of t^0_{GE} is straightforward. Here first the more general and complex case is treated that additionally a random spatial distribution $B_{\mathrm{i}}(\boldsymbol{r})$ of the z component of the magnetic field around the average value B_0 is present. In this section the applied gradient is considered to be switched on at the time of excitation, i.e., $\tau = 0$. The gradient direction is chosen to be y as in the low-field instrument presented in Sect. 3.2. Thus the angular velocity of Larmor precession is expressed in the rotating frame of reference as

$$\omega(\boldsymbol{r}, t) = -\gamma[(G_{\mathrm{p}} + G(t))y + B_{\mathrm{i}}(\boldsymbol{r})]. \tag{8.1}$$

The gradient echo is the maximum of the complex transverse magnetization

$$M^{+}(t) = \iiint_V \rho(\boldsymbol{r}) \exp(i\phi(\boldsymbol{r}, t))\mathrm{d}^3 r \tag{8.2}$$

after the refocusing pulse. Taking into account the change in sign resulting from the refocusing pulse the time and space dependent phase reads

[1] The presented calculations were performed in the context of the DFG project "Entwicklung eines NMR-gestützten Kapillarrheometers" with D. Mertens. Further details and experimental results are to be published.

E.H. Hardy, *NMR Methods for the Investigation of Structure and Transport*,
DOI 10.1007/978-3-642-21628-2_8, © Springer-Verlag Berlin Heidelberg 2012

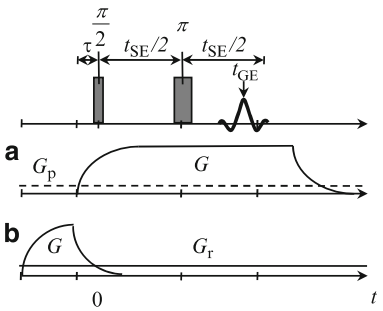

Fig. 8.1 "EDDI" sequence. Without application of a gradient $G(t)$ as in (**a**) or (**b**) the $\pi/2$ and π rf pulses produce a spin echo at the echo time t_{SE}. Here it is investigated at which time t_{GE} an echo occurs if a gradient $G(t)$ is switched and if constant gradients as well as other inhomogeneities of the magnetic field are present

$$\phi(\boldsymbol{r},t) = -\int_0^{t_{SE}/2} \omega(\boldsymbol{r},t)\mathrm{d}t + \int_{t_{SE}/2}^{t} \omega(\boldsymbol{r})\mathrm{d}t'. \tag{8.3}$$

The integrand after the refocusing pulse is time independent as $G(t)$ is assumed to have reached a constant value $\hat{G}$ at this time. A dimensionless function $g(t)$ is used to describe the time dependence before refocusing, i.e.,

$$G(t) = \hat{G}g(t). \tag{8.4}$$

With the further definition of the average quantity

$$\bar{g} = \frac{2}{t_{SE}}\int_0^{t_{SE}/2} g(t)\mathrm{d}t \tag{8.5}$$

the phase is expressed as

$$\begin{aligned}\phi(\boldsymbol{r},t) &= \gamma[(G_p + \hat{G}\bar{g})y + B_i(\boldsymbol{r})](t_{SE}/2 - 0)\\ &\quad -\gamma[(G_p + \hat{G})y + B_i(\boldsymbol{r})](t - t_{SE}/2)\\ &= \gamma\left[\left(G_p + \hat{G}\frac{1+\bar{g}}{2}\right)y + B_i(\boldsymbol{r})\right]t_{SE}\\ &\quad -\gamma[(G_p + \hat{G})y + B_i(\boldsymbol{r})]\,t.\end{aligned} \tag{8.6}$$

Without inhomogeneity $B_i(\boldsymbol{r})$ an echo with full amplitude $\iiint_V \rho(\boldsymbol{r})\mathrm{d}^3r$ (neglecting natural T_2 relaxation) is obtained if phase is zero for all y, i.e., for

$$t = t_{GE}^0 = t_{SE}\frac{G_p + \hat{G}\frac{1+\bar{g}}{2}}{G_p + \hat{G}}. \tag{8.7}$$

As $1 + \bar{g} < 2$ the gradient echo without permanent gradient G_p occurs indeed before t_SE. This is also the case in presence of G_p unless both gradients are of different polarity and if the permanent gradient dominates.

With the field inhomogeneity the time with phase zero depends on position:

$$t^0(\boldsymbol{r}) = t_\mathrm{SE} \frac{(G_\mathrm{p} + \hat{G}\frac{1+\bar{g}}{2})y + B_\mathrm{i}(\boldsymbol{r})}{(G_\mathrm{p} + \hat{G})y + B_\mathrm{i}(\boldsymbol{r})}. \tag{8.8}$$

In order to determine the time of the gradient echo for the integrated signal it is first assumed that the imaginary part of the total signal (8.2) is small enough to be neglected. The maximum is then searched for by taking the time derivative of the real part:

$$\frac{\partial}{\partial t}\mathrm{Re}(M^+(t)) = -\iiint_V \rho(\boldsymbol{r}) \sin(\phi(\boldsymbol{r},t)) \frac{\partial}{\partial t}\phi(\boldsymbol{r},t)\mathrm{d}^3 r. \tag{8.9}$$

It is zero at t_GE. Inserting the phase (8.6) and expanding the sine to first order leads to

$$\begin{aligned} 0 = \iiint_V \rho(\boldsymbol{r})\gamma \Bigg[\Bigg(\left(G_\mathrm{p} + \hat{G}\frac{1+\bar{g}}{2} \right) y + B_\mathrm{i}(\boldsymbol{r}) \Bigg) t_\mathrm{SE} \\ -((G_\mathrm{p} + \hat{G})y + B_\mathrm{i}(\boldsymbol{r}))\, t_\mathrm{GE} \Bigg] \\ \gamma \left[\left(G_\mathrm{p} + \hat{G} \right) y + B_\mathrm{i}(\boldsymbol{r}) \right] \mathrm{d}^3 r. \end{aligned} \tag{8.10}$$

Separation of the gradient- and SE time yields

$$\begin{aligned} \iiint_V \rho(\boldsymbol{r})[(G_\mathrm{p} + \hat{G})y + B_\mathrm{i}(\boldsymbol{r})]^2 \mathrm{d}^3 r\, t_\mathrm{GE} \\ = \iiint_V \rho(\boldsymbol{r}) \left[\left(G_\mathrm{p} + \hat{G}\frac{1+\bar{g}}{2} \right) y + B_\mathrm{i}(\boldsymbol{r}) \right] \\ \left[(G_\mathrm{p} + \hat{G})y + B_\mathrm{i}(\boldsymbol{r}) \right] \mathrm{d}^3 r\, t_\mathrm{SE}. \end{aligned} \tag{8.11}$$

Assuming that integrals with mixed products $yB_\mathrm{i}(\boldsymbol{r})$ can be neglected due to the random nature of $B_\mathrm{i}(\boldsymbol{r})$ integrals involving the homogeneous gradient and the field inhomogeneity can be separated:

$$t_\mathrm{GE} = t_\mathrm{SE} \left\{ \frac{G_\mathrm{p} + \hat{G}\frac{1+\bar{g}}{2}}{G_\mathrm{p} + \hat{G}} \frac{Y}{Y+I} + \frac{I}{Y+I} \right\}. \tag{8.12}$$

For the integrals over squared fields the abbreviations

$$I = \iiint_V \rho(\boldsymbol{r}) B_\mathrm{i}(\boldsymbol{r})^2 \mathrm{d}^3 r \tag{8.13}$$

and

$$Y = \iiint_V \rho(\boldsymbol{r})[(G_\mathrm{p} + \hat{G})y]^2 \mathrm{d}^3 r = (G_\mathrm{p} + \hat{G})^2 \iiint_V \rho(\boldsymbol{r}) y^2 \mathrm{d}^3 r \tag{8.14}$$

have been introduced.

In the limit of vanishing inhomogeneity ($I = 0$) the simple relation (8.7) is recovered from (8.12). For $I \neq 0$ the additional fields lead to a difference between t_SE and t_GE that is smaller than it is for t^0_GE. The magnitude of the effect is estimated for the low-field system shown in Fig. 3.4 on p. 86. It is assumed that the spin density ρ is constant. The integral in (8.13) is expressed using the probability density p_i (or spectrum) of the field:

$$I = \rho V \int_{-\infty}^{\infty} p_\mathrm{i}(B_\mathrm{i}) B_\mathrm{i}^2 \mathrm{d}B_\mathrm{i} = \rho V \sigma_\mathrm{i}^2. \tag{8.15}$$

For a rather high value of 440 Hz for the standard deviation of the frequency distribution in the spectrum the corresponding value for the field is

$$\sigma_\mathrm{i}^2 = (2\pi 440/\gamma)^2 = 10^{-10}\,\mathrm{T}^2\,, \tag{8.16}$$

where γ denotes the gyromagnetic ratio of the proton. For a sample with constant spin density, cross section A, and length l_y positioned in the middle of the gradient system, (8.14) yields

$$Y = \rho A (G_\mathrm{p} + \hat{G})^2 \int_{-l_y/2}^{l_y/2} y^2 \mathrm{d}y = \rho V \frac{1}{12} (G_\mathrm{p} + \hat{G})^2 l_y^2. \tag{8.17}$$

The observed length of the sample is about 3 cm. With typical values of 1 mT/m and 10 mT/m for G_p and $\hat{G}$, respectively, their contribution amounts to

$$\frac{1}{12} (G_\mathrm{p} + \hat{G})^2 l_y^2 = 10^{-8}\,\mathrm{T}^2. \tag{8.18}$$

Inserting 10 ms for t_SE and 0.95 for $(1 + \bar{g})/2$ into (8.7) yields $-500\,\mu$s for the echo shift in the absence of further inhomogeneities, i.e., also $G_\mathrm{p} = 0$. Including the above permanent gradient reduces the shift to $-455\,\mu$s. According to (8.12) this shift is further reduced to $-450\,\mu$s in the presence of field inhomogeneities. The difference of $5\,\mu$s can be detected using a short DW of $1\,\mu$s. However, it is neglected against larger effects and the simpler expression (8.7) is applied. In the

case of more pronounced inhomogeneities and weaker gradients the validity of this approximation has to be reconsidered.

8.2 Permanent Gradient and Rising Properties

Here and in the following it is assumed that further inhomogeneities as discussed in Sect. 8.1 can be neglected against switched and permanent or remanent gradients. The gradients are assumed to be in y direction. In this case the expression for the magnetization phase (8.3) reduces to

$$\begin{aligned}\phi(y,t) &= -\gamma y \left\{ -\int_0^{t_{SE}/2} [G_p + G(t)]\mathrm{d}t + \int_{t_{SE}/2}^{t} [G_p + G(t')]\mathrm{d}t' \right\} \\ &= -\gamma y\, \tilde{m}_0(t). \end{aligned} \tag{8.19}$$

In (8.19) and in the following the definition of the zeroth moment of the effective gradient after the refocusing pulse

$$\tilde{m}_0(t) = -\int_0^{t_{SE}/2} [G_p + G(t)]\mathrm{d}t + \int_{t_{SE}/2}^{t} [G_p + G(t')]\mathrm{d}t' \tag{8.20}$$

is used.

If gradient G is switched on before excitation as depicted in Fig. 8.1a the function g in (8.4) is replaced by $g(t-(-\tau))$. Assuming again that the asymptotic gradient amplitude $\hat{G}$ is already reached at the refocusing pulse the effective moment is expressed as

$$\tilde{m}_0(t) = -G_p \frac{t_{SE}}{2} - \hat{G} \int_0^{t_{SE}/2} g(t+\tau)\mathrm{d}t + (G_p + \hat{G}) \left(t - \frac{t_{SE}}{2} \right). \tag{8.21}$$

With the transformation $t' = t + \tau$ the condition $\tilde{m}_0(t_{GE}) = 0$ reads

$$-G_p \frac{t_{SE}}{2} - \hat{G} \int_{\tau}^{t_{SE}/2+\tau} g(t')\mathrm{d}t' + (G_p + \hat{G}) \left(t_{GE} - \frac{t_{SE}}{2} \right) = 0. \tag{8.22}$$

The part of the integral with $g(t > t_{SE}/2) = 1$ can be solved. Interchanging the limits of the remaining integral leads to

$$\hat{G} \int_{t_{SE}/2}^{\tau} g(t')\mathrm{d}t' = \hat{G}\tau - \hat{G} \left(t_{GE} - \frac{t_{SE}}{2} \right) - G_p (t_{GE} - t_{SE}) \,. \tag{8.23}$$

Differentiation with respect to τ and insertion of definition (8.4) finally yields

$$G(\tau) = \hat{G}\left(1 - \frac{\partial t_{\mathrm{GE}}}{\partial \tau}\right) - G_{\mathrm{p}}\frac{\partial t_{\mathrm{GE}}}{\partial \tau}. \tag{8.24}$$

One application of (8.24) is the determination of the rising properties of the switched gradient. The second term on the right-hand side can be omitted if G_{p} is compensated by a shim gradient.[2] If the permanent gradient is known, e.g., from an imaging experiment with frequency encoding on a sample with defined geometry, the asymptotic amplitude $\hat{G}$ of $G(\tau)$ can be derived from (8.24) with $\tau = 0$:

$$\hat{G} = G_{\mathrm{p}}\left.\frac{\partial t_{\mathrm{GE}}}{\partial \tau}\right|_{\tau=0}\left(1 - \left.\frac{\partial t_{\mathrm{GE}}}{\partial \tau}\right|_{\tau=0}\right)^{-1}. \tag{8.25}$$

It was used that $G(0) = 0$.

Another application is the determination of the permanent gradient G_{p} if $\hat{G}$ is known. Choosing $\tau = 0$ in (8.22) yields

$$G_{\mathrm{p}}(t_{\mathrm{SE}} - t_{\mathrm{GE}}) + \hat{G}\int_0^{t_{\mathrm{SE}}/2} g(t')\mathrm{d}t' - \hat{G}\left(t_{\mathrm{GE}} - \frac{t_{\mathrm{SE}}}{2}\right) = 0. \tag{8.26}$$

A preliminary measurement with compensated permanent gradient allows the measurement of the gradient echo time $t_{\mathrm{GE},0}$ yielding for the integral

$$\int_0^{t_{\mathrm{SE}}/2} g(t')\mathrm{d}t' = t_{\mathrm{GE},0} - \frac{t_{\mathrm{SE}}}{2}. \tag{8.27}$$

Insertion into (8.26) leads to the final result

$$G_{\mathrm{p}} = \hat{G}\frac{t_{\mathrm{GE}} - t_{\mathrm{GE},0}}{t_{\mathrm{SE}} - t_{\mathrm{GE}}}. \tag{8.28}$$

8.3 Determination of Decay Properties

If the gradient is switched off before excitation of transverse magnetization as depicted in Fig. 8.1b the decay properties can be investigated. The decaying gradient after excitation, denoted as $D(t)$ spoils the transverse magnetization. In order to obtain a gradient echo a known permanent gradient is applied, denoted here as read gradient G_{r}. Assuming this time that the switched gradient has completely decayed at the refocusing pulse, the relation corresponding to (8.22) reads

[2] This can be performed automatically by minimization of the spectral line width.

$$G_{\mathrm{r}}(t_{\mathrm{SE}} - t_{\mathrm{GE}}) + \int_{\tau}^{t_{\mathrm{SE}}/2+\tau} D(t')\mathrm{d}t' = 0. \tag{8.29}$$

By assumption the integral is zero after $t_{\mathrm{SE}}/2$. Interchanging the integral limits and derivation with respect to τ yields, in analogy to (8.24),

$$D(\tau) = -G_{\mathrm{r}} \frac{\partial t_{\mathrm{GE}}}{\partial \tau}. \tag{8.30}$$

8.4 Combined Effect of Transient and Permanent Gradients

8.4.1 Determination of the Effects

In Sects. 8.2, 8.3, and 8.5 it is shown how permanent and transient effects caused by a single pulsed gradient can be studied. Here the combined effect of transient and permanent gradients resulting from a pair of pulsed gradients is studied, see Fig. 8.2. Pairs of pulsed gradients are employed in the measurement of diffusion or flow. In the following, a model for $\tilde{m}_0(t)$ in the cases of gradient-pulse sequences depicted in Fig. 8.2a, b is presented.

In both cases care is taken to prepare a reproducible state of the effects. For the remanent permanent gradient as function of the pulsed-gradient amplitude a strong hysteresis was observed. Therefore at each new pulsed-gradient amplitude first a gradient-pulse train with decreasing amplitude and alternating polarity is applied. This minimizes the remanent permanent gradient. Then N_{d} dummy repetitions of the sequence with the pair of pulsed gradients is executed without data acquisition.

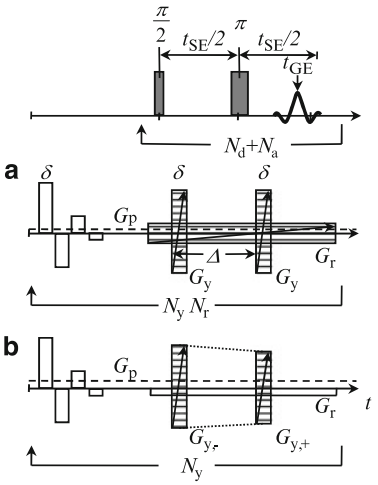

Fig. 8.2 Permanent-gradient and mismatch compensation (PGMC) sequence. Gradient-pulse scheme (**a**) is applied to measure the effects. They are subsequently compensated using scheme (**b**)

As a result, a reproducible remanent permanent gradient G_p depending on the pulsed-gradient amplitude is observed.

In gradient-pulse scheme (a) an incremented read gradient G_r is superimposed to the permanent gradient. The pulsed gradients G_y before and after the rf refocusing pulse have the same asymptotic amplitude $\hat{G}$, duration δ, and time separation Δ. The first dimension of the experiment is the acquisition time, the second dimension the read-gradient variation, and the third dimension, as in diffusometry or velocimetry, the variation of $\hat{G}$. Due to transient effects such as eddy currents and other experimental effects the gradients experienced by the sample deviate from the ideal rectangular shape represented in Fig. 8.2. The time dependence of the experienced gradient is described using a dimensionless function as in (8.4), denoted as $g_-(t)$ for the first gradient and as $g_+(t)$ for the second. Thus the zeroth moment of the effective gradient after time $t_\mathrm{SE}/2$ of the rf refocusing pulse is expressed as

$$\begin{aligned}\tilde{m}_0(t) &= (G_\mathrm{p} + G_\mathrm{r})(t - t_\mathrm{SE}) - \hat{G}\int_0^{t_\mathrm{SE}/2} g_-(t)\mathrm{d}t \\ &\quad + \hat{G}\int_{t_\mathrm{SE}/2}^{t} [g_-(t') + g_+(t')]\mathrm{d}t' \,. \end{aligned} \tag{8.31}$$

In the following it is assumed that both functions for the time dependence differ only by the time shift Δ and that a simple superposition of the gradient fields is applicable. For the sake of simplicity $\Delta = t_\mathrm{SE}/2$ is chosen, as it is usually the case in the experiment. Insertion of $g_+(t) = g_-(t - t_\mathrm{SE}/2)$ into (8.31) and omission of the index "-" yields

$$\begin{aligned}\tilde{m}_0(t) &= (G_\mathrm{p} + G_\mathrm{r})(t - t_\mathrm{SE}) \\ &\quad - \hat{G}\left[\int_0^{t_\mathrm{SE}/2} g(t)\mathrm{d}t - \int_{t_\mathrm{SE}/2}^{t} [g(t') + g(t' - t_\mathrm{SE}/2)]\mathrm{d}t'\right] \\ &= (G_\mathrm{p} + G_\mathrm{r})(t - t_\mathrm{SE}) \\ &\quad - \hat{G}\left[\int_0^{t_\mathrm{SE}/2} g(t)\mathrm{d}t - \int_{t_\mathrm{SE}/2}^{t} g(t')\mathrm{d}t' - \int_0^{t-t_\mathrm{SE}/2} g(t')\mathrm{d}t'\right] \\ &= (G_\mathrm{p} + G_\mathrm{r})(t - t_\mathrm{SE}) \\ &\quad + \hat{G}\left[\int_{t_\mathrm{SE}/2}^{t-t_\mathrm{SE}/2} g(t')\mathrm{d}t' + \int_{t_\mathrm{SE}/2}^{t} g(t')\mathrm{d}t'\right]. \end{aligned} \tag{8.32}$$

In order to allow for an analytical solution of the integrals an exponential decay is assumed after the gradient is switched off at time δ:

$$g(t > \delta) = g_0 \exp\left(-\frac{t - \delta}{t_\mathrm{d}}\right). \tag{8.33}$$

Insertion into (8.32) for times $t > t_{SE}/2 + \delta$ leads to

$$\begin{aligned}\tilde{m}_0(t) = {} & (G_p + G_r)(t - t_{SE}) \\ & + \hat{G} g_0 \exp(\delta/t_d) t_d \left[2 \exp\left(-\frac{t_{SE}/2}{t_d} \right) \right. \\ & \left. - \exp\left(-\frac{t - t_{SE}/2}{t_d} \right) - \exp\left(-\frac{t}{t_d} \right) \right]. \end{aligned} \tag{8.34}$$

Here the condition for the gradient echo $\tilde{m}_0(t_{GE}) = 0$ leads to a transcendental equation:

$$\begin{aligned}& (G_p + G_r)(t_{GE} - t_{SE}) + \hat{G} g_0 \exp(\delta/t_d) t_d \left[2 \exp\left(-\frac{t_{SE}/2}{t_d} \right) \right. \\ & \left. - \exp\left(-\frac{t_{GE} - t_{SE}/2}{t_d} \right) - \exp\left(-\frac{t_{GE}}{t_d} \right) \right] = 0. \end{aligned} \tag{8.35}$$

In order to compensate the permanent and transient effects the unknown permanent gradient G_p as well as the fraction g_0 and the time constant t_d for the transient effect have to be determined for each amplitude of the pulsed gradient $\hat{G}$. Possibly these quantities also depend on the time separation $t_{SE}/2$ and the gradient duration δ. For each amplitude of the pulsed gradient the gradient-echo times $t_{GE,j}$ can be extracted precisely from the echoes measured with varied read gradient $G_{r,j}$. Thus the unknown values can be obtained by a numerical minimization[3] of the left-hand side of (8.35)

$$\min_{G_p, g_0, t_d} \sum_j [\tilde{m}_0(t_{GE,j}, G_{r,j}, \hat{G}, t_{SE}, \delta; G_p, g_0, t_d)]^2. \tag{8.36}$$

The gradient separation and duration are chosen as in the experiment to be executed with compensation. For a reliable minimization a sufficient number of read gradients around the expected value of the permanent gradient should be chosen. As initial guess for the permanent gradient G_p a fraction of the respective pulsed-gradient amplitude $\hat{G}$ is set, e.g., 10^{-3}. Likewise for the initial value of the exponentially decaying function g_0 a small number of e.g., 10^{-3} is chosen. The time constant t_d is in the range of milliseconds.

Alternatively the unknown quantities can be determined for each pulsed-gradient amplitude using a single read-gradient amplitude if the expression for the entire echo signal

[3] As (8.35) cannot be solved for t_{GE} a minimization has to be used instead of a fit. This was performed using the "lsqnonlin" function of MATLAB®. Fitting is a special case of minimization. For the signal fit described below the dedicated function "lsqcurvefit" was used.

$$M^{+}(t) = \int \rho(y) \exp(-i\gamma \tilde{m}_0(t)\, y)\mathrm{d}y \tag{8.37}$$

with $\tilde{m}_0(t)$ given by (8.34) is fitted to the measured signal. The spin-density profile $\rho(y)$ detected by the rf coil can be determined experimentally. If it is approximated by a combination of cosine sections and linear parts the integral can be solved analytically, simplifying the fitting procedure. The cosine sections yield for the signal

$$\begin{aligned} f^{+}(t) &= \int_{y_1}^{y_2} \cos(ky) \exp(-i\gamma \tilde{m}_0(t)\, y)\mathrm{d}y \\ &= \left[\exp(-i\gamma \tilde{m}_0(t) y) \frac{i\gamma \tilde{m}_0(t) \cos(ky) - k \sin(ky)}{(\gamma \tilde{m}_0(t))^2 - k^2} \right]_{y_1}^{y_2}. \end{aligned} \tag{8.38}$$

In the fit the real parts of the measured and calculated signal normalized to maximum one were used. Here the results of the minimization (8.36) were chosen as initial guesses. For a symmetrically detected spin density with $y_1 = -y_2$ the integral can be significantly simplified.

8.4.2 Compensation of the Effects

Compensation of the permanent and transient effects at the time of the echo signifies:

1. $\tilde{m}_0(t_{\mathrm{SE}}) = 0$, i.e., $t_{\mathrm{GE}} = t_{\mathrm{SE}}$ and
2. no gradient experienced at t_{SE}.

Condition 1 cannot be satisfied by the application of a time-independent read gradient. Instead the asymptotic amplitude $\hat{G}_+$ of the pulsed gradient after the rf refocusing pulse is modified with respect to the amplitude of the first gradient $\hat{G}_-$, see Fig. 8.2 with gradient-pulse scheme (b). Insertion of condition 1 in (8.31) with the assumption of a simple time shift for the dimensionless function yields

$$-\hat{G}_- \int_0^{t_{\mathrm{SE}}/2} g(t)\mathrm{d}t + \hat{G}_- \int_{t_{\mathrm{SE}}/2}^{t_{\mathrm{SE}}} g(t)\mathrm{d}t + \hat{G}_+ \int_0^{t_{\mathrm{SE}}/2} g(t)\mathrm{d}t = 0. \tag{8.39}$$

Solving this equation for the corrected second asymptotic amplitude shows that the relative correction amounts to the ratio of the integral in the second half of the pulse sequence to the integral in the first half. The first integral is largely dominated by the ideal value $\int_0^{\delta} 1\mathrm{d}t = \delta$. Approximating the first integral by this result yields

$$\hat{G}_+ = \hat{G}_- \left(1 - \frac{1}{\delta} \int_{t_{\mathrm{SE}}/2}^{t_{\mathrm{SE}}} g(t)\mathrm{d}t \right). \tag{8.40}$$

If the exponential decay (8.33) is assumed solving of the integral leads to

$$\hat{G}_+ = \hat{G}_- \left(1 - g_0 \exp(\delta/t_\mathrm{d}) \frac{t_\mathrm{d}}{\delta} \left[\exp\left(-\frac{t_\mathrm{SE}/2}{t_\mathrm{d}}\right) - \exp\left(-\frac{t_\mathrm{SE}}{t_\mathrm{d}}\right)\right]\right) \tag{8.41}$$

for condition 1.

Condition 2 requires that at time t_SE the superposition of all gradients equals zero. Assuming again a common time function shifted by the gradient separation condition 2 reads

$$G_\mathrm{p} + G_\mathrm{r} + \hat{G}_- g(t_\mathrm{SE}) + \hat{G}_+ g(t_\mathrm{SE}/2) = 0. \tag{8.42}$$

In the exponential approximation condition 2 is fulfilled by application of the read gradient

$$G_\mathrm{r} = -G_\mathrm{p} - g_0 \exp(\delta/t_\mathrm{d}) \left[\hat{G}_- \exp\left(-\frac{t_\mathrm{SE}}{t_\mathrm{d}}\right) + \hat{G}_+ \exp\left(-\frac{t_\mathrm{SE}/2}{t_\mathrm{d}}\right)\right] \tag{8.43}$$

with $\hat{G}_+$ given by (8.41).

8.4.3 Simplified Model

The transcendental equation (8.35) can be solved approximately if the gradient-echo time is close to the SE time, $t_\mathrm{GE} \approx t_\mathrm{SE}$. First the third exponential in the parenthesis is neglected as its negative argument is then approximately twice that of the other two exponentials. It has to be assumed in addition that the SE time t_SE is much larger than the decay time t_d. Writing the second exponential as $\exp(-(t_\mathrm{GE} - t_\mathrm{SE})/t_\mathrm{d}) \exp(-t_\mathrm{SE}/(2t_\mathrm{d}))$ and factorization yields

$$(G_\mathrm{p} + G_\mathrm{r})(t_\mathrm{GE} - t_\mathrm{SE}) + \hat{G} g_0 t_\mathrm{d} \exp\left(\frac{\delta - t_\mathrm{SE}/2}{t_\mathrm{d}}\right) \left[2 - \exp\left(-\frac{t_\mathrm{GE} - t_\mathrm{SE}}{t_\mathrm{d}}\right)\right] = 0. \tag{8.44}$$

The remaining exponential with t_GE is replaced by the linear approximation for the case that $(t_\mathrm{GE} - t_\mathrm{SE})/t_\mathrm{d}$ is close to one:

$$(G_\mathrm{p} + G_\mathrm{r})(t_\mathrm{GE} - t_\mathrm{SE}) + \hat{G} g_0 t_\mathrm{d} \exp\left(\frac{\delta - t_\mathrm{SE}/2}{t_\mathrm{d}}\right) \left[1 + \frac{t_\mathrm{GE} - t_\mathrm{SE}}{t_\mathrm{d}}\right] = 0. \tag{8.45}$$

Collection of the terms linear in t_GE and factorization of the gradient-pulse duration δ in the term independent of t_GE leads to

$$\left[G_\mathrm{p} + G_\mathrm{r} + \hat{G} g_0 \exp\left(\frac{\delta - t_\mathrm{SE}/2}{t_\mathrm{d}}\right)\right](t_\mathrm{GE} - t_\mathrm{SE}) + \hat{G} g_0 \frac{t_\mathrm{d}}{\delta} \exp\left(\frac{\delta - t_\mathrm{SE}/2}{t_\mathrm{d}}\right)\delta = 0. \tag{8.46}$$

The simplified model (8.46) corresponds to the case in which a modified permanent gradient

$$G'_\mathrm{p} = G_\mathrm{p} + \hat{G} g_0 \exp\left(\frac{\delta - t_\mathrm{SE}/2}{t_\mathrm{d}}\right) \tag{8.47}$$

exists and in which the second gradient pulse of duration δ has an apparent amplitude mismatch with respect to the first amplitude of

$$G_\mathrm{m} = \hat{G} g_0 \frac{t_\mathrm{d}}{\delta} \exp\left(\frac{\delta - t_\mathrm{SE}/2}{t_\mathrm{d}}\right). \tag{8.48}$$

Consistently, neglecting the first exponential in (8.41) corresponds to the subtraction of G_m from the amplitude of the second gradient-pulse amplitude. Likewise this approximation corresponds in (8.43) to the compensation of G'_p. The simplified equation (8.46) can be solved for t_GE or $t_\mathrm{SE} - t_\mathrm{GE}$ leading to a hyperbola:

$$t_\mathrm{SE} - t_\mathrm{GE} = \delta \frac{G_\mathrm{m}}{G'_\mathrm{p} + G_\mathrm{r}}. \tag{8.49}$$

For each amplitude of the pulsed gradient the unknown quantities G_m and G'_p can be determined by a fit of (8.49) to experimentally observed echo-time shifts as a function of read-gradient amplitude.

8.4.4 Comparison of Both Models

The simplified model expressed in the hyperbola (8.49) is phenomenological if no explanation is provided for the modified permanent gradient G'_p or the mismatch of the gradient amplitudes G_m. A similar model is already presented in [1]. The description leading to (8.34) is a physical model in the sense that the observed effects are explained by the linear superposition of an exponential decay following each pulsed gradient, the two functions differing only by the time shift of the gradient pulses.

In the conducted experiments corrections with the results G'_p and G_m of the simple model (8.49) were sufficient to remove the effects on the echo position and shape. As to be expected from the assumption $t_\mathrm{GE} \approx t_\mathrm{SE}$ in the derivation the hyperbola is not a good model for large echo-time shifts, but these are left out from the fit. Experimental shifts for three different values of the pules-gradient amplitude are plotted as crosses (+) in Fig. 8.3. The dashed line represents the fitted hyperbola. The more complex model (8.35) can be provided with $G_\mathrm{p}, g_0, t_\mathrm{d}$ obtained from the minimization. Then the gradient-echo time in this model can be determined by a

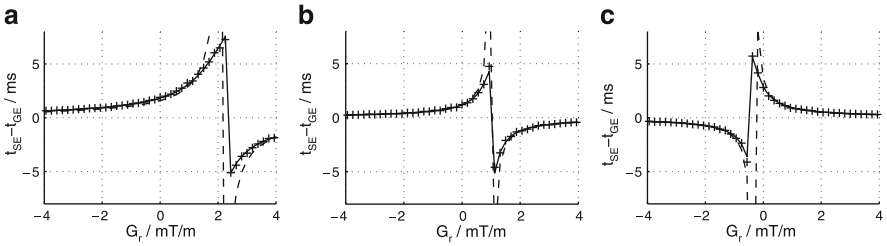

Fig. 8.3 Echo-time shift in the PGMC sequence as a function of read-gradient amplitude. Crosses (+): experimental results. *Dashed line*: fit of the simplified model. *Solid line*: time shift obtained from the minimization of the more complex model, leading to a close agreement. (**a**) $\hat{G} = -0.95$ T/m. (**b**) $\hat{G} = -0.25$ T/m. (**c**) $\hat{G} = 0.25$ T/m

numerical search for the root in the vicinity of the measured gradient-echo time.[4] The agreement of the experimental echo-time shifts with the ones from the more complex model represented as solid lines in Fig. 8.3 is significantly better than for the simple model (8.49). However, it has to be noted that the more complex model is more flexible, having three instead of two parameters.

As corrections using the simple model were sufficient in the studied cases the questions arise if the more complex model really describes the effects more accurately and if this model has practical advantages.

Two indications were found that the more complex model provides indeed a more accurate description. Independent measurements of the permanent gradient as the ones presented above and below result in a significantly lower value than the one obtained by the simple model. This is to be expected from (8.47) as the modified permanent gradient is augmented by contributions of the transient effects. In addition to the considerations involving only the gradient-echo time the entire signal predicted by the two models can be compared to the experimental signal. After determination of the detected spin density the signal is computed using (8.37) with the effective zeroth moment either from the more complex model (8.34) or using the modified permanent gradient and apparent gradient-amplitude mismatch obtained from the simple model. As can be seen from Fig. 8.4 the agreement of the experimental signal (dots) with the results of the more complex model (solid line) is better than with the signal computed using the simple model (dashed line). In particular, the more complex model is capable of reproducing experimentally observed features such as two gradient echoes, see Fig. 8.4g.

Depending on the accuracy of the more complex model two practical advantages are given. As the included transient effects are time dependent the three parameters can be obtained from a single fit to an experimental signal. No variation of the read gradient G_r is required. In addition the two parameters of the simple model, i.e., modified permanent gradient and apparent mismatch are valid for a specific

[4]Here using the "fzero" function of MATLAB®.

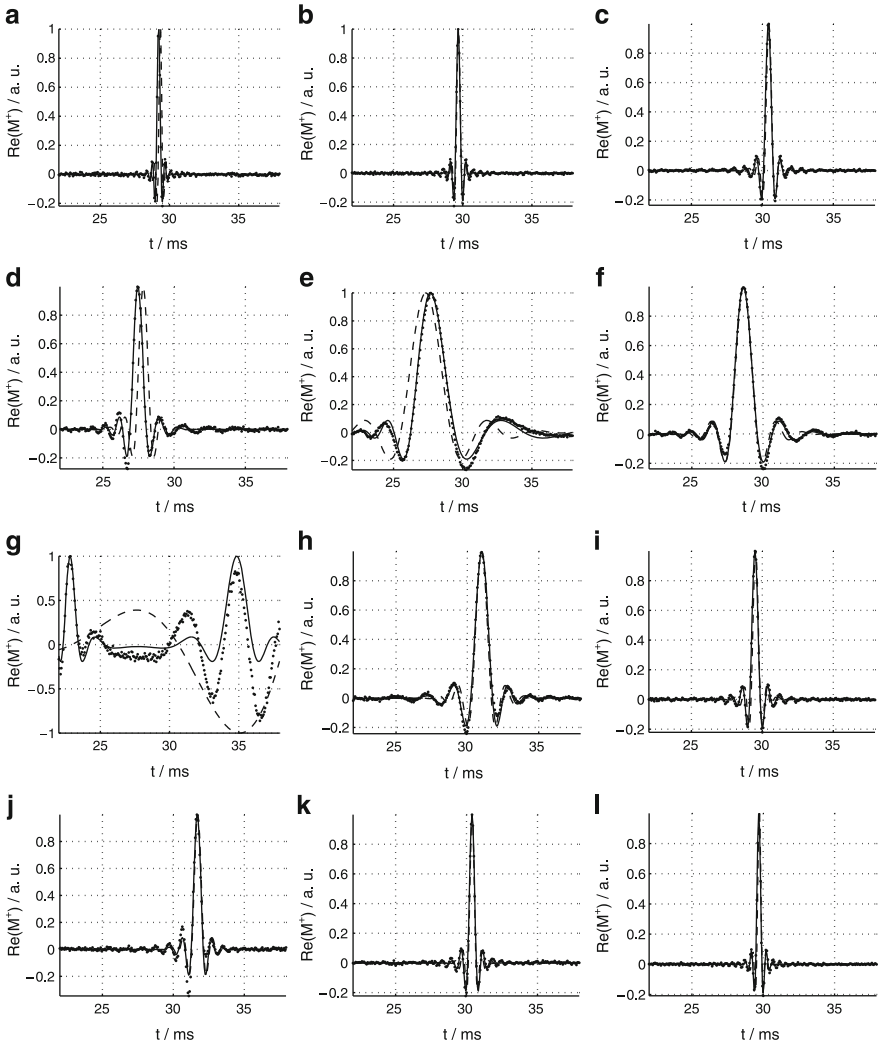

Fig. 8.4 Signal in the PGMC sequence for different amplitudes of the pulsed gradient and read gradient. *Dots*: experimental results. *Dashed line*: signal calculated with the effective zeroth moment corresponding to the simplified model. Solid line: fit of the more complex model. Calculations require the detected spin-density profile as input. *Left column*: $\hat{G} = -0.95$ T/m. *Central column*: $\hat{G} = -0.25$ T/m. *Right column*: $\hat{G} = 0.25$ T/m. First Row ((**a**) to (**c**)): $G_r = -3.0$ mT/m. Second Row ((**d**) to (**f**)): $G_r = 0.6$ mT/m. Third Row ((**g**) to (**i**)): $G_r = 2.3$ mT/m. Fourth Row ((**j**) to (**l**)): $G_r = 4.1$ mT/m

combination of t_{SE} and δ. The dependence on these experimental parameters is included in the expressions (8.41) and (8.43) that determine the compensation in the more complex model. However, it has to be verified that the parameters G_p, g_0, t_d

obtained from the minimization or signal fit do not depend on the gradient duration or separation. If this is not the case assuming a multiexponential decay could provide a sufficiently accurate description.

8.5 Sequence with Storing Period

A pulse sequence with storing period for the NMR measurement of pulsed gradients is shown in Fig. 8.5. The rf part starts with a stimulated echo, see also Fig. 4.35, p. 152. It is followed by a SE detection of the stimulated echo. The pulsed gradient G to be studied acts on the phase of transverse magnetization created by the excitation pulse during time δ. Half of the magnetization is stored on the z axis by the second rf pulse which has also nutation angle $\pi/2$. It only relaxes by longitudinal relaxation that can be significantly slower than transverse relaxation. Neither the decay of the pulsed gradient nor the rising of gradients switched on for the detection period affect longitudinal magnetization. During the detection period with SE time t_{SE} constant gradients are used. In the rf part three time scales can be suitably chosen: the duration of preparation δ, the storing period σ, and the echo time. In addition, the amplitude of the constant gradient during detection can be set to an appropriate value for a precise characterization of the pulsed gradient. The relevant equations of this method are derived in the following.

For an excitation pulse with B_1 in $-y$ direction the initial phase of transverse magnetization is zero. If the average gradient during the preparation period δ is denoted as $\bar{G}$ the phase before the second rf pulse amounts to

$$\phi(y, \delta_-) = -\gamma y \bar{G} \delta. \tag{8.50}$$

The second rf pulse with B_1 in y direction rotates the x component of transverse magnetization back to the z axis. Consequently the longitudinal magnetization after the second rf pulse has a y dependence due to the preparation with gradient $\bar{G}$ and

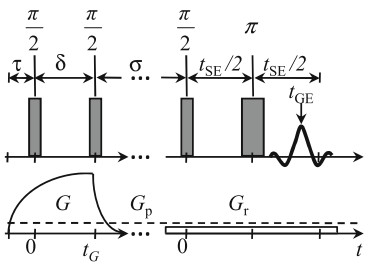

Fig. 8.5 "EGBERT" sequence. The rf part is a spin-echo (SE) detected stimulated echo (STE). The pulsed gradient G to be characterized acts on the magnetization phase during time δ between excitation and storage. This is investigated using a weaker constant gradient in the SE detection period

in general due to the y dependence of spin density $\rho(y)$:

$$M_z(y, \delta_+) = \rho(y) \cos(\phi(y, \delta_-)). \tag{8.51}$$

During the storing period σ inhomogeneities of the magnetic field do not influence longitudinal magnetization and longitudinal relaxation is neglected. It is assumed that the remaining transverse magnetization is spoiled during the storing period by T_2^* relaxation. The detection period in the form of a spin echo starts with the third $\pi/2$ pulse which is chosen as origin of the detection time axis t. With a constant gradient G_d during detection the magnetization phase after the refocusing π pulse at $t_\mathrm{SE}/2$ reads

$$\phi(y, t) = -\gamma y G_\mathrm{d}(t - t_\mathrm{SE}). \tag{8.52}$$

In the calculation of the signal according to e.g., (8.37) the spin density with the modulation given by (8.51) has to be inserted:

$$M^+(t) = \int \rho(y) \cos(\phi(y, \delta_-)) \exp(i\phi(y, t)) \, \mathrm{d}y. \tag{8.53}$$

The argument of the cosine is abbreviated by ϕ_δ and the argument of the exponential by $i\phi_t$. Application of the Euler formula and transformation of the products into sums yields

$$M^+(t) = \int \rho(y) \left\{ \frac{1}{2}[\cos(\phi_\delta + \phi_t) + \cos(\phi_\delta - \phi_t)] + \frac{i}{2}[\sin(\phi_\delta + \phi_t) - \sin(\phi_\delta - \phi_t)] \right\} \mathrm{d}y. \tag{8.54}$$

Insertion of (8.50) and (8.52) produces for the arguments of the trigonometric functions

$$\phi_\delta \pm \phi_t = -\gamma y[\bar{G}\delta \pm G_\mathrm{d}(t - t_\mathrm{SE})]. \tag{8.55}$$

For a sample with constant spin density ρ which is symmetric with respect to the origin $y = 0$ of the gradient system the integral of the sine functions is zero for all times. The integral of the cosine functions is maximal if the argument is zero for all coordinates y. Accordingly two echoes with half height are obtained at the gradient-echo times

$$t_\mathrm{SE} - t_\mathrm{GE1} = \delta \frac{\bar{G}}{G_\mathrm{d}} \tag{8.56}$$

and

$$t_\mathrm{SE} - t_\mathrm{GE2} = -\delta \frac{\bar{G}}{G_\mathrm{d}}. \tag{8.57}$$

The gradient echoes are symmetric with respect to a spin echo. The latter can be observed as longitudinal magnetization without phase encoding is generated by longitudinal relaxation during the storage period. Subtracting (8.56) and (8.57) leads

to the final expression for the gradient-echo time difference which can be determined accurately in the experiment:

$$\frac{t_{\mathrm{GE2}} - t_{\mathrm{GE1}}}{2} = \delta \frac{\bar{G}}{G_{\mathrm{d}}}. \tag{8.58}$$

8.5.1 Determination of Permanent Gradients

The sequence shown in Fig. 8.5 can be used to measure remanent permanent gradients G_{p}, as the sequences presented in Sects. 8.2 and 8.4. For this purpose a constant gradient G_{c} is applied during the entire duration of the experiment, see below. In addition a read gradient G_{r} is superimposed during the detection period. It is switched on at the beginning of the storing period σ so that it has settled when transverse magnetization is generated. Insertion of $\bar{G} = G_{\mathrm{p}} + G_{\mathrm{c}}$ and $G_{\mathrm{d}} = G_{\mathrm{p}} + G_{\mathrm{c}} + G_{\mathrm{r}}$ in (8.58) and solving for G_{p} yields

$$G_{\mathrm{p}} = -\frac{\delta\, G_{\mathrm{c}} - (G_{\mathrm{c}} + G_{\mathrm{r}})(t_{\mathrm{GE2}} - t_{\mathrm{GE1}})/2}{\delta - (t_{\mathrm{GE2}} - t_{\mathrm{GE1}})/2}. \tag{8.59}$$

It is assumed that the applied gradients G_{c} and G_{r} are known. However, for the determination of G_{p} from the above equation the sign of $t_{\mathrm{GE2}} - t_{\mathrm{GE1}}$ has to be known, whereas the experiment yields only the absolute value of the time difference. According to (8.58) the sign is equal to the sign of the fraction $(G_{\mathrm{p}} + G_{\mathrm{c}})/(G_{\mathrm{p}} + G_{\mathrm{c}} + G_{\mathrm{r}})$. Thus it can be arranged, e.g., by the choice $G_{\mathrm{c}} > 0$, $G_{\mathrm{r}} > 0$, and $G_{\mathrm{c}} > |G_{\mathrm{p}}|$ that $t_{\mathrm{GE2}} - t_{\mathrm{GE1}}$ is positive.

8.5.2 Determination of Pulsed Gradients

A further application of the sequence represented in Fig. 8.5 is the characterization of pulsed gradients with high amplitude. In the simplest case no additional permanent gradient is present (or it is compensated by a constant gradient). Then in the preparation period only the gradient to be studied is active and in the detection period only the read gradient G_{r}. If the first gradient G is switched on with a delay τ before the first rf pulse and is expressed as in (8.4) using a dimensionless function (8.58) results in

$$\bar{G}(\tau) = \hat{G}\frac{1}{\delta}\int_{\tau}^{\tau+\delta} g(t)\mathrm{d}t = \frac{t_{\mathrm{GE2}} - t_{\mathrm{GE1}}}{2\delta} G_{\mathrm{r}}. \tag{8.60}$$

In order to achieve a good time resolution the preparation time δ should be kept short, e.g., 25 μ s. This is also necessary as otherwise the time shifts according to (8.58) can become too long to be measured for $\tilde{G} \gg G_{\mathrm{r}}$. In addition short rf pulses are required to avoid slice selection.

Reference

1. Hrovat MI, Wade CG (1981) NMR pulsed-gradient diffusion measurements.1. Spin-echo stability and gradient calibration. J Magn Reson 44(1):62–75

Chapter 9
Imaging with an Inhomogeneous Gradient

Usually in imaging experiments it is assumed that the superimposed magnetic field has a homogeneous gradient, i.e., a linear dependence on the respective spatial coordinate. Deviations from linearity lead to distortions of image intensity and geometry [1]. In the following it is shown that these distortions can be calculated analytically for a realistic spatial dependence of the superimposed field.

An inhomogeneous gradient in x direction is considered. The ideal expression $B_z = B_0 + G_x x$ for the superimposed field in (2.26) is replaced by a more realistic function exhibiting a close to linear dependence in the center and approaching a constant value outside the central region:

$$B_z(x) = B_0 + G_x a \tan^{-1}(x/a). \tag{9.1}$$

The derivative of (9.1) or gradient has the value G_x at $x = 0$ and fades off to zero for large $|x|$. At $x = \pm a$ the gradient has decayed to half of its value in the center, $G_x/2$. For the magnetization phase the expression

$$\phi(x,t) = -\gamma \int_0^t G_x(t') a \tan^{-1}(x/a)\, \mathrm{d}t' \tag{9.2}$$

$$= -k_x a \tan^{-1}(x/a) \tag{9.3}$$

is obtained instead of (2.35) and the experimental signal is calculated by

$$M^+(k_x) = \int \rho(x) \exp[-i k_x a \tan^{-1}(x/a)] \mathrm{d}x \tag{9.4}$$

instead of (2.38). The integral transform in (9.4) is no longer a Fourier transform with conjugated variables k_x and x. Consequently the inverse Fourier transform according to (2.39) does not yield the spin density. However, the result of the inverse Fourier transform can be calculated if (9.4) is expressed as Fourier transform by a substitution of variable. The new variable is the counterpart of k_x in the phase factor.

E.H. Hardy, *NMR Methods for the Investigation of Structure and Transport*,
DOI 10.1007/978-3-642-21628-2_9,

Thus the inner function of the variable transformation is given by

$$\tilde{x} = \phi(x) = a \tan^{-1}(x/a). \tag{9.5}$$

For the chosen function the required derivative

$$\mathrm{d}\tilde{x}/\mathrm{d}x = \phi'(x) = \frac{1}{1 + (x/a)^2} \tag{9.6}$$

as well as the inverse function

$$x = \phi^{-1}(\tilde{x}) = a \tan(\tilde{x}/a) \tag{9.7}$$

can be calculated analytically. Insertion into (9.4) yields

$$M^{+}(k_x) = \int \rho(a \tan(\tilde{x}/a)) \exp[-i k_x \tilde{x}]\{1 + \tan^2(\tilde{x}/a)\}\mathrm{d}\tilde{x}. \tag{9.8}$$

Accordingly inverse Fourier transformation of the measured signal produces

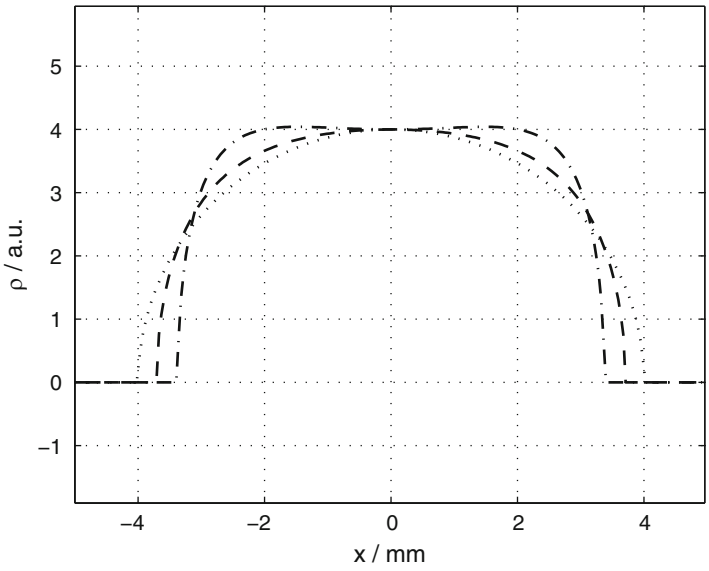

Fig. 9.1 Result of imaging with an inhomogeneous gradient according to (9.1). For the observed spin density the common case of a homogeneous spin density in a cylinder with radius R projected on a direction perpendicular to the tube axis is chosen. Points: ideal gradient. *Dashed line*: $a = 2R$. *Dash-dotted line*: $a = 1.25R$

$$\rho(a\tan(\tilde{x}/a))\{1+\tan^2(\tilde{x}/a)\}. \tag{9.9}$$

The spin density as function of $\tilde{x}$ appears compressed as for $\tilde{x} \in [-a\pi/2\ a\pi/2]$ the argument of the spin density covers the entire interval $[-\infty\ \infty]$. Additionally the apparent spin density is increasingly exaggerated outside the center.

Examples of distortions for a simple spin density and different values of a are shown in Fig. 9.1. The observed spin density corresponds to the common case of a homogeneous spin density in a circular tube with radius R projected on a direction perpendicular to the tube axis:

$$\rho(x) = c\sqrt{R^2 - x^2}\ . \tag{9.10}$$

The constant c is the value of the spin density in the 2D case. Imaging with the assumed inhomogeneous gradient produces the result

$$\tilde{\rho}(\tilde{x}) = c\sqrt{R^2 - a^2\tan^2(\tilde{x}/a)}\{1+\tan^2(\tilde{x}/a)\}. \tag{9.11}$$

Reference

1. Kimmich R (1997) NMR tomography, diffusometry, relaxometry. Springer-Verlag, Berlin, Heidelberg, New York

Index

E.H. Hardy, *NMR Methods for the Investigation of Structure and Transport*,
DOI 10.1007/978-3-642-21628-2, © Springer-Verlag Berlin Heidelberg 2012

N

O

P

Q

R

S